

Dissertation
submitted to the
Combined Faculties for the Natural Sciences and for Mathematics
of the Ruperto-Carola University of Heidelberg, Germany
for the degree of
Doctor of Natural Sciences

presented by
Delia Lisa Bucher, M.Sc.
born in Göppingen, Germany
Oral-examination: 19th of April 2018

Functional characterization of flat clathrin lattices during endocytosis and cell migration

Referees:

Prof. Dr. Felix Wieland

Dr. Steeve Boulant

Table of Contents

ACKNOWLEDGEMENTS	IX
LIST OF ABBREVIATIONS	XI
1 ABSTRACT	1
2 INTRODUCTION	3
2.1 CLATHRIN-MEDIATED ENDOCYTOSIS (CME)	3
2.1.1 ENDOCYTOSIS: DIFFERENT INTERNALIZATION ROUTES TO THE ENDOSOMAL PATHWAY	3
2.1.2 THE CLATHRIN TRISKELION	4
2.1.3 THE MOLECULAR MECHANISM OF CME	6
2.2 FLAT CLATHRIN LATTICES	10
2.2.1 THE ROLE OF FLAT CLATHRIN COATS IN CCP FORMATION	10
2.2.2 ENDOCYTIC FUNCTIONS OF LARGER FLAT CLATHRIN ARRAYS	11
2.2.3 NON-ENDOCYTIC FUNCTIONS OF FLAT CLATHRIN LATTICES	12
2.3 CELLULAR INTERACTIONS WITH THE ECM	15
2.3.1 MOLECULAR COMPOSITION OF FAS	15
2.3.2 ADHESION DYNAMICS	16
2.3.3 ECM ASSEMBLY AND REMODELLING	17
3 AIM OF THIS THESIS	21
4 RESULTS	23
4.1 CELL LINE-SPECIFIC CHARACTERISTICS OF CLATHRIN COATS	23
4.1.1 CELL TYPE-SPECIFIC DYNAMICS OF CME	23
4.1.2 DIFFERENCES OF CME AT ATTACHED AND NON-ATTACHED PM PARTS	26
4.1.3 CELL TYPE-SPECIFIC SIZE AND MORPHOLOGY OF CCSS	30
4.2 INVESTIGATION OF STRUCTURAL CHANGES OF THE CLATHRIN COAT DURING CCP FORMATION	38
4.2.1 EM AND CLEM ANALYSIS OF CCSS DO NOT SUPPORT EXISTING GROWTH MODELS	38
4.2.2 MODELLING OF CCP ASSEMBLY REVEALS BENDING OF THE COAT BEFORE REACHING FULL SURFACE AREA	41
4.2.3 STARTING POINT OF ACQUIRING CURVATURE IS MARKED BY A CHANGE IN THE AP2/CLATHRIN RATIO	44
4.2.4 HIGH MEMBRANE TENSION INHIBITS THE FLAT-TO-CURVED TRANSITION OF CCSS	47
4.3 ROLE OF CLATHRIN-COATED PLAQUES IN CELL MIGRATION	51
4.3.1 SWITCH FROM FAS TO CLATHRIN-COATED PLAQUES DURING CELL MIGRATION	51
4.3.2 DRUG-INDUCED SWITCH FROM FAS TO CLATHRIN-COATED PLAQUES	55
4.3.3 INTEGRINS RECRUIT AND STABILIZE CLATHRIN-COATED PLAQUES	59
4.3.4 REMODELLING OF ECM AS A SIGNAL FOR CLATHRIN-COATED PLAQUE FORMATION	63
4.3.5 CLATHRIN-COATED PLAQUES FORM AT TOPOGRAPHICAL CUES	72
4.3.6 SWITCH FROM FAS TO CLATHRIN-COATED PLAQUES REGULATES CELL MIGRATION	75

5	DISCUSSION AND CONCLUSION	79
5.1	DIFFERENTIAL REGULATION OF CME DYNAMICS AND CLATHRIN COAT MORPHOLOGY BY CELL TYPE-SPECIFIC FACTORS AND PM IDENTITY	79
5.2	FLAT-TO-CURVED TRANSITION DURING CLATHRIN-MEDIATED ENDOCYTOSIS CORRELATES WITH A CHANGE IN CLATHRIN-ADAPTOR RATIO AND IS REGULATED BY MEMBRANE TENSION	84
5.3	CLATHRIN-COATED PLAQUES ARE ADHESION STRUCTURES INVOLVED IN REGULATION OF CELL MIGRATION	88
5.4	CONCLUSION ON THE FUNCTIONS OF FLAT CLATHRIN LATTICES	94
6	MATERIALS AND METHODS	95
6.1	MATERIALS	95
6.1.1	BUFFERS, SOLUTIONS AND REAGENTS	95
6.1.2	ENZYMES, PRIMER, OLIGONUCLEOTIDES, PLASMIDS, ANTIBODIES, AND FLUORESCENT REAGENTS	97
6.1.3	BACTERIAL CULTURE	101
6.1.4	CELL CULTURE	102
6.2	METHODS	103
6.2.1	BACTERIAL TRANSFORMATION	103
6.2.2	DNA ISOLATION	103
6.2.3	AGAROSE GEL ELECTROPHORESIS	103
6.2.4	POLYMERASE CHAIN REACTION (PCR)	104
6.2.5	RESTRICTION DIGESTION	104
6.2.6	LIGATION	104
6.2.7	GATEWAY CLONING	104
6.2.8	CLONING OF SHORT HAIRPIN RNA (SHRNA) ENCODING VECTOR FOR LENTIVIRUS PRODUCTION	105
6.2.9	LENTIVIRUS PRODUCTION	105
6.2.10	BACMAM PRODUCTION	106
6.2.11	SUBCULTURING OF MAMMALIAN CELLS	107
6.2.12	FREEZING AND THAWING OF MAMMALIAN CELLS	107
6.2.13	TRANSFECTION	107
6.2.14	TRANSDUCTION	108
6.2.15	CLEANING OF COVERSLEIPS FOR MICROSCOPY	108
6.2.16	COATING OF COVERSLEIPS	108
6.2.17	WESTERN BLOT (WB)	109
6.2.18	EM AND CLEM OF CLATHRIN STRUCTURES USING METAL REPLICAS OF UNROOFED MEMBRANE SHEETS	109
6.2.19	TRANSFORMATION OF IMAGES FOR CLEM	110
6.2.20	TEM AND CLEM ANALYSIS OF CCSS	111
6.2.21	WIDEFIELD EPIFLUORESCENCE MICROSCOPY	111
6.2.22	SPINNING DISC CONFOCAL MICROSCOPY	111
6.2.23	TOTAL INTERNAL REFLECTION FLUORESCENCE (TIRF) MICROSCOPY	111
6.2.24	STED NANOSCOPY	112
6.2.25	IMMUNOFLUORESCENCE	112
6.2.26	LIVE-CELL MICROSCOPY OF CME AT BOTTOM AND TOP PM	112
6.2.27	OSMOTIC SHOCK EXPERIMENT	113
6.2.28	INHIBITOR-INDUCED DISASSEMBLY OF FAS	113
6.2.29	INHIBITION OF SPECIFIC INTEGRINS	114
6.2.30	IMAGING OF FIBRONECTIN FIBRILLOGENESIS	114
6.2.31	ECM DEGRADATION ASSAY	115

6.2.32	GENERATION OF ADHESIVE MICROPATTERNS BY PHOTO-PATTERNING	116
6.2.33	PRODUCTION OF 3D-MICROPATTERNS BY SOFT LITHOGRAPHY	116
6.2.34	SURFACE TOPOGRAPHY MEASUREMENTS USING AFM	117
6.2.35	SEQUENTIAL SEEDING OF CELLS ON GRIDDED COVERSLEPS	117
6.2.36	TRACKING OF CLATHRIN STRUCTURES	118
6.3	MODELLING OF GROWTH BEHAVIOUR OF CCPs	119
6.3.1	CONSTANT AREA MODEL	119
6.3.2	DATA FITS	120
6.3.3	RELATE FLUORESCENCE INTENSITY AND SURFACE AREA BY MEANS OF CLEM	121
6.3.4	RELATE DIFFERENT FM DATASETS	121
6.3.5	RELATE EM AND FM DATASETS	121
6.3.6	DATA FILTERING	122
6.3.7	PARAMETER CHOICE AND DATA FITTING	123
6.3.8	CALCULATION OF THE SIZE HISTOGRAM	123
6.3.9	CURVATURE ACQUISITION DURING GROWTH: UPDATED MODEL	124
6.3.10	DATA FITS, PARAMETER CHOICE AND DATA FITTING	125
6.3.11	CALCULATION OF THE SIZE HISTOGRAM	126
6.3.12	CURVATURE ACQUISITION DURING GROWTH: FLAT-TO-CURVED TRANSITION CORROBORATES WITH THE CHANGE OF CLATHRIN/AP2 RATIO	126
6.3.13	LIVE CELL FM ANALYSIS RESAMPLING	126
6.3.14	CALCULATION OF THE RATIO HISTOGRAM DURING THE OSMOTIC SHOCK	127
6.3.15	QUANTIFICATION OF AGREEMENT BETWEEN MEASURED AND PREDICTED SIZE HISTOGRAMS	127
7	REFERENCES	129

Acknowledgements

Research can only be successful as a result of a strong team effort. I want to thank everybody who contributed to this work and/or supported me during the last years. The following list is by far not complete but everybody not included will receive my thanks in person.

I would like to thank Steeve Boulant, for his support and belief in me. I deeply appreciate the hours of scientific discussions with you and your unconventional way of running the lab. I am grateful that you gave me the opportunity to work and decide in my own way while always giving me encouragement. I am very thankful to Megan Stanifer. You brought order to where there was chaos and provided me help all the time I needed it. Thanks to all the old and new lab members as well as the rotation students who made the lab a great place to work.

I want to acknowledge the collaboration with Ulrich Schwarz and Felix Frey. It was a pleasure to work with you and it helped me to look at issues from a new perspective. Many thanks to Justin W. Taraska and Kem A. Sochacki for their invitation and their hospitality. I learned so much from you during my stay in Bethesda and you made me feel at home across the ocean.

I would like to thank Vibor Laketa and Ulrike Engel for their support on microscopy. I am thankful to Susann Kummer for her help with the STED microscopy. Our chats had the power to light up the dark microscopy room for me. Special thanks to Ada Cavalcanti for her help with everything concerning cell adhesion and her student Chiara Zambarada for her support with adhesive micropatterns. I always enjoyed working and discussing science with you. Thanks to Christian Huck for the AFM measurements. For you it was straightforward but for me it was a huge help. I want to acknowledge the work of Veronika Saharuka who helped me to establish the 3D-micropatterns during her internship. Working with you was a great experience and I wish you all the best for your own PhD.

I am very thankful to all my friends for their support during the last years. Thanks to my former flatmates (Melissa, Karo and Selina) for distracting me from work; to Anne for countless dinners; to Anika for caring words during hard times; to Julia for encouraging discussions; to my friends from Konstanz (Anka, Carmen and Ursula) for our weekend getaways; to my friends from school (Annegret, Anja, Becci, Jani, Nina, Steffi and Stefka) for their endless friendship.

I am incredibly grateful for all the support, care and love I receive from my family (Hans, Verena, Nico and Tim). Without you I could not have done it. And last but not least, I want to give heartfelt thanks to Jan for always being by my side.

List of abbreviations

2D	two-dimensional
3D	three-dimensional
AAK1	AP2 associated kinase 1
ADAM	a disintegrin and metalloproteinase
ADAMT	a disintegrin and metalloproteinase with thrombospondin motifs
AFM	atomic force microscopy
Amp	ampicillin
AP1, 2, 3	adaptor protein 1, 2, 3
ARH	autosomal recessive hypercholesterolemia
BAR	BIN/Amphiphysin/Rsv
BSA	bovine serum albumin
CAM	chloramphenicol
CB1R	cannabinoid receptor 1
CCP	clathrin-coated pit
CCR5	C-C chemokine receptor type 5
CCS	clathrin-coated structure
cFN	cellular fibronectin
ch-TOG	colonic hepatic tumour overexpressed gene
CHC	clathrin heavy chain
CLC	clathrin light chain
CLEM	correlative light and electron microscopy
CLIC/GEEC	clathrin-independent carrier/glycosylphosphatidylinositol-anchored protein enriched early endosomal compartment
CME	clathrin-mediated endocytosis
CVAK104	coated-vesicle-associated kinase of 104 kDa
Dab2	disabled homolog 2
DIC	differential interference contrast

DYRK1A	dual specificity tyrosine-phosphorylation-regulated kinase 1A
ECM	extracellular matrix
EDTA	ethylenediaminetetraacetic acid
eGFP	enhanced green fluorescent protein
EGFR	epidermal growth factor receptor
EM	electron microscopy
EPS15	epidermal growth factor substrate 15
FA	focal adhesion
FAK	focal adhesion kinase
FBS	fetal bovine serum
Fcho	Fer/Cip4 homology domain-only
FEME	fast endophilin-mediated endocytosis
FM	fluorescence microscopy
FNdFBS	fibronectin-depleted fetal bovine serum
FRAP	Fluorescence recovery after photobleaching
GAK	G-associated kinase
GAP	GTPase-activating protein
GEF	Guanine nucleotide exchange factor
Gen	gentamicin
GLUT4	glucose transporter type 4
GPCR	G-protein coupled receptors
Hsc70	heat shock cognate 71 kDa protein
IF	immunofluorescence
IL-2R β	interleukin-2 receptor β
iPALM	interferometric photoactivation and localization microscopy
Kan	kanamycin
LDLR	low-density lipoprotein receptor
LINC	linker of the nucleoskeleton and cytoskeleton

LPAR1	lysophosphatidic acid receptor 1
LRP6	low-density lipoprotein-related protein 6
MAP	mitogen-activated protein
MMP	matrix metalloproteinase
MOR	μ -opioid receptor
MRTF-A	myocardin related transcription factor-A
NG2	proteoglycan neural/glial antigen 2
OCRL	oculocerebrorenal syndrome of Lowe
p130Cas	p130 Crk-associated substrate
PCR	Polymerase chain reactions
PDL	poly-D-lysine
PDMS	polydimethylsiloxane
PEG	polyethylene glycol
PEI	polyethylenimine
PFA	paraformaldehyde
pFN	plasma fibronectin
PI	phosphoinositides
PI(3,4,5)P ₃	phosphatidylinositol (3,4,5)-trisphosphate
PI(3,4)P ₂	phosphatidylinositol (3,4)-bisphosphate
PI(4,5)P ₂	phosphatidylinositol (4,5)-bisphosphate
PLL	poly-L-lysine
PM	plasma membrane
PM	plasma membrane tension
Puro	puromycin
RECK	reversion-inducing Cys-rich protein with Kazal motif
RNAi	RNA interference
ROCK	Rho-associated protein kinase
SDS-PAGE	sodium dodecyl sulfate polyacrylamide gel electrophoresis

shRNA	short hairpin RNA
SNX9	sorting nexin 9
STED	stimulated emission depletion
TACC3	transforming acidic coiled protein 3
TEM	transmission electron microscopy
TfR	transferrin receptor
TGN	trans-Golgi network
TIMP	tissue inhibitor of metalloproteinases
TIRF	from total internal reflection fluorescence
UVO	ultraviolet/ozone
VASP	vasodilator-stimulated phosphoprotein
WB	Western blot
WGA	wheat germ agglutinin
YAP	Yes-associated protein
YAZ	transcriptional coactivator with PDZ-binding motif
β 1AR	β 1-adrenergic receptor

1 Abstract

Clathrin is a unique scaffold protein, which forms polyhedral cages at the plasma membrane. Adaptor proteins recruit clathrin to the plasma membrane where the triskelion-shaped clathrin units interact with each other and assemble into flat and curved lattices. The function of the curved clathrin-coated pits in forming clathrin-coated vesicles via dynamin-dependent scission during endocytosis is well studied. On the contrary, the role of the flat hexagonal clathrin arrays remains ambiguous and has been a controversial topic for decades.

In this PhD thesis, we used different microscopic techniques (live-cell confocal microscopy, stimulated emission depletion nanoscopy, transmission electron microscopy, correlative light and electron microscopy) combined with mathematical modelling or micrometre-scale manipulation of substrates to unravel the role of flat clathrin lattices during two cellular processes: 1) Endocytosis and 2) Cell migration.

1) We describe a novel clathrin-coated pit formation mechanism in which clathrin arrays first assemble as flat clathrin-coated structures until they reach around 70% of the final clathrin content. At that point a change in the adaptor/clathrin ratio marks the conversion from a flat to curved lattice and further addition of clathrin triskelia leads to the creation of a complete and invaginated clathrin-coated pit. We could show that the flat-to-curved transition of the clathrin coats is sensitive to the biophysical properties of plasma membrane and can be block by elevated plasma membrane tension.

2) We found a so far undescribed spatial relation between disassembling focal adhesions and newly forming larger flat clathrin lattices, called clathrin-coated plaques, during cell migration. We demonstrated that clathrin-coated plaques containing the extracellular matrix receptors integrins are generated at topographical cues of remodelled extracellular matrix and regulate cell migration as novel adhesive unit.

These specific functions put a new focus on the poorly understood flat clathrin coats and highlight the multiple cellular applicability of clathrin arrays.

Zusammenfassung

Clathrin ist ein einzigartiges Gerüstprotein, welches polyedrische Käfige an der Plasmamembran bildet. Adapterproteine rekrutieren Clathrin zur Plasmamembran wo die dreibeinigen Clathrin-Bausteine miteinander interagieren und sich zu flachen und eingekrümmten Gittern aneinanderlagern. Die Funktion der gekrümmten *clathrin-coated pits* während der Endozytose zur Bildung von *clathrin-coated vesicles* mittels Dynamin-abhängiger Abschnürung ist gut erforscht. Hingegen bleibt die Rolle der flachen hexagonalen Clathrin-Strukturen noch unklar und ist seit Jahrzehnten ein kontroverses Thema.

In dieser Doktorarbeit benutzten wir unterschiedliche mikroskopische Methoden (konfokale Lebendzell-Mikroskopie, *stimulated emission depletion nanoscopy*, Transmissionselektronenmikroskopie, korrelative Licht- und Elektronenmikroskopie) in Kombination mit mathematischen Modellierungen und Manipulation von Substraten im Mikrometerbereich um die Aufgabe von flachen Clathrin-Gittern in zwei zellulären Prozessen aufzudecken: 1) Endozytose und 2) Zellmigration.

1) Wir beschreiben einen neuen Entstehungsmechanismus für *clathrin-coated pits*, in welchem sich Clathrin zunächst zu flachen Strukturen zusammenlagert bis diese ungefähr 70% der endgültigen Clathrin-Trimeren enthalten. An diesem Punkt wird die Umwandlung von einem flachen zu einem gekrümmten Gitter durch eine Änderung im Adapter/Clathrin-Verhältnis angezeigt und die weitere Anlagerung von Clathrin-Triskelia führt zur Bildung eines fertigen und eingestülpten *clathrin-coated pit*.

2) Wir entdeckten einen bislang unbeschriebenen räumlichen Zusammenhang zwischen dem Abbau von Fokalen Adhäsionen und der Entstehung von größeren flachen Clathrin-Gittern, den so genannten *clathrin-coated plaques*, während der Zellmigration. Wir wiesen nach, dass *clathrin-coated plaques*, welche Integrine (Rezeptoren für die extrazelluläre Matrix) enthalten, an topografischen Markierungen von umorganisierter extrazellulärer Matrix gebildet werden und als neuartiges Anheftungselement die Zellmigration regulieren.

Diese spezifischen Funktionen setzen einen neuen Schwerpunkt auf die kaum verstandenen flachen Clathrin-Strukturen und zeigen die vielfältige zelluläre Einsetzbarkeit von Clathrin-Gittern auf.

2 Introduction

2.1 Clathrin-mediated endocytosis (CME)

2.1.1 Endocytosis: Different internalization routes to the endosomal pathway

The lipid bilayer of the plasma membrane (PM) surrounding cells separates the cytoplasm from the extracellular space. This barrier is necessary to generate a compartmentalized intracellular milieu where enzymatically catalysed chemical reactions take place. While small molecules (e.g. O₂, N₂, CO₂, and ethanol) can pass the PM by diffusion, cells had to develop different uptake mechanisms for larger and charged molecules that cannot pass the lipid bilayer. Passive and active transport of molecules over the PM is facilitated by transmembrane proteins, which serve as channels or transporters within the lipid bilayer (Yang and Hinner, 2015). Other molecules can be internalized by engulfment and further trafficking of PM-derived vesicles to the endosomal pathway (Doherty and McMahon, 2009). Such uptake pathways are commonly referred to endocytosis (Doherty and McMahon, 2009).

The mechanisms by which cells manage to form these endocytic vesicles can be separated in dynamin-dependent or -independent pathways according to their mechanism of membrane scission (Fig.2.1). Dynamin, a large GTPase, can mediate fission of vesicles from the PM by polymerizing around the neck of invaginated PM parts (Ferguson and De Camilli, 2012). In contrast, dynamin-independent endocytic pathways are often facilitated by actin polymerization, which helps to generate endocytic carriers of different size (Ferreira and Boucrot, 2017). For example, phagocytosis (Freeman and Grinstein, 2014; Gordon, 2016) and macropinocytosis (Mercer and Helenius, 2012; Marques, Grinstein and Freeman, 2017) are used to engulf large PM parts for the uptake of large particles and fluid, respectively. Other dynamin-independent uptake pathways like clathrin-independent carrier (CLIC)/glycosylphosphatidylinositol-anchored protein enriched early endosomal compartment (GEEC)-type endocytosis (Sabharanjak *et al.*, 2002; Kirkham *et al.*, 2005; Lundmark *et al.*, 2008), flotillin- (Glebov, Bright and Nichols, 2005) or Arf6-dependent endocytosis (Naslavsky, Weigert and Donaldson, 2004) are associated with smaller vesicular or tubular invaginations for specific cargo uptake. During dynamin-dependent endocytosis like clathrin-mediated endocytosis (CME) (McMahon and Boucrot, 2011), caveolae-dependent endocytosis (Parton and del Pozo, 2013; Cheng and Nichols, 2016), interleukin-2 receptor β (IL-2R β) pathway (Lamaze *et al.*, 2001; Sauvonnnet, Dujeancourt and Dautry-Varsat,



Figure 2.1: Different endocytic pathways. Schematic illustration of vesicle formation at the PM via dynamin-dependent and -independent mechanisms. Colour code: Actin (orange), dynamin (red), clathrin (black).

2005; Basquin *et al.*, 2015), and fast endophilin-mediated endocytosis (FEME) (Boucrot *et al.*, 2014), small pits (<200 nm in diameter) are formed at the PM.

Classically, endocytic routes are also separated in clathrin-dependent and -independent. While CME is a well-studied process, other endocytic pathways are less understood and even controversially discussed. Some of the so far described endocytic pathways might not work autonomous but only in combination with other uptake pathways (e.g. flotillin (Amaddii *et al.*, 2012; Sorkina, Caltagarone and Sorkin, 2013)) or might even not contribute to endocytosis at all (e.g. caveolae (Parton and del Pozo, 2013; Cheng and Nichols, 2016)). Although it is clear that clathrin-independent endocytosis includes regulated uptake mechanisms for special cargo, clathrin-dependent endocytosis is considered the most important constitutive and regulated uptake pathway for a broad variety of cargo proteins and receptors (Bitsikas, Corrêa and Nichols, 2014).

2.1.2 The clathrin triskelion

Endocytic clathrin-dependent vesicles are formed by a complex scaffolding coat consisting of multiple clathrin-associated proteins and clathrin molecules themselves. Together, they assemble at precise PM sites and drive the formation of clathrin-coated pits (CCPs) by complex mechanisms, which ultimately lead to the generation and stabilization of PM invaginations and dynamin-driven release of vesicles into the cytosol.

The building block of the clathrin-dependent uptake pathway is the clathrin triskelion, which is composed of three clathrin heavy chains (CHCs) and three clathrin light chains (CLCs) (Kirchhausen and Harrison, 1981; Ungewickell and Branton, 1981) (Fig.2.2a). There are two human isoforms of CHC. The ubiquitously expressed CHC17, and the CHC22, mostly

expressed in muscle and fat tissue, which show 85% amino acid similarity (Liu *et al.*, 2001; Wakeham *et al.*, 2005). While CHC17 is involved in CME as well as other intracellular processes, CHC22 has been shown to be important in muscle cells and fat cells in which it specifically mediates the intracellular traffic of glucose transporter type 4 (GLUT4) from its storage compartments to the PM (Vassilopoulos *et al.*, 2009; Dannhauser *et al.*, 2017). Since this PhD thesis focuses on the process of CME, this work only relates to CHC17 and this heavy chain will be referred to as CHC. For CLC, two human isoforms have been described, CLCa and CLCb, with 60% amino acid identity (Wakeham *et al.*, 2005). Both of these light chains associate with CHC17 but not with CHC22 (Liu *et al.*, 2001; Towler *et al.*, 2004). Although general CME is not affected by depletion of CLCs (Huang *et al.*, 2004; Poupon *et al.*, 2008), internalization of specific cargo (i.e. G-protein coupled receptors (GPCRs)) (Ferreira *et al.*, 2012), recruitment of proteins involved in actin polymerization to clathrin-coated structures (CCSs) (Chen and Brodsky, 2005), intracellular trafficking of mannose-6 phosphate receptor (Poupon *et al.*, 2008) as well as trafficking processes regulating cell migration (Majeed *et al.*, 2014; Chen *et al.*, 2017) have been linked to CLCs.

Within a clathrin triskelion, each CHC represents one leg with three domains: A globular terminal domain at the N-terminus, a bent distal segment, and a proximal region close to the tripod region (also called vertex), where CHCs trimerize (Kirchhausen and Harrison, 1984; Fotin *et al.*, 2004) (Fig. 2.2a). CLCs associate with the proximal segment of CHCs via their ordered central α -helical domain (Ungewickell, 1983; Chen *et al.*, 2002). The unique geometry of clathrin triskelia enables them to assemble into polyhedral cages by interacting with their proximal and distal segments (Smith, Grigorieff and Pearse, 1998; Musacchio *et al.*, 1999) (Fig. 2.2b). In such a lattice, one CHC leg from a triskelion runs from its own tripod region along two vertices of neighbouring triskelia. While the proximal and distal segments are facing outwards on such a

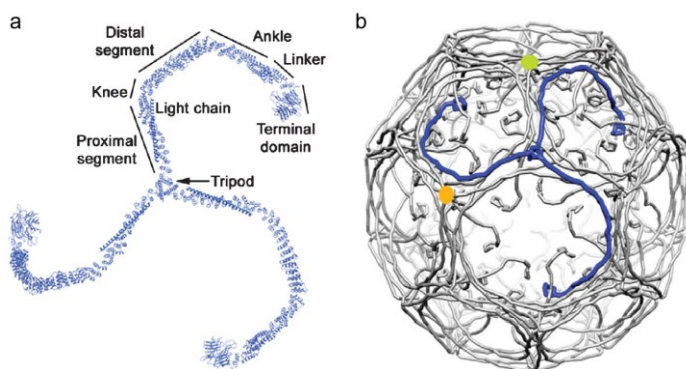


Figure 2.2: The clathrin triskelion as the unit of clathrin scaffolds. (a) Structure of a clathrin triskelion built up by three CHCs and three CLCs. Distinct domains of CHC are labelled. CLCs are represented by the ordered α -helical segments. (b) Packaging of clathrin triskelia into a polyhedral basket. One triskelion is highlighted in blue. Three vertices are marked by the centre of the blue triskelion and the green and orange dot. Illustrations were taken from Xing *et al.* (2010).

cage, the terminal domain turns inwards to be able to interact with proteins between the clathrin coat and the PM (Kirchhausen and Harrison, 1984; ter Haar *et al.*, 1998). For that purpose, there are different protein binding sites at the N-terminus of CHC that can interact with specific motifs of clathrin adaptors (e.g. clathrin-box motifs (LΦXΦ[D/E]; Φ: bulky hydrophobic amino acid) of adaptor protein 1,2, and 3 (AP1, AP2, and AP3), β-arrestin, amphiphysin, AP180, and epsin (ter Haar, Harrison and Kirchhausen, 2000) and W-box motifs (PWXXW, X: any amino acid) of amphiphysin and sorting nexin 9 (SNX9) (Ramjaun and McPherson, 1998; Miele *et al.*, 2004)).

Besides its function during CME at the PM, clathrin has been described to be involved in other processes. The proposed functions of larger flat clathrin lattice at the PM in signalling and cell adhesion will be introduced in paragraph 2.2.3. CCSs have been observed at intracellular membranes of the trans-Golgi network (TGN) (Mogelsvang *et al.*, 2004; Klumperman, 2011), endosomes (Raiborg *et al.*, 2002; Bonifacino and Rojas, 2006; Johannes and Popoff, 2008; Shields and Piper, 2011) as well as multivesicular bodies (Hurley and Hanson, 2010; Henne, Buchkovich and Emr, 2011), where they act in cargo sorting and intracellular traffic routes. Apart from these functions at membranes, clathrin is involved in regulatory processes during cell division. During mitosis, clathrin localizes to the mitotic spindle (Okamoto, McKinney and Jeng, 2000; Royle, Bright and Lagnado, 2005; Booth *et al.*, 2011). As a part of the transforming acidic coiled protein 3 (TACC3)/colonic hepatic tumour overexpressed gene (ch-TOG)/clathrin complex, clathrin helps crosslinks and stabilizes microtubular kinetochor fibres to regulate the segregation of chromosomes (Booth *et al.*, 2011; Royle, 2012). A separate clathrin pool at the spindle pole is important for to reassembly of fragmented mitotic Golgi clusters after mitosis (Radulescu, Siddhanta and Shields, 2007; Radulescu and Shields, 2012).

2.1.3 The molecular mechanism of CME

The process of CME involves a coordinated recruitment and assembly of numerous proteins. It can be separated into four different steps: 1) Nucleation, 2) CCP assembly, 3) scission, and 4) uncoating (Fig.2.3). Each step is characterized by the recruitment of different, often specific, clathrin-accessory proteins involved in regulating various molecular and ultrastructural steps of CME. While some steps are tightly linked to one crucial protein (e.g. scission and dynamin (Ferguson and De Camilli, 2012)), other functions are shared between several proteins (e.g. function in coupling of the clathrin coat to the actin cytoskeleton is mediated by the three epsin proteins (Messa *et al.*, 2014) or membrane-remodelling at early stages of CME is mediated by

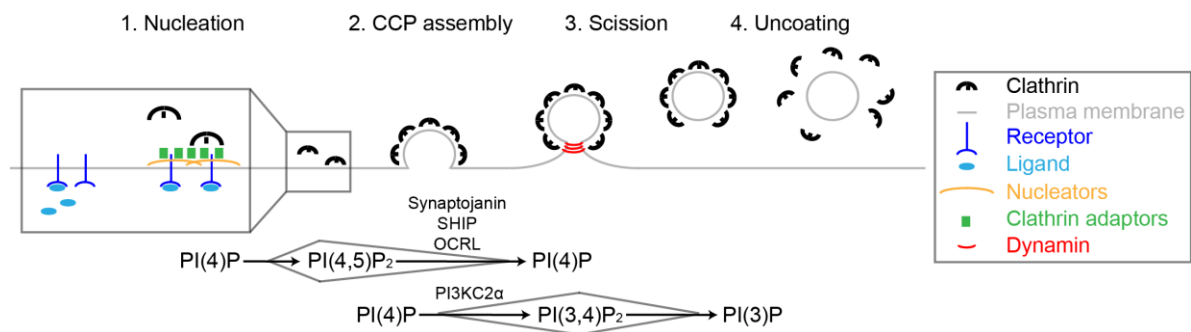


Figure 2.3: Steps of CME. Schematic illustration of the four steps during CME. The sequence of nucleation (1), CCP assembly (2), scission (3), and uncoating (4) with key proteins as well as PIP levels during each step are shown. Colour code: Clathrin (black), PM (grey), receptor (blue), ligand (turquoise), nucleators (orange), clathrin adaptors (green), and dynamin (red).

Fer/Cip4 homology domain-only (Fcho) proteins and epidermal growth factor substrate 15 (EPS15) (Wang *et al.*, 2016)).

During the initial nucleation step of CME, the clathrin adaptor AP2 needs to be recruited to specific PM parts to drive clathrin recruitment and assembly (Collins *et al.*, 2002). AP2 can bind to the PM by interacting with transmembrane cargo proteins and phosphoinositides (PIs) (Ohno *et al.*, 1995; Collins *et al.*, 2002; Höning *et al.*, 2005). By the help of early clathrin nucleators (like Fcho1/2 and EPS15/R), AP2 gets into its open conformation and can bind to specific motifs on cargo proteins (i.e. tyrosine-based motifs (YXX Φ) (Collawn *et al.*, 1990; Jadot *et al.*, 1992) and dileucine-based motifs ([DE]XXXL[LI]) (Letourneur and Klausner, 1992; Pond *et al.*, 1995)) and phosphatidylinositol 4,5-bisphosphate (PI(4,5)P₂) (Henne *et al.*, 2010; Umasankar *et al.*, 2014; Ma *et al.*, 2016). Other clathrin adaptors can help to recruit certain cargo to CCS assembly sites (e.g. the alternative clathrin adaptors disabled homolog 2 (Dab2), Numb, and autosomal recessive hypercholesterolemia (ARH) protein, which bind to NPXY-signals of the low-density lipoprotein receptor (LDLR) and the β integrin subunit) (Sorkin, 2004; Traub, 2009; Reider and Wendland, 2011). Subsequently, clathrin is recruited to the PM by interacting with AP2 and other adaptors mainly via its terminal domain (ter Haar, Harrison and Kirchhausen, 2000; Reider and Wendland, 2011; Traub and Bonifacino, 2013; Kelly *et al.*, 2014).

Additional clathrin triskelia and numerous accessory proteins are recruited to the assembling CCP and drive the formation and scission of CCV from the PM through very complex coordinated actions (McMahon and Boucrot, 2011; Taylor, Perrais and Merrifield, 2011). During the assembly of clathrin into polyhedral cages, other proteins help to build and form the soccer ball shaped CCPs. For example, BIN/Amphiphysin/Rsv (BAR)-proteins like amphiphysin,

SNX9, and endophilin play a role in membrane bending and dynamin recruitment (Qualmann, Koch and Kessels, 2011; Daumke, Roux and Haucke, 2014). Actin nucleation proteins like huntingtin interacting protein 1 related (HIP1R) and cortactin recruit the actin polymerization machinery to CCSs (Kaksonen, Toret and Drubin, 2006). Kinases like AP2 associated kinase 1 (AAK1) (Conner and Schmid, 2002; Ricotta *et al.*, 2002), coated-vesicle-associated kinase of 104 kDa (CVAK104) (Conner and Schmid, 2005), and dual specificity tyrosine-phosphorylation-regulated kinase 1A (DYRK1A) (Murakami *et al.*, 2012) phosphorylate and thereby regulate the functions and activation status of different proteins within the clathrin coat. Beside the orchestrated recruitment of proteins, the conversion and turnover of PIs is crucial and is regulated by PI-kinases and -phosphatases during CCP formation (Posor, Eichhorn-Grünig and Haucke, 2015) (Fig. 2.3). The initial PI(4,5)P₂ involved in adaptor accumulation (Boucrot *et al.*, 2006; Antonescu *et al.*, 2011) is turned over by PI-5'-phosphatases, for example synaptojanin (Chang-Ileto *et al.*, 2011), Src homology 2 (SH2)-containing tyrosine phosphatase-1 (SHIP) (Nakatsu *et al.*, 2010), and oculocerebrorenal syndrome of Lowe (OCRL) (Erdmann *et al.*, 2007). The concomitant generation of phosphatidylinositol 3,4-bisphosphate (PI(3,4)P₂) by the PI-3'-kinase PI3K-C2 α is involved in SNX9 recruitment (Posor *et al.*, 2013; Schöneberg *et al.*, 2017). While the dynamic sequence of protein recruitment can be followed with live-cell microscopy, the ultrastructural changes of the clathrin coat during CCP formation only visible in EM is technically difficult to address. The topic of ultrastructural changes of the clathrin coat during CCP formation will be introduced in paragraph 2.2.1.

For scission, the neck of CCPs needs to be constricted by membrane bending proteins like SNX9 or endophilin (Gallop *et al.*, 2006; Ferguson *et al.*, 2009; Schöneberg *et al.*, 2017). Afterwards dynamin can be recruited and assembles in a ring-link structure around the constricted PM neck (Reubold *et al.*, 2015). By the use of GTP-hydrolysis, dynamin mediates the final fission process (Sweitzer and Hinshaw, 1998; Stowell *et al.*, 1999). Although actin is generally not necessary for CCV formation in mammalian (Fujimoto *et al.*, 2000; Boucrot *et al.*, 2006), under certain conditions (for example elevated plasma membrane tension (PMT) (Boulant *et al.*, 2011) or big cargo proteins (Cureton *et al.*, 2010)) actin polymerization facilitates membrane invagination and scission.

The clathrin scaffold around CCV needs to be uncoated to allow vesicle trafficking to the endosomal pathway. The chaperon heat shock cognate 71 kDa protein (Hsc70) (Schlossman *et al.*, 1984; Rothman and Schmid, 1986) together with its co-chaperone G-associated kinase (GAK) (Greener *et al.*, 2000; Umeda, Meyerholz and Ungewickell, 2000) or auxilin (Ungewickell

et al., 1995; Xing *et al.*, 2010) help to disassemble the clathrin coat rapidly after CCV formation (Ehrlich *et al.*, 2004; Merrifield, Perrais and Zenisek, 2005; Massol *et al.*, 2006).

Although, we have gained valuable information about the temporal and dynamic recruitment and functions of many proteins involved during CME using live-cell microscopy, the precise regulation of the complex interplay between cargos, endocytic accessory proteins, lipids and the main player clathrin is still under investigation.

2.2 Flat clathrin lattices

2.2.1 The role of flat clathrin coats in CCP formation

Shortly after the first description of vesicles with a clathrin coat by Pearse in 1975 (Pearse, 1975), CCSs were studied at the PM by transmission electron microscopy (TEM) of metal replicas from unroofed cells (Heuser, 1980; Maupin and Pollard, 1983). This experimental approach revealed the presence of both curved as well as flat clathrin lattice at the PM. While curved CCSs display polyhedral coats composed of hexagons and pentagons, flat CCSs display mostly hexagons. By chronologically ordering CCSs of different morphology into a logical sequence as well as visualizing newly forming CCSs after removal of clathrin coats from the PM by potassium depletion, flat CCSs have been historically proposed to represent precursors of invaginated CCPs (Heuser, 1980, 1989; Larkin, Donzell and Anderson, 1986). But the fixed samples imaged by TEM could not provide direct proof for the sequence of structural changes from a flat to a curved clathrin lattice. With the use of fluorescently tagged fusion proteins, it became possible to follow the course of CME but with the cost of lower resolution compared to TEM (Gaidarov *et al.*, 1999; Merrifield *et al.*, 2002; Ehrlich *et al.*, 2004). During that time, the idea of a flat-to-curved conversion during CCP formation was challenged. The general notion took over that this flat-to-curved conversion would not be energetically favourable since it would involve a dramatic rearrangement of the flat hexagonal lattice to introduce pentagons at the right positions (Kirchhausen, 2009). A constant curvature model for the formation of CCPs was proposed which involves CCS assembly as curved structures right from initiation of coat formation (Kirchhausen, 2009; Lampe, Vassilopoulos and Merrifield, 2016) (Fig. 2.4a top). While the curvature would be kept constant, the CCS would grow by adding more clathrin molecules at the rim of the coat to ultimately form a CCP. The flat CCSs seen in TEM were assumed to be rather associated with unproductive abortive structures that would form at the PM and rapidly disassemble without forming a CCV (Kirchhausen, 2009; Loerke *et al.*, 2009; Aguet *et al.*, 2013).

In the recent years, multiple evidence was gathered for a mechanism of CCP formation involving restructuring of the clathrin coat. Fluorescence recovery after photobleaching (FRAP) experiments provided evidence for a high turnover of molecules within the clathrin coat (Wu *et al.*, 2001, 2003; Avinoam *et al.*, 2015). It was shown that clathrin molecules as well as adaptors underneath the clathrin lattice layer rapidly exchange. This proofed that clathrin coats are not rigid but highly dynamic, which is a prerequisite for major rearrangements

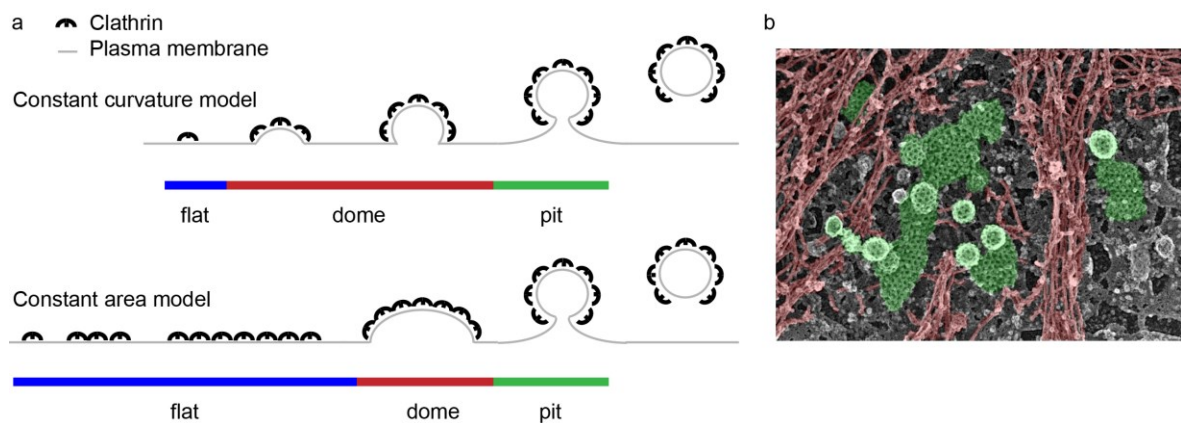


Figure 2.4: Putative involvement of flat clathrin lattice in CCP formation. (a) Schematic of the constant curvature and constant area models. The constant curvature model describes CCP formation from a CCS, which forms as a curved structures from the start of assembly and keeps the degree of curvature constant during the growth of the clathrin coat. The constant area model assumes the assembly of an initial flat clathrin lattice containing all clathrin molecules in this configuration. By the rearrangement of this flat coat, curvature is gradually achieved while keeping the surface area of the lattice constant. The stages of different curvature (flat (blue), dome (red), and pit (green)) are marked for both growth models. Illustration was taken from Bucher *et al.* (2018). (b) TEM image from metal replica of unroofed U373 cells showing flat clathrin lattice connected to curved dome and pit structures at the rim. Clathrin (green) and actin (red) are pseudo-coloured.

necessary for flat structures to transform into curved pits. A recent correlative light and electron microscopy (CLEM) study by Avinoam *et al.* (2015) brought back the idea of flat to-curved conversion. They showed that flat CCSs can have the same clathrin content as CCPs. They reconstructed the sequence of CCP formation from EM snapshots using the presence of dynamin as indication of the progression in CME. In this way, they suggested a constant area model in which CCSs would first assemble as flat structures with the complete clathrin molecule content of a CCP (Avinoam *et al.*, 2015; Lampe, Vassilopoulos and Merrifield, 2016). This flat lattice would then rearrange to convert into a curved pit (Fig.2.4a bottom). Although the improvement of correlating the clathrin coat morphology to fluorescence microscopy (FM) helped to interpret the coats seen in electron microscopy (EM) in a temporal series, more work is still needed to proof this model and to understand the mechanism of restructuring clathrin lattice.

2.2.2 Endocytic functions of larger flat clathrin arrays

While CCPs are uniform in diameter (around 100 nm), flat clathrin coats differ in size (up to $1 \mu\text{m}^2$ in area) (Heuser, 1980; Maupin and Pollard, 1983; Grove *et al.*, 2014). In TEM images, it was observed that some of the larger flat structures, called clathrin-coated plaques, could even

have invaginated CCPs at their rim (Heuser, 1980; Maupin and Pollard, 1983) (Fig. 2.4b). This suggests that flat structures can serve as budding platform for CME. From a theoretical point of view, the rearrangement of a flat coat into a curved pit would be most likely at the rim of a hexagonal lattice (den Otter and Briels, 2011). These flat structures were often brought in context with non-terminal events seen in live-cell FM. (Merrifield, Perrais and Zenisek, 2005; Taylor, Perrais and Merrifield, 2011) The pinching of CCPs from a CCS that stays at the PM was proven with an elegant pH sensitive cargo to monitor fission of CCPs from the PM by Merrifield *et al.* (2015). Recently improvements in FM made it even possible to visualize formation of CCP at flat clathrin structures using lattice light sheet super-resolution microscopy (Li *et al.*, 2015).

It was also suggested that clathrin-coated plaques could be internalized as a flat lattice by a different mechanism compared to canonical CCPs (Saffarian, Cocucci and Kirchhausen, 2009). This internalization pathway is assumed to take longer than the canonical CME, occurs only at attached PM parts and is actin-dependent. How exactly the membrane underneath a large flat clathrin lattice would be sufficiently constricted to allow dynamin-mediated scission is not clear and so far, it was not possible to visualize endocytic carrier formation following such a mechanism using EM.

Although there exists strong evidence that larger flat CCSs play a role in endocytic processes either through CME using a non-canonical pathway or as persistent budding platform for CCP formation, the molecular and structural mechanism of CCV generation from flat clathrin lattices as well as the physiological relevance are still unclear.

2.2.3 Non-endocytic functions of flat clathrin lattices

The function of clathrin cages in the formation of vesicles for endocytosis is well established, but especially flat clathrin coats have been associated with other cellular functions (Lampe, Vassilopoulos and Merrifield, 2016). Generally, a coat at the PM could allow for functions like clustering of transmembrane proteins and generating of microdomains, which would give clathrin coats the potential for a multifunctional structure.

Early EM studies showed clathrin-coated membrane parts in close contact with the substrate suggesting an adhesive function (Maupin and Pollard, 1983). The extracellular matrix (ECM) receptors integrins have been shown to localize to flat clathrin coats where they might be involved in anchoring the membrane to the substrate (De Deyne *et al.*, 1998; Chetrit, Ziv and Ehrlich, 2009; Vassilopoulos *et al.*, 2014; Lampe, Vassilopoulos and Merrifield, 2016; Elkhatib *et*

al., 2017). Such adhesive CCSs were suggested to stabilize costameres, which are specialized attachment sites of sarcomeres to the PM found in skeletal muscle (Vassilopoulos *et al.*, 2014) (Fig. 2.5a). Together with integrins and α -actinin, flat clathrin coats seem to play a crucial role in the organization of costameres structures, which might explain a link of autosomal-dominant centronuclear myopathy to a mutation in the gene encoding for dynamin2 (Bitoun *et al.*, 2005; Böhm *et al.*, 2012). A recent study revealed the involvement of tubular clathrin coats in cell adhesion and migration in a three-dimensional (3D) collagen matrix (Elkhatib *et al.*, 2017) (Fig. 2.5b-c). While focal adhesions (FAs) are the main adhesive structures on a two-dimensional (2D) substrate, tubular clathrin/AP2 lattices seem to take over the adhesive function in a 3D context by pinching collagen fibres and stabilizing cell protrusions. Although these studies strongly suggest a role of CCSs in cell adhesion, the regulatory mechanism of such adhesive patches as well as the physiological relevance in different cells and tissues is still unclear. Furthermore, the localization of integrins to CCSs might also result in endocytosis of these receptors and thereby removal of adhesive complexes. Although CME is not the only uptake pathway described for endocytic uptake of integrins, several studies associate the colocalization of integrins and clathrin coats to FA disassembly (Nishimura and Kaibuchi, 2007; Caswell, Vadrevu and Norman, 2009; Ezratty *et al.*, 2009; Teckchandani *et al.*, 2012; Yu *et al.*, 2015; De Franceschi *et al.*, 2016).

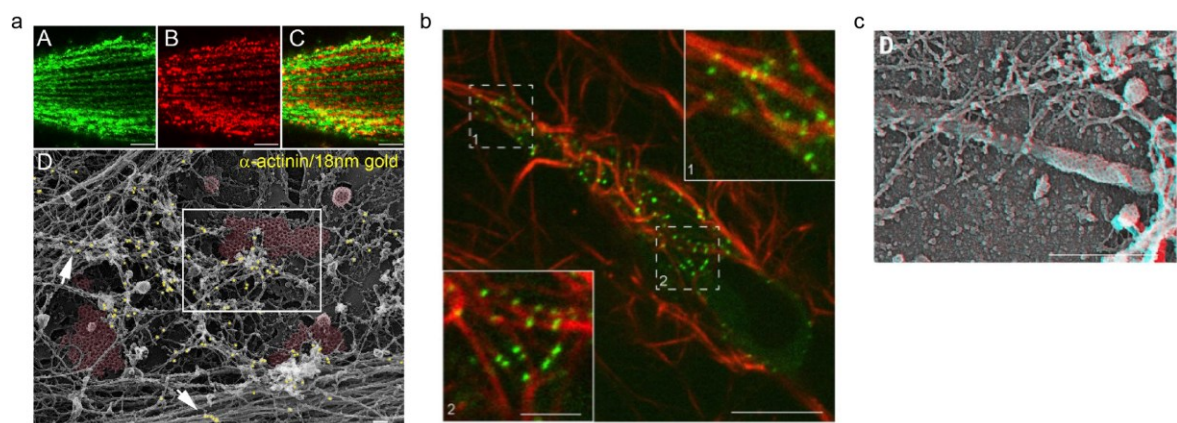


Figure 2.5: Non-endocytic functions of CCS. (a) α -actinin and actin organization on large flat CCS in primary myotubes. (A-C) Immunofluorescence staining of primary mouse myotubes. A: α -actinin, B: CHC, C: merged image. Scale bars: 5 μ m (D) Adherent plasmalemmal sheet from primary myotubes labelled with α -actinin antibodies. Fold particles are pseudo-coloured yellow. Scale bar: 100nm. Image was taken from Vassilopoulos *et al.* (2014). Republished with permission of The Rockefeller University Press. (b-c) Adhesive tubular clathrin/AP2 lattices pinching collagen fibres in a 3D matrix. (b) FM image. Collagen fibres (red), CCS (green). Scale bar: 10 μ m, 3 μ m (box) (c) EM image. Scale bar: 500nm. Images (b and c) were taken from Elkhatib *et al.* (2017). Reprinted with permission from AAAS.

Not only integrins but also other transmembrane receptors have been reported to be enriched at flat clathrin coats (e.g. C-C chemokine receptor type 5 (CCR5) (Grove *et al.*, 2014), epidermal growth factor receptor (EGFR) (Garay *et al.*, 2015; Leyton-Puig *et al.*, 2017), low-density lipoprotein-related protein 6 (LRP6) (Kim *et al.*, 2013), and lysophosphatidic acid receptor 1 (LPA1) (Leyton-Puig *et al.*, 2017)). While internalization of receptors by CME can lead to desensitization or signalling from intracellular compartments, the stabilization of receptors at the PM can also modulate receptor signalling. Flat clathrin coats have been suggested to perform efficient endocytosis of receptors after stimulation (Leyton-Puig *et al.*, 2017). Other studies show receptor clustering and stabilization at the PM at flat CCSs without internalization (Kim *et al.*, 2013; Grove *et al.*, 2014; Garay *et al.*, 2015). Both possibilities can have a dramatic effect on the downstream signalling events and might be differentially regulated in a receptor- and ligand-dependent manner. The multiple impacts of flat CCSs on receptor localization add an additional layer of complexity to receptor signalling. It is still unclear what determines if a CCS serves for internalization or stabilization of receptors at the PM and how this is regulated on the molecular level.

2.3 Cellular interactions with the ECM

2.3.1 Molecular composition of FAs

Multicellular organisms rely on organization of cells into ordered tissue by cell-to-cell as well as cell-to-substrate contacts (Abedin and King, 2010). Such contacts mediate the connection between the extracellular environment (ECM or neighbouring cells) and the cytoskeleton via transmembrane receptors and are involved in many signalling processes (Cavallaro and Dejana, 2011; Horwitz, 2012). Integrins are the main transmembrane proteins linking the complex ECM to the actin cytoskeleton (Barczyk, Carracedo and Gullberg, 2010). Together with adaptor, scaffold and signalling proteins, they assemble into multi-layered adhesive units, called FAs, which allow cells to transmit force across the PM for processes like cell migration and ECM remodelling (Vicente-Manzanares, Choi and Horwitz, 2009; Parsons, Horwitz and Schwartz, 2010; Geiger and Yamada, 2011; Sun, Guo and Fässler, 2016). Additionally, FAs provide information by chemical and physical sensing of the ECM which allow cells to adapt to their environment (Parsons, Horwitz and Schwartz, 2010; Geiger and Yamada, 2011; Sun, Guo and Fässler, 2016).

The network of proteins interacting and building the linkage between integrins and the actin stress fibres is called integrin adhesome, which contains over 200 described proteins in different layers (Horton *et al.*, 2016). The composition of FA has been investigated for years (Zamir and Geiger, 2001; Horton *et al.*, 2016) and the information gained from proteomics (Manninen and Varjosalo, 2016) as well as structural studies (Case and Waterman-Storer, 2015; Xia and Kanchanawong, 2017) contributed to a detailed picture of its multiprotein complex. Structural studies using cryo-electron tomography revealed organisation of FA proteins into doughnut-shaped particles, which are connected to actin stress fibres via shorter actin filaments (Patla *et al.*, 2010) and interferometric photoactivation and localization microscopy (iPALM) helped to understand the vertical organization of protein layers within FAs (Kanchanawong *et al.*, 2010) (Fig. 2.6a).

The first layer consists of integrin receptors, which span over the PM into the extracellular space. Integrins are heterodimers of transmembrane proteins with one α and one β subunit (Hynes, 2002; Barczyk, Carracedo and Gullberg, 2010). In mammals, there have been 24 heterodimers reported made from 18 α and 8 β subunits with distinct as well as overlapping ECM ligands (Takada, Ye and Simon, 2007; Barczyk, Carracedo and Gullberg, 2010). While the extracellular part binds to ECM molecules, the intracellular tails of integrins are linked to the

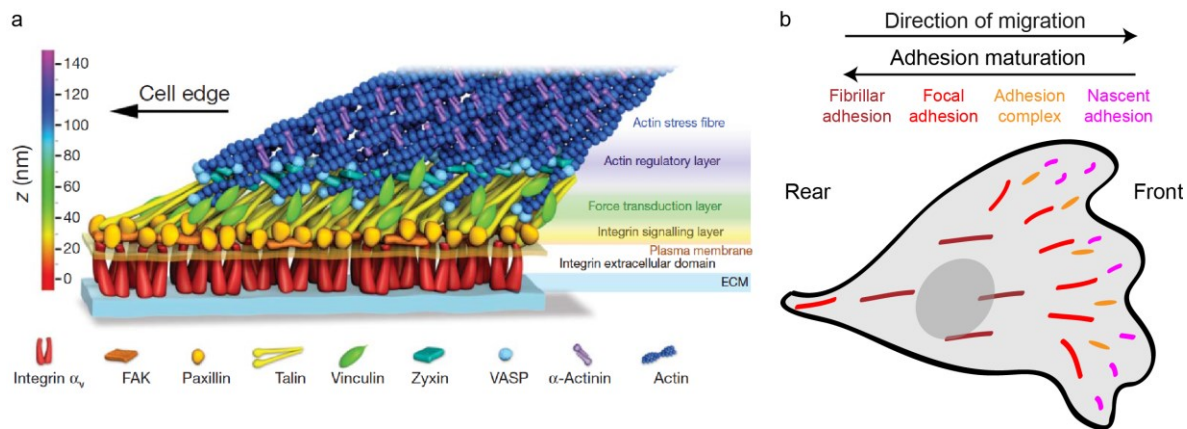


Figure 2.6: Composition and dynamics of integrin-based adhesion complexes. (a) Scheme of FAs with nanoscale position of FA proteins as determined by iPALM. Illustration was adapted from Kanchanawong *et al.* (2010). Reprinted by permission from Springer Nature, Kanchanawong *et al.* (2010), copyright (2010). (b) Dynamics of integrin-based adhesions during cell migration. Initially nascent adhesions (magenta) form at the lamellipodium. They can either be turned over or mature into adhesion complexes (orange) and further into stable FAs (red). FAs can convert into elongated fibrillar adhesions (dark red) associated with ECM remodelling.

actin stress fibres via integrin-actin linkers like talin (Campbell and Ginsberg, 2004; Critchley, 2009) and vinculin (Ziegler, Liddington and Critchley, 2006). Other layers contain FA-associated proteins involved in processes like actin regulation and bundling (e.g. vasodilator-stimulated phosphoprotein (VASP) (Holt, Critchley and Brindle, 1998), α -actinin (Otey and Carpen, 2004), zyxin (Hirata, Tatsumi and Sokabe, 2008)) and signal transduction (e.g. focal adhesion kinase (FAK) (Parsons, 2003), paxillin (Brown and Turner, 2004)).

2.3.2 Adhesion dynamics

Adhesion complexes need to be dynamic to allow mechanotransduction and signalling involved in cellular processes like cell adhesion and cell migration (Parsons, Horwitz and Schwartz, 2010; Geiger and Yamada, 2011; Vicente-Manzanares and Horwitz, 2011). New contacts have to be formed and stabilized at locations where they are needed whereas old obstructive adhesions have to be disassembled. While Rho GTPases (i.e. Rac, Rho, and Cdc42) control the formation and maturation of FAs by regulating actin-mediated protrusions and myosin II-mediated contractility (Nobes and Hall, 1995; Jaffe and Hall, 2005; Machacek *et al.*, 2009), integrin signalling regulates the actin cytoskeleton via Rho GTPase regulators (i.e. Guanine nucleotide exchange factors (GEFs) and GTPase-activating proteins (GAPs)) (Tomar and Schlaepfer, 2009; Lawson and Burrige, 2014). This generates a complex interplay of feedback

loops that is influenced by multiple extracellular and intracellular factors resulting in adhesion dynamics.

During the course of FA establishment, first small, short-lived (turnover around 60 seconds) adhesion sites called nascent adhesions are formed at the lamellipodium (Parsons, Horwitz and Schwartz, 2010; Geiger and Yamada, 2011) (Fig. 2.6b). It is not clear how they are nucleated. Probably an interplay between extracellular clustering of integrins by binding to ECM molecules (Miyamoto *et al.*, 1995) and/or intracellular actin polymerization as template for integrin activation initiates nascent adhesions (Alexandrova *et al.*, 2008; Choi *et al.*, 2008). These dynamic attachment sites can either be disassembled within seconds or mature while moving further back from the leading edge to larger, dot-like focal complexes stable for several minutes (Parsons, Horwitz and Schwartz, 2010; Geiger and Yamada, 2011). This maturation depends on myosin II-dependent generation of tension as well as linkage of integrins to actin filaments (Choi *et al.*, 2008). The adhesion complexes can then mature further to larger (3-10 μ m long), persistent FAs connected to actin stress fibres (Dubash *et al.*, 2009; Geiger, Spatz and Bershadsky, 2009). FA can convert into fibrillar adhesions, another kind of adhesion sites involved in remodelling of ECM, which are highly elongated adhesions and located under the cell body (Zamir *et al.*, 2000). During adhesion maturation, the serial conversion of different adhesive complexes is a continuous process in which the molecular composition of adhesions changes (Zamir *et al.*, 1999; Zamir and Geiger, 2001). The abundance of the different kinds of adhesions heavily depends on the cell type as well as on the protein composition and physical features of the ECM (Parsons, Horwitz and Schwartz, 2010; Geiger and Yamada, 2011).

2.3.3 ECM assembly and remodelling

The ECM is an essential part of multicellular organisms present in all tissue not only to support physical shape but also to regulate morphogenesis, differentiation as well as homeostasis by providing biochemical and mechanical signals (Bonnans, Chou and Werb, 2014; Humphrey, Dufresne and Schwartz, 2014). Composed of water, polysaccharides and proteins, the ECM is a highly complex and dynamic network (Frantz, Stewart and Weaver, 2010; Mouw, Ou and Weaver, 2014). The molecular composition that determines the chemical and mechanical properties of the ECM is very specific to its purpose and identity (Mouw, Ou and Weaver, 2014). There are two main types of ECM: 1) The interstitial matrix, that surrounds cells as a fibrous mesh, and 2) the basement membrane, a sheet-like network which serves to separate epithelia from the underlying tissue and stroma (Singh, Carraher and Schwarzbauer, 2010; Mouw, Ou and Weaver, 2014). The ECM is constantly remodelled by deposition, rearrangement, and

degradation of components and misregulation of this process is associated with diseases like fibrosis, osteoarthritis or cancer (Butcher, Alliston and Weaver, 2009; Frantz, Stewart and Weaver, 2010; Bonnans, Chou and Werb, 2014; Zhen and Cao, 2014; Nagelkerke *et al.*, 2015).

ECM proteins and associated factors collectively called matrisome comprise more than 300 proteins, including fibrous proteins, glycoproteins, and proteoglycans (Hynes and Naba, 2012). Mostly produced by fibroblasts, they are assembled into a mesh of intertwined protein fibres (Humphrey, Dufresne and Schwartz, 2014). For example collagen, the most abundant fibrous protein within interstitial matrix, is a triple helical protein built of three peptide chains (Ricard-Blum, 2011). During collagen synthesis, first procollagen triple helices are assembled and modified in the endoplasmatic reticulum and golgi apparatus (Myllyharju, 2005; Mouw, Ou and Weaver, 2014). After secretion, the procollagen is cleaved into collagen in the extracellular space where it can self-assemble into collagen fibrils (Hulmes, 2002; Mouw, Ou and Weaver, 2014). Collagen fibrils are further cross-linked by lysyl oxidases to build supramolecular structures (Lucero and Kagan, 2006), which can be organized and combined with other ECM molecules into cables and sheets by cell-mediated force transmission to the matrix (Velling *et al.*, 2002; Li *et al.*, 2003; Meshel *et al.*, 2005; Dahlmann-Noor *et al.*, 2007). The glycoprotein fibronectin is another fibrous component of the ECM (Singh, Carraher and Schwarzbauer, 2010; Schwarzbauer and DeSimone, 2011). Fibronectin is secreted as a soluble dimer that can bind to integrins to initiate fibronectin tethering to the cell surface and the further interaction of fibronectin dimers (Hocking, Sottile and McKeown-Longo, 1994; Hocking, Smith and McKeown-Longo, 1996; García, Schwarzbauer and Boettiger, 2002; Singh, Carraher and Schwarzbauer, 2010). By applying force, cryptic binding sites of the fibronectin molecules get exposed by conformational change, which leads to fibronectin assembly into fibrillar structures (Zhong *et al.*, 1998; Baneyx, Baugh and Vogel, 2002; Yoneda *et al.*, 2007). This process, which is often associated with $\alpha 5 \beta 1$ integrins and fibrillar adhesions, is called fibronectin fibrillogenesis (Pankov *et al.*, 2000; Ohashi, Kiehart and Erickson, 2002; Ilić *et al.*, 2004; Singh, Carraher and Schwarzbauer, 2010).

The process of ECM degradation involves several proteases and regulatory proteins (Bonnans, Chou and Werb, 2014). Matrix metalloproteinases (MMPs) are the main enzymes cleaving ECM components (Mott and Werb, 2004; Bonnans, Chou and Werb, 2014). They are produced as soluble as well as membrane-anchored proteases and mostly need to be activated by proteolytic cleavage (mediated by either other MMPs or Ser proteases) (Mott and Werb, 2004; Bonnans, Chou and Werb, 2014). Besides MMPs, adamalysins (a disintegrin and metalloproteinases (ADAM) and ADAM with thrombospondin motifs (ADAMTS)) and meprins

are other families of ECM proteases which help and regulate the process of ECM deconstruction (White, 2003; Apte, 2009; Singh, Carraher and Schwarzbauer, 2010; Prox, Arnold and Becker-Pauly, 2015). Cleavage of ECM proteins is further regulated by factors like tissue inhibitor of metalloproteinases (TIMPs) and reversion-inducing Cys-rich protein with Kazal motif (RECK), which inhibit ECM protease activity (Baker, Edwards and Murphy, 2002; Cruz-Munoz and Khokha, 2008; Khokha, Murthy and Weiss, 2013).

The ECM provides chemical as well as physical cues that regulate cell behaviour during development, wound healing and disease. The protein composition of each ECM is important for integrin signalling and proper cell adhesion. During enzymatic cleavage, protein fragments with different properties compared to the original protein can be generated and factors immobilized on the ECM (e.g. growth factors and chemokines) can be released (Murphy, 2008; Bonnans, Chou and Werb, 2014). The mechanical aspects of the ECM, which are linked to its protein composition, represent another layer of signals, which can be sensed by cellular mechanotransduction (Humphrey, Dufresne and Schwartz, 2014; Iskratsch, Wolfenson and Sheetz, 2014; Sun, Guo and Fässler, 2016). The mechanical properties of the ECM are detected via force transmission between FAs and the ECM (Sun, Guo and Fässler, 2016). This information is then converted into biochemical signals via enzymatic reactions (i.e. extension-induced phosphorylation of p130 Crk-associated substrate (p130Cas) through Src family kinases (Sawada *et al.*, 2006) and regulation of FAK activation (Zhou *et al.*, 2015)) or changes in conformation of stretchable proteins (e.g. talin (del Rio *et al.*, 2009) and filamin (Ehrlicher *et al.*, 2011; Rognoni *et al.*, 2012)). Mechanotransduction can lead to rapid cellular responses (e.g. cell stiffening through the regulation of RhoA (Guilluy *et al.*, 2011)) and ultimately long-term changes in gene expression (e.g. through transcription factors like Yes-associated protein (YAP)/ transcriptional coactivator with PDZ-binding motif (TAZ) (Dupont *et al.*, 2011; Aragona *et al.*, 2013) or myocardin related transcription factor-A (MRTF-A) (Olson and Nordheim, 2010; O'Connor and Gomez, 2013) or linker of the nucleoskeleton and cytoskeleton (LINC complex) (Isermann and Lammerding, 2013)) as well as epigenetic regulation (Yang *et al.*, 2014). Through the combination of these mechanically induced signalling pathways, the stiffness, elasticity, and topography of the ECM network influences important cellular processes like cell differentiation in stem cell niches (Engler *et al.*, 2006; Ahmed and French-Constant, 2016) and cell migration during development and wound healing (Gasiorowski, Murphy and Nealey, 2013; Charras and Sahai, 2014).

It became clear that the ECM is not only a scaffold for tissue organization but has great impact on cell behaviour. Since cells are driving the constant ECM renewal and remodelling, this

generates a feedback loop in the overall regulation and homeostasis of an organism. To understand the relationship between cells and the ECM will help to fight diseases and will be a huge step forward in tissue engineering.

3 Aim of this thesis

Although frequently observed in EM since the 1980's, the function of flat clathrin lattices remains still elusive. For a long time, they have been considered artefacts of culturing cells on substrates but recent studies point to potential roles in CCP formation and cell adhesion. This PhD thesis investigates the function of flat clathrin lattice in endocytosis and cell migration. For this purpose, this work is divided into three topics: 1) Cell line-specific characteristics of clathrin coats, 2) Investigation of structural changes of the clathrin coat during CCP formation, 3) Role of clathrin-coated plaques in cell migration.

1) CME has been studied using diverse cell types showing differences in the dynamics and ultrastructural organisation of CCSs. Since most of the studies rely on limited use of methods, the connection between dynamical and structural observations are still poorly defined. Therefore, we comprehensively characterized the dynamics and ultrastructure of CCSs formed in different cell lines (BSC-1, Swiss3T3, and U373) as well as at different PM parts (attached versus non-attached, bottom versus top). We used live-cell confocal microscopy, stimulated emission depletion (STED) nanoscopy, TEM and CLEM to reveal cell type-specific features of CME.

2) Flat clathrin coats have been suggested to represent precursors of curved CCPs. However, the dynamics of the structural rearrangement of flat clathrin lattices during CCP formation remains unclear. We used a combination of microscopy (live-cell confocal FM, TEM and CLEM) and mathematical modelling to gain new insight into the sequence allowing the ultrastructural conversion from flat to curved lattices during CCP assembly. Additionally, we addressed the impact of PMT on curvature acquisition of clathrin coats.

3) CCSs associated with integrins have been implicated in FA disassembly as well as cell adhesion. Especially larger flat arrays called clathrin-coated plaques found at the bottom PM are assumed to be involved in such processes but their role in regulating adhesion dynamics during cell migration is poorly understood. Here, we investigated the temporal relationship of CCSs and FAs during cell migration and ECM remodelling. Additionally, we addressed the putative role of clathrin-coated plaques in cell adhesion and migration using live-cell FM. Furthermore, we investigated the extracellular signals, which induce clathrin-coated plaque formation by visualizing ECM remodelling and providing defined substrate topography.

4 Results

4.1 Cell line-specific characteristics of clathrin coats

CME is a well-studied process and is important in many cellular uptake processes at the PM (McMahon and Boucrot, 2011). Cells from different parts of an organism use CME for specialized purpose (McMahon and Boucrot, 2011; Saheki and De Camilli, 2012; Antonescu, McGraw and Klip, 2014). Therefore, CME might be regulated in a cell type-specific manner to fulfil the needs of different functions. In the past 40 years, a range of different cell types was used to investigate CME and the overall conclusion of these studies is that there are major differences in the mechanisms of CME between cell types (Saffarian, Cocucci and Kirchhausen, 2009; Grove *et al.*, 2014) as well as within cell types (Snijder *et al.*, 2009) and even within the same cell (e.g. differences between the leading edge and the trailing tail of migrating cells) (Liu *et al.*, 2009; Batchelder and Yarar, 2010; Kural *et al.*, 2015).

To characterize CME in different cell lines as well as within the same cell, we chose three cell lines widely used in the field: 1) BSC-1, a green monkey kidney epithelial cell line (Ehrlich *et al.*, 2004; Boucrot *et al.*, 2006; Saffarian, Cocucci and Kirchhausen, 2009), 2) Siwss3T3, a mouse fibroblast cell line (Merrifield *et al.*, 2002; Merrifield, Perrais and Zenisek, 2005; Yarar, Waterman-Storer and Schmid, 2005; Saffarian, Cocucci and Kirchhausen, 2009), and 3) U373, a human glioblastoma cell line (Massol *et al.*, 2006; Saffarian, Cocucci and Kirchhausen, 2009; Kural *et al.*, 2015). We used 1) live-cell microscopy to investigate the dynamics of CME and to compare CME at different regions of the PM, 2) STED nanoscopy to visualize CCSs with high resolution, 3) EM to gain information about clathrin coat morphology, as well as 4) CLEM to correlate fluorescence signals to the ultrastructure of clathrin coats.

4.1.1 Cell type-specific dynamics of CME

To investigate the dynamics of CME, we used cell lines stably expressing the sigma 2 subunit of the clathrin adaptor AP2 fused to enhanced green fluorescent protein (eGFP), further called AP2-eGFP. Live-cell spinning disc microscopy of the three cell lines revealed large differences in the dynamics and lifetime of CME (Fig. 4.1). BSC-1 cells showed only transient CCSs with a short lifetime (around a minute) (Fig. 4.1a-b). Swiss3T3 cells had transient CCSs with short and longer lifetime (up to 5 minutes), whereas U373 cells additionally exhibited persistent CCSs (over 10 minutes) (Fig. 4.1a-b).

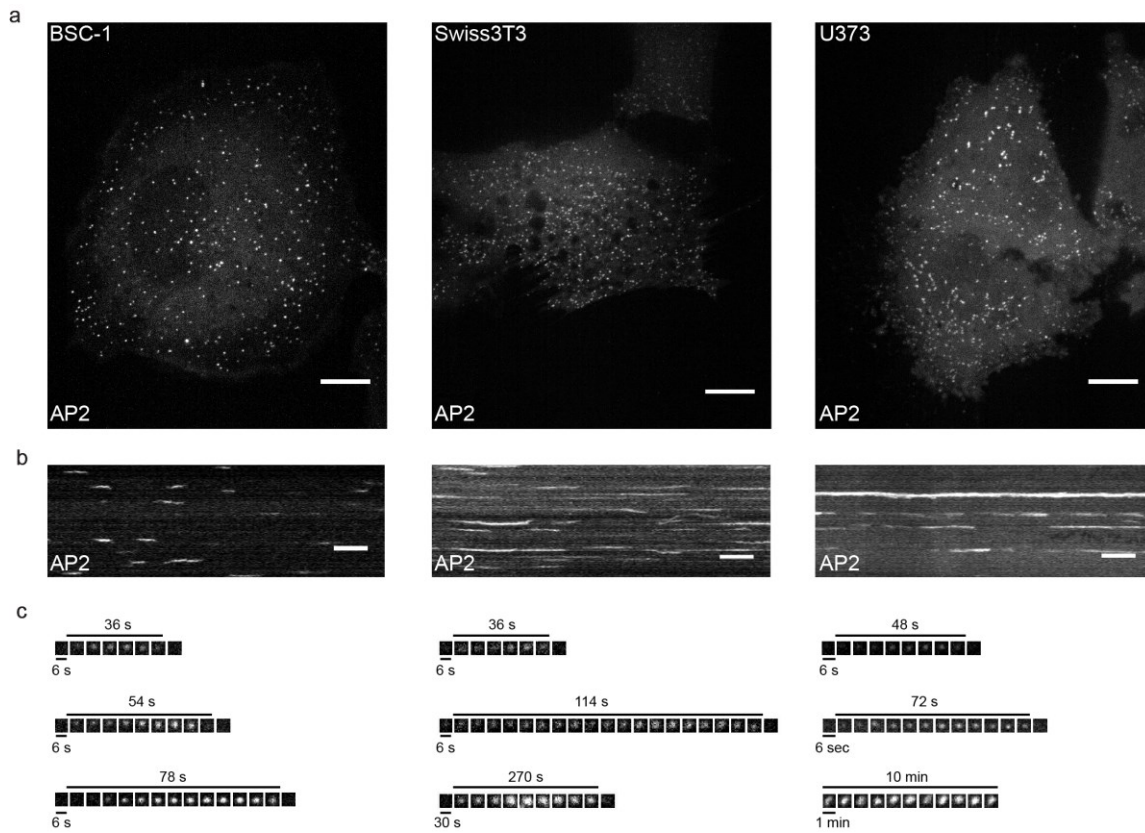


Figure 4.1: Live-cell microscopy of CME. (a) Live-cell spinning disc confocal microscopy of BSC-1 (right), Swiss3T3 (middle), and U373 (left) stably expressing AP2-eGFP growing on poly-D-lysine (PDL)-coated coverslips. Imaging was performed 12-16 hours after seeding. Scale bar: 10 μ m. (b) Representative kymograph from a 10 minute long movie with a frame rate of 3 seconds for each cell line to follow CCSs over time. Scale bar: 1 min. (c) Serial zoom-ins on selected events of CME to highlight difference in the dynamics of CME between the cell lines. Frame rate 6 seconds, 30 second or 1 minute. Panels a-c of (right) were taken from Bucher *et al.* (2018).

To analyse the fluorescence intensity profiles of AP2-eGFP during CME in these cell lines, we performed tracking of CCSs using a probabilistic particle tracking method (Godinez and Rohr, 2015). The short transient CCSs in BSC-1 showed a relatively homogeneous population of CME regarding both lifetime and maximal fluorescence intensity (Fig.4.2a). In contrast, CME in Swiss3T3 had a much broader distribution in lifetime with similar maximal fluorescence intensity (Fig.4.2a). In U373 cells, we found a huge variability in lifetime as well as maximal fluorescence intensity (Fig.4.2a). A closer look at the differences in lifetime showed that 95% of the CME in BSC-1, Swiss3T3, and U373 possessed a lifetime under 75 seconds, 120 seconds, and 141 seconds, respectively (Fig. 4.2b-c). In U373, the characteristically persistent CCSs represented 1.2% of all CCSs tracked in a 10 minute long movie. In contrast, this CME

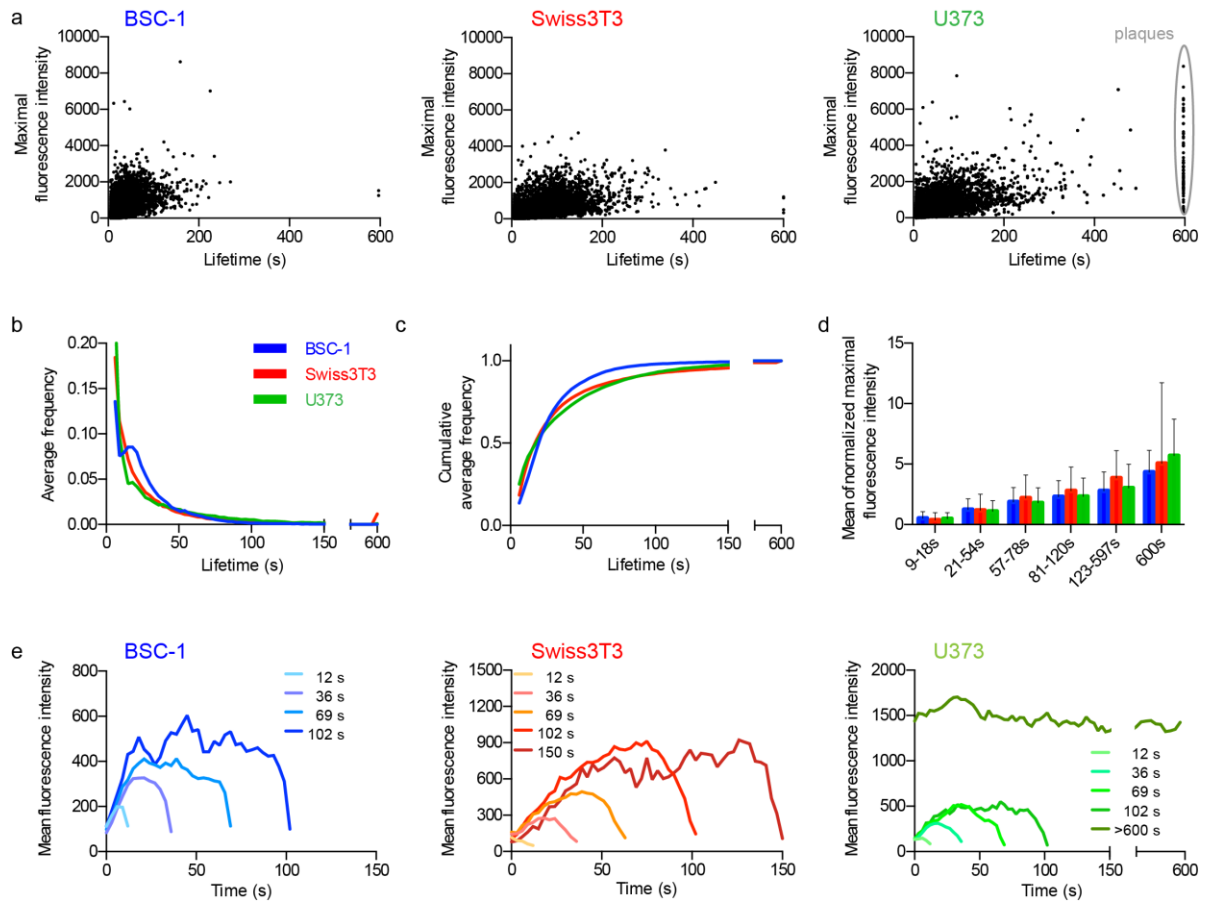


Figure 4.2: Distinct dynamics of CME in different cell lines. Analysis of tracking of AP2-eGFP in BSC-1, Swiss3T3, and U373 cells. Tracking using a probabilistic particle tracking method (Godinez and Rohr, 2015) was performed by Jan-Philip Bergeest and William J. Godinez. Analysis of the tracks has been performed with automated workflows using KNIME. (a) Lifetime versus maximal fluorescence intensity of AP2-eGFP of CME tracks for BSC-1 (left, blue), Swiss3T3 (middle, red), and U373 (right, green). Persistent clathrin-coated plaques are marked by a grey circle. Shown are plots of a representative cell of each cell line. Each dot represents one tracked CME event of a 10 minute long movie. Number of tracks: 14,694 (BSC-1), 13,313 (Swiss3T3), and 11,252 (U373) (b) Average lifetime frequency of CME in the three cell lines. Shown is the mean frequency of 5 cells. (c) Cumulative average lifetime frequency of CME in the three cell lines. Shown is the mean cumulative frequency of 5 cells. (d) Lifetime cohort analysis of the maximal fluorescence intensity of CME in the three cell lines. The tracked CME events were grouped into six lifetime cohorts (9-16 s, 21-54 s, 57-78 s, 81-120 s, 123-597 s, and 600 s). The maximal fluorescence intensity was normalized to the mean maximal fluorescence intensity of each 10 minute long movie. For each cohort the mean of the normalized maximal fluorescence intensity from 5 cells of each cell line is shown; the error bars represent the SD. (b, c, and d are computed from 81,545 (BSC-1), 68,164 (Swiss3T3), and 50,865 (U373) tracks) (e) Average fluorescence intensity profile of AP2-eGFP during CME of the three cell lines. Shown is the mean fluorescence intensity of each time point for tracks with the same lifetime from one 10 minute long movie. Panels a,c, and e concerning BSC-1 were adapted from Bucher *et al.* (2018).

population represented under 0.1% in the other two cell lines (Fig. 4.2b-c). By dividing CME tracks into lifetime cohorts, we found that the maximal fluorescence intensity of CME correlates with the lifetime of CCSs (Fig. 4.2d). In other words, the longer the lifetime of a CCS, the bigger (the more fluorescent) the structure is. By computing average curves of fluorescence intensity profiles of CME with the same lifetimes, we found that the transient CCSs (from 12 to 102 seconds) have a similar initial rate of fluorescence increase (initial growth rate of CCSs) (Fig. 4.2e). For longer-lived structures, a plateau phase was observed with a duration correlating with the CCS lifetime (Fig. 4.2e). The persistent CCSs in U373 cells showed similar fluorescence intensity over the whole imaged time (Fig. 4.2e).

In summary, live-cell microscopy of AP2-eGFP showed cell type-specific characteristics of lifetime as well as fluorescence intensity of CME. When distinguished by their lifetime, we will from now on differentiated between transient CCPs (lifetime <5 min) and persistent clathrin-coated plaques (lifetime > 10 min).

4.1.2 Differences of CME at attached and non-attached PM parts

It has been described that the dynamics of CME is dependent on the biochemical and biophysical properties of the PM part from which CCVs are formed (Liu *et al.*, 2009; Saffarian, Cocucci and Kirchhausen, 2009; Boulant *et al.*, 2011). These properties are influenced by the identity of the PM (dorsal vs. ventral), the lipid composition and the actomyosin cortex underneath the PM (Shewan, Eastburn and Mostov, 2011; Iburguren, López and Escribá, 2014; Köster and Mayor, 2016). All these factors affect the properties of the PM and as a consequence the processes that occur there.

We addressed the question if adhesion of the PM affects the dynamics of CME in the three cell lines. Therefore, we used two approaches to separately analyse dynamics of CME at attached and non-attached PM parts within the same cell: 1) Imaging of the bottom and top PM and 2) Growing cells on adhesive micropatterns.

To separately analyse CME at the bottom and the top PM, we imaged AP2-eGFP at the bottom PM of cells in a single focal plane and at the top PM by taking small z-stacks to cover the top 2 μm of the cells (Fig. 4.3a). For the top PM, tracking of CME was performed on a z-projection of the images. In all three cell lines, we found transient CCPs at all PM parts (Fig. 4.3b-c). The maximal fluorescence intensity of transient CCPs at the top PM was comparable to the one at the bottom PM (Fig. 4.3b). A direct comparison of CME at the bottom and top PM showed overall shorter lifetime at the top (Fig. 4.3c). Particularly for U373, we found that the persistent

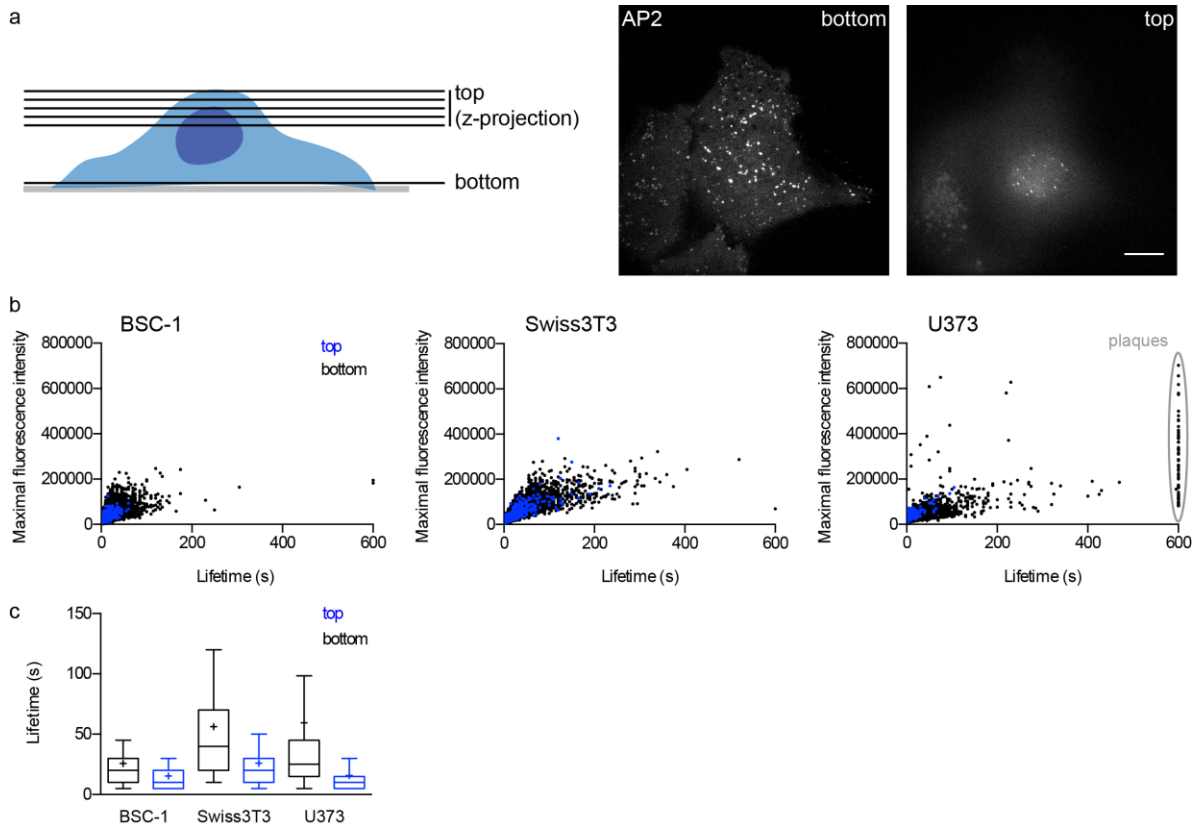


Figure 4.3: Comparison of CME at bottom and top PM. (a) Schematic of imaging strategy. AP2-eGFP was imaged at the bottom PM, in a single focal plane, for 10 minutes with a frame rate of 5 seconds. The top PM was imaged by taking a z-stack of 5 images with a spacing of $0.5\ \mu\text{m}$ at the very top of the same cell. For tracking of CME on the top PM, a maximal intensity z-projection was used. Scale bar: $10\ \mu\text{m}$. (b) Lifetime versus maximal fluorescence intensity of AP2-eGFP of CME tracks from the top (blue) and the bottom (black) PM of the same cell for BSC-1 (left), Swiss3T3 (middle), and U373 (right). Shown are plots of a representative cell of each cell line. Each dot represents one tracked CME event of a 10 minute long movie. Persistent clathrin-coated plaques are marked by a grey circle. Number of tracks at bottom PM: 5,479 (BSC-1), 2,872 (Swiss3T3), and 1,874 (U373). Number of tracks at top PM: 746 (BSC-1), 359 (Swiss3T3), and 118 (U373). (c) Box and whiskers plot showing the lifetime distributions of CME at the top (blue) and the bottom (black) PM of the three cell lines computed from three cells of each cell line. Whiskers represent 10-90 percentile, box represents second and third quartile, the line marks the median, and the cross marks the mean. Number of tracks at bottom PM: 13,594 (BSC-1), 8,117 (Swiss3T3), and 4,472 (U373). Number of tracks at top PM: 1,814 (BSC-1), 877 (Swiss3T3), and 587 (U373).

clathrin-coated plaques were only formed at the bottom PM and not at the top (Fig. 4.3b, right panel).

Since monitoring of CME at the top PM is challenging due to imaging and tracking of objects in a 3D-volume, we decided to generate attached and non-attached PM parts in the same focal plane. This was achieved by growing cells on adhesive micropatterns (Théry, 2010). The

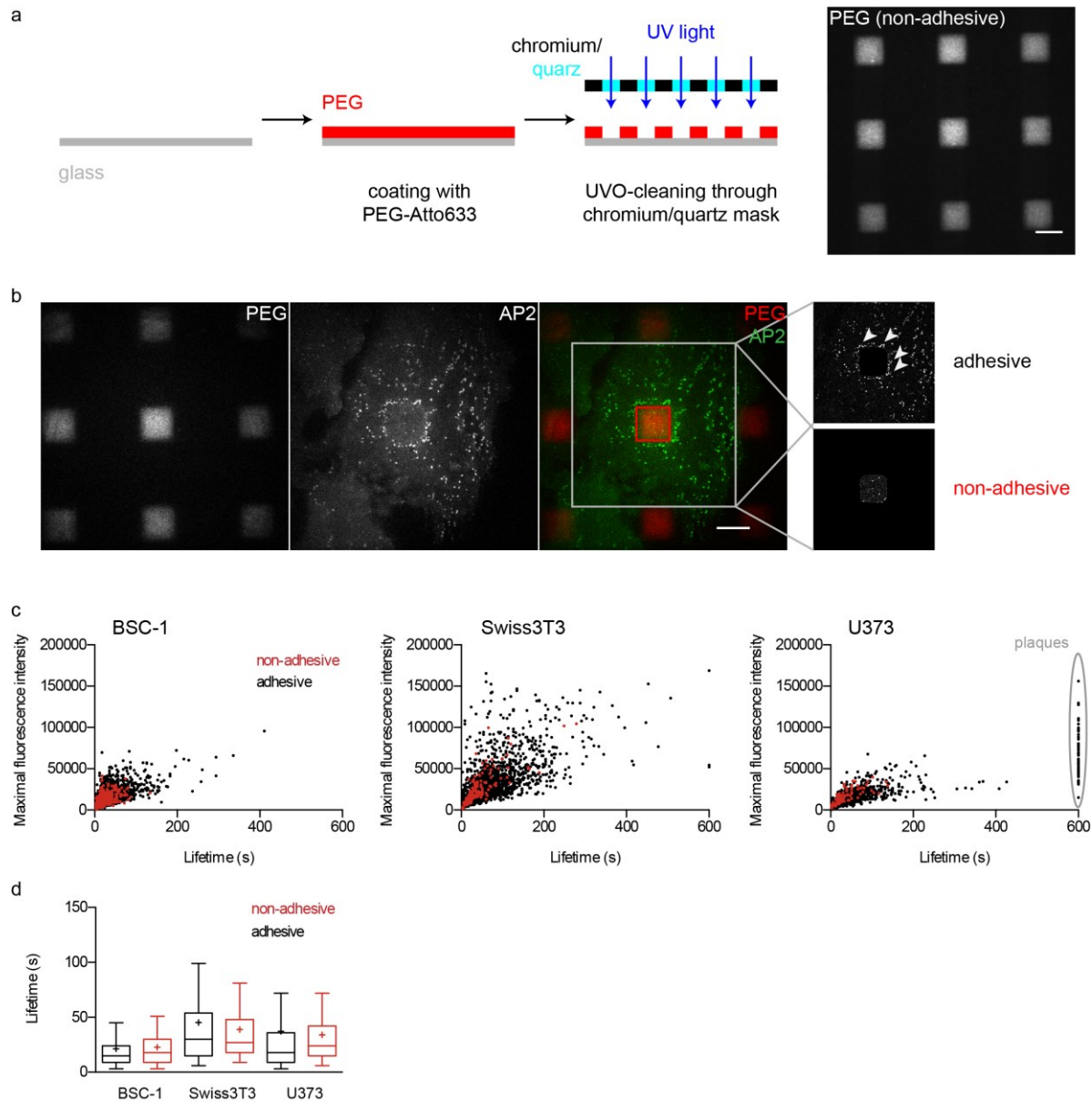


Figure 4.4: Comparison of CME at attached and non-attached PM parts using adhesive micropatterns.

(a) Schematic illustrates the production of adhesive micropatterns using photo-patterning. First, glass coverslips were passivated by coating with Atto633-labelled PLL-g-PEG. Spatially controlled UVO-cleaning through a chromium/quartz mask was performed to generate a micropattern of adhesive and non-adhesive regions. Left: Image of the adhesive micropattern used in this experiment consisting of $10\ \mu\text{m} \times 10\ \mu\text{m}$ squares of PEG with a spacing of $10\ \mu\text{m}$. Scale bar: $10\ \mu\text{m}$. (b) Example of a U373 cell stably expressing AP2-eGFP (green) growing on an adhesive micropattern of Atto633-labelled PEG (red). Adhesive (black) and non-adhesive (red) PM parts were separated by the PEG signal for further analysis of CME dynamics. Some clathrin-coated plaques on the attached PM part at the border to non-adhesive areas are marked by white arrowheads. Scale bar: $10\ \mu\text{m}$. (c) Lifetime versus maximal fluorescence intensity of AP2-eGFP of CME tracks from adhesive (black) and non-adhesive (black) PM parts of the same cell for BSC-1 (left), Swiss3T3 (middle), and U373 (right). Shown are plots of a representative cell of each cell line. Each dot represents one tracked CME event of a 10 minute long movie imaged with a frame rate of

3 seconds. Persistent clathrin-coated plaques are marked by a grey circle. Number of tracks at attached PM parts: 5,851 (BSC-1), 2,360 (Swiss3T3), and 2,849 (U373). Number of tracks at non-attached PM parts: 573 (BSC-1), 157 (Swiss3T3), and 87 (U373). (d) Box and whiskers plot showing the lifetime distributions of CME at attached (black) and non-attached (red) PM parts of the three cell lines computed from four to six cells for each cell line. Whiskers represent 10-90 percentile, box represents second and third quartile, the line marks the median, and the cross marks the mean. Number of tracks at attached PM parts: 25,832 (BSC-1), 16,842 (Swiss3T3), and 8,672 (U373). Number of tracks at non-attached PM parts: 1,655 (BSC-1), 1,148 (Swiss3T3), and 388 (U373).

adhesive micropatterns were produced using photo-patterning (Théry, 2010; Pitaval *et al.*, 2013). They consist of non-adhesive parts passivated with polyethylene glycol (PEG) and adhesive parts where PEG was oxidized using ultraviolet/ozone (UVO)-cleaning through a chromium/quartz photomask to render them adhesive (Fig. 4.4a). We produced micropatterns with non-adhesive squares with the dimensions of $10\mu\text{m} \times 10\mu\text{m}$ and a spacing of $10\mu\text{m}$ in x and y. We used Atto633-labelled PEG for visualization of the passivated regions. Therefore, the labelled fluorescent parts correspond to the non-adhesive areas. Cells growing on these patterns could attach only to the non-passivated adhesive parts but stretched over non-adhesive parts without affecting their physiological cell morphology (Fig. 4.4b). Using this approach, attached and non-attached PM parts could be found at the bottom PM of the same cell. By imaging AP2-eGFP dynamics at the bottom PM of cells growing on such adhesive micropatterns, the dynamics of CME at adhesive and non-adhesive areas could be measured (Fig. 4.4b). Tracking and analysis of CME showed that in all three cell lines only transient CCPs were formed at non-adhesive areas (Fig. 4.4c-d). The maximal fluorescence intensity of CME at attached PM parts was comparable to CME at non-attached PM parts (Fig. 4.4c). Overall, the transient CCPs at adhesive and non-adhesive parts were similar in lifetime (Fig. 4.4c). Importantly, the characteristic persistent clathrin-coated plaques found in U373 cells were found exclusively at the attached PM parts (Fig. 4.4c, right panel). Strikingly, we found that clathrin-coated plaques often aligned at the border between adhesive and non-adhesive areas (Fig. 4.4b).

Together these studies of CME at attached and non-attached PM parts revealed that transient CCPs can form at all parts of the PM in the three cell lines independent on its nature (adhesive vs. non-adhesive or ventral vs. dorsal). On the contrary, U373 cells possess a very specific kind of CCPs, the persistent clathrin-coated plaques, which form exclusively at attached PM parts (ventral or adhesive parts).

4.1.3 Cell type-specific size and morphology of CCSs

Live-cell confocal FM is a powerful tool to investigate dynamic processes in living cells but has disadvantages regarding resolution (Kirchhausen, 2009). Since the size of CCSs is most of the time below the diffraction limit of FM, confocal FM cannot resolve their size and separate CCSs that are closer than half of the wavelength of the light used for imaging (roughly around 250nm for green light) (Abbe diffraction limit) (Abbe, 1873). Additionally FM does not provide information about the ultrastructural organization of the clathrin coat (Kirchhausen, 2009).

To gain information about the ultrastructural size and morphology of CCSs in the three cell lines we used: 1) STED nanoscopy, 2) TEM of metal replicas from unroofed cells, and 3) CLEM.

For STED nanoscopy, we used an immunofluorescence staining with an anti-CLC antibody of wild type BSC-1, Swiss3T3, and U373 cells (Fig. 4.5a-c). With this approach, we could image CCSs with resolution below the diffraction limit. We were able to see ring structures, which represent invaginated CCP, since its spherical shape leads to an accumulation of CLC signal at the rim (Fig. 4.5d). Analysis of the size of CCSs found in the different cell lines revealed that the size distribution in all cell lines had similar median values around 30,000 nm² (Fig. 4.7b). In

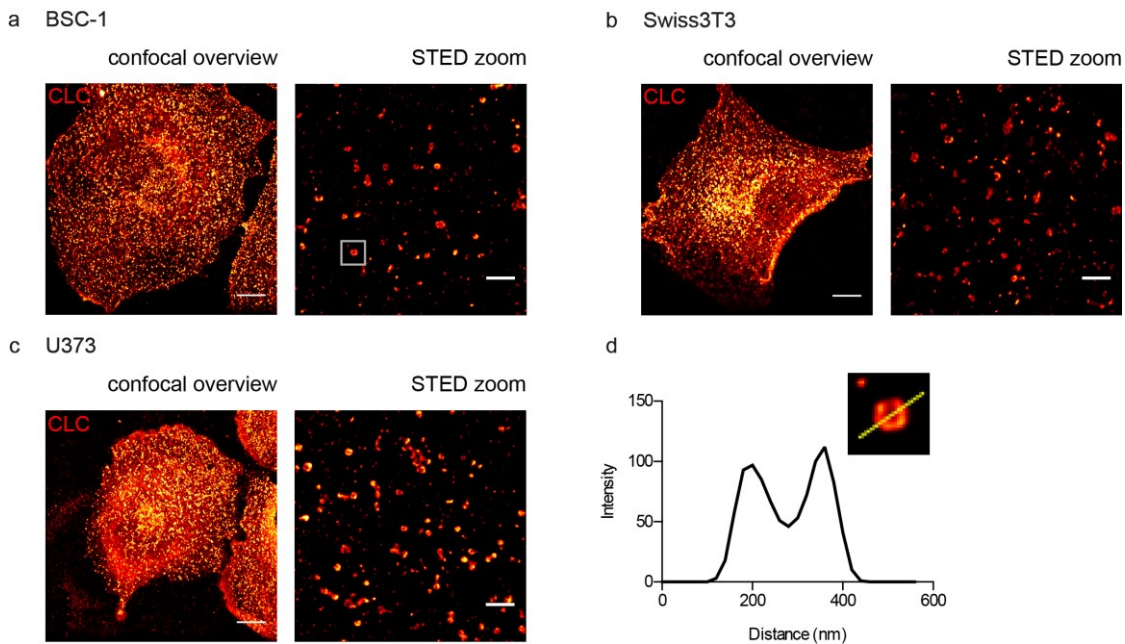


Figure 4.5: STED nanoscopy of CCS in intact cells. STED nanoscopy of (a) BSC-1, (b) Swiss3T3, and (c) U373. CCS were immunostained with an anti-CLC antibody (red) antibody. Left: confocal overview, scale bar: 5 μm. Right: STED view of CLC, scale bar: 1 μm. (d) Example of the CCP marked by the grey box in (a) and its intensity line profile. Yellow line marks the axes measured for the intensity line profiles. The data of this figure has been produced jointly with Susann Kummer, Heidelberg University. Panel a and d were adapted from Bucher *et al.* (2018).

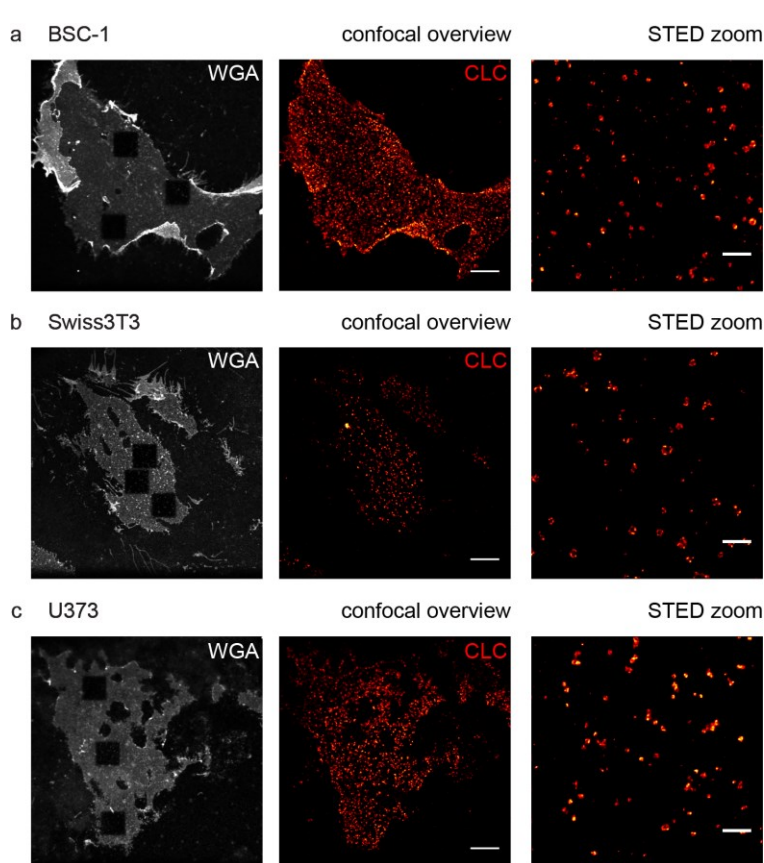


Figure 4.6: STED nanoscopy of CCS on unroofed PM sheets. STED nanoscopy of unroofed PM sheets from (a) BSC-1, (b) Swiss3T3, and (c) U373. BSC-1 cells were unroofed by sonication; the remaining attached PM was stained with WGA (grey). CCS were immunostained with an anti-CLC antibody (red). Left: confocal overviews, scale bar: 5 μm . Right: STED view of CLC, scale bar: 1 μm . The data of this figure has been produced jointly with Susann Kummer, Heidelberg University. Panel a was taken from Bucher *et al.* (2018).

contrast to the relatively small CCSs found in BSC-1 (only 5% of all clathrin structures were bigger than $80,000 \text{ nm}^2$), we could measure bigger structures in Swiss3T3 and U373 (around 15% of all clathrin structures were bigger than $80,000 \text{ nm}^2$ in both cell lines) (Fig. 4.7a-b). The broader size distribution of CCSs found in Swiss3T3 and U373 compared to BSC-1 is consistent with the broader distribution of maximal fluorescence intensity of AP2-eGFP found in live-cell microscopy (Fig. 4.2).

Although we could identify spherical shaped CCPs with STED nanoscopy, the morphology of clathrin coats was still not completely resolved with this technique. Furthermore, the use of immunolabelling with a primary and secondary antibody distorts the size measurements due to the size of the antibody complex (Huang, Bates and Zhuang, 2009). To gain more detailed structural information of CCSs, we investigated the clathrin coats in the three cell lines by TEM of metal replicas from unroofed cells (Heuser, 1980). This method enables us to look at the morphology of CCSs with very high resolution revealing the 3D structure of the polyhedral cages. The TEM method involves an unroofing step, in which sonication is used to remove the cell body to leave behind only the attached PM sheet (Heuser, 1980). We first investigated using STED nanoscopy if this unroofing procedure affects CCS. Cells were unroofed and

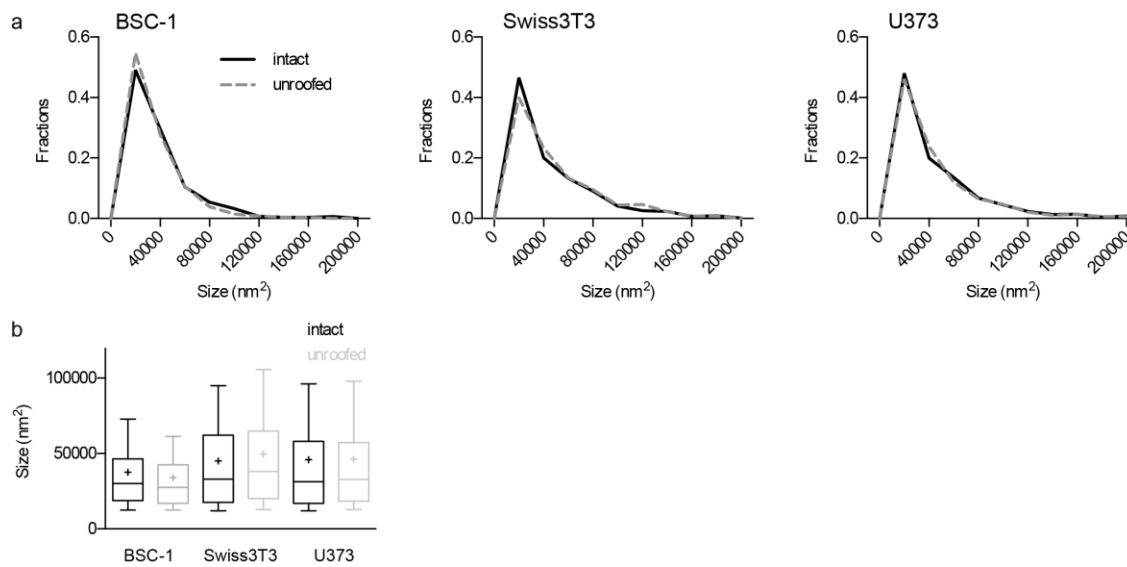


Figure 4.7: Comparative STED nanoscopy analysis of CCS in intact vs. unroofed cells. (a) Analysis of the size distribution of CCS in intact (black) and unroofed (grey) cells of BSC-1 (left), Swiss3T3 (middle), and U373 (right). Analysis was performed with CCS from five cells per conditions with three STED pictures per cell. Number of CCS for intact cells: 820 (BSC-1), 822 (Swiss3T3), and 1,162 (U373). Number of CCS for unroofed cells: 1,169 (BSC-1), 627 (Swiss3T3), and 1,431 (U373). (b) Box and whiskers plot showing the size distributions of CCS in intact (black) and unroofed (grey) cells of the three cell lines. Whiskers represent 10-90 percentile, box represents second and third quartile, the line marks the median, and the cross marks the mean. The data of this figure has been produced jointly with Susann Kummer, Heidelberg University. Panel a was adapted from Bucher *et al.* (2018).

stained with an anti-CLC antibody and fluorescently labelled wheat germ agglutinin (WGA), a lectin that binds to glycoconjugates (Chazotte, 2011), to identify PM sheets (Fig. 4.6). Using STED nanoscopy, we could not detect a difference in the morphology nor in the size between CCSs found in intact and unroofed cells in any of the cell lines (Fig. 4.6-7). Therefore, we concluded that the unroofing step in the sample preparation for TEM does not alter the size of CCSs. Sample preparation was performed as depicted in Fig. 4.8, and imaging of montages covering whole PM sheets to observe several hundreds of CCSs in the three cell lines was performed by TEM (Fig. 4.9a). The investigation of CCSs on the PM sheets revealed different morphologies of clathrin coats: flat, slightly curved dome, deeply invaginated pit structures as well as flat structures with budding dome or pits at the edge (Fig. 4.9b). Strikingly, the three cell lines showed different ratios between these morphologies and some of the structural shapes were unique for certain cell lines. In BSC-1, we found only flat, dome, and pit structures with a ratio of around 5:2:3, respectively (Fig. 4.9b-c). The majority of CCSs in Swiss3T3 was flat (around 70%) and the abundance of dome and pit structures was similar (around 15%) (Fig. 4.9b-c). In contrast, U373 showed the highest percentage of pit structures

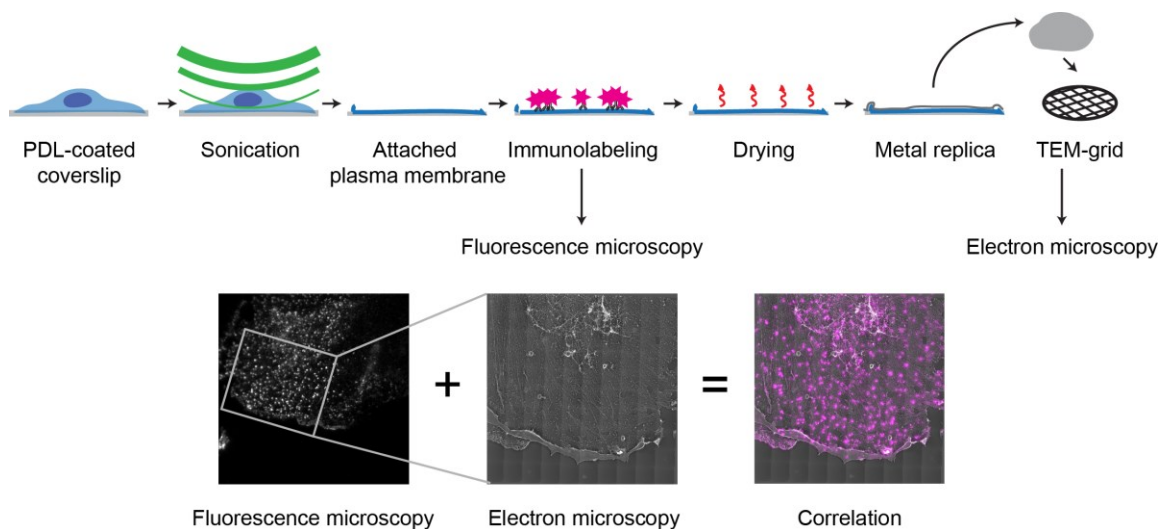


Figure 4.8: CLEM using TEM of metal replicas from unroofed cells. Schematic representation of the CLEM approach (Upper part). For TEM imaging only, the immunolabelling step was skipped. Cells growing on poly-D-lysine (PDL)-coated coverslips were unroofed by sonication. Attached PM sheets were immunostained and imaged using FM. Samples were then critical-point dried and a metal replica was created and lifted from the sample onto a TEM grid for imaging in TEM. (Lower part) The FM and TEM pictures were then correlated to combine their information. The white inset box represents the area observed by TEM. The figure was taken from Bucher *et al.* (2018).

(approximately 50%), around 25% flat and 15% dome structures as well as around 10% flat structures with domes or pits budding from the edge of the array, a morphology that was almost not present in the other two cell lines (Fig. 4.9b-c).

By measuring the projected area of each clathrin coat, we estimated and compared the size of the different CCS morphologies in the different cell lines. While BSC-1 had flat, dome, and pit structures with similar projected areas of around $15,000 \text{ nm}^2$, CCSs in the other cell lines could grow much bigger in size (Fig. 4.10a). We found large flat and dome structures in Swiss3T3 with mean projected areas of $65,000 \text{ nm}^2$ and $55,000 \text{ nm}^2$, respectively (Fig. 4.10a). In U373, only flat structures were large (mean projected area of $22,000 \text{ nm}^2$) especially when they displayed budding structures on the edge, which had a mean projected area of $55,000 \text{ nm}^2$ (Fig. 4.10a).

To further describe the CCSs, we calculated the circularity of their shape (circularity of 1 corresponds to a perfect circle). Flat, dome, and pit structures in BSC-1 cells were nearly circular with mean circularities of over 0.98 for all three morphologies (Fig. 4.10b). The circularity of CCS in Swiss3T3 was less robust. In particular, pits in Swiss3T3 were frequently elongated in shape (Fig. 4.10b). Although dome and pit structures in U373 exhibited a high circularity with a mean over 0.99, flat structures, especially those with budding structures at the edge, were less

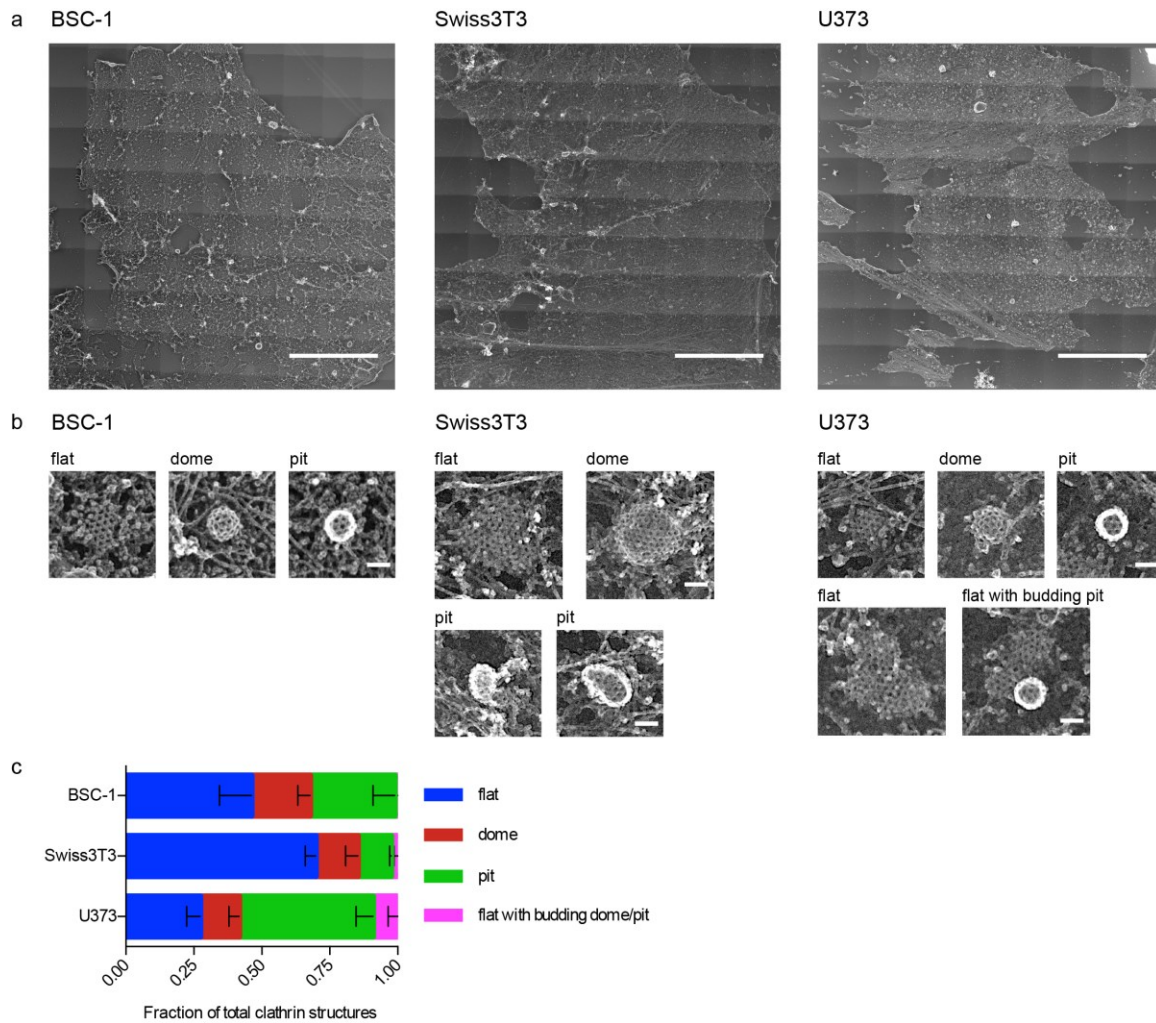


Figure 4.9: Ultrastructural characterisation of CCS by TEM. (a) TEM of metal replica of unroofed PM sheets from of BSC-1 (left), Swiss3T3 (middle), and U373 (right). Overview of whole membranes, scale bar: 10 μm . (b) Representative examples of morphological categories found in the three cell lines: Flat, dome, pit, and flat with budding dome/pit. Scale bar: 100 nm. (c) Fraction of flat (blue), dome (red), pit (green), and flat with budding dome/pit (magenta) CCS on PM sheets. Results are calculated from three to four different membranes for each cell line. Total number of CCS: 2,384 (BSC-1), 1,208 (Swiss3T3), and 3,627 (U373). Means with SD are shown. The data of this figure has been produced jointly with Kem A. Sochacki, NIH Bethesda. The panels a-c concerning BSC-1 cells were adapted from Bucher *et al.* (2018).

circular with means of 0.96 and 0.72 respectively (Fig. 4.10b). Overall, we found a universal negative correlation between projected area and circularity: the bigger the clathrin structure gets the less circular it becomes. This observation was most striking for flat clathrin structures with and without budding domes or pits (Fig. 4.10c, blue and magenta dots).

To correlate fluorescence signal with coat morphology, we performed CLEM using immunofluorescence staining against CHC (Fig. 4.8 and 4.11). We could correlate fluorescence

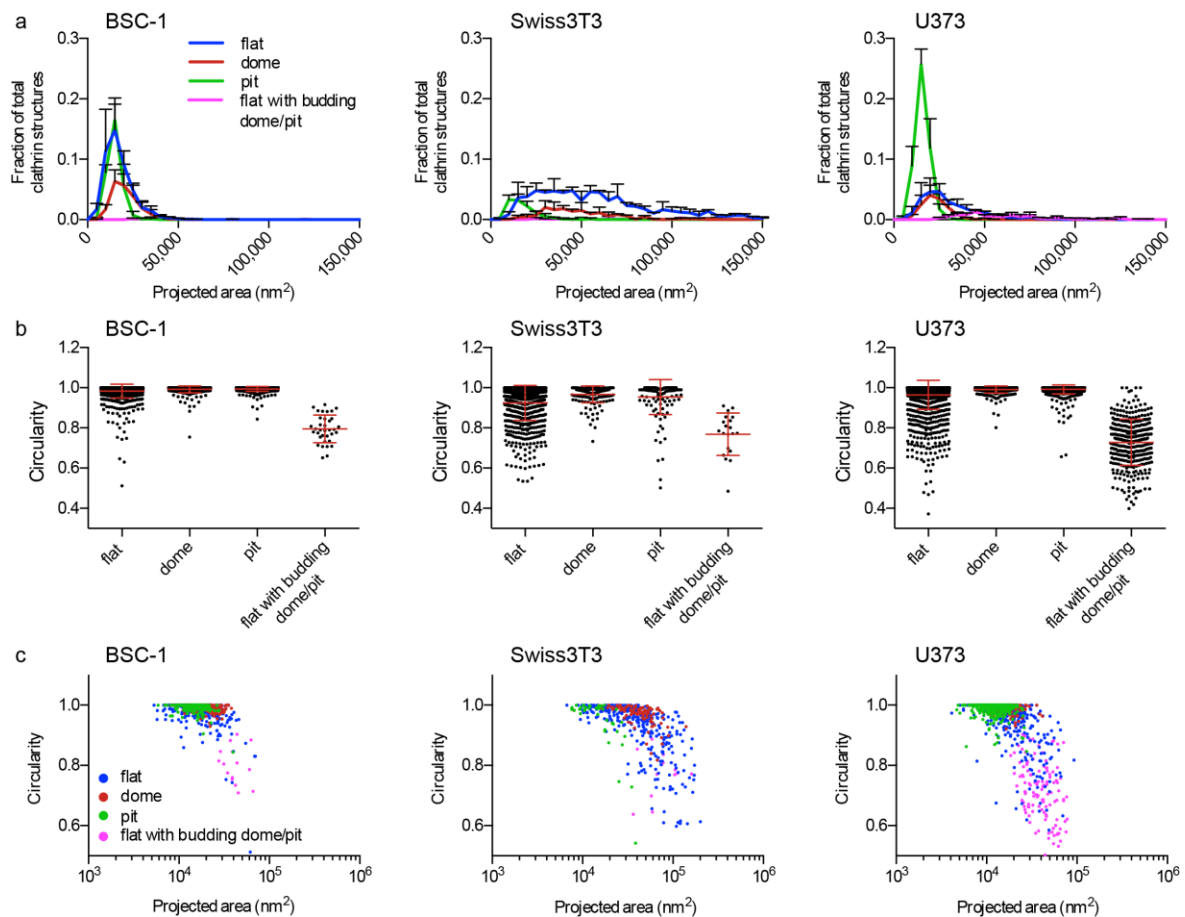


Figure 4.10: Comprehensive ultrastructural analysis of CCS in by TEM. (a) Projected area distribution of the different clathrin morphologies (flat (blue), dome (red), pit (green), and flat with budding dome/pit (magenta)) found in BSC-1 (left), Swiss3T3 (middle), and U373 (right). Means with SD are shown. (b) Circularity of CCS with different morphologies of BSC-1 (left), Swiss3T3 (middle), and U373 (right). Line (red) represents the mean with SD. Each dot represents one CCS. Results of (a) and (b) are calculated from three to four different membranes for each cell line. Total number of CCS: 2,384 (BSC-1), 1,208 (Swiss3T3), and 3,627 (U373). (c) Circularity and size of CCS with different morphologies (flat (blue), dome (red), pit (green), and flat with budding dome/pit (magenta)). Each dot represents one CCS. Shown are the results of one representative PM sheet of BSC-1 (left), Swiss3T3 (middle), and U373 (right). The data of this figure has been produced jointly with Kem A. Sochacki, NIH Bethesda.

signal to CCSs of different morphology (Fig.4.11a). We found a positive correlation between size and fluorescence signal of CCS in all three cell lines (Fig.4.11b). Some of the clathrin coats that could be identified in TEM were so close together that they could not be distinguished by FM due to the diffraction limit. We classified them as multiple structures (Fig.4.11a). This phenomenon was more severe in Swiss3T3 and U373 compared to BSC-1 (around 40% of all fluorescence signal in Swiss3T3 and U373 compared to 17% in BSC-1), which makes BSC-1 cells a good cell line to study single CCSs by FM. The persistent clathrin-coated plaques with

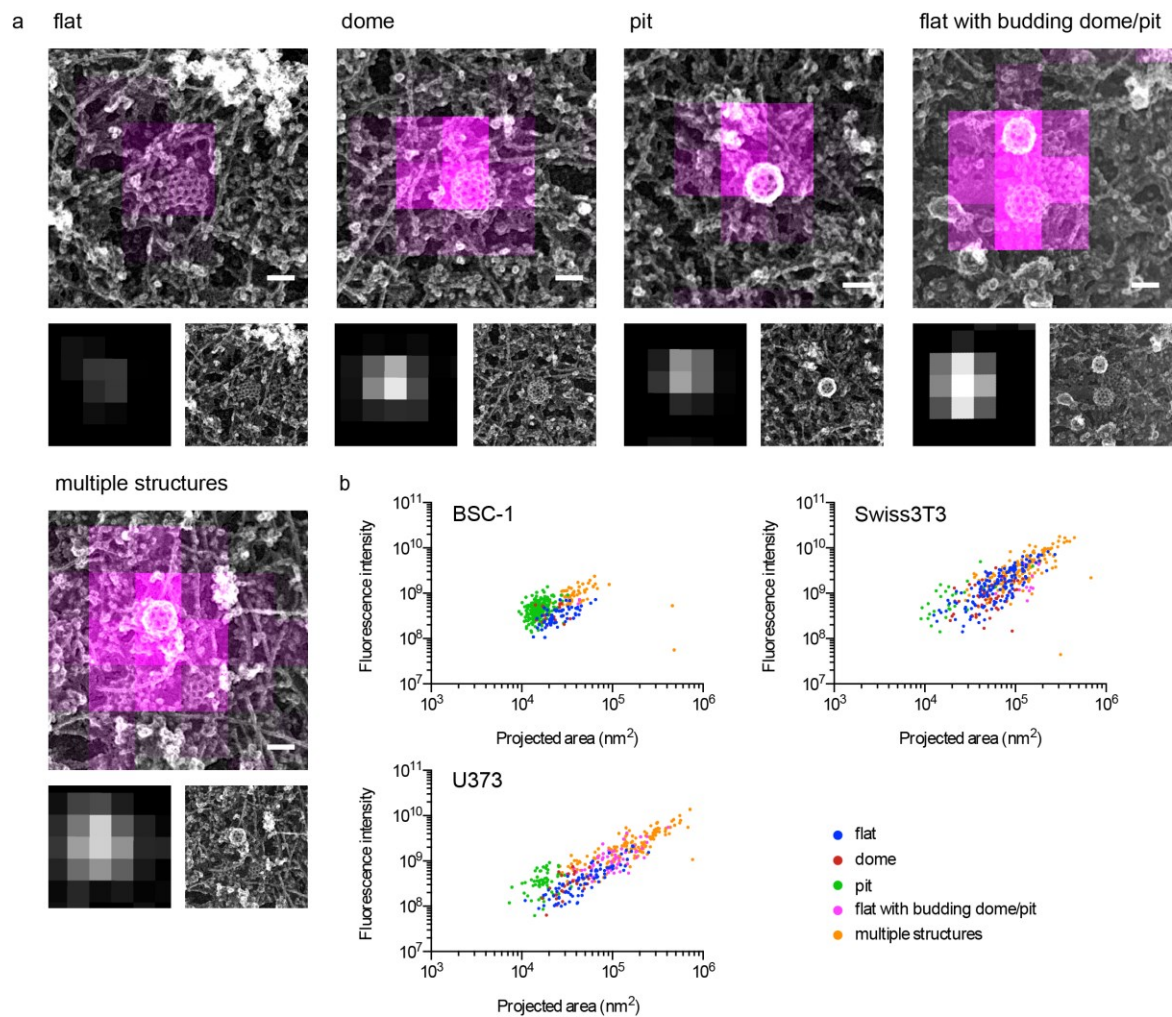


Figure 4.11: CLEM of CCS. (a) Examples of flat, dome, pit, flat with budding dome/pit, and multiple structures, which cannot be distinguished by FM, observed with CLEM. Top panel: CLEM, lower left: FM, lower right: TEM; scale bar: 100 nm. (b) Correlation of size and fluorescence intensity (CHC antibody, X22) of all CCSs sorted by their different morphologies (flat (blue), dome (red), pit (green), flat with budding dome/pit (magenta), and multiple structures (orange)). Graphs show representative CLEM analysis of one PM sheet for BSC-1 (top left), Swiss3T3 (top right), and U373 (bottom). Total number of CCS: 559 (BSC-1), 407 (Swiss3T3), and 456 (U373). The data of this figure has been produced jointly with Kem A. Sochacki, NIH Bethesda. The panel a and b (BSC-1) were adapted from Bucher *et al.* (2018).

high fluorescence intensity found in U373 using live-cell microscopy (Fig. 4.2a) are most likely flat clathrin structures with or without budding domes or pits since they show the highest fluorescence intensity in CLEM (Fig. 4.11b). Furthermore, the persistent clathrin-coated plaques (Fig. 4.2a) as well as the flat structures with budding domes or pits (Fig. 4.9c) are unique for U373 cells when compared to the other cell lines used in this study, which indicates that they are the same CCSs.

Overall, the structural analysis of clathrin coats uncovered cell type-dependent size and morphology distributions of CCSs that are most likely a consequence of differential regulation of coat formation and growth behaviour. When distinguished by their ultrastructure, we will from now on describe and differentiate between small deeply invaginated CCP and large flat clathrin-coated plaques, which can pinch off CCPs from their rim.

4.2 Investigation of structural changes of the clathrin coat during CCP formation

The ultrastructural steps during CCP formation have been a controversial topic for many years (Heuser, 1980; Larkin, Donzell and Anderson, 1986; Kirchhausen, 2009; Avinoam *et al.*, 2015; Lampe, Vassilopoulos and Merrifield, 2016). On the basis of EM and FM data, two assembly models have been proposed: The constant curvature model and the constant area model (Fig. 2.4a) (Lampe, Vassilopoulos and Merrifield, 2016). We challenged these two models by using a combination of experimental data (FM, TEM, and CLEM) and mathematical growth modelling to evaluate their possibility and refine our current understanding of the structural changes of CCSs during CCP assembly.

The text and figures of the following paragraphs (4.2.1-4.2.4) have been adapted from Bucher *et al.* (2018). This corresponds to a co-first author accepted manuscript resulting directly from my PhD research project.

4.2.1 EM and CLEM analysis of CCSs do not support existing growth models

To address whether CCP formation follows the constant curvature model or the constant area model (Fig. 4.12a) (Lampe, Vassilopoulos and Merrifield, 2016), we chose BSC-1 cells, a widely used cellular model to study CME (Ehrlich *et al.*, 2004; Boucrot *et al.*, 2006; Saffarian, Cocucci and Kirchhausen, 2009). BSC-1 cells present homogenous CME events in regard to both lifetime as well as intensity profiles and lack the long-lived flat clathrin-coated plaques (Fig. 4.1-2, 4.9-10) (Saffarian, Cocucci and Kirchhausen, 2009; Grove *et al.*, 2014). Both models predict different growth profiles for the surface and projected area of CCSs during CCP formation. The constant curvature model implies that the projected area will quickly be smaller than the surface area. In contrast, the constant area model proposes that both projected and surface area initially show similar growth but then the projected area should drop significantly as bending starts (Fig. 4.12b).

To comprehensively characterise the ultrastructural organisation of CCSs in BSC-1 cells, we performed TEM of metal replicas from unroofed PMs (Fig. 4.9 and 4.12c-e). CCSs in TEM images of whole PM sheets were counted, categorised as flat, dome or pit structures and their size was measured as projected area (Fig. 4.12c-e). For the constant curvature model, we would expect no flat structures at all and no dome structures that exceed the projected area of pits (Fig. 4.12a-b). In contrast, our EM data reveals that around 50% of the CCSs in BSC-1

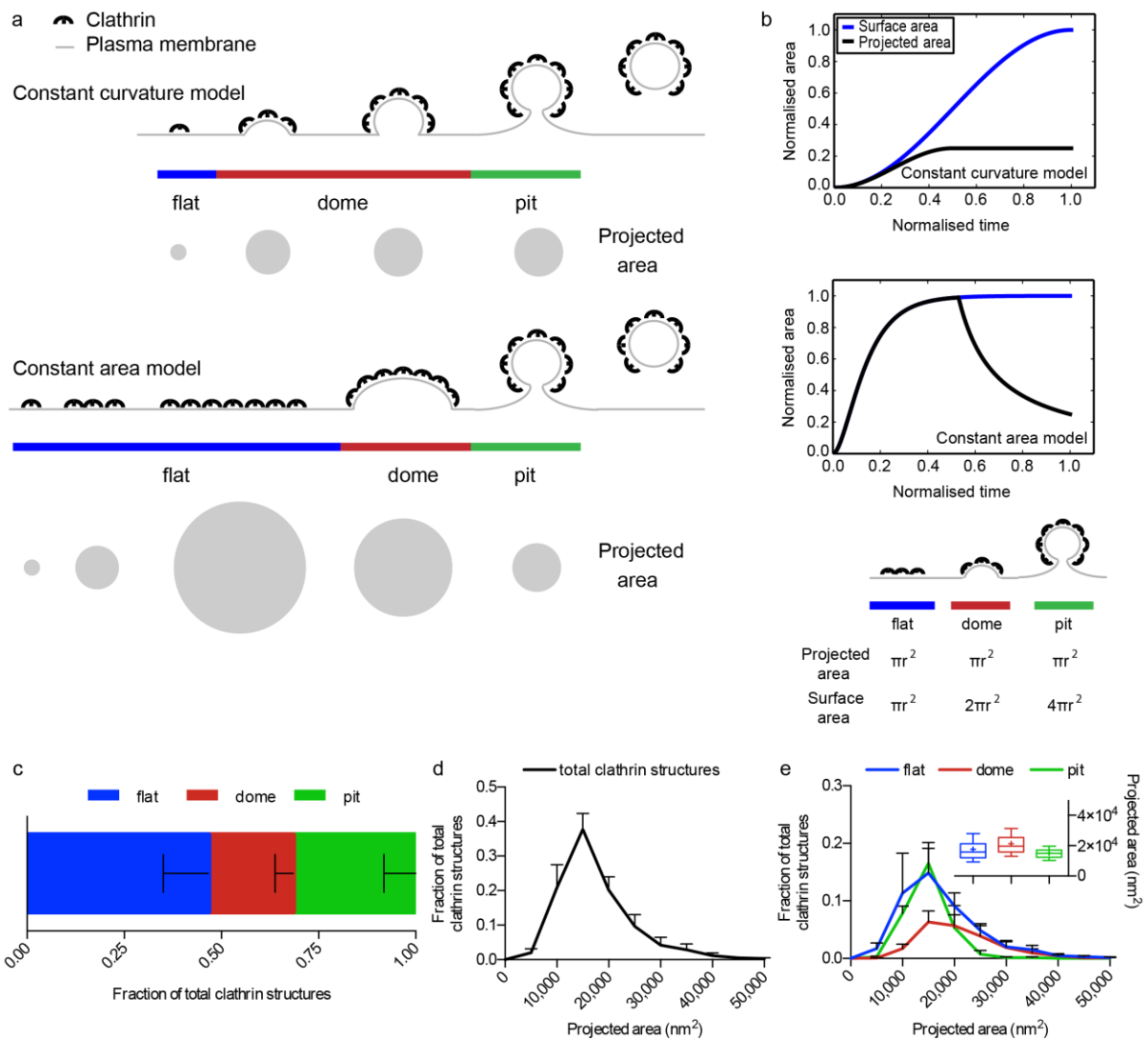


Figure 4.12: Comprehensive ultrastructural characterisation of CCSs in BSC-1 cells by TEM. (a) Schematic of the constant curvature and constant area models. The stages of different curvature (flat (blue), dome (red), pit (green)) and the variation of projected area, which can be assessed during TEM imaging, is depicted for both growth models. (b) Difference between projected area (black) and surface area (blue) during the course of CCP formation according to the two models. The schematic illustrates the relationship between projected area and surface area for flat, dome (approximately a hemisphere), and pit (approximately a complete sphere) CCSs. (c) Fraction of flat (blue), dome (red) and pit (green) CCSs in whole PM of BSC-1 cell. (d) Projected area distribution of all CCSs (black) measured by TEM. (e) Projected area distribution of the different clathrin morphologies (flat, dome, pit). A box/whiskers plot of the projected area is shown in the inset. Mid-line represents median, cross represents the mean and the whiskers represent the 10 and 90 percentiles. Results are calculated from three different membranes (number of CCSs per membrane: 746, 869, and 739); means with SD are shown. The data of this figure has been produced jointly with Kem A. Sochacki, NIH Bethesda. This figure has been adapted from Bucher *et al.* (2018).

correspond to flat CCSs (Fig. 4.12c) and that a large fraction of the flat and dome structures has a projected area larger than the projected area of the pits (Fig. 4.12e). Since BSC-1 cells do not have clathrin-coated plaques (Fig. 4.1-2, 4.9-10) (Saffarian, Cocucci and Kirchhausen, 2009; Grove *et al.*, 2014), these results demonstrate that the constant curvature model cannot explain the CCS size distribution, in agreement with the recent results by Avinoam *et al.* (2015). Since the existence of flat CCSs seems to argue in favour of the constant area model, we would expect that some flat structures have the same projected area as the surface area of fully formed pits (Fig. 4.12a-b). Since the surface area of a spherical pit ($4\pi r^2$, Fig. 4.12b) is four times larger than its projected area (πr^2 , Fig. 4.12b), we would expect the mature flat structures to have around four times the projected area of pits (Fig. 4.12b). Instead, we found no flat structures at all with a projected area four times larger than the mean projected area of CCPs (Fig. 4.12e). Additionally, the constant area model would imply that the projected area of dome structures (which resembles a hemisphere) is reduced by a factor of two when converting to CCPs. Instead we found only a slight increase of the mean projected area of domes compared to pits (Fig. 4.12e, distribution and inset box/whiskers). Together, these observations argue against the constant area model.

To further challenge the two growth models, we used a CLEM approach (Sochacki *et al.*, 2014, 2017) (Fig. 4.8). BSC-1 cells were immunostained with a clathrin heavy chain antibody and the fluorescence intensity of CCSs was correlated to their size and ultrastructural organisation measured using TEM of metal replicas (Fig. 4.13). CCS were classified according to their ultrastructural organization observed by TEM as flat, dome and pit structures. Some of the CCS could be separated and identified by TEM but not by FM due to its lower resolution (i.e. multiple CCSs appearing as one fluorescent object). We classified them as “multiple structures” (Fig. 4.11a) and excluded them from further analysis. Since fluorescence intensity correlates to the surface area of CCSs, we would expect the intensity to increase with increasing contact angle for the constant curvature model (Fig. 4.12a-b). In case of the constant area model, we would expect equal intensity for the largest flat, domes, as well as all pit structures (Fig. 4.12a-b). However, our CLEM analysis clearly revealed that flat and dome structures have similar fluorescence intensities while pits tend to display higher fluorescence intensities (Fig. 4.13a and c). These flat CCSs had a mean fluorescence intensity of around 70% of the pits (Fig. 4.13a box/whiskers; mean fluorescence intensity for flat CCSs: 1.6×10^8 ; pits: 2.3×10^8). In conclusion, our TEM and CLEM analyses argue that neither of the proposed growth models fully explains the observed ultrastructural distribution and corresponding fluorescence intensities of CCSs in BSC-1 cells.

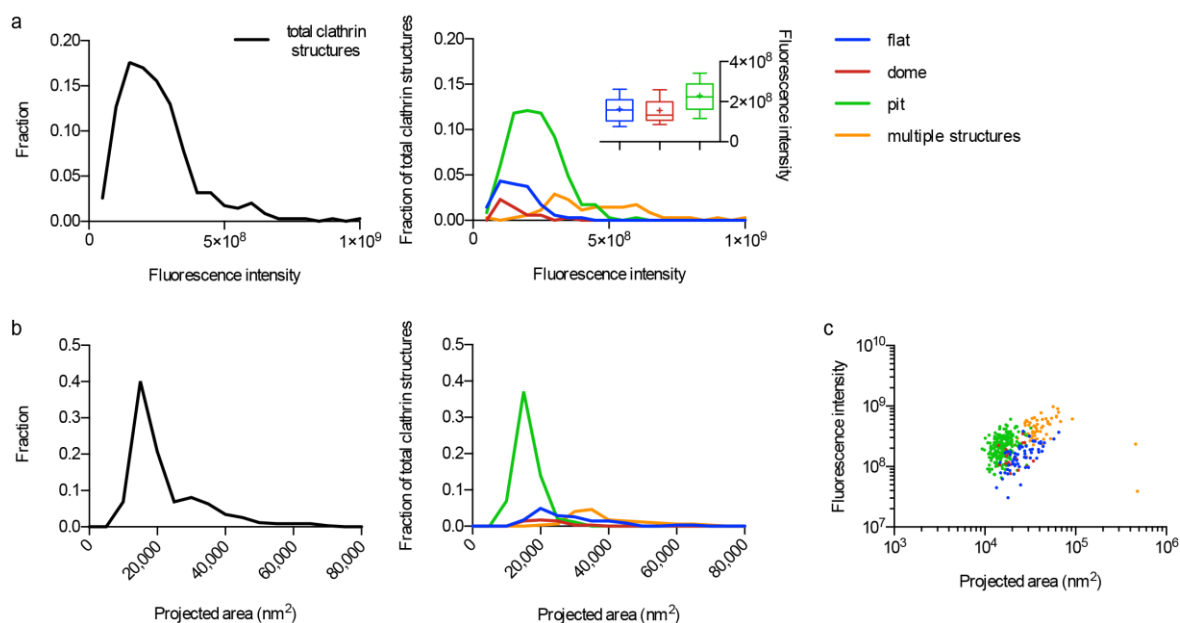


Figure 4.13: CLEM of CCSs. (a) Fluorescence intensity distribution (clathrin heavy chain antibody, X22) of all CCS (black line, left panel) and of flat (blue), dome (red), pit (green) CCSs, and multiple structures which cannot be distinguished by fluorescence microscopy (orange) (right panel). A box/whiskers plot of the fluorescence intensity is shown in the inset. Mid-line represents median, cross represents the mean and the whiskers represent the 10 and 90 percentiles. (b) Projected area distribution of all CCSs (black line, left panel) and of the different clathrin morphologies (right panel). (c) Correlation of size and fluorescence intensity of all CCSs sorted by their different morphologies. Graphs show one representative CLEM result with a total of 347 CCSs from one PM. The data of this figure has been produced jointly with Kem A. Sochacki, NIH Bethesda. This figure has been adapted from Bucher *et al.* (2018).

4.2.2 Modelling of CCP assembly reveals bending of the coat before reaching full surface area

Although EM of metal replicas is a high-resolution microscopy technique revealing detailed information about the size and ultrastructure of CCSs, it only provides snapshots of the dynamic process of CCP assembly (Higgins and McMahon, 2017). In contrast, live fluorescence microscopy (FM) of CME mostly allows the characterisation of the dynamics of different proteins during the formation of CCSs but does not provide ultrastructural information (Kirchhausen, 2009). To obtain a more comprehensive dynamical picture, we used mathematical modelling of clathrin growth behaviour to combine the ultrastructural information from EM with the dynamic information obtained from total internal reflection fluorescence (TIRF) microscopy of fluorescently tagged CLC. Our approach is to estimate the morphology distribution of CCSs by fitting growth curves to individual CME fluorescence profiles. As the formation of CCSs is a

complex process with numerous yet unknown variables, here the modelling approach is used only to combine and compare the different data sets (FM, TEM and CLEM), with minimal assumptions on the underlying mechanisms. To correlate the temporal information of CCS dynamics obtained by live FM to the size information of these CCSs obtained by TEM we used CLEM to convert the fluorescence signal into surface area (see Materials and methods 6.3.3-5). Since we found a substantial number (around 50%) of flat CCSs with projected areas similar to pits (Fig. 4.12c and e), we rule out the possibility that the constant curvature model might be the dominant growth behaviour in BSC-1 cells. We therefore modelled the growth of CCSs according to the constant area model. For this, CCSs first initiate as flat circular planar discs that grow to a finite size before bending (Fig. 4.14a). We assume growth of a CCS to be possible only at its edge, because incorporation of new triskelia in the area is expected to be energetically and topologically unfavourable. To avoid explosive growth and to lead to a stable situation, however, this process has to be balanced by another process. Geometrically the simplest possible model is that growth is limited by a process coupled to the area of the planar disc. Dissociation over the area would be such a process, but alternatively one could think of negative biochemical feedback increasing in proportion to the area (Fig. 4.14a and Materials and methods 6.3.1-2 and 8). By fitting the resulting growth equation (Fig. 4.14a Equation 1) and assigning the three different morphologies to the individual intensity profiles obtained by TIRF microscopy (Fig. 4.14b), we could calculate the size and morphology distribution of CCSs as predicted by the constant area model (Fig. 4.14c). As we are following the constant area model, CCSs grow flat to their final size, which is represented by the plateau phase of the growth curves (blue area in Fig. 4.14b). Within the constant area model, the ratio of domes and pits is directly proportional to their transformation dynamics. We exploited the distribution of domes and pits observed in EM (40:60%, respectively) (Fig. 4.12c and in Avinoam *et al.* 2015 (Fig. 6.1)), to define the time necessary to ultrastructurally rearrange a flat CCS to dome (red area) and a dome to CCP (green area) (Fig. 4.14b and see Materials and methods 6.3.1). To calculate the size and morphology distribution of CCSs, we have to neglect the predicted objects for which sizes fall under the detection limit of TEM which we have determined as being the smallest object that can be confidently identified as clathrin coat by TEM (Fig. 4.14b, dashed line). This ensures that both the calculated and measured data sets are similarly restricted. Comparison of the calculated distribution to the acquired EM data reveals that the ratio between the flat, dome, and pit structures is biased toward flat structures compared to the EM data (Fig. 4.14g). Additionally, the means of the predicted size distributions of flat and pit structures are clearly separated with a shift of the flat projected area towards bigger sizes (Fig. 4.14c and i,

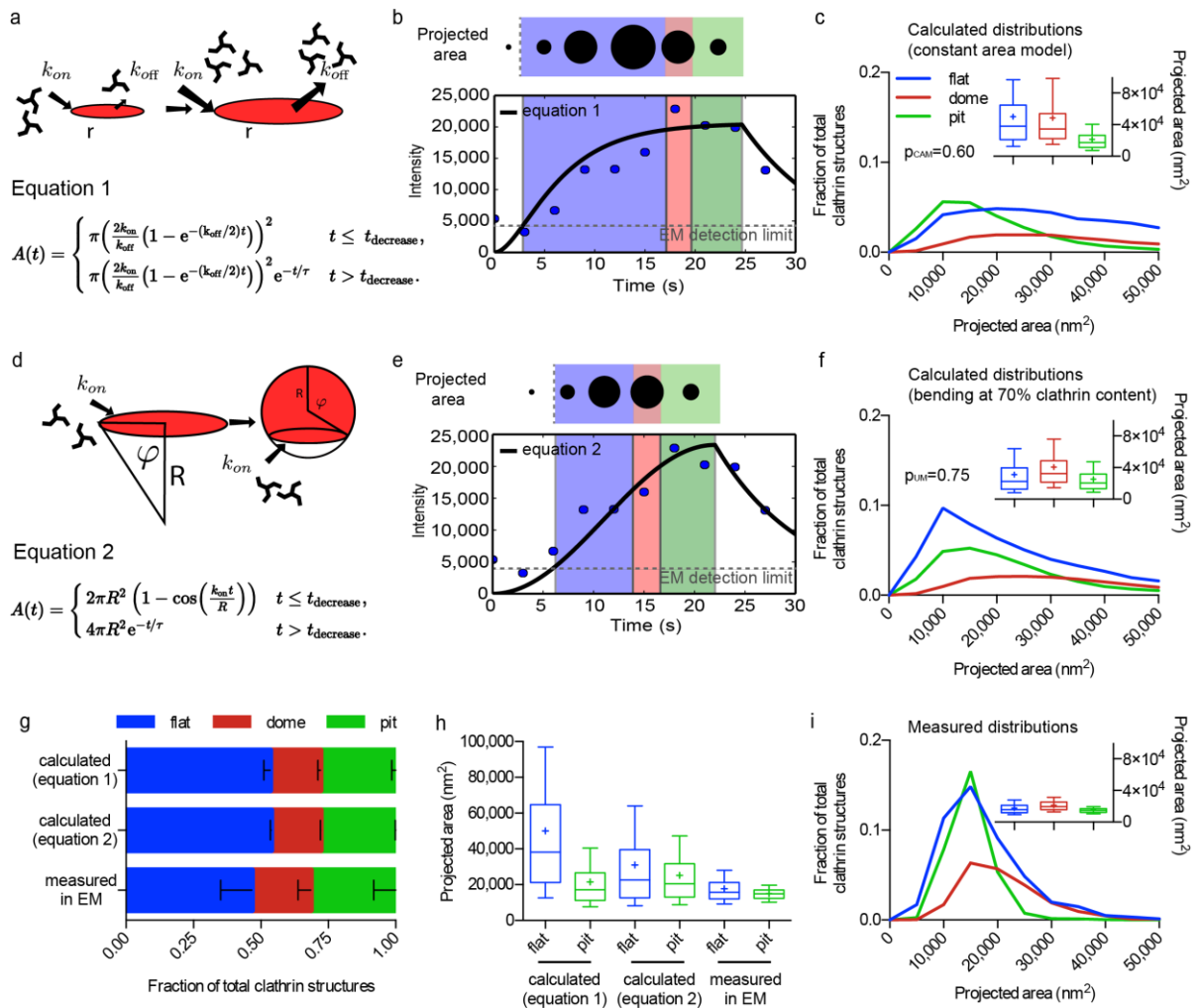


Figure 4.14: Mathematical modelling of CCS growth from intensity profiles of individual CME events. (a) Mathematical representation of the constant area model, flat-to-curved transition happens at the time when clathrin reaches its final content. (b) Example of a clathrin intensity track fitted by the constant area model. Blue dots represent measured intensity of a single CME event; black line represents the fit with equation 1, dashed grey line marks the EM detection limit. The schematic on the top illustrates the calculated projected area and assigned curvature, flat (blue), dome (red), and pit (green). (c) Calculated projected area and curvature distributions of the CCS according to the constant area model for 4927 FM tracks of four different cells. P-value of Welch's t-test to compare the predicted to the measured distribution in panel h. A box/whiskers plot of the projected area is shown in the inset. Mid-line represents median, cross represents the mean and the whiskers represent the 10 and 90 percentiles. (d) Mathematical representation of the updated growth model where a flat clathrin patch grows and the flat-to-curved transition happens before reaching the final clathrin content. (e and f) same as (b and c) but using equation 2. (g) Comparison of the predicted ratio of flat, dome, and pit structures from both growth model (equation 1 (a) and equation 2 (d)) and the distribution obtained from TEM imaging. Results are calculated for 4927 FM tracks of four different cells; means with SD are shown. (h) Direct comparison of the projected area distribution of flat and pit structures calculated by equation 1 and 2 as well as measured in EM, box/whiskers plot. (i) TEM data as shown in Fig. 4.12e. Modelling has been performed by Felix Frey, Heidelberg University. This figure has been taken from Bucher *et al.* (2018).

box/whiskers and Fig. 4.14h). In agreement with our TEM and CLEM results, our mathematical modelling approach thus demonstrates that the constant area model does not correctly describe the assembly process of CCPs in BSC-1 cells.

Given the high proportion of flat structures (Fig. 4.12c), we reasoned that CCSs start as flat structures and then acquire curvature before reaching the full clathrin content (Fig. 4.14d and Materials and methods 6.3.9-11). In contrast to the constant area model (Fig. 4.14a), now the system has an intrinsic mechanism to stop growth, namely formation of a sphere and therefore needs no balancing mechanism (no regulation by the area) besides the regulation by curvature in a minimal model. As we previously observed that the clathrin content of flat structures represents 70% of the clathrin content of CCPs (Fig. 4.13a, box/whiskers), we reasoned that transition from flat to dome occurs at 70% of their final clathrin content (Fig. 4.14e, blue area). Similar to the constant area model we defined conversion to domes (red area) and pits (green area) according to their relative ratio observed in TEM. The resulting growth equation was again fitted to the individual intensity profiles of CME events (Fig. 4.14e). To test the different models, we compare them on the level of size and morphology distributions (instead of single trajectories). Our approach therefore represents the typical statistics of the system and is not meant to describe single trajectories that are prone to depend strongly on molecular details. As a matter of fact, the calculated ratio between the flat, dome, and pit structures is similar as before and biased towards flat structures (Fig. 4.14g), but in contrast now the calculated size and morphology distribution fit the EM data better than the distribution according to the constant area model. The means of the predicted projected area of both the flat and pit have similar sizes (Fig. 4.14f and h, box/whiskers). These findings strongly support a model where assembly of a CCP initiates flat and then acquires curvature at around 70% of its final clathrin content.

4.2.3 Starting point of acquiring curvature is marked by a change in the AP2/clathrin ratio

The flat-to-curved transition of a CCSs requires major ultrastructural reorganisation of the coat (den Otter and Briels, 2011). To acquire curvature, according to Euler's theorem the hexagonal organisation of the clathrin triskelia needs to reorganise into a polyhedral assembly including 12 pentagons (den Otter and Briels, 2011). The clathrin lattice in flat structures is mostly composed of hexagons (Heuser, 1980; Maupin and Pollard, 1983). Although it has been shown using FRAP that the clathrin coat is highly dynamic, which is a prerequisite for such rearrangement

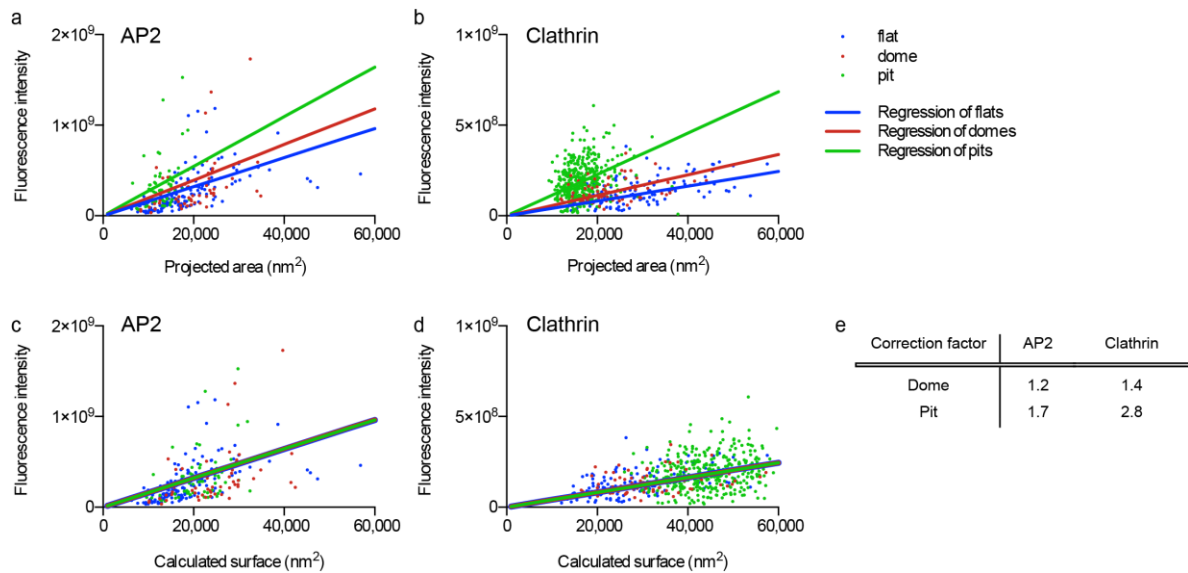


Figure 4.15: The relative amount of AP2 and clathrin molecules per surface unit of a CCS is curvature dependent. CLEM analysis of CCS labelled with AP2-eGFP (a) or clathrin heavy chain antibody (b). Flat (blue), dome (red), and pit (green). Lines in the corresponding colour show linear regression of the projected area and of the fluorescence intensity. CLEM analysis of CCSs corrected according to the regression of flat structures labelled with AP2-eGFP (c) or clathrin heavy chain antibody (d). Projected areas of dome and pit structures of the CLEM analysis were multiplied by a correction factor to fit the linear regression of flat CCSs. Lines in the corresponding colour show linear regression of the calculated surface and the fluorescence intensity. (e) Table shows correction factors for dome and pit structures for AP2-eGFP or clathrin heavy chain labelling used in (c) and (d). Calculations have been performed by Felix Frey, Heidelberg University. This figure has been taken from Bucher *et al.* (2018).

(Wu *et al.*, 2001, 2003; Avinoam *et al.*, 2015), it is still puzzling what regulates the organisation of triskelia in the coat and what coordinates the flat-to-curved transition. It was proposed before that the ratio of the adaptor AP2 to clathrin changes within the growth of CCPs (Saffarian and Kirchhausen, 2008; Loerke *et al.*, 2011; Sochacki *et al.*, 2017). Therefore, we correlated the relative amount of AP2 and the ultrastructural organisation of CCS. We performed CLEM analysis using BSC-1 cells expressing AP2-eGFP (Fig. 4.15a) and correlated these results to clathrin immunostaining CLEM (Fig. 4.15b). To find the relationship between fluorescence intensity and the surface of CCSs, the measured projected area needs to be corrected for the curvature to obtain the surface area of the CCSs (Fig. 4.12b). For flat structures, projected area and surface area are identical, thus we used the linear regression of flat coats as a reference to correct the projected area of both domes and pits. Assuming the geometry of a hemisphere for domes and an almost complete sphere for pits we expect a correction factor of ≤ 2 for domes and $2 < x \leq 4$ for pit structures if the relationship between fluorescence intensity and surface area is independent of curvature (Fig. 4.12b). The correction factors inferred for domes and pits were

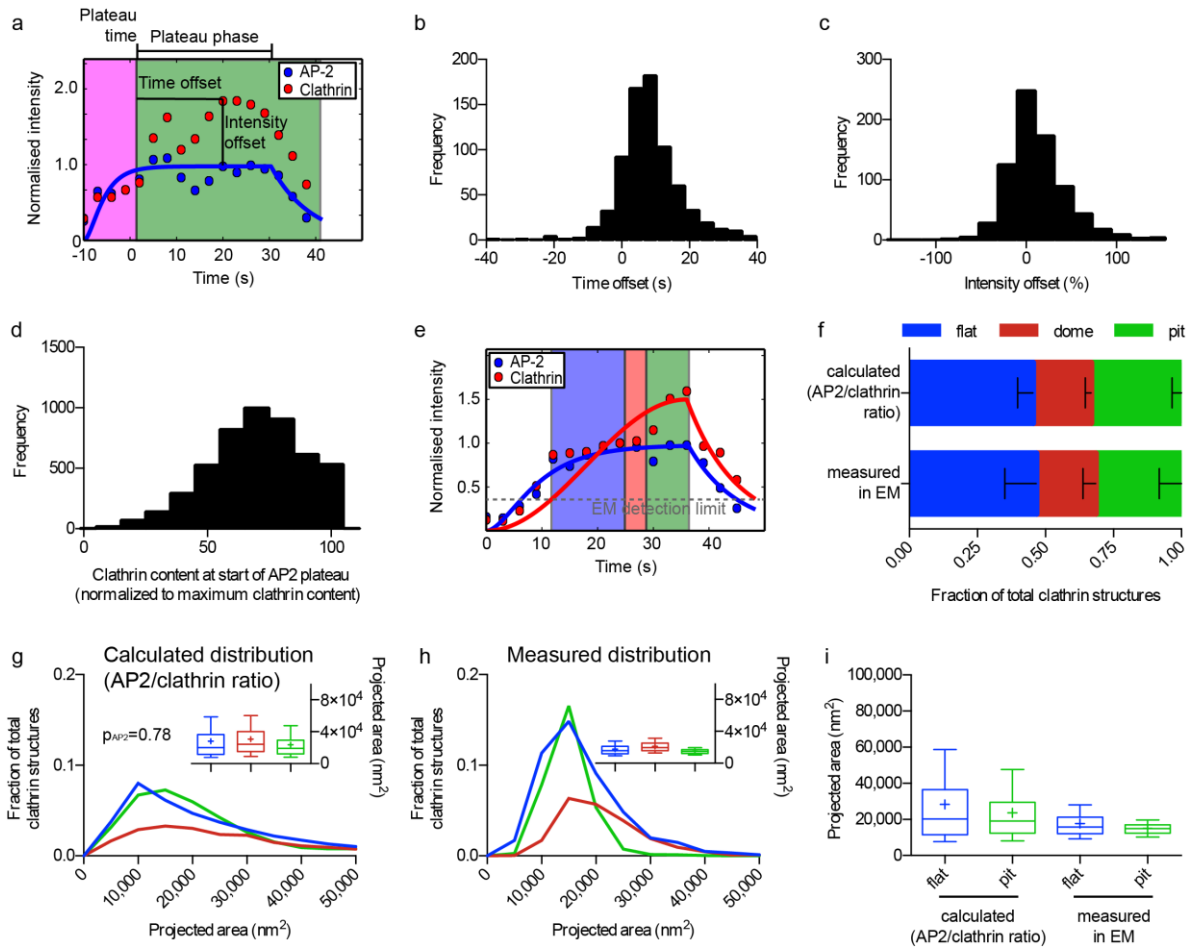


Figure 4.16: Change in the AP2/clathrin ratio is associated with flat-to-curved transition. (a) Example of an AP2 (blue) and clathrin (red) intensity profile from an individual CME event. The AP2 profile was fitted to equation 1 to find the time when AP2 signal plateaus. The fluorescence intensity of AP2 and clathrin were normalised to the fluorescence intensity of the time when the fitted AP2 profile reaches its plateau. Time offset (difference between the time AP2 plateaus and clathrin reaches its maximum intensity) and intensity offset (excess of maximal clathrin signal over AP2 maximum intensity) are indicated in the profiles. Quantification of the time offset (b) and the intensity offset (c) for 754 tracks of one single cell. (d) Quantification of the clathrin content at the time when AP2 reaches its plateau from 4927 FM tracks. The clathrin signal was normalised to the maximal clathrin signal in each track. (e) Example of an AP2 (blue) and clathrin (red) profile fitted to equation 1 and 2, respectively. These fits were used to calculate the size and curvature distributions of the CCSs in (f and g). (f) Comparison of the calculated ratio of flat, dome, and pit structures to the measured ratio in TEM. Results calculated from 4927 FM tracks from four different cells; means with SD are shown. (g) Calculated projected area of the CCSs using a growth model where the flat-to-curved transition corroborates with the change of clathrin/AP2 ratio (when AP2 signal reaches its plateau phase) for 4927 FM tracks of four different cells. P-value of Welch's t-test to compare the predicted to the measured distribution in panel f. A box/whiskers plot of the projected area is shown in the inset. (h) TEM data as shown in Fig. 4.12e (i) Direct comparison of the projected area distribution of flat and pit structures calculated according to the AP2/clathrin ratio as well as measured in EM, box/whiskers plot. Modelling has been performed by Felix Frey, Heidelberg University. This figure has been taken from Bucher *et al.* (2018).

1.4 and 2.8, respectively, which are within the expected ranges (Fig. 4.15d-e and Fig. 4.12b). Strikingly, the correction factors for AP2 CLEM were smaller than expected, especially for the pit structures (domes: 1.2; pits: 1.7) (Fig. 4.15c and e). This reveals that the AP2/clathrin ratio in a CCS differs depending on its curvature and that this ratio is reduced within the coat as curvature increases.

As the AP2/clathrin ratio depends on the curvature of CCSs (Fig. 4.15) and as AP2 partitions at different nanoscale zone in relation to the edge of the clathrin lattice during the different stages of CCS formation (Sochacki *et al.*, 2017), we hypothesised that the change in the AP2/clathrin ratio correlates with the stage at which a flat CCS bends to form a CCP. Using cells expressing both AP2-eGFP and CLC fused to the fluorescent protein tdtomato, we analysed the intensity profiles of AP2 and CLC during CME. While AP2 profiles often show a distinct plateau phase, the intensity of CLC continues to increase until the end of an endocytic event (Fig. 4.16a). By normalising the fluorescence intensities of AP2 as well as CLC to the time point when the AP2 signal plateaus, we can calculate the time offset between the time AP2 signal reaches its plateau and the time point CLC reaches its maximal intensity (Fig. 4.16a-b). Similarly, we defined the intensity offset of clathrin over AP2 (Fig. 4.16a and c). We found that the time offset was around 10 second (Fig. 4.16b) and that the intensity offset of clathrin over AP2 was around 15% (Fig. 4.16c). We hypothesised that the time point when AP2 reaches its plateau and therefore the AP2/clathrin ratio changes marks the starting point of bending. We performed another round of CCP assembly modelling, this time using both AP2 and CLC intensity profiles and defining the time point of flat-to-curved transition when AP2 reaches its plateau phase (Fig. 4.16e and Materials and methods 6.3.12-13). At this precise time, the mean clathrin content reached around 70% of its maximal value (Fig. 4.16d). Using these new parameters, the predicted ratio of flat, dome, and pit structures perfectly matched the EM data (Fig. 4.16f) and the means of the predicted projected area of both the flat and pit CCS have similar sizes (Fig. 4.16g-h, box/whiskers and 4.16i). This AP2/clathrin ratio model better resembles the parameters measured in EM compared to both the constant curvature and constant area models (Fig. 4.14h and 4.16i). These findings strongly support a model where flat-to-curved transition correlates with the concomitant change in the AP2/clathrin ratio.

4.2.4 High membrane tension inhibits the flat-to-curved transition of CCSs

By inducing curvature to the PM, the CCS needs to act against the PMT. Higher PMT has been shown to increase the lifetime of clathrin events at the PM (Boulant *et al.*, 2011; Ferguson *et al.*, 2016) and modelling of the energetic cost of membrane bending suggests that it affects the

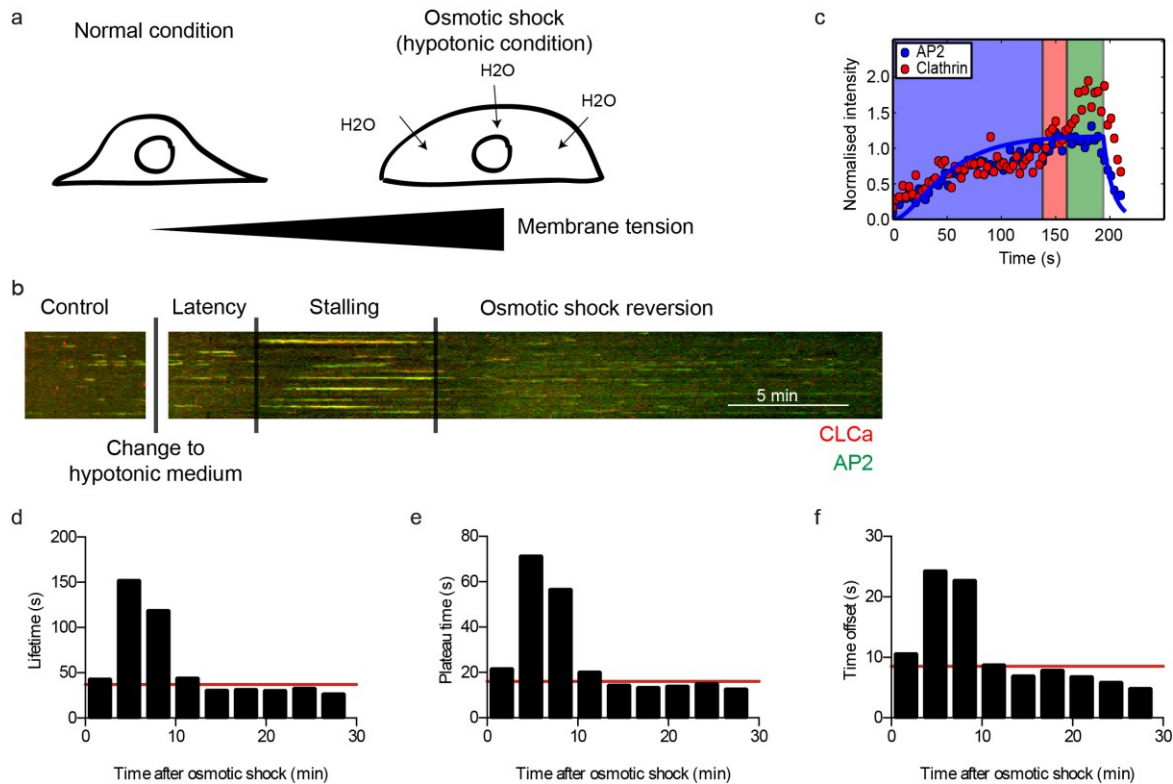


Figure 4.17: Osmotic shock induces stalling of CCSs. (a) Illustration of the effect of osmotic shock on BSC-1 cells. Hypotonic medium was applied to BSC-1 cells, inducing osmotic swelling that results in an increase in PMT. The same BSC-1 expressing fluorescently tagged clathrin light chain and AP2 proteins was followed from 5 minutes prior (internal control) until 30 minutes post hypotonic medium application using spinning disc confocal microscopy. (b) Kymograph of AP2-eGFP (green) and clathrin light chain a-tdtomato (red) expressing BSC-1 cells. The dynamics of CCP was recorded during 5 minutes prior to osmotic shock until 30 minutes post-osmotic shock. The time after applying the hypotonic medium can be divided into latency, stalling, and osmotic shock reversion time depending on the effect on CME dynamics. Scale bar: 5 min. (c) Representative AP2 (blue) and clathrin (red) intensity profile from an individual CME event during the time of stalling fitted to equation 1 to quantify the plateau time. (d) Quantification of the lifetime of CME events during osmotic shock experiments for 1607 tracks of one single cell. CME events were binned in 3 minute intervals in respect to the onset of osmotic shock. Red line indicates lifetime of CME prior to osmotic shock. (e) Quantification of the plateau time of AP2 of individual CME events during osmotic shock experiments (as defined in Fig. 4.16a) for 1607 tracks of one single cell. CME events were binned in 3 minutes intervals in respect to the onset of osmotic shock. Red line indicates plateau time of CME prior to osmotic shock. (f) Quantification of the time offset between AP2 plateau and clathrin maximum of individual CME events during osmotic shock experiments (as defined in Fig. 4.16a) for 1607 tracks of one single cell. CME events were binned in 3 minutes intervals in respect to the onset of osmotic shock. Red line indicates time offset of CME prior to osmotic shock. Calculations have been performed by Felix Frey, Heidelberg University. This figure has been taken from Bucher *et al.* (2018).

morphology of the CCS (Saleem *et al.*, 2015; Hassinger *et al.*, 2017). But the effects of increasing PMT on the ultrastructural organisation of CCSs have not been investigated in living cells. We monitored the dynamics of clathrin and AP2 during osmotic shock in which the PMT was increased by applying hypotonic medium inducing osmotic swelling of the cells (Boulant *et al.*, 2011) (Fig. 4.17a). Following a short latency period, we observed that CCS stalled at the PM. This effect was transient and cells quickly reverted to normal clathrin dynamics (Fig. 4.17b and d). Since the growth dynamics of clathrin is stalled under osmotic conditions we now determined the flat-to-curved transition time not by determining the time when AP2 reaches its plateau but by calculating when CLC intensity exceeds the AP2 intensity by 5%, which we

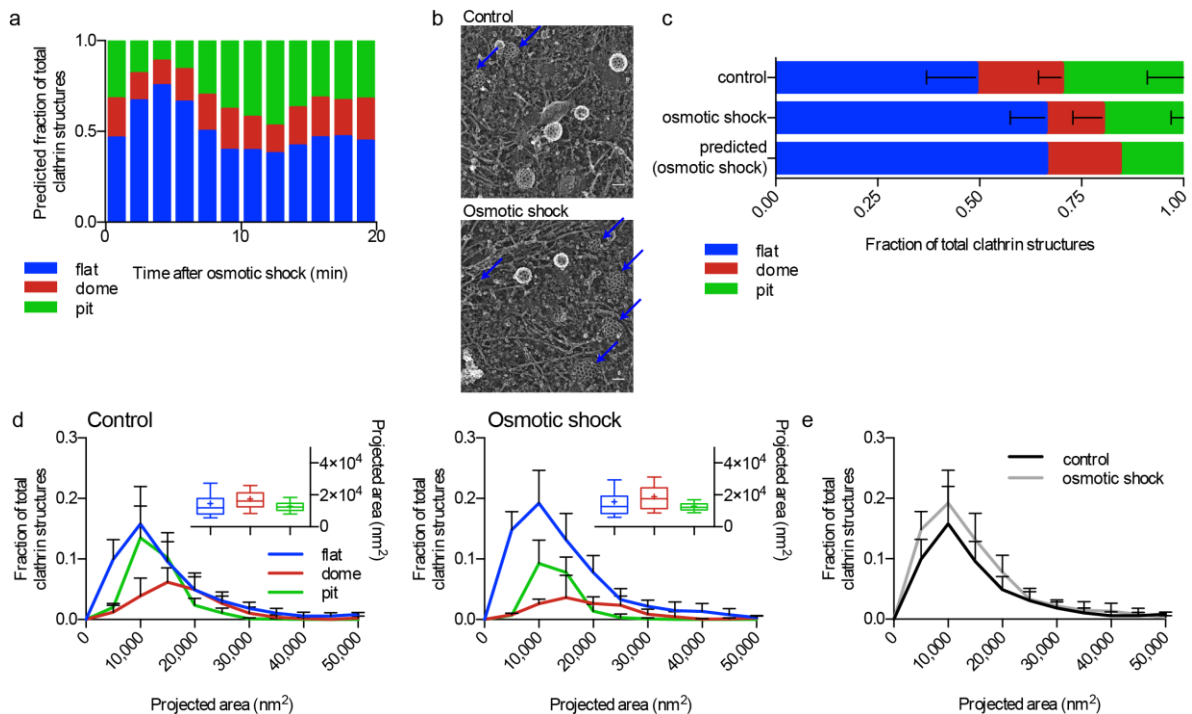


Figure 4.18: Osmotic shock blocks flat-to-curved transition of CCSs. (a) Predicted ratio of flat (blue), dome (red), and pit (green) structures calculated from the binned AP2 and clathrin profiles of CME events (Fig. 4.17c) during osmotic shock for 1357 tracks. (b) Examples of CCS under normal and osmotic shock conditions. Blue arrows point to flat structures. (c) Comparison of measured and predicted frequency of flat, dome, and pit structures under normal and osmotic shock conditions. (d) Projected area distribution of the different clathrin morphologies under normal and osmotic shock conditions. A box /whiskers plot of the projected area is shown in the inset. Mid-line represents median, cross represents the mean and the whiskers represent the 10 and 90 percentiles. (e) Comparison of projected area distributions of flat CCS under normal and osmotic shock conditions. Results are calculated from four different membranes (number of CCS per membrane: normal conditions 267, 308, 229, and 323; osmotic shock: 395, 99, 351, and 201); means with SD are shown. The EM data of this figure has been produced jointly with Kem A. Sochacki, NIH Bethesda. Modelling has been performed by Felix Frey, Heidelberg University. This figure has been taken from Bucher *et al.* (2018).

controlled to yield similar results under unperturbed isoosmotic conditions (Materials and methods 6.3.14). Using fitted AP2 and unfitted CLC intensity profiles under osmotic shock, we showed that the CCSs display a longer AP2 plateau phase (Fig. 4.17c and e) and that the time offset was increased compared to normal conditions (Fig. 4.17f and 4.16b). According to our findings that the change in AP2/clathrin ratio coordinates the flat-to-curved transition of CCS, the delayed offset in the AP2/clathrin ratio under higher PMT suggests that the flat-to-curved transition is suppressed and that the coats are flat under this condition.

By looking at the AP2/clathrin ratio during osmotic shock, we predicted that during the stalling phase, 70% of the CCS would be flat (Fig. 4.18a). To test this notion, we performed EM of metal replica of CCSs under osmotic shock (Fig. 4.18b). We found an accumulation of flat CCSs under osmotic shock compared to normal conditions and the frequency was comparable to our predictions from the AP2 and CLC profiles (Fig. 4.18c). These flat structures, as well as the dome and pit structures, have the same size distribution as under normal conditions (Fig. 4.18d box/whiskers and 4.18e). The EM data confirms that under higher PMT the flat-to-curved transition of CCS is inhibited. Using mathematical modelling and individual clathrin and AP2 intensity profiles acquired under osmotic shock, we could predict the morphology of the stalled CCSs. This finding is in agreement with our proposed growth model, which describes that a change in AP2/clathrin ratio represents the precise moment at which the flat-to-curved transition occurs.

4.3 Role of clathrin-coated plaques in cell migration

The role of transient small, invaginated CCPs in cargo uptake during CME is well established (McMahon and Boucrot, 2011). The persistent larger flat clathrin-coated plaques are less characterized and their function is still unclear. To investigate the role of clathrin-coated plaques, we chose U373 as a model cell line since they form characteristic clathrin-coated plaques as shown in paragraph 4.1. We used live-cell FM, inhibition of FAs as well as chemical and physical extracellular cues to unravel the signals that induce clathrin-coated plaque formation and their role during cell migration.

4.3.1 Switch from FAs to clathrin-coated plaques during cell migration

Clathrin-coated plaques form exclusively at attached PM parts, which are in contact with a substrate (Fig.4.3 and 4.4). One difference between attached and non-attached PMs is the formation of FAs. To test if clathrin-coated plaques are involved in FA formation or disassembly, we looked for colocalization with FA proteins. FAs consist of three main layers: 1) Integrins spanning the PM to serve as ECM receptors; 2) adaptor proteins which link integrins to the 3) actin stress fibres (Fig.2.6a). Actin stress fibres did not colocalize with clathrin-coated plaques (Fig.4.19a-c), however we could detect actin patches at clathrin-coated plaques (Fig. 4.19c), but actin puncta are generally no marker for FAs. Different markers of FAs (such as the adaptor proteins vinculin, zyxin, paxillin, and FAK) were also not detected at clathrin-coated plaques (Fig.4.19a-c and 4.20). Interestingly, only certain integrins ($\beta 1$ and $\alpha \beta 5$) could be detected in clathrin-coated plaques but in the absence of other FA markers (Fig.4.19d-f and 4.25a-c). Together the lack of clear colocalization between FAs and clathrin-coated plaques and the spatial separation of their locations (clathrin-coated plaques are found rather central within a cell whereas FAs at the periphery of the cells) do not support a role of clathrin-coated plaques in FA formation or disassembly. However, the fact that some integrins were found at clathrin-coated plaques might suggest a function at late stages of FA disassembly namely the recycling of integrins.

FAs are highly dynamic complexes that mature over time and their turnover is crucial for cell migration (Parsons, Horwitz and Schwartz, 2010; Geiger and Yamada, 2011; Vicente-Manzanares and Horwitz, 2011). To further investigate the role of clathrin-coated plaques during FA disassembly, we used long-time live-cell FM to follow FA together with clathrin dynamics during cell migration. In U373 expressing AP2-eGFP and mcherry-fusion proteins of FA adaptors (vinculin, zyxin, paxillin, and FAK), we could observe that the positions where FA

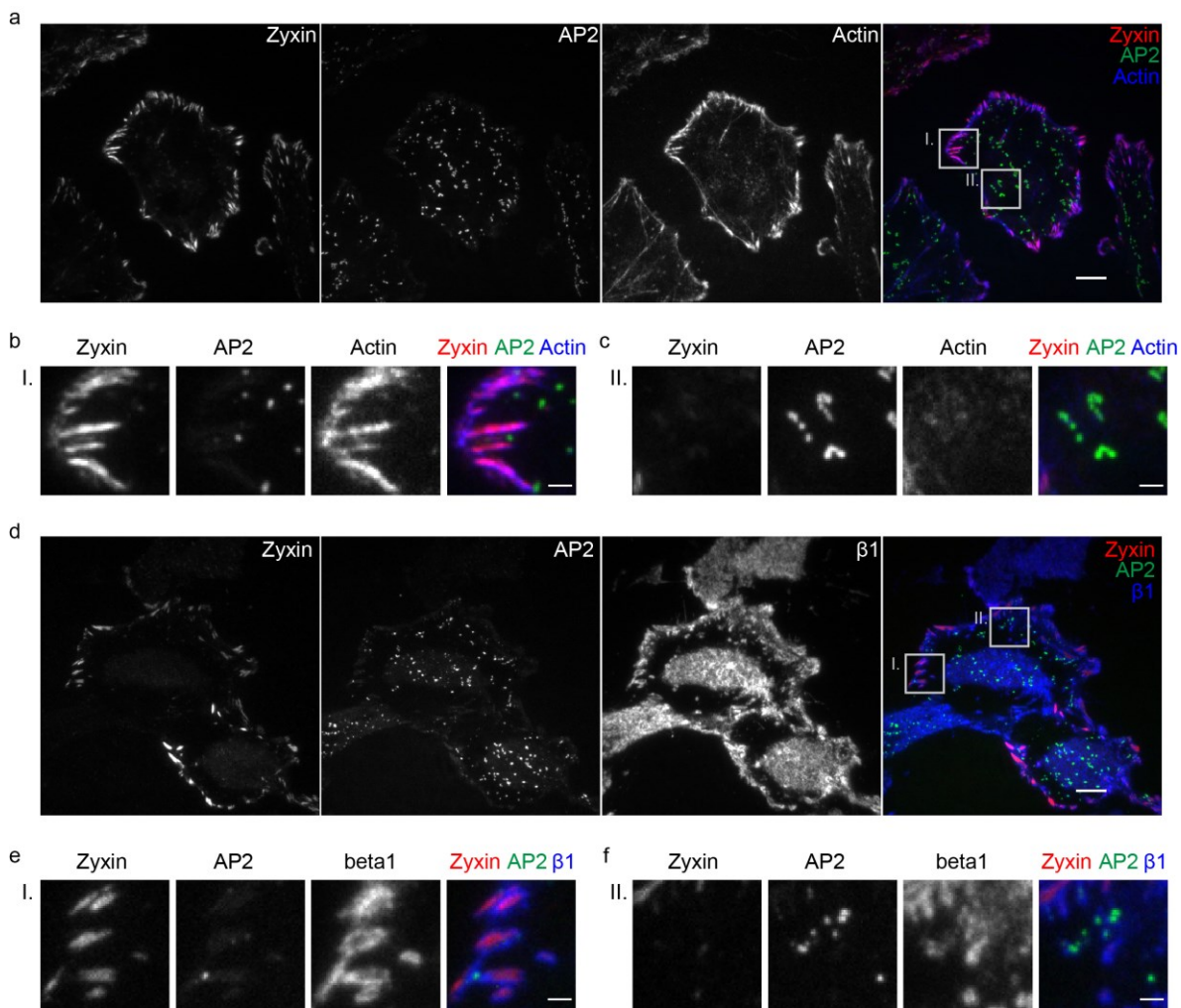


Figure 4.19: Clathrin-coated plaques do not colocalize with FAs. Representative images from total internal reflection fluorescence (TIRF) microscopy of U373 stably expressing AP2-eGFP (green) and transiently expressing mcherry-zyxin (red) stained for (a-c) actin with Alexa Fluor 647-labelled phalloidin (blue) or (d-e) integrin $\beta 1$ (blue). (b and e) Zoom on FAs marked by mcherry-zyxin. (c and f) Zoom in on clathrin-coated plaques marked by AP2-eGFP. Scale bar: 10 μm (a and d) or 2 μm (b, c, e, and f).

disassembled often marked the location of newly formed persistent clathrin-coated plaques (Fig. 4.20). A merge of the FA signal from earlier time points and the AP2 signal at later time points highlights those FAs that got replaced by CCS (Fig. 4.20). Quantification of the fluorescent signals of both the FA and the CCS markers revealed that the signal for the FA adaptors always completely disappeared before the clathrin-coated plaques started to form at that location (data not shown). This was true for all FA adaptors tested (zyxin, vinculin, FAK, and paxillin). Since FAs are larger than clathrin-coated plaques (around 5 μm (Kanchanawong *et al.*, 2010) compared to around 1 μm (Fig. 4.10) in length, respectively), the position formerly covered by a FA was often occupied by several clathrin-coated plaques in close vicinity (Fig. 4.20b, d, f, h).

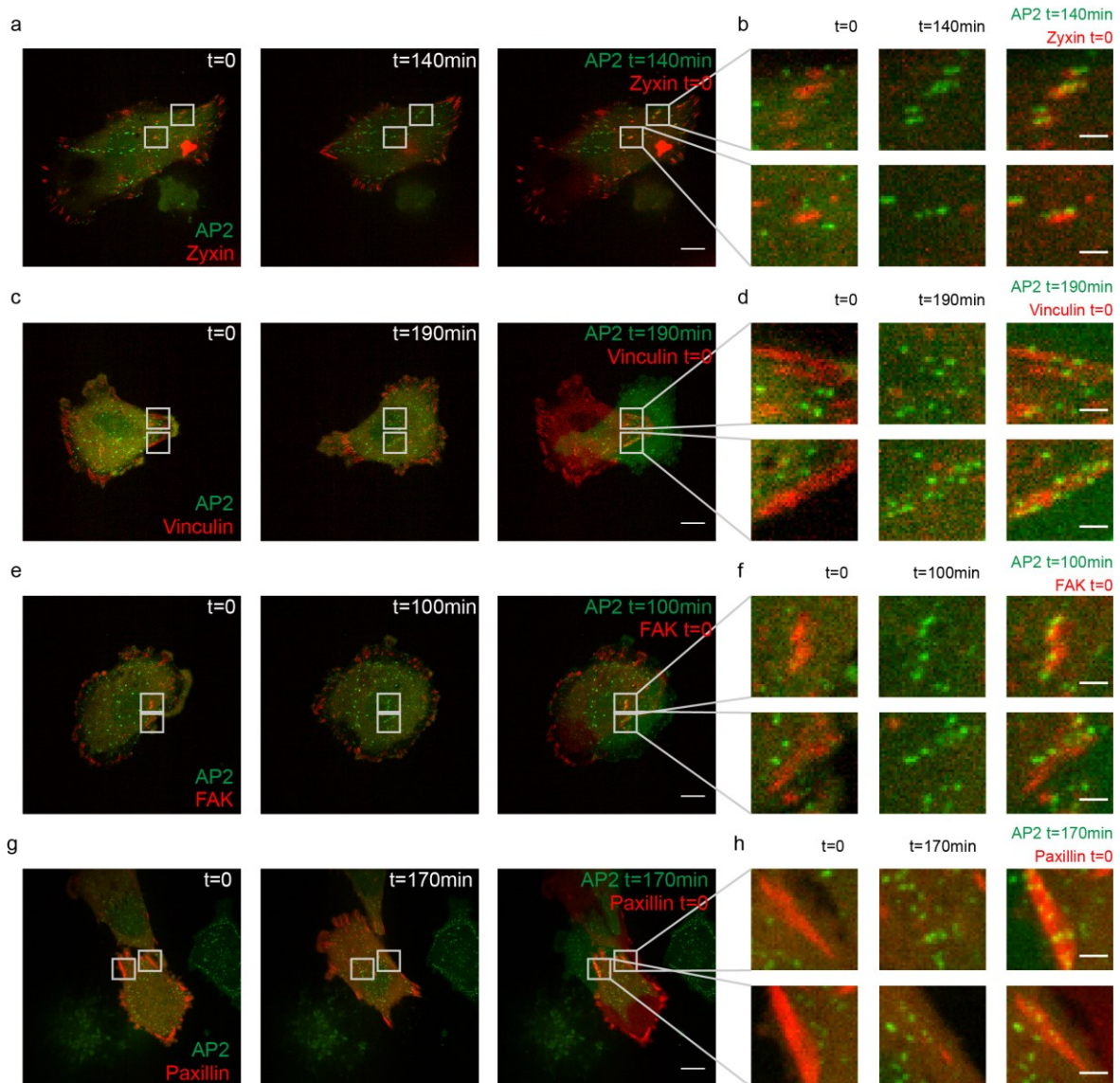


Figure 4.20: Switch from FAs to clathrin-coated plaques during cell migration in U373. Long-time live-cell confocal spinning disc microscopy of U373 stably expressing AP2-eGFP (green) and transiently expressing FA proteins fused to mcherry: mcherry-zyxin (a and b), mcherry-vinculin (c and d), mcherry-FAK (e and f), or mcherry-paxillin (g and h) (red). (a, c, e, and g) Overview of a representative migrating cell at time 0 (left) and a later time point (140, 190, 100, or 170 minutes, respectively) (middle). (Right) Merged images of the FA protein signal at time 0 (red) and the AP2-eGFP signal at the later time point (green). Scale bar: 10 μm . (b, d, f, and h) Zoom in on FAs that switch to clathrin-coated plaques. (Left) Time point 0, (middle) later time point, and (right) merged image of the FA protein signal at time 0 and the AP2-eGFP signal at the later time point. Scale bar: 2 μm .

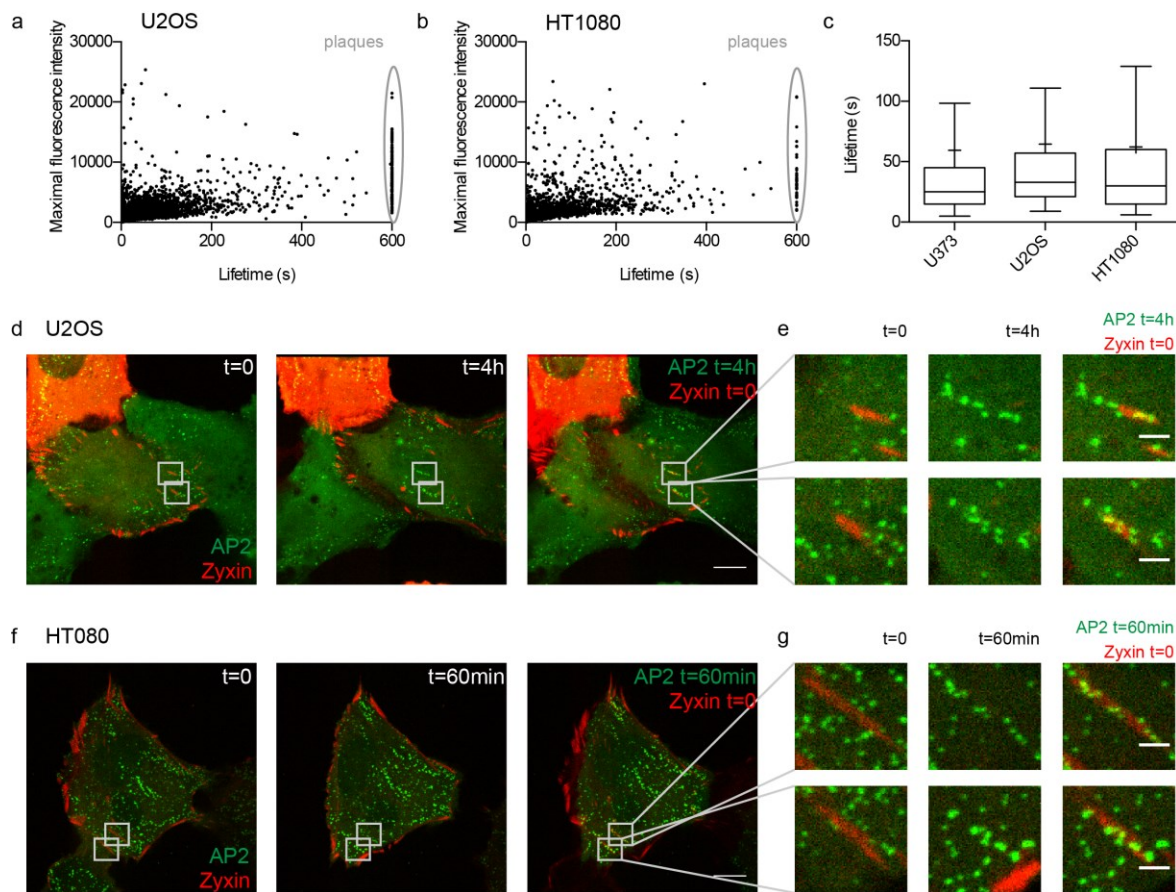


Figure 4.21: Switch from FAs to clathrin-coated plaques during cell migration in U2OS and HT1080. Lifetime versus maximal fluorescence intensity of AP2-eGFP of CME tracks for U2OS (a) and HT1080 (b). Shown are plots of a representative cell of each cell line. Each dot represents one event in a 10 minute long movie. Number of tracks: 5,492 (U2OS) and 3,287 (HT1080). (c) Box and whiskers plot showing the lifetime distributions of CME in U373, U2OS, and HT1080 computed from three to four cells for each cell line. Whiskers represent 10-90 percentile, box represents second and third quartile, the line marks the median, and the cross marks the mean. Number of tracks: 4,472 (U373), 19,366 (U2OS), and 7,144 (HT1080). Long-time live-cell confocal spinning disc microscopy of U2OS (d and e) and HT1080 (f and g) stably expressing AP2-eGFP (green) and transiently expressing mcherry-zyxin (e and g) (red). (d and f) Overview of a representative migrating cell at time 0 (left) and a later time point (4 hours and 60 minutes for U2OS and HT1080, respectively) (middle). (Right) Merged image of the FA protein signal at time 0 (red) and the AP2-eGFP signal at the later time point (green). Scale bar: 10 μ m. (e and f) Zoom in on FAs that switch to clathrin-coated plaques. (Left) Time point 0, (middle) later time point, and (right) merged image of the FA protein signal at time 0 and the AP2-eGFP signal at the later time point. Scale bar: 2 μ m.

Analysis of their dynamics revealed that the clathrin-coated plaques formed during such a process were very persistent and stayed at that position up to several hours (data not shown). The main reason for the disassembly of such plaques was that cells migrated away from their original positions.

To control that this observation is not cell type-specific, we performed long-time live-cell microscopy of AP2-eGFP and mcherry-zyxin of other cell lines known to form clathrin-coated plaques (Fig.4.21). We found that the human osteosarcoma cell line U2OS as well as the human fibrosarcoma cell line HT1080 showed CCS dynamics similar to U373 cells with characteristic persistent clathrin-coated plaques (Fig.4.21 a-c). Using a similar approach as described above for the U373 cells, we could observe clathrin-coated plaque formation at positions where FAs got disassembled in both of these cell lines (Fig.4.21 d-g).

Together, our long-time live-cell FM approach revealed a so far undescribed process in which FAs are disassembled at the PM and are replaced by CCSs that we have identified from their dynamic and fluorescence intensity characteristics as clathrin-coated plaques. We call this novel process switch from FAs to clathrin-coated plaques. We propose that this is a general process since we observed this switch in all tested cell types, which form clathrin-coated plaques. Although a lot of the clathrin-coated plaques found in a cell could be associated with this switch there were also clathrin-coated plaques, which did not have a clear correlation to FA disassembly. These plaques might be formed by another mechanism and might serve different functions.

4.3.2 Drug-induced switch from FAs to clathrin-coated plaques

FA maturation during cell migration is a relatively slow process (several minutes to hours) and the location and timing of FA disassembly are unpredictable during random migration (Petrie, Doyle and Yamada, 2009; Parsons, Horwitz and Schwartz, 2010; Vicente-Manzanares and Horwitz, 2011). To be able to induce and quantify the switch from FAs to clathrin-coated plaques, we tested if this process also occurs during drug-induced FA disassembly. For this assay, we tested two drugs: the Rho-associated protein kinase (ROCK) inhibitor Y-27632 (Riento and Ridley, 2003) and Blebbistatin, a myosin II inhibitor (Vicente-Manzanares *et al.*, 2009). Both of these drugs lead to the disassembly of actin stress fibres and thereby recycling of FAs (Riento and Ridley, 2003; Vicente-Manzanares *et al.*, 2009) (Fig.4.22a-b). We studied the kinetics of stress fibre and FA disassembly under ROCK inhibitor (10 μ M) and Blebbistatin (20 μ M) treatment and found similar kinetics for both inhibitors (Fig.4.22c-d). After around 10 minutes treatment with either of the two inhibitors, more than half of the cells did not show stress fibres and FAs. This number could even be reduced to less than 25% after 20 minutes of drug treatment (Fig.4.22c-d).

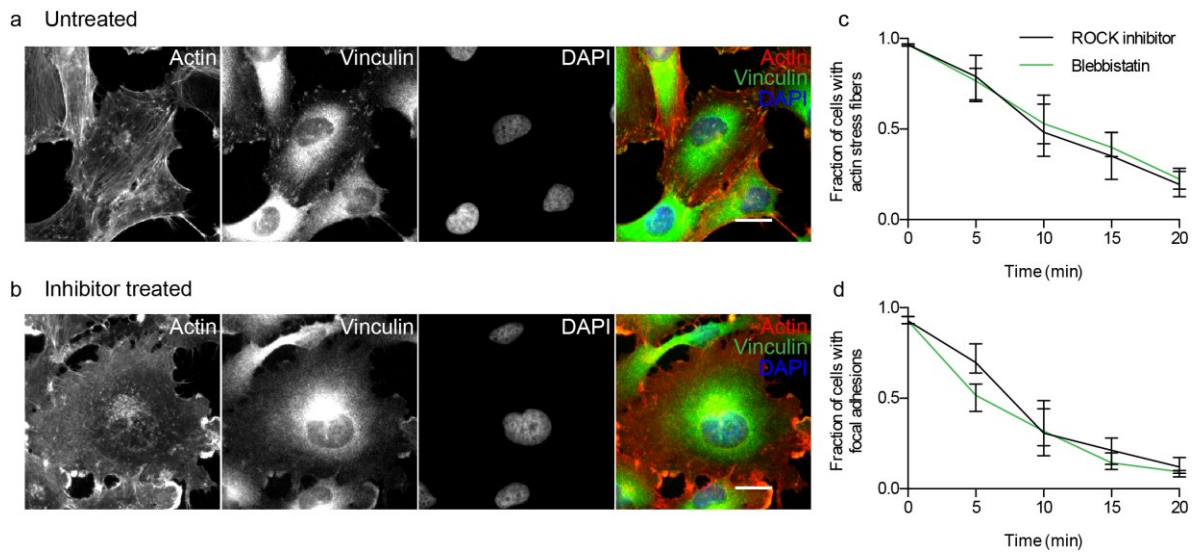


Figure 4.22: Kinetics of drug-induced FA disassembly. Representative images of widefield microscopy of untreated (a) and inhibitor treated (b) U373 cells stained for actin with Alexa Fluor 647-labelled phalloidin (red), vinculin (green) and DNA with DAPI (blue). Scale bar: 10 μ m. Kinetics of stress fibre (c) and FA (d) disassembly by treatment with ROCK inhibitor (10 μ M, black) or Blebbistatin (20 μ M, green). The graph shows the mean with SD of each time point. The results are computed from three independent experiments with over a hundred cells per experiment. The data of this figure has been produced by Veronika Saharuka, Heidelberg.

To investigate if the drug-induced disassembly of FAs leads to a switch to clathrin-coated plaques, we performed live-cell microscopy of U373 expressing AP2-eGFP and mcherry-zyxin under drug treatment (Fig.4.23). To be able to identify the position where FAs have been disassembled, cells were imaged first before drug treatment and then followed under drug treatment for 30 minutes. We observed the switch from FAs to clathrin-coated plaques by treatment with ROCK inhibitor as well as Blebbistatin (Fig.4.23a and e). The merge of the FA signal before drug treatment and of the AP2 signal after drug treatment highlights those FAs that got switched to clathrin-coated plaques (Fig.4.23a, b, e, and f). The CCSs that formed at the position of previously found FAs were very persistent as they stayed for the rest of the drug treatment (Fig.4.23 c and g). Even when the drug was washed out, clathrin-coated plaques that formed during the drug-induced switch were persistent while new FAs and actin stress fibres were formed (data not shown). Analysis of the fluorescence intensity during the switch process revealed that zyxin was almost fully removed from the specific membrane location before being replaced by AP2 (Fig.4.23 d and h).

To quantify the switch from FAs to clathrin-coated plaques, we check for colocalization of FAs before and clathrin-coated plaques after drug treatment (Fig.4.24a). We developed an automated workflow to quantify the switch by object-based colocalization. Since we know that

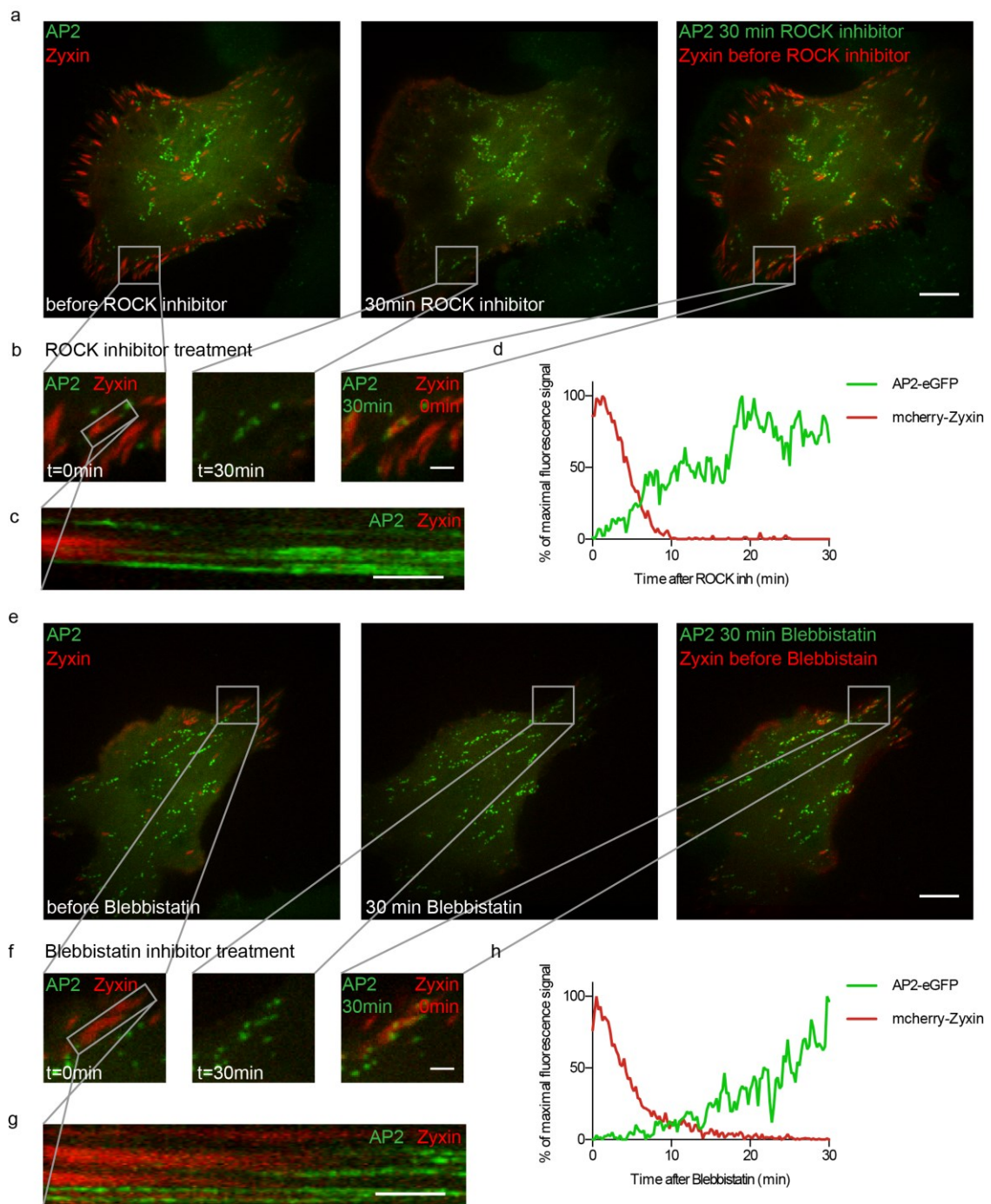


Figure 4.23: Drug-induced switch from FAs to clathrin-coated plaques. Live-cell confocal spinning disc microscopy of representative U373 cells stably expressing AP2-eGFP (green) and transiently expressing mcherry-zyxin (red) treated with ROCK inhibitor ($10\mu\text{M}$) (a-d) or Blebbistatin ($20\mu\text{M}$) (e-h). (a and e) Overview of a representative cell before (left) and 30 minutes after drug treatment (middle). (Right) Merged image of the mcherry-zyxin signal before (red) and the AP2-eGFP signal after drug treatment (green). Scale bar: $10\mu\text{m}$. (b and f) Zoom in on a FA that switches to clathrin-coated plaques. (Left) Before, (middle) 30 minutes after drug treatment, and (right) merged image of the mcherry-zyxin signal before and the AP2-eGFP signal after drug treatment.

Scale bar: 2 μm . (c and g) Kymograph of the switch from FA to clathrin-coated plaques shown in b and f during the 30-minute drug treatment. Scale bar: 5 min. (d and h) Normalized fluorescence intensity profiles of AP2-eGFP (green) and mcherry-zyxin (red) of the switch from FA to clathrin-coated plaques shown in b and f.

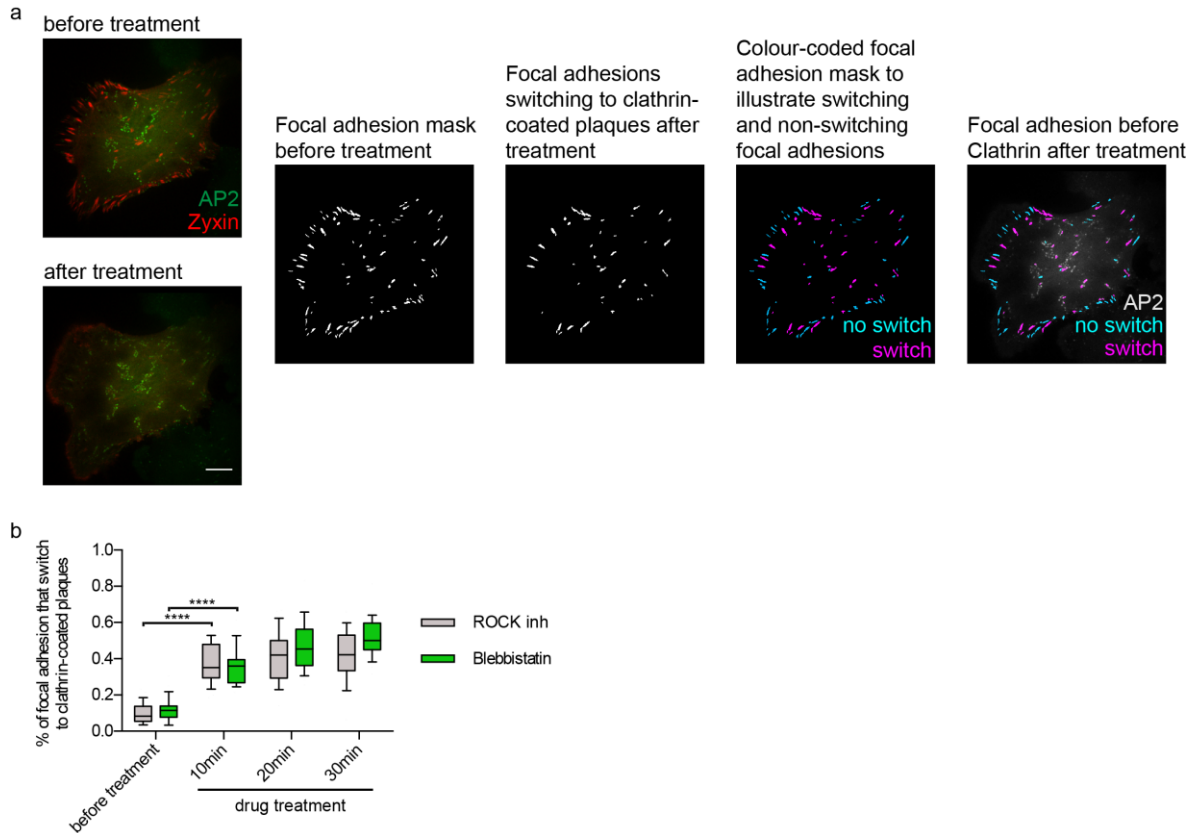


Figure 4.24: Quantification of drug-induced switch from FAs to clathrin-coated plaques. (a) Illustration of the analysis workflow used to automatically quantify the switch from FAs to clathrin-coated plaques using KNIME. Live-cell spinning disc confocal microscopy of U373 stably expressing AP2-eGFP (green) and transiently expressing mcherry-zyxin (red) was performed before and after drug-treatment. For the quantification, a binary mask of the mcherry-zyxin signal before the treatment was used to count the number of FAs and to perform colocalization analysis between FAs and CCSs after the treatment defined by a binary mask of the AP2-eGFP signal. FAs were categorized into switching (magenta) and non-switching (blue) and the percentage of FAs that switch to clathrin-coated plaques was calculated. For this analysis, only FAs were considered which position was still covered by the cell after drug treatment. The AP2-eGFP signal of the image before the drug treatment was used as a detection control. Scale bar: 10 μm . (b) Quantification of the switch from FAs to clathrin-coated plaques during ROCK inhibitor (10 μM , grey) and Blebbistatin (20 μM , green) treatment. Whiskers represent 10-90 percentile, box represents second and third quartile, and the line marks the median. Results are computed from three repetitions. Statistical analysis: t test, $n=28$ (ROCK inhibitor) or $n=30$ (Blebbistatin), $P<0.01$.

FAs and CCSs do not colocalize at any time, we used the AP2 signal from the same time point as the FA signal before the drug treatment as a negative control. The analysis of the negative control showed that the automated workflow detected that around 10% of FAs colocalized with CCSs in the same time point before drug treatment, we considered that value as background, which was due to false detection by CCSs in close proximity to FAs (Fig.4.24 b, before treatment). After drug treatment the percentage of FAs before treatment colocalizing with CCSs after treatment increased significantly (Fig.4.24b). Already after 10 minutes, over 35% of the FAs switch to clathrin-coated plaques and this number increased further for longer time of treatment (over 40% after 20 minutes of drug treatment) (Fig. 4.24b).

In summary, we could show that the switch from FAs to clathrin-coated plaques happened not only during the disassembly of FAs during cell migration but can also be induced on-demand by pharmacological compound-mediated FA disassembly (Fig.4.23 and 4.24). This inhibitor approach provides us with a powerful tool to study the role of this switch from FA to clathrin-coated plaques. In the rest of this work, we decided to mostly use ROCK inhibitor treatment as a highly reproducible way of inducing the switch process.

4.3.3 Integrins recruit and stabilize clathrin-coated plaques

CCSs form after recruitment of clathrin adaptors to transmembrane proteins at the PM (Reider and Wendland, 2011; Traub and Bonifacino, 2013). Given our observation that integrins display partial colocalization with clathrin-coated plaques (Fig.4.19), these ECM receptors might remain at the position where FAs have been disassembled and subsequently recruit the clathrin machinery to form clathrin-coated plaques. To test the role of integrins in clathrin-coated plaque formation and stabilization, we first checked for colocalization of different integrins at clathrin-coated plaques. Like observed in Fig.4.19, we could find $\beta 1$ and $\alpha \beta 5$ integrins but no $\beta 3$ integrins at clathrin-coated plaques under normal conditions (Fig.4.25a-c). To investigate the role of integrins in stabilizing clathrin-coated plaques, we treated cells with the integrin antagonist, Cilengitide. The cyclic RGD (Arg-Gly-Asp) peptide Cilengitide specifically inhibits $\alpha \beta 3$, $\alpha \beta 5$, and $\alpha 5 \beta 1$ integrins by binding to the extracellular domain of integrins and competing with RGD motifs found in ECM proteins (Dechantsreiter *et al.*, 1999; Mas-Moruno, Rechenmacher and Kessler, 2010). We performed live-cell microscopy of U373 expressing AP2-eGFP under Cilengitide treatment. We could show that clathrin-coated plaques that were persistent before, started to disassemble during Cilengitide treatment after around 10 minutes (Fig. 4.25d and e). During the disassembly, clathrin-coated plaques formed smaller and transient CCSs, which resembled CCPs (Fig.4.25e).

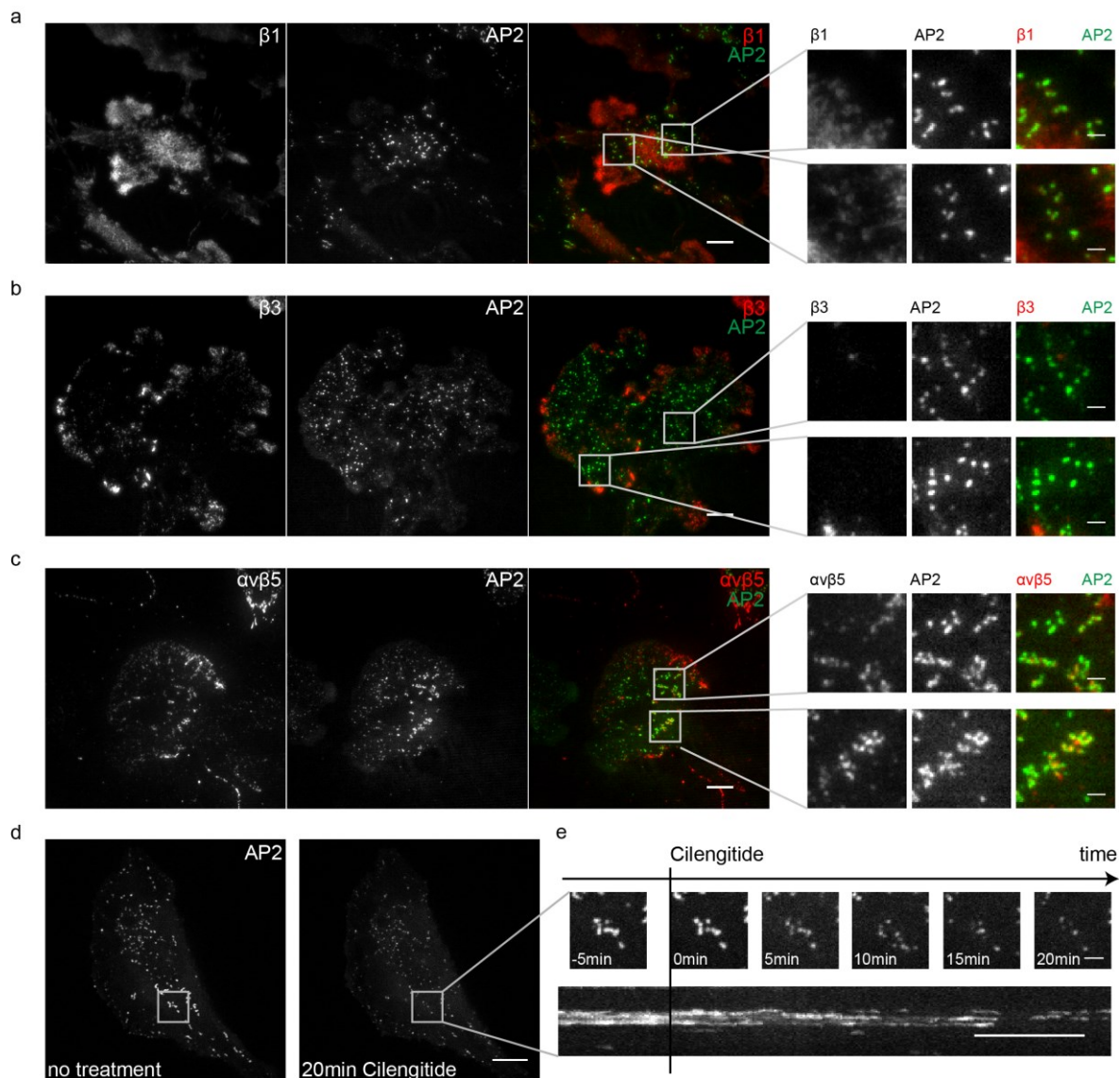


Figure 4.25: Clathrin-coated plaques are stabilized by integrins. (a-c) TIRF microscopy of U373 stably expressing AP2-eGFP (green) immunostained for integrin (a) $\beta 1$, (b) $\beta 3$, and (c) $\alpha v \beta 5$ (red). Shown is a representative cell (left) with zoom-in on clathrin-coated plaques (right). Scale bar: 10 μm (left), 2 μm (right). (d) Live-cell spinning disc confocal microscopy of U373 stably expressing AP2-eGFP treated with Cilengitide (10 μM) for 20 minutes. Shown is a representative cell before (left) and after 20 minutes treatment with Cilengitide (right). Scale bar: 10 μm . (e) Serial zoom-in (top) and kymograph (bottom) of clathrin-coated plaques marked in d. Serial zoom-in with a time frame of 5 minutes and kymograph following clathrin-coated plaque disassembly over 20 minutes of Cilengitide treatment. Clathrin-coated plaques were imaged 5 minutes before treatment to show their persistence. Scale bar: 2 μm (zoom-in), 5 min (kymograph).

To investigate if integrins are also involved in recruiting clathrin-coated plaques to the former position of disassembled FAs, we check for colocalization of integrins with clathrin-coated plaques after ROCK inhibitor treatment. We focused our analysis on clathrin-coated plaques at the periphery of the cells where the switch from FA to clathrin-coated plaques often takes place and where normally less conventional clathrin-coated plaques are found. We could find $\beta 1$ and $\alpha \nu \beta 5$ integrins but no $\beta 3$ integrins colocalizing with clathrin-coated plaques at the cell periphery formed after ROCK inhibitor treatment (Fig. 4.26 a-c). This suggests that these integrins were left from the FAs, which disassembled during the drug treatment, and in turn, these integrins were responsible for the recruitment of clathrin-coated plaques.

Integrin heterodimers are considered to mediate adhesion to different ECM substrates. Although integrin-ligand binding is rather promiscuous, there are some binding motifs in ECM proteins, which are recognized only by certain integrin receptors (Humphries, Byron and Humphries, 2006; Barczyk, Carracedo and Gullberg, 2010). Since we found only specific integrins at clathrin-coated plaques, we tested if certain substrates would be more efficient for the switch from FAs to clathrin-coated plaques. $\beta 1$ found in clathrin-coated plaques is forming heterodimers with a broad range of α subunits resulting in integrins binding to a variety of ECM proteins (Brakebusch and Fässler, 2005). Of note, almost all collagen binding integrins contain the $\beta 1$ subunit (Zeltz and Gullberg, 2016). The other integrin we identified at clathrin-coated plaques, $\alpha \nu \beta 5$, is an RGD-binding integrin with vitronectin as main ligand (Cheresh *et al.*, 1989; Freed *et al.*, 1989; Smith *et al.*, 1990). While $\beta 3$, which we could not detect at clathrin-coated plaques, is mainly found in the $\alpha \nu \beta 3$ heterodimer that binds to RGD motif containing ECM proteins like fibronectin and vitronectin (Boettiger *et al.*, 2001). We compared the efficiency of the drug-induced switch from FAs to clathrin-coated plaques on glass, collagen, and fibronectin. Since we use fetal bovine serum (FBS)-containing medium for our assay, the main adhesive protein on glass substrate is vitronectin (Hayman *et al.*, 1985). Glass and collagen as substrate were similarly efficient in promoting the switch process as determined using our quantification approach described in Fig. 4.24. Precisely, we found that the same percentage of FAs got replaced by clathrin-coated plaques after 20 minutes of ROCK inhibitor treatment on both substrates (Fig. 4.26d). On the contrary, on fibronectin coating, cells showed a reduced number of FAs switching to clathrin-coated plaques in the drug-induced assay (Fig. 4.26d).

Together, these experiments revealed the association of integrins with clathrin-coated plaques and suggest integrins being the main transmembrane protein recruiting clathrin-coated plaques during the switch from FAs to clathrin-coated plaques. Our results suggest that $\beta 1$ and $\alpha \nu \beta 5$ integrins but not $\beta 3$ integrins are directly involved in this process. The fact that not all integrins

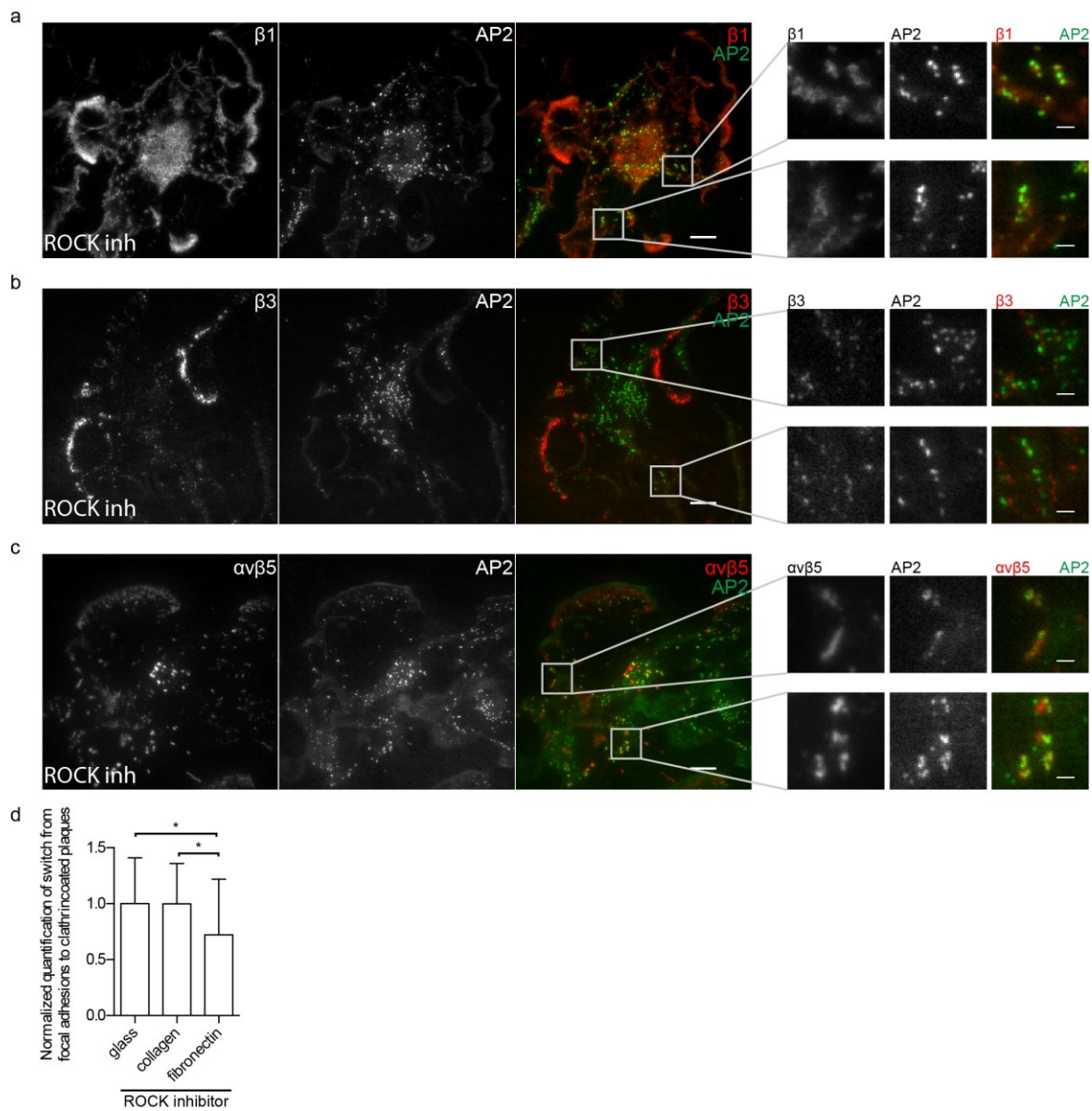


Figure 4.26: Integrins colocalize with clathrin-coated plaques during drug-induced switch from FAs to clathrin-coated plaques. (a-c) TIRF microscopy of U373 stably expressing AP2-eGFP (green) immunostained for integrin (a) β 1, (b) β 3, and (c) α v β 5 (red) treated with ROCK inhibitor (10 μ M) for 20 minutes. Shown is a representative cell (left) with zoom-in on clathrin-coated plaques (right). Scale bar: 10 μ m (left), 2 μ m (right). (d) Normalized quantification of the switch from FAs to clathrin-coated plaques after 20 minutes of ROCK inhibitor (10 μ M) treatment on different substrate: glass (grey), collagen (green), and fibronectin (red). Data was normalized to the mean on glass. Shown is the mean with SD computed from three repetitions. Statistical analysis: t test, n=25 (glass), n=24 (collagen), and n=28 (fibronectin), P<0.05.

are equally involved in the switch, suggests substrate specificity for this process. We found that the ROCK inhibitor-induced switch from FAs to clathrin-coated plaques was more efficient on substrates like glass and collagen than on fibronectin, which verifies the importance of the substrate for this process. Clathrin-plaques are stabilized at the PM by integrins. These integrins at clathrin-coated plaques might still act as ECM receptors and as such might provide cells with additional adhesive units. Therefore, clathrin-coated plaques might serve as FA-like adhesion structures.

4.3.4 Remodelling of ECM as a signal for clathrin-coated plaque formation

Although the switch from FAs to clathrin-coated plaques is a highly reproducible process, which is found in almost all cells, not all FAs promote the recruitment of clathrin-coated plaques to the place where they disassemble. In the drug-induced assay around 50% of the FAs do not switch to clathrin-coated plaques (Fig. 4.24b). From long-time live-cell microscopy, we saw that the position of a clathrin-coated plaque could be recognized again by the same cell. When a cell left a precise position and returned later to this location, clathrin-coated plaques could be often found at the same position where they were previously observed (Fig. 4.27a). Even another cell, which replaced a cell at a certain position, often formed clathrin-coated plaques at the same spots as the cell that was there before (Fig. 4.27a). Therefore we tested if there is an extracellular signal, which induces clathrin-coated plaque formation at specific positions.

For this we used gridded coverslips to perform a correlative sequential seeding approach to find back precisely specific positions (Fig. 4.27b). First, U373 expressing AP2-eGFP were imaged on gridded coverslips to identify the position of clathrin-coated plaques. Then these cells were removed from the gridded coverslip by ethylenediaminetetraacetic acid (EDTA) treatment and, in a second step, new U373 expressing AP2-eGFP were seeded on the same grid to analyse the position of clathrin-coated plaques in those cells. We found that clathrin-coated plaques formed in the second round of seeded cells at the same position where they were identified in the first round of seeded cells (Fig. 4.27c-d). When the gridded coverslip was cleaned with trypsin or KOH after removing the cells, there were less clathrin-coated plaques in the second round of seeded cells forming at the same place where they have been in the first round of seeded cells (Fig. 4.27c). In summary, our results strongly suggest that there is an extracellular signal that induces clathrin-coated plaque formation at specific positions. This signal appears to be left in the extracellular environment by clathrin-coated plaques or FAs that converted to clathrin-coated plaques. This signal is likely proteic as it can be removed from surfaces by trypsin digestion.

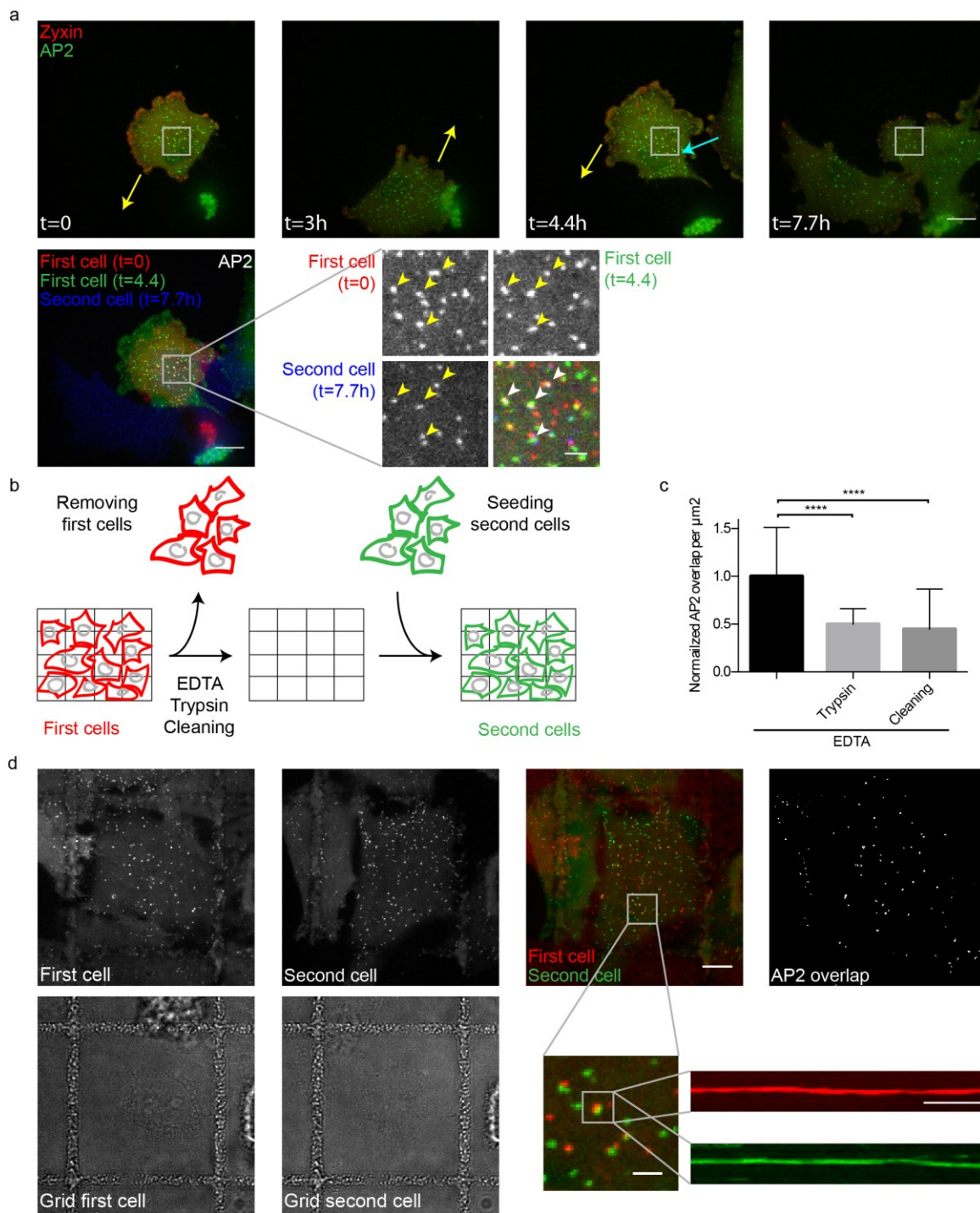


Figure 4.27: Extracellular signal induces clathrin-coated plaque formation. (a) Long-time live-cell confocal spinning disc microscopy of U373 stably expressing AP2-eGFP (green) and transiently expressing mcherry-zyxin (red). (Top) Snapshots of a time series of two representative cells moving over the same area. Arrows point in the direction of cell migration (first cell: yellow, second cell: blue). (Bottom left) Merged images of the AP2-eGFP signal at three time points (first cell at $t=0$: red, first cell at $t=4.4$ h: green, second cell at $t=7.7$ h: blue). Zoom-in on CCVs found at the same positions in all three time points marked by arrow heads. (b) The schematic illustrates the

sequence of the experiment using gridded coverslips. A first round of cells (red) was imaged to identify the position of CCSs and cells were then removed by EDTA solution. The gridded coverslip was either left untreated or treated with trypsin to digest proteins or cleaned with a sequence of KOH, acetone, and ethanol to remove organic material. Afterwards a second round of cells (green) was seeded on the same gridded coverslip and imaged to identify the position of CCSs and to compare it with the position of CCSs identified within the first round of seeded cells. (c) Quantification of overlapping CCSs in the first and second round of cells using gridded coverslips. Results were normalized to the mean of the overlap of untreated gridded coverslips. Shown are the normalized mean with SD. Statistical analysis: t test, number of analysed images: n=31 (untreated), n=16 (trypsin), and n=15 (cleaning), $P < 0.01$. (d) Live-cell spinning disc confocal microscopy of two rounds of U373 stably expressing AP2-eGFP on the same position of a gridded coverslip with no treatment before seeding the second round of cells. AP2-eGFP signal of first (top left) and second (top middle left) round of cells. The panels underneath show the corresponding brightfield image of the grid. (Top middle right) Merged image of AP2-eGFP in first cell (red) and second cell (green). (Top right) Binary mask of AP2-eGFP overlap. (Bottom right) Zoom-in on representative overlapping CCSs from both rounds of seeded cells. Kymographs of a 5 minute long movies of a representative CCS from both rounds of seeded cells. Scale bar: 10 μm (overviews), 2 μm (zoom-in), and 1 min (kymograph).

It is known that cells use FAs to remodel their surrounding ECM (Singh, Carraher and Schwarzbauer, 2010; Bonnans, Chou and Werb, 2014; Mouw, Ou and Weaver, 2014). To test the hypothesis that clathrin-coated plaques recognize ECM remodelled by FAs, we visualized two kinds of ECM remodelling processes: fibronectin fibrillogenesis and gelatine digestion.

Cells build up their surrounding ECM by bundling proteins like fibronectin and collagen (Singh, Carraher and Schwarzbauer, 2010; Mouw, Ou and Weaver, 2014). In case of fibronectin, this process is referred to fibronectin fibrillogenesis and is mediated by FAs (Singh, Carraher and Schwarzbauer, 2010). We visualized fibronectin fibrillogenesis by the use of medium containing labelled fibronectin. Long-time live-cell microscopy of U373 expressing AP2-eGFP and mcherry-zyxin in medium containing labelled fibronectin showed that U373 cells take fibronectin from the medium and bundle it with their FAs into fibres (Fig. 4.28a). We could observe the switch from FAs to clathrin-coated plaques at such fibronectin fibres (Fig. 4.28a-d). During the switch, the fibres were partially degraded during the disassembly of FAs and the degradation continued when clathrin-coated plaques were formed (Fig. 4.28b-d). To investigate if fibronectin fibres recruit clathrin-coated plaques, we performed drug-induced FA disassembly assay on U373 cells grown in medium containing labelled fibronectin (Fig. 4.28e-h). By quantifying the percentage of FAs switching to clathrin-coated plaques in respect to whether the FAs displayed or not fibronectin fibres, we found that the switch is much more efficient when fibronectin fibres are detected at FAs (Fig. 4.28h). This experiments revealed that the formation of fibronectin fibres by FA-mediated bundling of soluble fibronectin generates a proteic structure left after FA disassembly, which seems to efficiently induce clathrin-coated plaque formation.

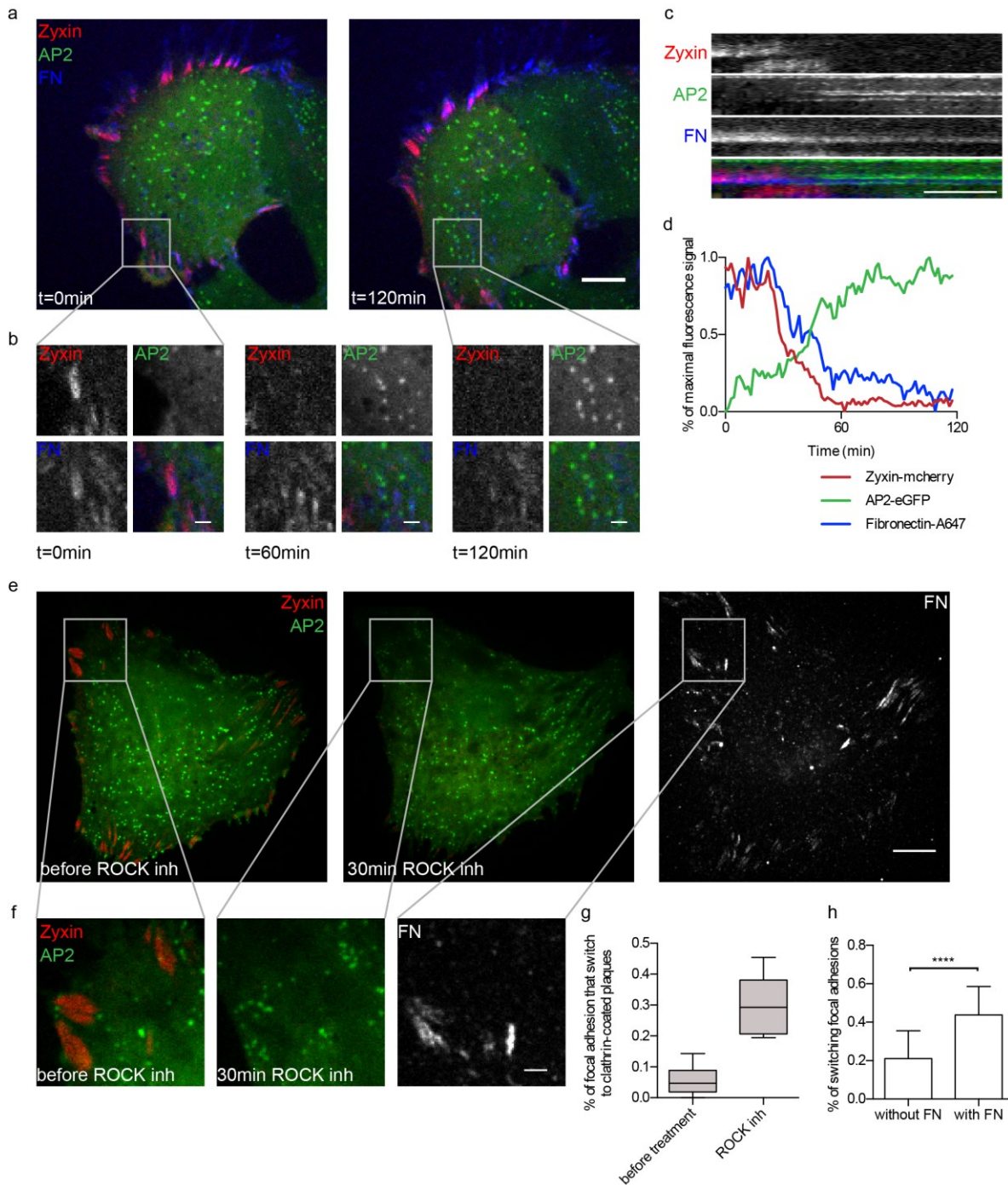


Figure 4.28: Clathrin-coated plaques are recruited to fibronectin fibres formed by FA-mediated fibrillogenesis. (a-d) Long-time live-cell confocal spinning disc microscopy of migrating U373 stably expressing AP2-eGFP (green) and transiently expressing mcherry-zyxin (red) on cellular fibronectin (cFN)-coated coverslips with medium containing Alexa Fluor 647-labelled plasma fibronectin (pFN) (blue). (a) Representative cell which shows labelled fibronectin fibres on which switch from FA to clathrin-coated plaques occurs at time 0 (left) and a later time point (120 minutes) (right). Scale bar: 10 μ m (b) Zoom-in on time 0, 60 minutes, and 120 minutes to follow switch from FA to clathrin-coated plaques on the fibronectin fibre underneath. Scale bar: 2 μ m (c) Kymograph of the

switch from FA to clathrin-coated plaques on the fibronectin fibres underneath shown in c. Scale bar: 30 min. (d) Normalized fluorescence intensity profiles of AP2-eGFP (green), mcherry-zyxin (red), and Alexa Fluor 647-labelled pFN (blue) of the switch from FA to clathrin-coated plaques shown in c. (e-h) Live-cell confocal spinning disc microscopy of U373 cells stably expressing AP2-eGFP (green) and transiently expressing mcherry-zyxin (red) on cFN-coated coverslips with medium containing Alexa Fluor 647-labelled pFN (grey, right) treated with ROCK inhibitor (10 μ M). (e-h) ROCK inhibitor treatment of cells growing on cFN-coated coverslips with medium containing Alexa Fluor 647-labelled pFN. (e) Representative cell before (left) and after 30 minutes ROCK inhibitor treatment (middle) and the corresponding Alexa Fluor 647-labelled pFN signal (right). Scale bar: 10 μ m (f) Zoom-in on the area marked by the box in e to illustrate drug-induced switch from FA to clathrin-coated plaques on fibronectin fibres. Scale bar: 2 μ m. (g) Quantification of the switch from FAs to clathrin-coated plaques during ROCK inhibitor treatment (10 μ M). Whiskers represent 10-90 percentile, box represents second and third quartile, and the line marks the median. Results are computed from two repetitions (n=9). (h) Analysis of percentage of switching FAs for FAs without and with pFN signal. Shown is the mean with SD. Statistical analysis: paired t test, n=9, P<0.01.

For processes like cell migration and development, it is necessary to locally remove ECM by enzymatic degradation (Bonnans, Chou and Werb, 2014). Digestion of ECM is mainly done by MMPs (Mott and Werb, 2004; Bonnans, Chou and Werb, 2014). In this protein family, we can find soluble and membrane bound members (Mott and Werb, 2004; Bonnans, Chou and Werb, 2014). MMP14, a transmembrane MMP found among others in FA complexes, can digest ECM proteins as well as process soluble pro-MMPs to activate them (Sato, Takino and Miyamori, 2005; Itoh, 2006; Wang and McNiven, 2012). To investigate if U373 digest ECM, we performed a gelatine degradation assay, in which cells were cultured on a labelled gelatine layer to visualise local degradation spots (see approach schematic in Fig.4.29a). U373 cells showed digested spots in the gelatine layer already after 24 hours post seeding (Fig.4.29c). The digestions were mainly done in small stripes often colocalizing with FAs. Knockdown of MMP14 (shMMP14) dramatically reduced the ability of U373 to degrade gelatine whereas cells overexpressing MMP14 (MMP14) digested gelatine to a greater extent (Fig.4.29b-d). This showed that U373 locally digest ECM at FAs and this degradation is mediated and/or regulated mostly by MMP14.

To investigate whether ECM digestions act as a signal for the induction of clathrin-coated plaques, we first looked for colocalization of MMP14 and clathrin-coated plaques. Under normal conditions, we found MMP14 enriched at clathrin-coated plaques (Fig.4.30a). This enrichment was even more pronounced at clathrin-coated plaques at the cell periphery when FAs were disassembled by ROCK inhibitor treatment (Fig.4.30b). By performing the drug-induced FA disassembly assay on labelled gelatine, we saw that the switch from FAs to clathrin-coated plaques is happening preferentially at FAs where gelatine has been noticeably digested

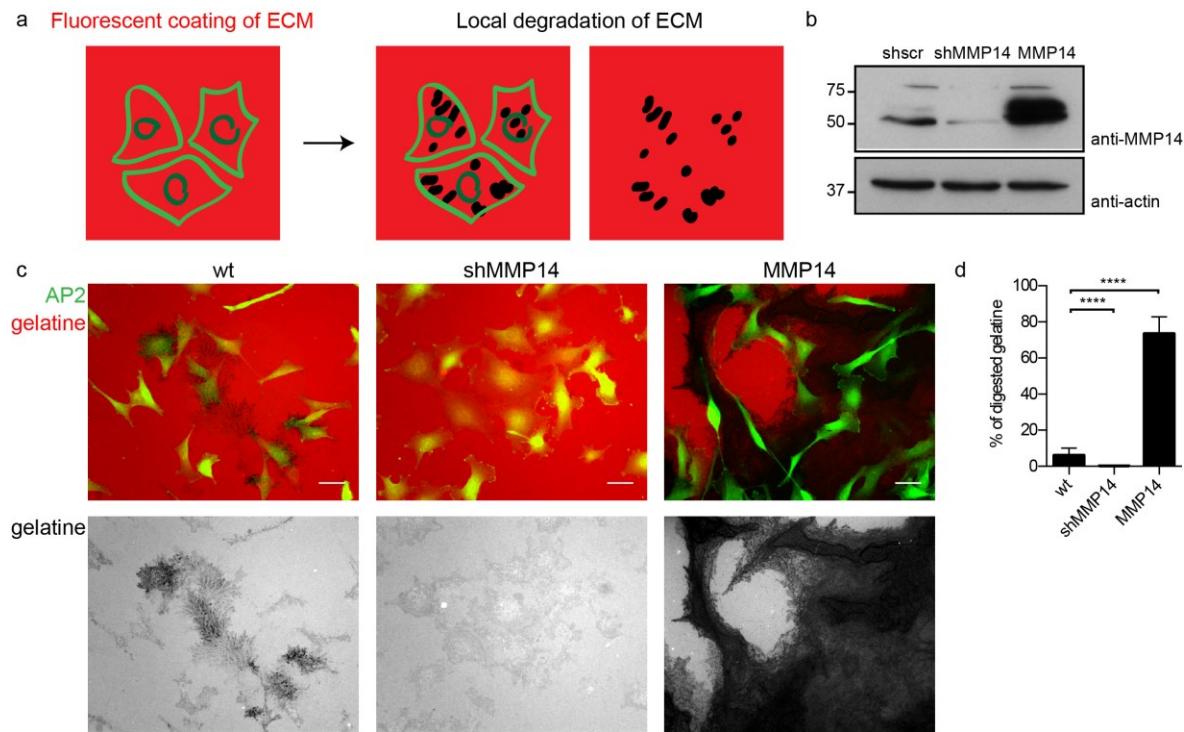


Figure 4.29: MMP14 is important for gelatine digestion in U373. (a) Schematic illustration of the gelatine degradation assay. Cells (green) growing on labelled gelatine (red) as a substrate to perform local enzymatic degradation of the gelatine layer, which can be visualized as loss of fluorescence signal at this spots (black). (b) Western blot showing the protein level of MMP14 of U373 cell lines stably expressing shscrambled (shscr), shMMP14, and overexpressing MMP14. The protein level of actin was used as loading control. (c) Representative images of widefield microscopy of U373 stably expressing AP2-eGFP (green) wild-type (wt), stable knock down for MMP14 (shMMP14), or stable overexpression of MMP14 (MMP14) on coverslips coated with Alexa Fluor 647-labelled gelatine (red). Scale bar: 10 μ m. (d) Analysis of the digested gelatine area from experiment shown in a. Shown is the mean with SD. Statistical analysis: t test, n=20 (wt), n=15 (shMMP14), n=5 (MMP14) P<0.01.

(Fig. 4.31a-d). To further investigate the role of ECM digestion in the switch of FAs to clathrin-coated plaques, we looked at the efficiency of this process in U373 with knockdown or overexpression MMP14. We could see a significant reduction in the efficiency of the switch process when MMP14 was knocked down. This reduction was even more pronounced by overexpression of MMP14 (Fig. 4.31e). Our results demonstrate that the switch from FAs to clathrin-coated plaques happens at regions that have been specifically modified (fibrillogenesis or digestion) by FAs. Additionally, these experiments show a tight connection between the enzymatic activity of MMP14 and the switch from FAs to clathrin-coated plaques. This strongly supports a model where FAs modifies the extracellular environment generating or depositing “anchoring” sites that are recognized by the clathrin machinery.

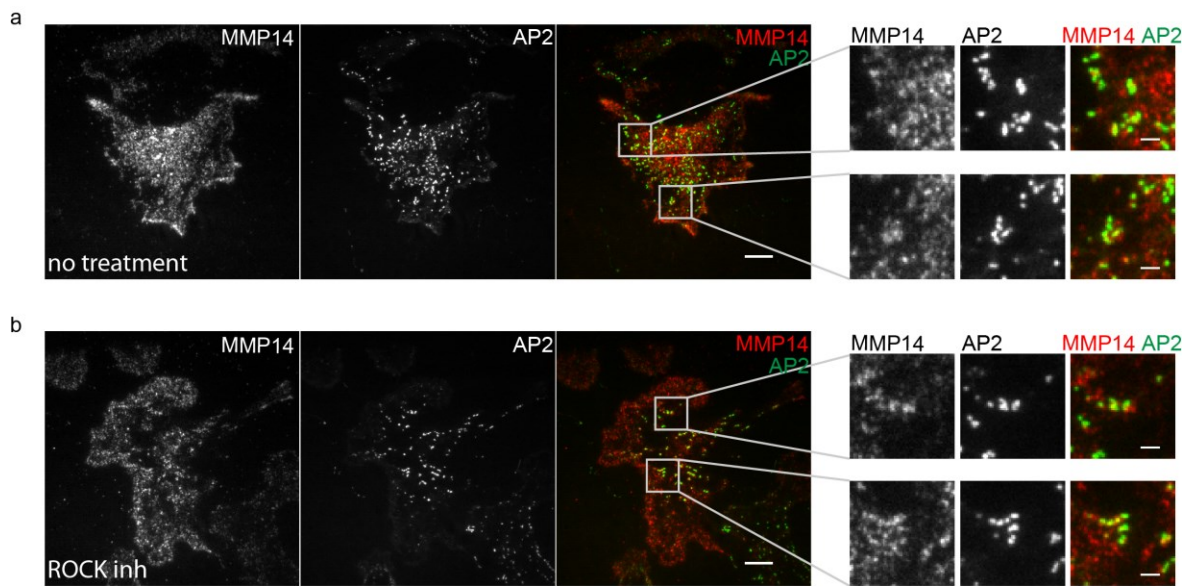


Figure 4.30: Clathrin-coated plaques associated with MMP14. TIRF microscopy of untreated (a) and ROCK inhibitor treated (10 μ M, 20 minutes) (b) U373 stably expressing AP2-eGFP (green) immunostained for MMP14 (red). Shown is a representative cell (left) with zoom-in on clathrin-coated plaques (right). Scale bar: 10 μ m (left), 2 μ m (right).

To check the relevance of ECM digestion as an extracellular signal for the switch from FAs to clathrin-coated plaques during cell migration, we performed long-time live-cell microscopy to follow the sequence of these processes. U373 expressing AP2-eGFP and mcherry-zyxin on labelled gelatine started to digest the ECM layer around 10 hours post seeding at FAs (Fig.4.32a). The switch from FAs to clathrin-coated plaques was preferentially occurring at digestions spots (Fig.4.32a-b). These degradations of gelatine were exclusively generated by FA and almost no further degradation was detectable after clathrin-coated plaque recruitment (Fig.4.32c-d). The digested spots were stable features of the gelatine layer and could be recognized not only by the cell that generated them but also by other cells that migrated toward this area (Fig.3.32e-g). Using long-time live-cell microscopy, we could observe, in some instances, cells remodelling the gelatine layer by local degradation and moving away from the digested spot. Cells covering these degradations at later time points were found to form clathrin-coated plaques at these precise digested spots (Fig.4.32e and g).

Altogether these results reveal that ECM remodelling is an important extracellular signal for clathrin-coated plaque formation. In the context of the switch from FAs to clathrin-coated plaques, the local formation of ECM protein fibres as well as enzymatic ECM digestions, both generated by FAs, are responsible for clathrin-coated plaque formation at these spots after FA

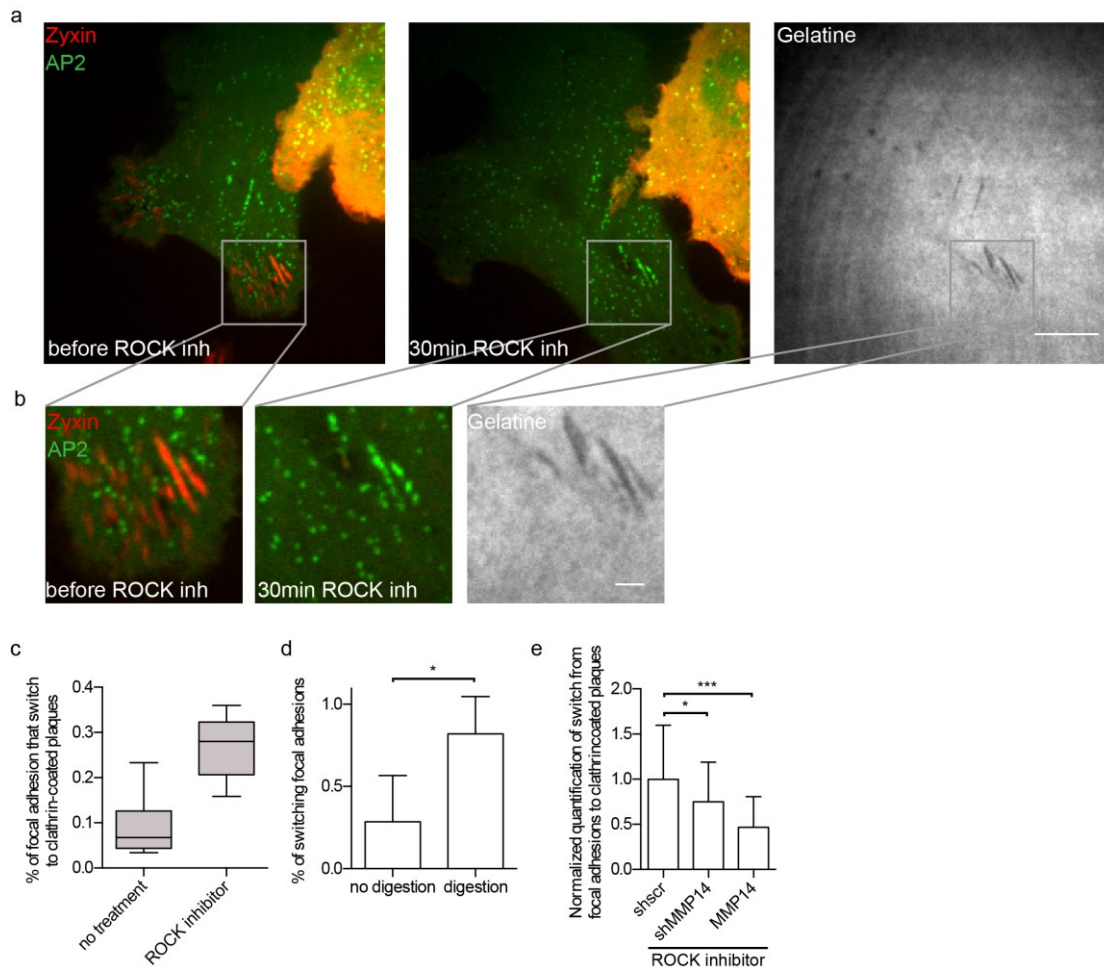


Figure 4.31: Clathrin-coated plaques are recruited to gelatine digestions formed by FA during drug-induced switch from FAs to clathrin-coated plaques. Live-cell confocal spinning disc microscopy of U373 cells stably expressing AP2-eGFP (green) and transiently expressing mcherry-zyxin (red) on coverslips coated with Alexa Fluor 647-labelled gelatine (grey) treated with ROCK inhibitor (10 μ M). (a) Overview of a representative cell, which shows labelled fibronectin fibres before (left) and after 30 minutes ROCK inhibitor treatment (middle). (Right) Overview of the Alexa Fluor 647-labelled gelatine signal. Scale bar: 10 μ m (b) Zoom in on the area marked by the box in a to illustrate drug-induced switch from FAs to clathrin-coated plaques on gelatine digestions. Scale bar: 2 μ m. (c) Quantification of the switch from FAs to clathrin-coated plaques during ROCK inhibitor treatment (10 μ M). Whiskers represent 10-90 percentile, box represents second and third quartile, and the line marks the median. Results are computed from two repetitions (n=6). (d) Analysis of percentage of switching FAs for FAs without and with gelatine digestion. Shown is the mean with SD. Statistical analysis: paired t test, n=7, P<0.05. (e) Normalized quantification of the switch from FAs to clathrin-coated plaques after 20 minutes of ROCK inhibitor (10 μ M) treatment of U373 knock down for or overexpressing MMP14. Data was normalized to the mean of U373 stably expressing shscrambled (shscr). Shown is the mean with SD computed from three repetitions. Statistical analysis: t test, n=28 (shscr), n=50 (shMMP14), and n=24 (MMP14), P<0.05.

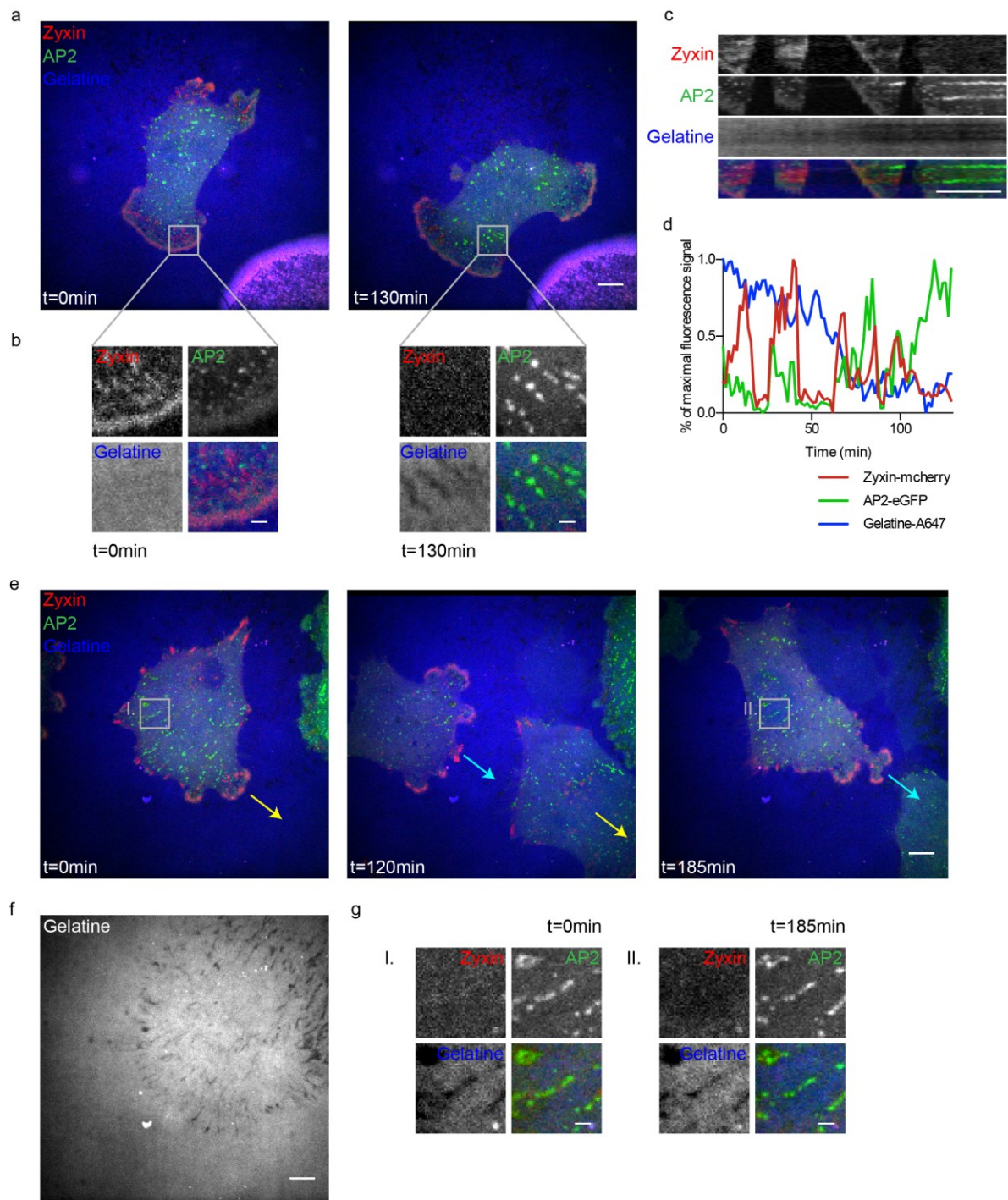


Figure 4.32: FA-induced digestions of gelatine can be sensed by clathrin-coated plaques in an intra- and intercellular manner. Long-time live-cell confocal spinning disc microscopy of migrating U373 stably expressing AP2-eGFP (green) and transiently expressing mcherry-zyxin (red) on coverslips coated with Alexa Fluor 647-labelled gelatine (blue). (a-d) Switch from FAs to clathrin-coated plaques on FA-induced gelatine digestions in migrating cells. (a) Representative cell which shows gelatine digestions generated by FAs on which switch from FA

to clathrin-coated plaques occurs. Shown at time 0 (left) and a later time point (130 minutes) (right). Scale bar: 10 μm (b) Zoom-in on time 0 and 130 minutes to follow switch from FA to clathrin-coated plaques on the gelatine digestions underneath. Scale bar: 2 μm (c) Kymograph of the switch from FA to clathrin-coated plaques on the gelatine digestion underneath shown in c. Scale bar: 30 min. (d) Normalized fluorescence intensity profiles of AP2-eGFP (green), mcherry-zyxin (red), and Alexa Fluor 647-labelled gelatine (blue) of the switch from FA to clathrin-coated plaques shown in c. (e-g) Gelatine digestions recognized by two individual cells. (e) Two representative cells migrating over gelatine digestions. Shown at time 0 (left) and a later time points (120 minutes (middle) and 185 minutes (right)) (right). Arrows (first cell: yellow; second cell: turquois) point in the direction of migrations. Scale bar: 10 μm . (f) Overview of the Alexa Fluor 647-labelled gelatine signal. Scale bar: 10 μm . (g) Zoom-in on time 0 and 185 minutes showing clathrin-coated plaques at gelatine digestions in both cells. Scale bar: 2 μm

disassembly. Furthermore, locally remodelled ECM could act as stable features that induce clathrin-coated plaque formation not only in the producer cell but also in other cells in an intercellular manner.

4.3.5 Clathrin-coated plaques form at topographical cues

Remodelled ECM can be seen as a chemical signal from restructured or degraded protein but also as physical cues providing cells topographical signals (Singh, Carraher and Schwarzbauer, 2010; Gasiorowski, Murphy and Nealey, 2013; Bonnans, Chou and Werb, 2014; Mouw, Ou and Weaver, 2014). To test the hypothesis that digested/remodelled ECM might provide cells topographical cues that induce clathrin-coated plaque formation, we investigated clathrin-coated plaque formation on 3D-micropatterns. For this aim, we established the production of optically clear micropatterns by soft lithography (Fig.4.33a). With this method, the micrometre size features of a polydimethylsiloxane (PDMS) master template were imprinted on a viscous optically clear adhesive, which could be cured by UV-light. We produced the PDMS master from diffraction gratings and evaluated the generated optically clear 3D-micropatterns by comparing the topography of the micropattern to the diffraction grating precursor using atomic force microscopy (AFM) (Fig.4.33b-f). Both surfaces showed an expected wave-like topography of lines with a frequency (peak to peak distance) of around 2 μm and a peak height of around 200nm (Fig.4.33f). No difference between the topography of the precursor and the resulting micropattern were observed, as such we used this method to reproducibly generate 3D-micropatterns with defined topographical features.

To investigate topographical cues as potential signals for clathrin-coated plaque formation, we grew U373 expressing AP2-eGFP on 3D-micropatterns. Cells reacted to the grating by stretching in the direction of the lines (Fig.4.34a). For instance we found FAs as well as actin stress fibres frequently aligned with the grating. Even CCSs were found in line with the 3D-

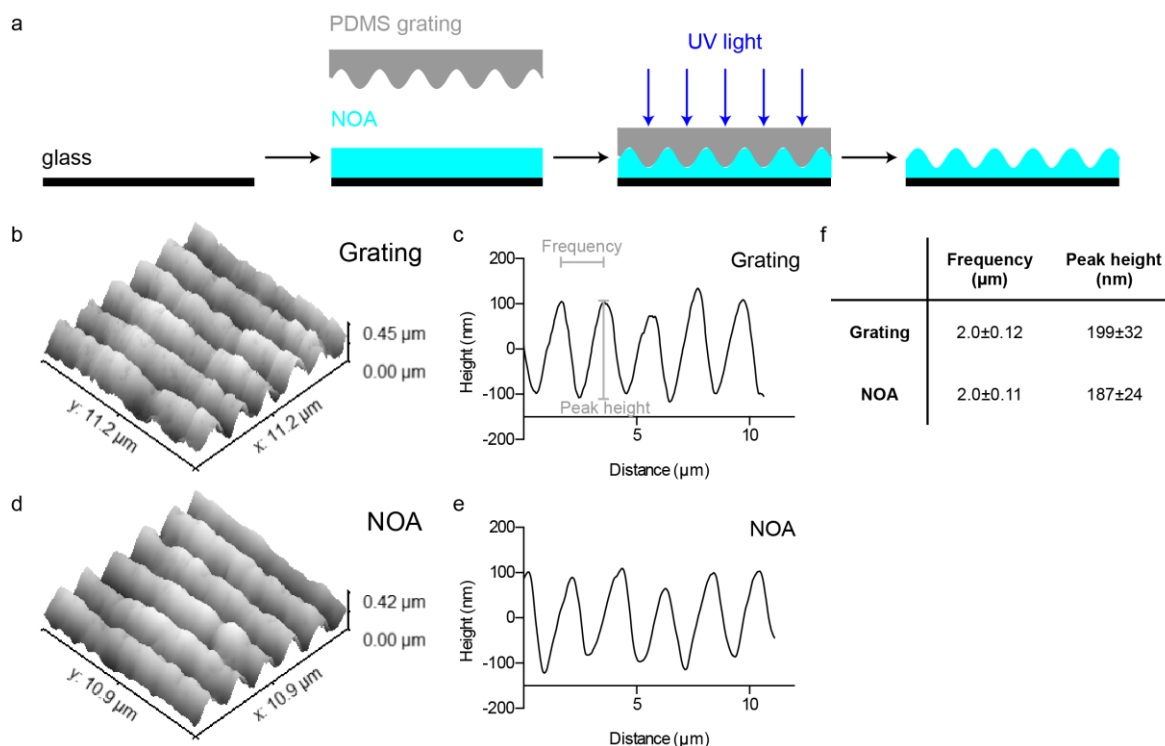


Figure 4.33: Production of optically clear 3D-micropatterns by soft lithography. (a) Schematic illustrates the production of optically clear 3D-micropatterns. First, a drop of optically clear adhesive (NOA, turquoise) was added on a glass coverslip and sandwiched by a PDMS grating (grey) generated from a diffraction grating. The optically clear adhesive was cured by UV-irradiation and finally, the PDMS grating was peeled from the optically clear 3D-micropatterns. (b-d) Comparison of the topography of the diffraction gratings (b-c) and the optically clear 3D-micropatterns (d-e) by atomic force microscopy (AFM). (b and d) 3D-representation of the topography found on diffraction gratings (b) and optically clear 3D-micropatterns (d). (c-e) Line profile of the topography shown in b and d. Frequency and peak height (grey) are shown. (f) Table lists the average frequency of lines and the peak height found on diffraction gratings and optically clear 3D-micropatterns. Shown are the mean with SD, computed from three AFM measurements, with $n=25$ (frequency) and $n=28$ (peak height). The 3D-micropattern used for this figure has been produced by Veronika Saharuka, Heidelberg. The AFM measurement has been performed jointly with Christian Huck, Heidelberg University.

micropatterns (Fig. 4.34a-b). The alignment of the CCSs could be emphasized by an x-projection along the lines to sum up the signal of all aligned CCSs (Fig. 4.34c). The analysis of the intensity profile of such an x-projection showed that the peaks of the fluorescence signal and the peaks from the 3D-micropattern imaged with differential interference contrast (DIC) microscopy were shifted by a quarter of the frequency (Fig. 4.34d). Depending on the change in the optical path length, DIC microscopy results in a relief-like image of unstained samples. By comparing the signal of the DIC image with known topography (data not shown), we could relate the DIC signal to the topographical changes of the 3D-micropattern (Fig. 4.24e). In our set up,

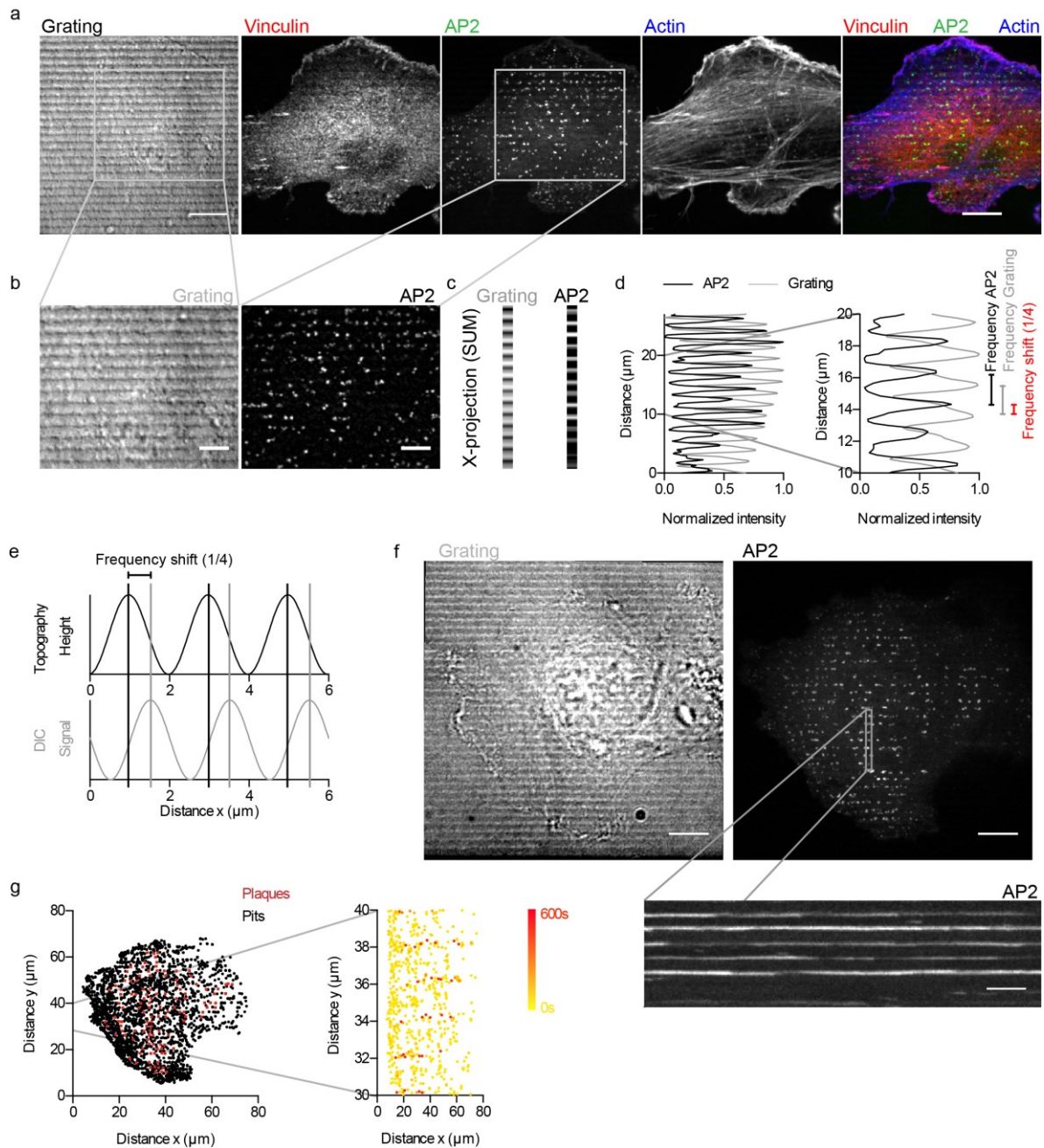


Figure 4.34: Position of clathrin-coated plaques is determined by topographical cues of the substrate.

(a) Spinning disc confocal microscopy of U373 stably expressing AP2-eGFP (green) growing on optically clear 3D-micropatterns (grey, DIC, left) stained for actin using labelled phalloidin (blue) and vinculin (red). Scale bar: 10 μm . (b) Zoom-in on the 3D-micropattern and the AP2 signal in the boxes marked in a. Scale bar: 5 μm (c) X-projection from the zoom-in shown in b. (d) (Right) Normalized intensity profile from the x-projection shown in c. (Left) Zoom-in on a smaller y scale highlighting the frequency shift of the peaks from the signal of AP2 and the grating. (e) Illustration of the relationship between topography of the 3D-micropattern (top) and the DIC signal (bottom). (f) Live-cell spinning disc confocal microscopy of U373 stably expressing AP2-eGFP (middle) growing on optically clear 3D-micropatterns (DIC, left). Scale bar 10 μm . (Right) Kymograph from a 10 minute long movie to follow

persistent clathrin-coated plaques 3D-micropatterns. Scale bar: 1 min. (g) (Right) Overview of x/y-position of the tracking results from the cell shown in e. CME tracks were categories as pits (transient, black dot) and plaques (persistent for >10 minutes, red squares). (Left) Zoom-in on a smaller y scale. CME tracks were colour-coded according to their lifetime from yellow (0s) to red (600s). The data of this figure has been produced jointly with Veronika Saharuka, Heidelberg.

the peaks of the DIC signal were shifted compared to the peaks of the 3D-micropattern by a quarter of the frequency, which means that CCSs aligned at the top of the linear topographical cues. To discriminate if the aligned CCSs were persistent clathrin-coated plaques or transient CCP, we performed live-cell microscopy on 3D-micropatterns. This revealed that aligned CCSs were persistent on top of the gratings (Fig. 4.34f). Transient CCPs could be found all over the attached PM with no preference to specific areas. However, persistent clathrin-coated plaques were exclusively formed on top of linear topographical cues (Fig. 4.34g).

The use of optically clear 3D-micropatterns showed that the formation of persistent clathrin-coated plaques could be guided by artificially generated topographical cues. This suggests that topographical changes in the substrate by ECM remodelling could be an important signal for the recruitment of clathrin-coated plaques to the former positions of the FAs.

4.3.6 Switch from FAs to clathrin-coated plaques regulates cell migration

Clathrin-coated plaque formation shows a strong connection to FA dynamics and location. It has been shown that direction of cell migration on a 2D-substrate is influenced by the orientation of FAs and the cytoskeleton (Petrie, Doyle and Yamada, 2009; Tamiello *et al.*, 2016). Likewise, we hypothesize that the formation of clathrin-coated plaques as additional adhesive structures might influence cell migration. To test this hypothesis, we performed migration assays on 3D-micropatterns (Fig. 4.35a). U373 expressing AP2-eGFP and mcherry-zyxin were allowed to migrate on gratings and their migration behaviour was characterized by tracking individual cells (Fig. 4.35a-c). Overall, U373 showed a tendency to migrate along the lines of the gratings (Fig. 4.35b). We measured the direction of the overall migration by determining the angle between the start and end point and found that almost 50% of the cells migrated with an angle of less than 15° along the lines (Fig. 4.35c). In contrast, fewer than 5% of the cells migrated across the lines (angle between 45-90°) (Fig. 4.35c). It is important to note that in this migration assay, we found that FAs as well as clathrin-coated plaques were in line with the grating (data not shown).

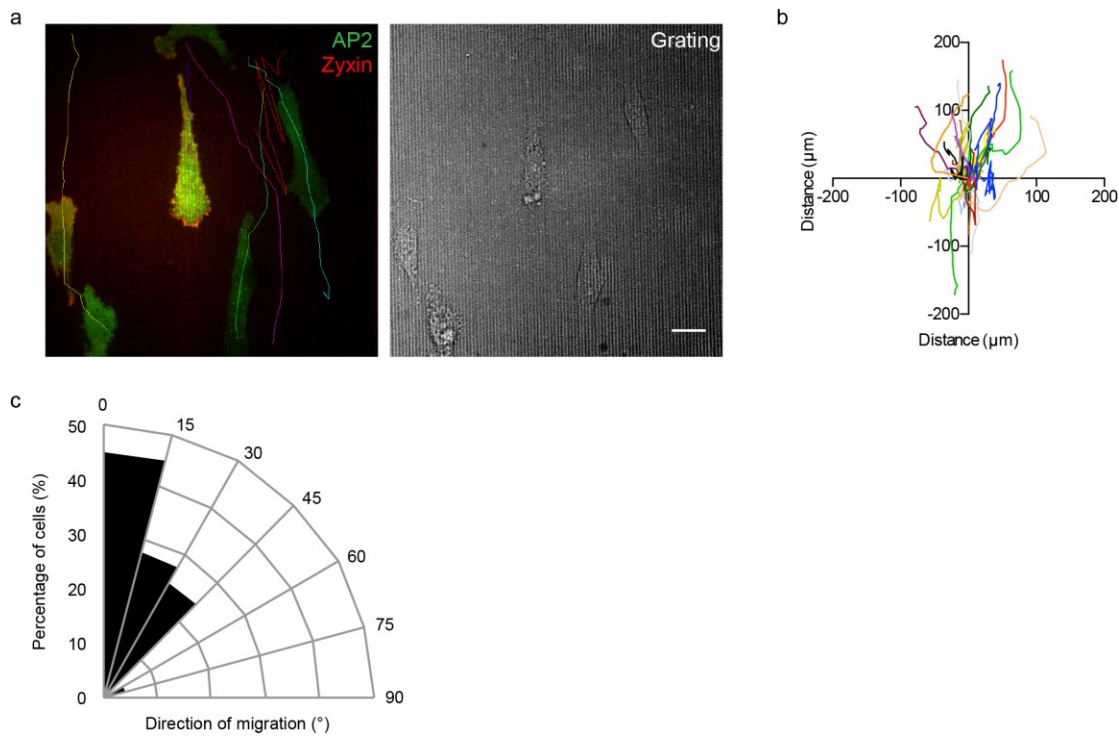


Figure 4.35: Cell migration is directed by topographical clues. Long-time live-cell spinning disc confocal microscopy of U373 stably expressing AP2-eGFP (green, left) and transiently expressing mcherry-zyxin (red, left) on optically clear 3D-micropattern (grey, DIC, right). Tracks of single cells are shown by multi-coloured lines Scale bar: 20 µm. (b) Migration trajectory map of U373 on 3D-micropattern, n=42. (c) Angular histogram of the direction of cell migration. Shown is the angle between start and end position of the tracks, n=29. The data of this figure has been produced jointly with Veronika Saharuka, Heidelberg.

To further investigate the role of clathrin-coated plaques in cell migration, we studied the influence of ECM remodelling on cell migration. First, we quantified the effect of local gelatine degradation on migration (Fig. 4.36a-c). We seeded U373 expressing AP2-eGFP on labelled gelatine layers and tracked cell migration in context of gelatine degradation. We found that the overall velocity of cell migration reduced when noticeable digestion of ECM was detectable (Fig. 4.36a and d). In general, the velocity of cell migration after the start of degradations was reduced to around 50% of the initial velocity (before start of degradation) (Fig. 4.36c). Furthermore, we analysed the behaviour of cell migration as cells face pre-existing gelatine digestions (Fig. 4.36d-e). U373 overexpressing MMP14 were used to pre-digest labelled gelatine layers. After removing the MMP14 overexpressing cells, U373 expressing AP2-eGFP were seeded on the pre-digested substrate. We found that the velocity of cell migration depended on the digestion status of the ECM. Cells migrating on non-digested gelatine displayed a certain velocity, which was reduced by more than half when cells encountered the

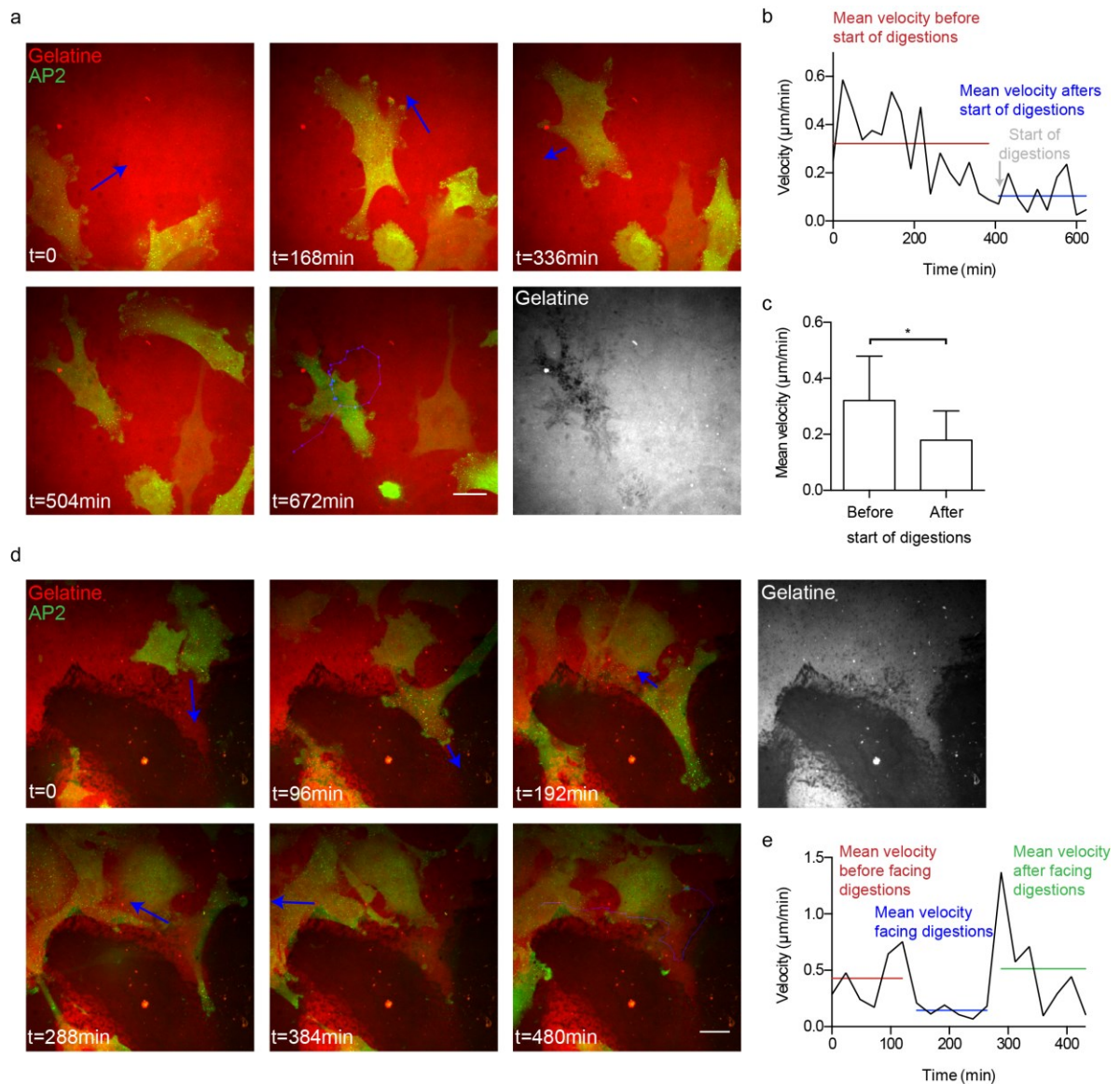


Figure 4.36: Velocity and direction of cell migration is affected by gelatine digestions. (a) Migration of U373 stably expressing AP2-eGFP (green) on Alexa Fluor 647-labelled gelatine (red) before and after digestions of the gelatine layer. Shown are snapshots of a representative cell from long-time spinning disc confocal microscopy. Blue arrows point into the direction of migration. The resulting gelatine digestions are shown in an extra panel (grey, bottom right). Scale bar: 20 μm . (b) Velocity of cell migration from the example shown in a. The mean before (red) and after (blue) the start of gelatine digestions were calculated and shown as coloured lines. (c) Comparison of mean velocity of cells before and after the start of gelatine digestions. Shown are the means with SD. Statistical analysis: paired t test, $n=9$, $P<0.05$. (d) Migration of U373 stably expressing AP2-eGFP (green) on pre-digested Alexa Fluor 647-labelled gelatine (red). The labelled gelatine layer was pre-digested by U373 overexpressing MMP14 and the cells were removed by lysis. Then U373 stably expressing AP2-eGFP were seeded on the pre-digested gelatine layer and imaged by long-time live-cell spinning disc confocal microscopy. Blue arrows point into the direction of migration. The gelatine digestions are shown in an extra panel (grey, top right). Scale bar: 20 μm .

(e) Velocity of cell migration from the example shown in d. The mean before (red) and after (green) as well as while (blue) facing the digestions were calculated and shown as coloured lines.

digested area (Fig. 4.36d-e). Importantly, upon facing the digested gelatine area, we found that cells formed clathrin-coated plaques on digested spots (Fig. 4.36d-e). After cells migrated to areas where naive non-digested gelatine was present, the overall velocity increased back to the initial migration speed (Fig. 4.36d-e).

By the generation of the gelatine digestion spots, cells produce extracellular signals for clathrin-coated plaque formation. The additional adhesive clathrin-coated plaques might slow down cell migration and retain cells at the digested areas. These extracellular cues might even direct cell migration in a similar manner as 3D-micropatterns of lines by orienting FAs as well as clathrin-coated plaques.

5 Discussion and conclusion

5.1 Differential regulation of CME dynamics and clathrin coat morphology by cell type-specific factors and PM identity

Over the past 40 years, clathrin-dependent uptake mechanisms have been studied using a broad range of biochemical and microscopic techniques (Robinson, 2015; Maib, Smythe and Ayscough, 2017). The development and enhancements of methods like cryo-EM (Fotin *et al.*, 2004), genome editing (Doyon *et al.*, 2011; Cocucci, Gaudin and Kirchhausen, 2014; Umasankar *et al.*, 2014), super-resolution microscopy (Huang *et al.*, 2008; Li *et al.*, 2015; Aguet *et al.*, 2016), and CLEM (Sochacki *et al.*, 2014, 2017; Avinoam *et al.*, 2015) helped to unravel more and more details regarding the mechanism of CME. It became clear that although CME is a widely used endocytic pathway, it might be regulated slightly different between cell lines (Saffarian, Cocucci and Kirchhausen, 2009; Grove *et al.*, 2014). However, most studies were conducted only in one cellular system, which makes it difficult to draw general conclusions. The purpose of this study was to compare and link the dynamical and structural bases of CME in different cell. We were able to define clear cell type-specific differences in CME providing us functional arguments to choose appropriate cell lines for further studies and characterization on specific CCSs.

In this work, we chose to compare BSC-1, Swiss3T3 and U373 cells. These three cell lines are widely used in the field of CME (Merrifield *et al.*, 2002; Ehrlich *et al.*, 2004; Merrifield, Perrais and Zenisek, 2005; Yarar, Waterman-Storer and Schmid, 2005; Boucrot *et al.*, 2006; Massol *et al.*, 2006; Saffarian, Cocucci and Kirchhausen, 2009; Kural *et al.*, 2015) and showed striking differences regarding CME dynamics and ultrastructural organization of the clathrin coat. BSC-1 form transient CCPs with a narrow distribution of short lifetime all over the PM (Fig. 4.1-4). The morphology of the relatively small clathrin coats in BSC-1 can range from flat, dome, to pit shape (Fig. 4.5, 9, and 10) and the individual CCSs are most of the time clearly distinguishable even with the resolution of confocal microscopy (Fig. 4.11). CCSs in Swiss3T3 are transient all over the PM but with a broader lifetime distribution compared to BSC-1 (Fig. 4.1-4). Most of the CCSs show large and flat morphology (Fig. 4.5, 9, and 10) and are often in close proximity to each other (Fig. 4.11). Beside transient CCPs with a broad range in lifetime, U373 form very persistent clathrin-coated plaques exclusively at the attached PM (Fig. 4.1-4). CCSs in U373 are diverse in their morphology and size; furthermore, flat CCSs are often connected to curved

structures (Fig.4.9-10). We believe these flat clathrin-coated plaques form budding pits at the rim. Although our approaches (live-cell FM and CLEM) cannot provide direct proof for CCP budding at a flat clathrin lattice, this process has been observed by pH-sensitive cargo (Merrifield, Perrais and Zenisek, 2005; Lampe *et al.*, 2014) and lattice light sheet microscopy (Li *et al.*, 2015) in other cell lines. In U373, we find regions with several CCSs closely together, which cannot be separated by confocal microscopy (Fig.4.11).

During CME, a coordinated interplay of over 50 described endocytic adaptor and accessory proteins are recruited to form and pinch off CCVs from the PM (McMahon and Boucrot, 2011). Several of these proteins have been described to control and regulate different steps during CME. For example the GTPase dynamin seems to play a dual role during CME. Besides its importance for membrane fission at late stage, dynamin is already recruited early during CCS formation and serves as an endocytic checkpoint during maturation (Loerke *et al.*, 2009; Aguet *et al.*, 2013). During this checkpoint, the recruitment of either of the two dynamin isoforms (dynamin1 or dynamin2) causes differences in the speed of CCP maturation as well as later trafficking events (Reis *et al.*, 2015). The accessory protein epsin has been shown to be important for generation of PM curvature (Ford *et al.*, 2002), linking the clathrin coat to the actin cytoskeleton (Messa *et al.*, 2014) as well as fission (Boucrot *et al.*, 2012; Messa *et al.*, 2014). While a triple knockout of all epsin isoforms has a dramatic effect on CME (Messa *et al.*, 2014), differences in their expression levels might affect only the dynamical or structural level of CME. The musclin proteins Fcho1 and Fcho2 play a crucial role in activation of AP2 (Hollopeter *et al.*, 2014; Umasankar *et al.*, 2014) and regulation of coat morphology and size (Mulkearns and Cooper, 2012; Umasankar *et al.*, 2014). Cells lacking both Fcho isoforms display clustered flat clathrin coats together with decelerated CME (Umasankar *et al.*, 2014; Ma *et al.*, 2016). Therefore, cell lines with predominant planar clathrin lattice might have reduced Fcho protein levels. In general, differential regulation of important proteins for CME by posttranslational modifications or expression levels in a cell type-specific manner might lead to difference in the dynamics or morphology of CCSs.

Not only proteins that are involved in building the clathrin coat, but also cargo proteins have been described to influence the maturation of CCSs. By directly affecting the rate of endocytosis, receptors can modulate signalling events. This regulation is best described for a subset of GPCRs. For example the GPCR β 1-adrenergic receptor (β 1AR) increases the CCS residence time at the PM by linkage to the actin cytoskeleton and a delayed recruitment of dynamin (Puthenveedu and von Zastrow, 2006). β 1AR has been shown to also increase CCS lifetime in an indirect manner by dissociation from β -arrestin and promoting β -arrestin

recruitment to CCSs where it increases the lifetime of CCSs to drives efficient mitogen-activated protein (MAP) kinase signalling from the PM (Eichel, Jullié and von Zastrow, 2016). For the cannabinoid receptor 1 (CB1R) a ligand-bias arrest of CCSs with CB1R- β -arrestin clusters leads to robust MAP kinase signalling (Flores-Otero *et al.*, 2014). The μ -opioid receptor (MOR), another GPCR, stalls CCSs during their maturation and controls the final scission by receptor ubiquitination (Henry *et al.*, 2012; Soohoo and Puthenveedu, 2013; Lampe *et al.*, 2014). For the LDLR it has been shown that expression levels of the receptor affect size and dynamics of CCSs in an adaptor-specific manner (Mettlen *et al.*, 2010). Although, we looked at constitutive CME, different expression levels of certain receptors as well as their specific adaptors might influence the overall dynamics and morphology of CCSs in a cell type-specific manner.

By comparing CME at different PM parts within the same cell, we revealed a slight reduction in the lifetime of CCSs formed at the top PM compared to the bottom PM in all three cell types (Fig.4.3). Additionally, the persistent clathrin-clathrin coated plaques in U373 cells only form at attached PM parts (Fig.4.4). This shows that CME is differentially regulated in a PM identity-dependent manner.

Differential regulation of CME at different PM parts has been described during various cellular processes. Most of the time, this spatiotemporal effect has been attributed to variations of the actin cortex as well as effective membrane tensions. Different mechanisms of CME at the top and bottom PM have been suggested in certain cell types and generally have been associated with differential requirement of actin to complete CCV formation (Saffarian, Cocucci and Kirchhausen, 2009; Boulant *et al.*, 2011). For example transient CCSs with longer lifetime at the bottom PM have been reported in some cell types (Saffarian, Cocucci and Kirchhausen, 2009). They have been described as flat clathrin coats that get internalized by an invert movement of the planar array in an actin-dependent manner (Saffarian, Cocucci and Kirchhausen, 2009). In specialized polarized epithelial cells, transient long-lived CCSs are found at the apical PM where the PMT is increased by microvilli rendering CME actin-dependent (Hyman, Shmuel and Altschuler, 2006; Boulant *et al.*, 2011). Even temporal changes of the PMT can modulate CCS dynamics and size. We showed that an increase in PMT leads to stalling of CME in a flat morphological state (Fig.4.17-18) (Bucher *et al.*, 2018). During cell spreading, PMT gets reduced which is accompanied by a reduction in the size as well as lifetime of CCSs (Willy *et al.*, 2017). A reverse effect has been observed for the impact of spreading area on CCSs. In this context, CCS dynamics and size was reduced by enlargement of the spreading area which influences cortical membrane tension as well as actin organization (Tan, Heureaux and Liu, 2015; Irajizad *et al.*, 2017). During cell migration, gradients of PMT are generated which leads to

a high heterogeneity of CCS dynamics (Willy *et al.*, 2017). This effect is most striking in the asymmetric CCP formation at the leading edge, where CCPs are only formed at the top PM (Kural *et al.*, 2015). Sites of cell adhesion have been suggested to regulate dynamics of CME in an integrin-mediated manner (Liu *et al.*, 2009; Batchelder and Yarar, 2010). Integrin adhesion modifies the actin cortex at adhesive PM parts, which leads to spatial modulation of cortical tension that might affect CME (Liu *et al.*, 2009; Batchelder and Yarar, 2010). Spatiotemporal regulation of the mechanism of CME might lead to controlled uptake of certain cargo. In this context, it has been shown that transferrin uptake occurs preferentially from adhesive PM parts although the PM distribution of transferrin receptor (TfR) was not spatially restricted (Grossier *et al.*, 2014). All these studies reveal a strong connection between CME regulation and membrane tension. Overcoming technical limitations in measuring spatiotemporal differences in membrane tensions with high resolution as well as separating the membrane tension from cortical tension will be a future challenge to shed light on differences of CME at certain PM parts due to local effective membrane tension.

Even less understood is the impact of differential lipid composition of certain PM parts on the regulation of CME. PIs play a crucial role in the maturation of CCSs (Posor, Eichhorn-Grünig and Haucke, 2015). During the progression of CME, generation and turnover of PI(4,5)P₂ regulates CCS nucleation as well as growth (Boucrot *et al.*, 2006; Zoncu *et al.*, 2007; Antonescu *et al.*, 2011). Later on PI(3,4)P₂ is needed to recruit BAR-proteins and complete the formation of a CCV (Posor *et al.*, 2013; Schöneberg *et al.*, 2017). Although local PI production and turnover are coordinated by the recruitment of PI kinases and phosphatases to the CCS (Posor, Eichhorn-Grünig and Haucke, 2015), this sequence might be influenced by PIs already present at the PM. The formation of PIs at the PMs is important for different signalling processes and membrane trafficking (Di Paolo and De Camilli, 2006; Schink, Tan and Stenmark, 2016). At the PM of polarized cells found in epithelia or during cell migration, gradients of PI(4,5)P₂ and phosphatidylinositol (3,4,5)-trisphosphate (PI(3,4,5)P₃) are used to establish polarized identity (Shewan, Eastburn and Mostov, 2011; Schink, Tan and Stenmark, 2016). The difference of the ratio between these signalling lipids and their metabolic intermediates might influence CME in a spatial manner. Although the role of PI(3,4,5)P₃ on CME is not clear, there seem to be enhanced endocytosis of certain receptors under elevated PI(3,4,5)P₃ levels (Nakatsu *et al.*, 2010; Laketa *et al.*, 2014). Furthermore, cholesterol has been shown to be important for CME and its abundance at certain PM parts might influence dynamics and size of CCSs (Rodal *et al.*, 1999; Subtil *et al.*, 1999; Ferguson *et al.*, 2016). Due to the abundance and turnover of lipids at

certain PM parts as well as the polarization state of cells, CME might be differentially influenced and regulated between cell lines.

With this work, we revealed differences of CME dependent on the cell type and the PM part at which the process occurs. The reasons for this discrepancy are still elusive. Further work needs to address the impact of multiple factors like protein expression levels, specific cargo as well as chemical and physical properties of the PM on CME to explain the observed differences and to understand the link to specific cellular functions.

5.2 Flat-to-curved transition during clathrin-mediated endocytosis correlates with a change in clathrin-adaptor ratio and is regulated by membrane tension

The text of the following paragraph (5.2) has been taken from Bucher *et al.* (2018).

The complex coordination of CCS formation during CME has been investigated for decades (Robinson, 2015; Maib, Smythe and Ayscough, 2017) and the field has been driven by the competition between the constant curvature versus the constant area models (Lampe, Vassilopoulos and Merrifield, 2016). Recent technological advances, in particular in CLEM, favoured the constant area model (Avinoam *et al.*, 2015). In this work, we implemented a multidisciplinary approach to combine information from EM, fluorescence intensity profiles of individual endocytic events and mathematical modelling of CCS growth to integrate different data sets into one common framework for the analysis of the ultrastructural rearrangement of CCS during CME.

By modelling the growth behaviour according to the two proposed growth models, we could calculate the expected size and morphology distribution of CCS (Fig.4.13). We could clearly demonstrate that neither of the proposed models explains the ultrastructural organisation and size distribution of CCS present in BSC-1 cells. Instead, our data supports a model in which CCSs first grow flat and then the flat-to-curved transition occurs at around 70% clathrin content (Fig. 5.1). Importantly, we demonstrated that this transition is directly linked to PMT and correlates with a change of the AP2/clathrin ratio within the coat. Increasing PMT results in inhibition of the change in AP2/clathrin ratio and the subsequent stalling of the ultrastructural rearrangement. Our conclusion that a change in AP2/clathrin ratio drives the flat-to-curved transition is consistent with our recent observation that AP2 (and other adaptor/accessory proteins) partitions in different nanoscale area of the clathrin coat and that the concentration of AP2 varies within these zones at various stage of CCS assembly (Sochacki *et al.*, 2017).

The growth behaviour of CCP assembly, determined in this work in BSC-1 cells, may also apply for other cell types. To test whether our growth model could explain the ultrastructural distribution of CCSs described in previous studies, we extended our mathematical model and calculated the predicted contact angle between the clathrin cage and the PM, the coated surface area and the radius of tip curvature of the CCSs (Fig.5.2). By comparing the model to the data set presented by Avinoam *et al.* (2015) describing the distribution and ultrastructural

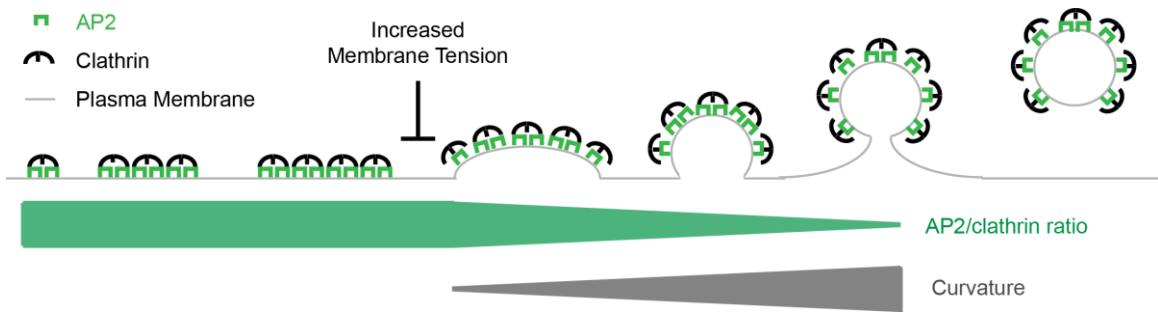


Figure 5.1: Model of CCP assembly. Schematic representation of the growth model of CCSs. CCSs initiate as flat clathrin array. They first grow in size in a flat morphology with a constant AP2/clathrin ratio. When they reach around 70 % of their full clathrin content, the AP2/clathrin ratio starts to decrease and the CCSs start acquiring their curvature. CCPs keep growing by adding additional clathrin molecules until formation and release of CCVs into the cytoplasm. The flat-to-curved transition of CCSs can be inhibited by increasing PMT resulting in an accumulation of flat structures. We propose that flat-to-curved transition is concomitant with bypassing the energy barrier necessary to curve the PM and that this critical step in CME is coordinated by the uncoupling of clathrin and AP2 characterised by their abrupt ratio decrease. This figure has been taken from Bucher *et al.* (2018).

organization of CCS in SK-MEL-2 cells, we could demonstrate that our growth model could also explain their observed distribution.

It was proposed earlier that the physical properties of the PM are influencing the morphology of CCSs because PMT energetically acts against curvature acquisition of the clathrin array (Boulant *et al.*, 2011; Saleem *et al.*, 2015; Hassinger *et al.*, 2017). We demonstrated the effect of increased PMT on CCS assembly in cells. Under high PMT, the accumulation of stalled flat CCSs at a stage prior to the change in AP2/clathrin ratio reveals an important step of CCP formation to overcome the PMT to acquire curvature. It is tempting to speculate that this change of AP2/clathrin ratio is a key event mandatory for curvature acquisition. The demonstrated interplay between AP2 and PMT shows that both biochemical and physical factors regulate CME. Surprisingly, the increase in PMT only changes the ratio between the different morphologies of CCS in favour of flat structures but does not affect their size (Fig. 4.18d-e). One could assume that a higher energy barrier of the PM might be counteracted by the clathrin system by the formation of larger flat CCSs, which could accumulate more energy for the bending process by molecular crowding of clathrin itself as well as BAR proteins incorporated in the coat (Rao and Haucke, 2011; Stachowiak *et al.*, 2012; Saleem *et al.*, 2015; Mim and Unger, 2017). Since under high PMT the flat CCSs still have the same size as under normal PMT, we suggest that there is an internal limitation of the coat size that might be regulated by certain components of the coat. Proteins that regulate the size of CCVs have been reported (Ritter *et al.*, 2013; Miller *et al.*, 2015) and it might be possible that the size of a flat clathrin lattice is

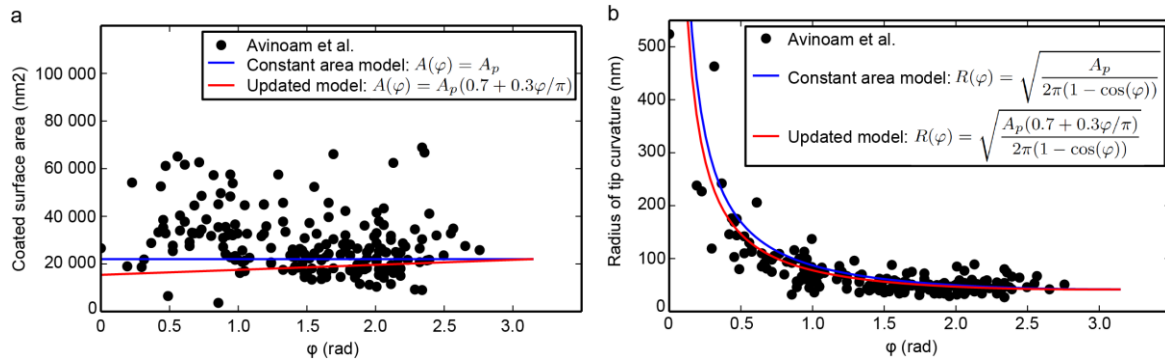


Figure 5.2: Updated growth model explains the CLEM data from Avinoam *et al.* (a) Clathrin coated surface area as a function of the growth angle ϕ . The constant area model where we assume $A=22,000\text{nm}^2$, corresponding to the most probable surface area(Kumar and Sain, 2016) is plotted (blue). Our updated model where we assume that the surface starts to bend when 70% of the final clathrin content is reached and grows the last 30% linear with ϕ plotted (red). The data (black dots) were extracted from Avinoam *et al.*(Avinoam *et al.*, 2015). (b) Radius of tip curvature as a function of the growth angle ϕ . Again, the constant area model (blue) and our updated model (red) are plotted. The radius of the tip curvature is given assuming that the clathrin structure exhibits the shape of a spherical cap. Then the tip curvature reads $R = \sqrt{A(\theta)/(2\pi(1 - \cos(\theta)))}$. The data (black dots) were extracted from Avinoam *et al.* (2015). Calculations have been performed by Felix Frey, Heidelberg University. This figure has been taken from Bucher *et al.* (2018).

controlled in a similar way. The fact that other cell types show much larger flat CCS under normal conditions, commonly referred to as clathrin-coated plaques (Fig.4.9) (Saffarian, Cocucci and Kirchhausen, 2009; Grove *et al.*, 2014), illustrates that the clathrin machinery is capable of forming large flat structures under certain conditions. But the factors necessary for clathrin-coated plaque formation have not been described so far. These clathrin-coated plaques might contribute to CME. Live-cell FM (Merrifield, Perrais and Zenisek, 2005; Li *et al.*, 2015) and EM (Heuser *et al.*, 1987) of such structures support budding of CCV from such plaques most probably from the edge, again illustrating the ability of a flat CCS to rearrange into a CCP further supporting that our observed flat-to-curved transition is indeed possible.

We could show that during coat assembly the AP2/clathrin ratio changes. This finding is in agreement with other FM (Saffarian and Kirchhausen, 2008; Loerke *et al.*, 2011; Ferguson *et al.*, 2016) and CLEM (Sochacki *et al.*, 2017) studies. Combining mathematical reasoning and CLEM demonstrated the correlation between the change in the AP2/clathrin ratio and the time of coat bending. We found that the biggest flat structures contain the same amount of AP2 compared to fully formed CCPs, while the clathrin content still increases an additional 30% as the coat rearranges from flat to CCPs. This suggests that acquisition of curvature is not linked to

addition of additional AP2 in the coat and strongly suggests that other proteins, in conjunction with clathrin might be involved in driving the ultrastructural rearrangement of the coat. Several other adaptor and accessory proteins have been proposed to influence the ultrastructure of the clathrin coat. Depletion of Fcho1 and 2 has been reported to alter the ordered hexagonal organisation of the flat clathrin lattices (Umasankar *et al.*, 2014). Other proteins like CALM and NECAP have been proposed to regulate the final size of a CCV (Ritter *et al.*, 2013; Miller *et al.*, 2015).

Our approach provides a unifying view on the process of CCP assembly where we demonstrate that CCPs initially grow as flat lattices and that change in clathrin/adaptor ratio correlates with the onset of coat curvature acquisition prior to the completion of coat polymerization. We propose that the proportion of different coat proteins could ultimately define the morphology of a clathrin structure and temporal changes of this proportion might initiate bending of the coat, allowing for dynamical regulation by the cell.

5.3 Clathrin-coated plaques are adhesion structures involved in regulation of cell migration

Clathrin has the ability to assemble into scaffolds of different size and shape. Endocytosis, the most studied function of clathrin, is associated with the transient formation of small deeply invaginated pits and subsequent fission of CCVs from the PM (McMahon and Boucrot, 2011). A different type of clathrin coats, namely the persistent larger flat clathrin-coated plaques, have been described for a long time but their function is still under debate (Lampe, Vassilopoulos and Merrifield, 2016). Here we provide evidence for a role of these clathrin-coated plaques in cell adhesion and migration by stabilizing integrins after FA disassembly at the PM (Fig.5.3). The formation of clathrin-coated plaques is induced by topographical cues generated by ECM remodelling. The sensing of this topography by spatial organization of clathrin-coated plaques might be involved in regulating cell migration through contact guidance mechanisms.

We describe a new process of initiating clathrin-coated plaque formation by the switch from FAs to clathrin-coated plaques (Fig.4.20 and 23). While FAs disassemble by disengaging integrins from actin stress fibres, FA adaptors get replaced by clathrin coats. The localization of integrin receptors in either FA or clathrin-coated plaques during this process is mutually exclusive. The so-formed integrin containing clathrin-coated plaques are persistent at the PM and seem to serve as additional adhesive structures.

Integrin trafficking is crucial for regulating cell adhesion and migration (Caswell, Vadrevu and Norman, 2009). Clathrin-dependent as well as clathrin-independent pathways have been associated with the internalization of integrin heterodimers (Caswell, Vadrevu and Norman, 2009). Localization of CCSs to FAs and integrins by the use of integrin-specific clathrin adaptors has been described and most of the time has been attributed to integrin endocytosis during FA disassembly. Integrin β subunits recruit the clathrin machinery by binding of the specific adaptors Dab2 (Chao and Kunz, 2009; Ezratty *et al.*, 2009; Teckchandani *et al.*, 2009, 2012; Yu *et al.*, 2015), Numb (Nishimura and Kaibuchi, 2007; Yu *et al.*, 2015), and ARH (Ezratty *et al.*, 2009) to NPXY-motifs in their cytoplasmic tail (Calderwood *et al.*, 2003). Recently, even some integrin α subunits have been shown to recruit the clathrin by an AP2 binding motif (De Franceschi *et al.*, 2016). In a more indirect way, the clathrin adaptor Stonin1 seems to regulate FA turnover by endocytosis of the proteoglycan neural/glia antigen 2 (NG2) as a co-receptor for integrins (Feutlinske *et al.*, 2015). Inconsistent with integrin endocytosis, integrins in clathrin-coated plaques seem to be stable at the PM, which speaks rather for a negative regulation of

integrin uptake. Upon integrin inhibition by cyclic RGD peptides, clathrin-coated plaques disassemble rapidly and presumably integrins are endocytosed by smaller transient endocytic CCSs (Fig. 4.25d and e). Interestingly, we saw a similar disassembly process of clathrin-coated plaques at the rear end of migrating cells (data not shown), which suggests regulated integrin disengagement from the ECM and their internalization at clathrin-coated plaques to break these FA-independent adhesion sites at the rear end and to allow for cell migration.

Few studies relate integrins in complex with CCSs to a function in cell adhesion. Large CCSs containing integrins have been observed in myotubes where they stabilize costameres, protein complexes linking the sarcomeres to the PM (De Deyne *et al.*, 1998; Vassilopoulos *et al.*, 2014) (Fig. 2.5a). CCSs containing Dab2 and integrin $\beta 1$ were described to play a role in initiating early cell-matrix contacts during cell spreading (Chetrit, Ziv and Ehrlich, 2009). In a 3D environment, specialized dynamic tubular CCSs containing integrins support attachment to collagen fibres (Elkhatib *et al.*, 2017) (Fig. 2.5b-c). Surprisingly, the exclusive adhesive function of these tubular CCSs is mediated rather by the engagement of clathrin adaptors to integrins than by the clathrin lattice itself since knock down of CHC does not abrogate their adhesion. Although the clathrin-coated plaques that we observe after FA disassembly seem to share some similarities to the integrin-containing CCSs observed so far, clathrin-coated plaques show novel important properties not described in this context. In contrast to the CCSs in myotubes that seem to serve a very specific function in muscle organization, clathrin-coated plaques are widely used by different cell types highlighting their potentially universal function in adhesion (Fig. 4.21). Although we see clathrin-coated plaques forming early during cell spreading (data not shown), we observe them also later during cell migration with a clear connection to former positions of FA. This argues for an additional adhesive function in parallel to FAs. Persistent clathrin-coated plaques form in a 2D environment but accumulate on topographical cues (Fig. 4.34). Besides their adhesive function, clathrin-coated plaques frequently form CCPs at the edge of the flat lattice pointing to an additional function as endocytic and/or signalling platform (Fig. 4.9-11). The combination of local adhesion as well as signalling might be important for modulating cell migration.

Besides a proposed adhesive function, clathrin-coated plaques have been implicated in signalling processes. The recruitment of receptors to the clathrin-coated microdomains is supposed to generate a signalling platform, which alters downstream signalling events as well as receptor internalization. Stable association of receptors with CCSs after ligand stimulation at the PM has been described for several receptors. During Wnt-signalling, the formation of stable LRP6 signalosomes is dependent on recruitment of the clathrin machinery by PI(4,5)P₂ while

LRP6 internalization is dispensable for further signalling events (Kim *et al.*, 2013). Stable clathrin lattice has been shown to recruit the chemokine receptor CCR5 after activation (Grove *et al.*, 2014). Furthermore, signalling of receptor tyrosine kinases like EGFR and Met via Akt activation is dependent on the location of the receptor to CCSs but not on receptor endocytosis (Garay *et al.*, 2015; Lucarelli *et al.*, 2016). The clustering of certain receptors in CCSs might serve an additional endocytic purpose. Several studies describe CCP formation at persistent flat clathrin lattice by EM (Heuser, 1980; Maupin and Pollard, 1983) (Fig. 4.9-11) as well as live-cell microscopy (Merrifield, Perrais and Zenisek, 2005; Lampe *et al.*, 2014; Li *et al.*, 2015). The specific internalization of receptors like LPAR1 and the regulation of down-stream signalling events by the disassembly of clathrin-coated plaques induced by receptor stimulation illustrates their putative combined function in endocytosis and signalling (Leyton-Puig *et al.*, 2017).

During CME, the membrane needs to be deformed to generate highly invaginated CCPs. Several proteins associated with membrane bending activity are recruited during different stages of the CCS assembly to implement curvature during CCP formation (McMahon and Boucrot, 2011; Qualmann, Koch and Kessels, 2011). While binding of BAR domains containing proteins can induce membrane curvature, they are also able to sense externally induced membrane deformation (Baumgart *et al.*, 2011; Simunovic *et al.*, 2015). Several N-BAR proteins have been shown to be recruited to inward deformations of the PM by cell adhesion to substrates with nanostructures (Galic *et al.*, 2012). With the right positive curvature, the formation of CCS hot spots at the PM can be triggered in a cargo-independent manner (Zhao *et al.*, 2017). This has been shown using artificial nanostructures like nanocones (Galic *et al.*, 2012), nanopillars (Zhao *et al.*, 2017), and beads as well as with collagen fibres (Elkhatib *et al.*, 2017). So far only transient CCPs or tubular clathrin lattice have been shown to be induced by sensing of membrane curvature. Here we show the generation of external topographical cues by different kinds of ECM remodelling to induce persistent flat clathrin-coated plaque formation (Fig. 4.28, 32 and 34). While it might sound contradictory that membrane curvature would induce a flat clathrin lattice, BAR-proteins are involved in early steps of clathrin nucleation. Some of these early BAR-proteins have only shallow curvature and have been found at the rim of flat clathrin structures (Qualmann, Koch and Kessels, 2011; Sochacki *et al.*, 2017). Fcho, one of the early F-BAR proteins in CME, has been suggested to participate in CCS nucleation as well as clathrin coat organization (Umasankar *et al.*, 2014; Ma *et al.*, 2016). Therefore, membrane curvature sensing proteins recruited during early steps of CCS assembly would be good candidates to induce clathrin-coated plaques at topographical cues.

The directionality of cell migration can be influenced by many external stimuli: Soluble chemical gradients (chemotaxis), substrate-bound chemical gradients (haptotaxis), substrate stiffness gradients (durotaxis), electric fields (electrotaxis) or aligned structures (contact guidance) (Petrie, Doyle and Yamada, 2009). By remodelling of the ECM for instance into fibres, cells generate structures that might serve as contact guidance cues. Since clathrin-coated plaques sense such external structures, they might be involved in establishing directionality of cell migration through contact guidance. Little is known of how cells sense topographical guidance cues and transfer this information into directed movements. It has been shown that cells align along microgrooves shortly after spreading (Tamiello *et al.*, 2016). This alignment on anisotropic substrates seem to be more efficient in certain cell lines than in others and dependent on groove height as well as groove and ridge width (Clark *et al.*, 1990, 1991; Kim *et al.*, 2009). Generally, this phenotype is suggested to be mediated by orientation of FAs and mechanotransduction through the actin cytoskeleton to the nucleus, which seems to control cell shape and direction of migration (Tamiello *et al.*, 2016). Details of the molecular process of cell alignment are still unclear and even the involvement of the actin cytoskeleton is under debate (Gerecht *et al.*, 2007; Provenzano, Inman, Eliceiri, Trier, *et al.*, 2008; Kubow *et al.*, 2017; Ray *et al.*, 2017). The arrangement of clathrin-coated plaques along the microgrooves as additional adhesive structures might be involved in orienting cell migration (Fig. 4.34-35). Since clathrin-coated plaques are more stable over time than the dynamic FAs, the persistent attachment to microgrooves might be important for keeping cells on this track. Furthermore the putative function as local signalling platform might be involved in establishing alignment of cells on anisotropic external cues. Besides helping to modulate directionality of intrinsic motility, clathrin-coated plaques seem to negatively influence the velocity of cell migration (Fig. 4.36). By serving as persistent adhesive structures, the induction of clathrin-coated plaques by external cues can slow down cell migration. The dual impact of clathrin-coated plaques on directionality and velocity might be important for the complex control of contact guidance in cell migration.

Although we studied migration on 2D substrates, contact guidance along topographical cues of ECM is important in 3D tissue environment. ECM is often organized in oriented fibres as seen for collagen (Mouw, Ou and Weaver, 2014) and fibronectin (Singh, Carraher and Schwarzbauer, 2010). The 3D topography of the ECM is crucial in development (Nakatsuji and E. Johnson, 1984; Yim *et al.*, 2010), axon outgrowth (Tysseling-Mattiace *et al.*, 2008) as well as tumour cell progression (Amatangelo *et al.*, 2005; Provenzano, Inman, Eliceiri, Knittel, *et al.*, 2008; Provenzano, Inman, Eliceiri, Trier, *et al.*, 2008; Erdogan *et al.*, 2017). Since cell migration in a 3D environment is supposed to be FA-independent, other mechanisms need to provide

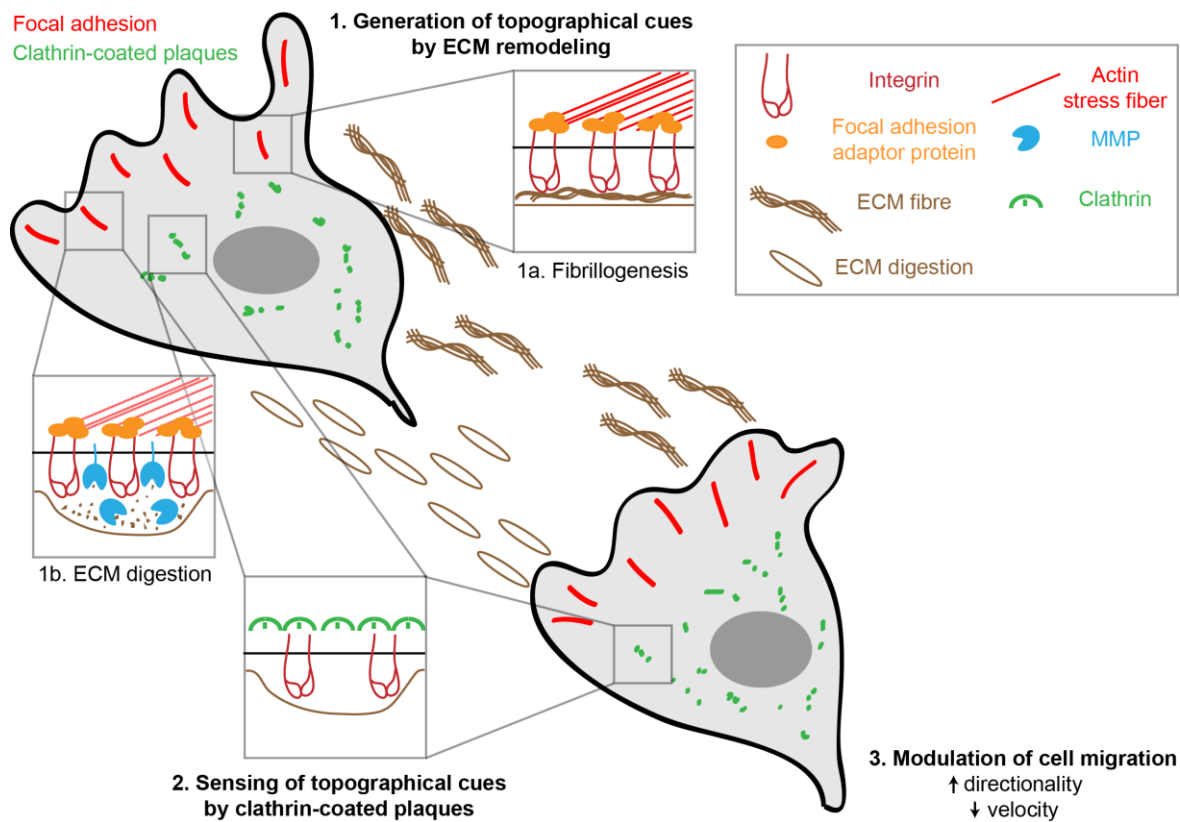


Figure 5.3: Role of clathrin-coated plaques in sensing remodelled ECM and modulating cell migration.

Schematic representation of the formation of clathrin coated-plaques during cell migration and their impact on this process. (1) During cell migration, cells remodel the ECM at FA by (1a) the creation ECM fibres or (1b) the enzymatic digestion of ECM proteins and thereby generate topographical cues. (2) After FA disassembly, clathrin-coated plaques containing integrin receptors can form at such topographical cues. The sensing of remodelled ECM by clathrin-coated plaques can (3) modulate cell behaviour and migration by enhancing directionality and reducing velocity.

adhesion to ECM fibres (Paluch, Aspalter and Sixt, 2016). Since clathrin-coated plaques contain integrins, well established ECM receptors, they would fit the requirements for such adhesive structures. Tubular clathrin lattices have been proposed to pinch collagen fibres and promote cell migration by stabilizing cell protrusions (Elkhatib *et al.*, 2017). Flat persistent clathrin-coated plaques and tubular transient clathrin lattices might be related structures in promoting adhesion to complex 3D environment in a FA-independent manner.

Altogether we propose that clathrin-coated plaques are participating in the complex regulation of cell migration (Fig. 5.3). ECM remodelling mediated by force transduction as well as enzymatic reactions at FAs generates topographical cues. These cues can comprise fibres of bundled ECM proteins (e.g. fibronectin or collagen) or digested ECM and modulate cell migration by

contact guidance. Clathrin-coated plaques are involved in sensing these extracellular cues and regulate directionality and velocity of cell migration.

The interplay between ECM organization and regulation of cellular behaviour by clathrin-coated plaques might be important for many processes like organ development, wound healing, and cancer progression. Further work needs to address the molecular mechanism of their adhesive function and signalling events at clathrin-coated plaques as well as the cause of their cell type-specific formation.

5.4 Conclusion on the functions of flat clathrin lattices

Flat clathrin lattices have been ignored or considered unproductive artefacts of cell culture for a long time. Since EM has been the only way to unambiguously identify this type of CCS, studies based on fluorescent microscopy only were insufficient to distinguish different curvature of clathrin coats. This limitation of the main microscopy method used in the field of CME led to the ignorance of the flat clathrin structures. Recent development of new methods like super-resolution microscopy as well as the combination of techniques, paved the way to better investigate the curvature-dependent function of clathrin coats.

Together with recent work in the field, we shaped a new awareness of the ultrastructural morphology of CCSs and their functional diversity. On the one hand, flat clathrin lattice can be involved in endocytosis by either serving as precursors of curved CCPs or as stable budding platform for CCV formation at the PM. On the other hand, larger flat clathrin coats associated with integrins regulate cell migration as adhesive units, which sense topographical cues of the extracellular environment. The formation and usage of the multiple functions of the clathrin lattice are regulated in a cell type-specific manner, which might be involved in specialized cellular functions. Since we only started to unravel the impact of flat clathrin coats at the PM on diverse cellular functions, more work is needed to understand their impact on health and disease.

6 Materials and methods

6.1 Materials

6.1.1 Buffers, solutions and reagents

All Buffers were made using ultrapure water (conductivity $<0.05\mu\text{S}$). Buffers, solutions and reagents not listed below are described together with the method for which they were used.

Table 6.1: General buffers, solutions and reagents.

Buffer/Solution/Reagent	Composition/Source
2-Propanol	Sigma (#33539-2.5L-R)
Acetone	Fisher Chemicals (A/0600/17)
Albumin Fraction V (pH7.0)	AppliChem (A1391,0250)
DMSO Desiccate	Life technologies (D12345)
Ethanol	Fisher Chemicals (E/0650DF/C17)
Formaldehyde solution (37 %)	Roth (#4979.1)
Glutaraldehyde solution (25 %)	Sigma (G5882)
Lysis buffer	84 mM Na_2HPO_4 , pH9.6 1% NP-40
Methanol	Fisher Chemicals (M/40000/PC17)
PBS	Sigma (P4417-100TAB)
Poly-L-lysine (PLL) solution	Sigma (P8920)
Stabilization buffer	30 mM HEPES, pH7.4 70 mM KCl 5 mM MgCl_2
TE Buffer	10 mM Tris-HCl, pH7.5 1 mM EDTA
Wash buffer I	100 mM Na_2HPO_4 , pH9.6 2 mM MgCl_2 2 mM EGTA
Wash buffer II	300 mM KCl 10 mM Na_2HPO_4 , pH7.5

Table 6.2: Buffers, solutions and reagents for SDS-PAGE

Buffer/Solution/Reagent	Composition/Source
Acrylamide/bis-acrylamide	Rotiphorese Gel 30 (37,5:1), Roth (#3029.1)
APS	10% (w/v) APS in H ₂ O, Roth (#9592.2)
ECL Western Blotting Detection Reagents	GE Healthcare (RPN2106)
Laemmli buffer (4 x)	0.2 M Tris-HCl, pH6.8 0.05 M EDTA 40% (v/v) glycerol 8% (w/v) SDS 4% (v/v) β-mercaptoethanol 0.08% (w/v) bromophenol blue
NP-40 lysis buffer	50 mM Tris, pH8.0 150 mM sodium chloride 1% (v/v) NP-40 + Protease Inhibitor (complete, EDTA-free, Roche, #11873580001)
Precision Plus Protein Dual Color Standards	BioRad (#1610374)
SDS-Tris-Glycine buffer (1 x)	25 mM Tris-base 200 mM Glycine 1% (w/v) SDS
Separating buffer (4 x)	1.5 M Tris, pH8.8 0.4% (w/v) SDS
Stacking buffer (4 x)	0.5 M Tris, pH6.8 0.4% (w/v) SDS
TBS	50 mM Tris-HCl, pH7.5 150 mM NaCl
TBST	50 mM Tris-HCl, pH7.5 150 mM NaCl 0.1% Tween
TEMED	Roth (#2367.1)
Transfer buffer	20 mM Tris-base 160 mM Glycine 20% methanol
Western Bright Chemilumineszenz Substrate Sirius	Biozym (#541021)

Table 6.3: Buffers, solutions and reagents for agarose gel electrophoresis

Buffer/Solution/Reagent	Composition/Source
1 kb Plus DNA Ladder	Invitrogen (#10787018)
Agarose Standard	Roth (#3810.3)
DNA loading dye (6x)	60% Glycerol 10mM Tris, pH7.5 60mM EDTA 0.03% bromphenol blue
Ethidium bromide (10 mg/ml)	MP Biomedicals (#ETBC1001)
TBE buffer (0.5%)	50mM Tris-base 50mM boric acid 1mM EDTA-Na ₂

6.1.2 Enzymes, primer, oligonucleotides, plasmids, antibodies, and fluorescent reagents

Table 6.4: Enzymes

Enzyme	Source	Application
AgeI-HF	NEB (R3552S)	Restriction digestion
BamHI	NEB (R0136S)	Restriction digestion
EcoRI	NEB (R0101S)	Restriction digestion
Gateway BP Clonase II Enzyme Mix	Invitrogen (#11789)	BP recombination
Gateway LR Clonase II Enzyme Mix	Invitrogen (#11791)	LR recombination
Phusion Hot Start II High-Fidelity DNA Polymerase	Thermo Scientific (#F-549L)	PCR
Proteinase K Solution	Invitrogen (AM2548)	Termination of clonase reactions
T4 DNA Ligase	NEB (M0202S)	Subcloning

Table 6.5: Primers and oligonucleotides

Primer/ Oligonucleotide	Sequence
mcherry-zyxin forward	GGGGACAAGTTTGTACAAAAAAGCAGGCTCAACCATGGTGAGCAAGGG CGAGGAGGATA
mcherry-zyxin reverse	GGGGACCACTTTGTACAAGAAAGCTGGGTCTTACGTCTGGGCTCTAGCA GTGTG
M13 forward	TGTA AACGACGGCCAGT
M13 reverse	CAGGAAACAGCTATGACC
shMMP14 forward	CCGGCATTGCATCTTCCCTAGATAGCTCGAGCTATCTAGGGAAGATGCA ATGTTTTTG
shMMP14 reverse	AATTCAAAAAACATTGCATCTTCCCTAGATAGCTCGAGCTATCTAGGGAAG ATGCAATG
shscrambled forward	CCGGCAACAAGATGAAGAGCACCAACTCGAGTTGGTGCTCTTCATCTTG TTGTTTTTG
shscrambled reverse	AATTCAAAAAACAACAAGATGAAGAGCACCAACTCGAGTTGGTGCTCTTC ATCTTGTTG
U6 primer	AGATATTAGTACAAAATACG

Table 6.6: Primary antibodies

Primary antibody	Source	Species	Application
anti- α β 5 integrin (P1F6)	Abcam (ab177004)	monoclonal mouse	IF: 1:100 (methanol/saponin)
anti- β actin	Sigma (A5441)	monoclonal mouse	WB: 1:5,000
anti- β 1 integrin (anti-CD19)	BD (#552828)	monoclonal rat	IF: 1:1,000 (formaldehyde/TritonX)
anti- β 3 integrin (anti-LIBS2, clone ab62)	Millipore (MABT27)	monoclonal mouse	IF: 1:100 (formaldehyde/TritonX)
anti-CHC (X22)	Abcam (ab2731)	monoclonal mouse	IF: 1:500-1,000 (formaldehyde/TritonX)
anti-CLC (CON.1)	Sigma (C1985)	monoclonal mouse	IF: 1:500-1,000 (formaldehyde/TritonX)
anti-MMP14 (EP1264Y)	Abcam (ab51074)	monoclonal rabbit	WB: 1:5,000 IF: 1:100 (formaldehyde/TritonX)
anti-vinculin (hVIN-1)	Sigma (V9131)	monoclonal mouse	IF: 1:800 (formaldehyde/TritonX)

WB: Western blot, IF: immunofluorescence

Table 6.7: Plasmids

Plasmid	Application	Prokaryotic resistance	Eukaryotic resistance
BacMam pCMV-DEST	Gateway vector to generate CMV-driven mammalian expression plasmid to generate recombinant bacmid DNA for BacMam production	Amp, CAM, Gen	-
BacMam pCMV-DEST mcherry-zyxin	CMV-driven mammalian expression plasmid to generate recombinant bacmid DNA for BacMam production	Amp, Gen	-
mcherry-FAK	CMV-driven mammalian expression of fusion protein	Kan	G418
mcherry-paxillin	CMV-driven mammalian expression of fusion protein	Kan	G418
mcherry-vinculin	CMV-driven mammalian expression of fusion protein	Kan	G418
mcherry-zyxin	CMV-driven mammalian expression of fusion protein	Kan	G418
pDONR 221	Gateway vector to generate entry clones	Kan	-
pENTR mcherry-zyxin	Gateway entry vector for LR reaction	Kan	-
pENTR MMP14	Gateway entry vector for LR reaction	Kan	-
pLKO.1 puro	Empty vector for U6-driven mammalian shRNA expression for lentivirus production	Amp	Puro
pLKO.1 shMMP14 puro	U6-driven mammalian shRNA expression for lentivirus production	Amp	Puro
pLKO.1 shscr puro	U6-driven mammalian shRNA expression for lentivirus production	Amp	Puro
pMDG.2	VSV-G envelope expressing plasmid for lentivirus production	Amp	-
psPAX	2nd generation lentiviral packaging plasmid for lentivirus production	Amp	-
pWPI MMP14	EF1a-driven mammalian expression vectors for lentivirus production	Amp	Puro
pWPI puro	Gateway vector to generate EF1a-driven mammalian expression vectors for lentivirus production	Amp, CAM	Puro
sigma2-eGFP	CMV-driven mammalian expression of fusion protein	Kan	G418
tdtomato-CLCa	CMV-driven mammalian expression of fusion protein	Kan	G418

Amp: ampicillin, CAM: chloramphenicol, Gen: gentamicin, Kan: kanamycin, Puro: puromycin

Table 6.8: Secondary antibodies

Secondary antibody	Source	Species	Application
anti-mouse IgG (H+L) Alexa Fluor 568	Invitrogen (A-11004)	polyclonal goat	IF: 1:1,000
anti-mouse IgG (H+L) Alexa Fluor 647	Invitrogen (A-21235)	polyclonal goat	IF: 1:1,000
anti-mouse IgG-Atto594	Sigma (76085-1ML-F)	polyclonal goat	IF: 1:200
anti-rabbit IgG (H+L) Alexa Fluor 568	Invitrogen (A-11011)	polyclonal goat	IF: 1:1,000
anti-rabbit IgG (H+L) Alexa Fluor 647	Invitrogen (A-21244)	polyclonal goat	IF: 1:1,000
anti-rat IgG (H+L) Alexa Fluor 647	Invitrogen (A-21247)	polyclonal goat	IF: 1:1,000
ECL anti-mouse IgG HRP	GE Healthcare (NA931)	polyclonal sheep	WB: 1:5,000
ECL anti-rabbit IgG HRP	GE Healthcare (NA934)	polyclonal donkey	WB: 1:5,000

Table 6.9: Fluorescent reagents

Fluorescent reagents	Source	Application
Alexa Fluor 647 NHS ester (succinimidyl ester)	Invitrogen (A37573)	Protein labelling
Alexa Fluor 647 Phalloidin	Invitrogen (A22287)	Staining: 1:50-200
Wheat germ Agglutinin, Alexa Fluor 647 conjugate	Invitrogen (W32466)	Staining: 1:200

6.1.3 Bacterial culture

All media for bacterial culture were made using ultrapure water (conductivity $<0.05\mu\text{S}$) and were sterilized by autoclaving. Antibiotics for selection were added after sterilization.

Table 6.10: Media and antibiotics for bacterial culture

Medium/Solution/Reagent	Composition/Source
Ampicillin (Amp) (1,000 x)	100 mg/ml in H ₂ O Roth (K029.2)
Kanamycin (Kan) (1,000 x)	50 mg/ml in H ₂ O Roth (T832.3)
LB-agar	Roth (X969.2)
LB-medium	Roth (X968.1)
SOB-medium	Roth (AE27.1)

Table 6.11: Bacteria strains

Bacteria strain	Source	Application
MAX Efficiency DH10Bac Competent Cells	Invitrogen (#10361012)	Generation of recombinant bacmid
Subcloning Efficiency DH5 α Competent Cells	Invitrogen (#18265017)	Subcloning, Plasmid amplification

6.1.4 Cell culture

Table 6.12: Media, solutions and reagents for cell culture

Medium/Solution/Reagent	Composition/Source
0.05 % Trypsin-EDTA	Gibco (#300-05425)
Cellfectin II Reagent	Invitrogen (#10362100)
DMEM	Gibco (#41965-039)
DMEM without phenol red	Gibco (#21063-029)
Cryomedium	45 % growth medium 45 % FBS 10 % DMSO
FBS	Biochrom (S0615)
Geneticin (G418)	Gibco (#10131-027)
IMDM	Gibco (#21980-032)
Lipofectamin 2000 Transfection Reagent	Invitrogen (#11668027)
Opti-MEM, reduced Serum Media	Gibco (#31985062)
Polyethylenimine (PEI) solution	1 mg/ml in H ₂ O
Penicillin Streptomycin (Pen/Strep)	Gibco (#15140)
Puromycin	10 mg/ml in H ₂ O, Sigma (P9620)
Sf-900 III SFM	Gibco (#12658019)

Table 6.13: Cell lines

Cell line	Description	Culture medium	Subculturing
BSC-1	African green monkey kidney epithelial cells	DMEM, 10 % FBS, 1 x Pen/Strep	1:5-1:20
Hek293T	Human embryonic kidney cells, transformed with large T antigen	IMEM, 10 % FBS, 1x Pen/Strep	1:5-1:20
HT1080	Human fibrosarcoma cells	DMEM, 10 % FBS, 1 x Pen/Strep	1:5-1:10
Swiss3T3	Mouse embryonic fibroblasts	DMEM, 10 % FBS, 1x Pen/Strep	1:5-1:10
U2OS	Human bone osteosarcoma	DMEM, 10 % FBS, 1 x Pen/Strep	1:5-1:10
U373	Human glioblastoma astrocytoma	DMEM, 10 % FBS, 1 x Pen/Strep	1:3-1:5
Sf9	Insect cells developed from ovaries of <i>Spodoptera frugiperda</i>	Sf-900 III SFM	1:5-1:10

6.2 Methods

The text of the paragraphs 6.2.13, 6.2.18-20, 6.2.22-25, and 6.2.27 has been adapted from Bucher *et al.* (2018).

6.2.1 Bacterial transformation

For transformation of DNA into bacteria, a heat shock using chemically competent bacteria was performed. In brief, subcloning reaction or plasmid DNA was mixed with appropriate bacteria and incubated for 20 minutes on ice. Afterwards a heat shock for 30 seconds at 42°C was performed and bacteria were put back on ice for 2 minutes. Bacteria were plated on LB agar plates with appropriate antibiotics for selection and incubated at 37°C overnight.

To test plasmid DNA, single colonies were picked to inoculate 5ml LB media with appropriate antibiotics for selection and incubated at 37°C overnight while shaking. Plasmid DNA was isolated and tested by restriction digestions and DNA sequencing using GATC sequencing service. To generate plasmid DNA stocks, positive bacteria colonies were used to inoculate 100ml LB media with appropriate antibiotics for selection and incubated at 37°C overnight while shaking. Plasmid DNA was isolated, dissolved in H₂O and stored at -20°C.

6.2.2 DNA isolation

Isolation of plasmid DNA from bacteria was done either with NucleoSpin Plasmid (Macherey-Nagel, 740588.250) for 5ml bacteria culture or with NucleoBond PC100 (Macherey-Nagel, 740573.100) for 100ml bacteria culture, according to manufacturer's instructions. Extraction of DNA from agarose gel, exchange of buffer, or clean-up was done with NucleoSpin Gel and PCR Clean-up (Macherey-Nagel, 740609.250), according to manufacturer's instructions.

6.2.3 Agarose gel electrophoresis

DNA fragments were separated by agarose gel electrophoresis. First, 0.8-1.2% (w/v) agarose in TBE buffer was heated until agarose was fully dissolved. The solution was cooled down to around 60°C and then ethidium bromide was added (1:10,000). The solution was poured into electrophoresis slides. When the agarose gel was solidified, it was directly used for gel electrophoresis. The DNA samples were mixed with DNA loading dye and separated using 100-120V for 1-2 hours. The DNA fragments were visualized by UV light.

6.2.4 Polymerase chain reaction (PCR)

Polymerase chain reaction (PCR) was performed using Phusion Hot Start II High-Fidelity DNA Polymerase following the manufacturer's protocol.

6.2.5 Restriction digestion

Restriction digestions were performed for subcloning purpose or for testing colony-isolated plasmids after cloning. For subcloning, 3-5 µg of plasmid DNA was used to set up a 50 µl restriction digestion reaction. For testing of cloning success, 1 µg of plasmid DNA was used to set up a 20 µl restriction digestion. For the restriction digestion reactions, appropriate restriction enzymes from NEB were used following the manufacturer's protocol.

6.2.6 Ligation

Ligation reactions were performed using T4 DNA Ligase form NEB. A 20 µl ligation reaction was set up following the manufacturer's protocol and incubated for 1 hour at room temperature.

6.2.7 Gateway cloning

The Gateway Technology (Invitrogen) was used for generating entry and expression plasmids. This highly efficient cloning system is based on site-specific recombination reactions using recombination sequences (*att*-sites) and enzymes, which catalyse recombination reactions (Clonases). This system uses a set of donor and destination vectors to quickly move DNA sequences between multiple vectors. Donor and destination vectors contain a cassette flanked by *att*-sites, which hold the *ccdB* gene for negative selection after recombination reaction and a chloramphenicol resistance gene (CM^R) for counterselection during propagation. Therefore, donor and destination vectors need to be propagated in *E.coli* strains resistant to CcdB effects. This cassette is removed by the recombination reactions and replaced by the gene of interest. More details on the system and the procedure can be found in the manufacturer's manual.

To generate entry vectors Gateway BP Clonase II Enzyme Mix was used. In brief, BP-recombination reactions between PCR products containing *attB*-sites and pDONR221 containing *attP*-sites were set up by mixing 150 ng of PCR product with 150 ng of pDONR221. TE buffer was added to reach a final volume of 8 µl. Finally 2 µl of BP Clonase II Enzyme Mix were added and incubated for 1-3 hours at 25 °C. 1 µl of Proteinase K was added to the reaction mix and incubated for 10 minutes at 37 °C. The reaction mix was transformed into DH5α as

described in paragraph 6.2.1. Plasmid DNA was isolated and sequenced with M13 forward and reverse primers.

To generate expression vectors Gateway LR Clonase II Enzyme Mix was used. In brief, LR-recombination reactions between Gateway entry vectors containing *attL*-sites and Gateway destination plasmids containing *attR*-sites were set up by mixing 150 ng of the entry vector with 150 ng of the destination vector. TE buffer was added to reach a final volume of 8 μ l. Finally 2 μ l of LR Clonase II Enzyme Mix were added and incubated for 1-3 hours at 25 °C. 1 μ l of Proteinase K was added to the reaction mix and incubated for 10 minutes at 37 °C. The reaction mix was transformed into DH5 α as described in paragraph 6.2.1.

6.2.8 Cloning of short hairpin RNA (shRNA) encoding vector for lentivirus production

Forward and reverse oligonucleotides containing short hairpin RNA (shRNA) sequence were designed according to RNA interference (RNAi) consortium (TRC) (<https://www.broadinstitute.org/scientific-community/science/projects/rnai-consortium/rnai-consortium>) and ordered from Eurofine. Complementary oligonucleotides were designed to generate 5' and 3' overhangs after annealing complementary to *Agel* and *EcoRI* restriction sites, respectively, for direct ligation into linearized vectors. While the *EcoRI* restriction site was kept intact by the oligonucleotide insertion, the *Agel* restriction site was destroyed, which was used for test digestions as described later. Oligonucleotides were diluted in H₂O at a concentration of 1 μ g/ μ l. 2.5 μ l of forward and reverse oligonucleotides were mixed with 5 μ l NEB Buffer 2 and 40 μ l H₂O. The oligonucleotide mix was heated at 95 °C for 5 minutes and slowly cooled down to room temperature for annealing of both strands. For the ligation reaction, 150 ng of pLKO.1 backbone, which has been sequentially digested with *EcoRI* and *Agel*, and 2 μ l annealed oligonucleotides were used. The whole ligation mix was used for transformation into DH5 α as described in paragraph 6.2.1.

Colonies were tested by digestion with *Agel* and *BamHI*. Insertion of oligonucleotides containing shRNA led to the loss of *Agel* restriction site. Therefore plasmids with successful insertion showed only one linearized vector band whereas religated plasmids were recognized by a double band. Plasmids were further controlled by sequencing with U6 primer

6.2.9 Lentivirus production

For lentivirus production, Hek293T cells were cultured in 10 cm dishes until 80% confluence. The cells were transfected with pMDG.2, psPAX, and the shRNA encoding pLKO.1 vector or the

pWPI vector containing the gene of interest using PEI. 50 µl of PEI (1 mg/ml) was diluted in 200 µl Opti-MEM and mixed well. 4 µg pMDG.2, 4 µg psPAX, and 8 µg pLKO.1 or pWPI were mixed with Opti-MEM to a final volume of 250 µl and mixed well. After 5 minutes, both solutions were mixed and vortexed and incubated for 20 minutes at room temperature. Then the transfection mix was added dropwise to cells. Culture medium was exchanged the next day. After another two days, the supernatant was harvested and centrifuged (10 minutes, 4,000xg) and filtered through a syringe filter (Millex-HA, 0.45 µm, Millipore, SLHA033SS). For short time storage, the lentivirus containing supernatant was kept at 4 °C; for long time storage, the supernatant was aliquoted and stored at -80 °C.

6.2.10 BacMam production

Markus Mukenhirm designed the BacMam expression system for mcherry-zyxin and produced the BacMam stock used in this work.

ViraPower BacMam Expression System (Life Technologies, A34227) was used to design and produce BacMam mcherry-zyxin for transduction of mammalian cell lines following the user guide.

In brief, the Gateway cloning system was used to generate the Gateway expression plasmid BacMam pCMV-DEST mcherry-zyxin. First, a Gateway entry plasmid containing the mcherry-zyxin sequence (pENTR mcherry-zyxin) was generated. The gene was amplified from the mammalian expression plasmid mcherry-zyxin using the primers mcherry-zyxin forward and reverse to flank the sequence with *attB*-sites by PCR. The PCR product was used to generate the pENTR mcherry-zyxin by BP-recombination reaction. pENTR mcherry-Zyxin was then used to generate the BacMAM pCMV-DEST mcherry-zyxin expression plasmid by LR-recombination reaction.

For transposition of the mcherry-zyxin gene into the bacmid, DH10Bac were transformed and incubated for two days at 37 °C. Using a blue white screen, positive colonies were selected which contained the recombinant bacmid. The bacmid DNA was isolated following the protocol described in the user guide.

To produce BacMam mcherry-zyxin, insect cells were transfected with the bacmid mcherry-Zyxin using Cellfectin II reagent to generate a P1 viral stock. This P1 baculoviral stock was used to amplify BacMam mcherry-Zyxin by infection of insect cells. This time, the infected insect cells were culture in a spinner flask to produce a high viral titre. Two rounds of amplification were

performed to produce a P2 and a P3 baculoviral stock. 3% FBS was added to the P3 baculoviral stock of BacMam mcherry-zyxin and stored in aliquots at -80 °C.

6.2.11 Subculturing of mammalian cells

Mammalian cells were cultured in appropriate growth medium at 37 °C and 5% CO₂. For subculturing, cells were rinsed with PBS and incubated for 3-5 minutes with 0.05% Trypsin/EDTA at 37 °C and 5% CO₂. After detaching, the cells were resuspended in complete medium. Subculturing was done every 2-3 days in an appropriate ratio.

6.2.12 Freezing and thawing of mammalian cells

Mammalian cells were cultured until reaching 80% confluence. Cells were detached as described before and pelleted by centrifugation (300xg, 3 minutes). The cells were resuspended in cryomedium at a concentration of 2-3x10⁶ cells per ml. Cells were frozen at a rate of -1 °C per minute in aliquots of 1ml in cryotubes to -80 °C. After three days cells were transferred to a liquid nitrogen tank.

To thaw mammalian cells, an aliquot of frozen cells was quickly thawed and transferred in 10ml growth medium. Cells were pelleted and resuspended in growth medium and transferred to a T25 flask for culturing. The growth medium was exchanged every 1-2 days until the cells recovered from thawing and then subculturing was performed as described above.

6.2.13 Transfection

Transfection of cells was done using Lipofectamine2000 if not stated otherwise. Cells were plated in 6-well plates one day before transfection. The next day, cells were transfected at 70-80% confluence. 2 µg DNA and 4-8 µl Lipofectamine2000 were separately mixed with 100 µl OptiMEM. The two solutions were mixed together. After incubation for 20 minutes at room temperature, the transfection mix was added drop-wise onto the cells.

For generation of stable cell lines, the growth medium was exchange for fresh growth medium after 8 hours. The cells were put under selection two days after transfection.

For live-cell imaging of BSC-1 AP2-eGFP transiently expressing tdtomato-CLCa, cells were seeded 8 hours after transfection and imaged 12-16 hours after seeding.

For live-cell imaging of cells transiently expressing fluorescently tagged FA proteins, the growth medium was exchange for fresh growth medium after 8 hours. The transfected cells were seeded 24 hours after transfection and imaged 6-8 hours after seeding.

6.2.14 Transduction

For transduction with lentivirus for generation of stable cell lines, 10,000 cells per well were seeded into 6-well plates together with 500 μ l of lentivirus containing supernatant. After 2 to 3 days, growth medium was exchange to selection medium with appropriate antibiotics. Cells were subcultured in selection medium for 2 weeks and then used for experiments.

For transduction with BacMam mcherry-zyxin, cells were seeded with BacMam mcherry-zyxin and were used for experiments 1 day after seeding. 30 μ l or 7 μ l BacMam mcherry-zyxin were used with 80,000 or 20,000 cells per well in 6-well or 24-well plates, respectively. 5 μ l BacMam mcherry-zyxin were used with 12,000 cells per well in μ -Slide 8 Well Glass Bottom dishes.

6.2.15 Cleaning of coverslips for microscopy

Coverslips were purchased from Thermo Scientific (diameter 12 mm, #1.5) or Marienfeld (diameter 24 mm, #1.5). Before usage, coverslips were cleaned first by 10 minutes sonication in 50 ml KOH (1M), followed by 10 minutes sonication in Acetone, 10 minutes sonication in Ethanol and finally 10 minutes sonication in millipore H₂O. Between the different solutions, coverslips were shortly rinsed with millipore H₂O. Coverslips were put on a tissue in a desiccator for drying overnight and then stored in a clean petri dish.

6.2.16 Coating of coverslips

For coating of coverslips with different proteins, clean coverslips with the appropriate size were used. First, the coverslips were sterilized with ethanol and washed three times with PBS. For cellular fibronectin (cFN) coating, cFN (from foreskin fibroblasts, stock 1 mg/ml; Sigma, F2518) was diluted in PBS. Coverslips were inverted on a drop containing 5 μ g/cm² cFN and incubated for 1 hour at room temperature followed by three washes with PBS. For poly-D-lysine (PDL) coating, the coverslips were inverted on a drop of PDL hydrobromide (mol wt 70,000-15,000, 0.01 % (w/v) in H₂O; Sigma, P6407) and incubated for 5 minutes at room temperature followed by three washes with H₂O. For collagen coating, coverslips were covered with collagen solution (from rat tail, 0.01 mg/ml in Ethanol; Sigma, C7661) overnight at 4 °C or 1-2 hour at 37 °C followed by three washes with PBS. Coated coverslips were directly used for experiments.

6.2.17 Western blot (WB)

For Western blot (WB) analysis, protein samples from cell lysates were produced. Cells were detached and pelleted (300 xg, 3 minutes). After one time washing with PBS, cells were pelleted again and the cell pellet was lysed with appropriate volume of NP-40 buffer for 30 minutes on ice. The cell lysate was spinned down for 20 minutes at 12,000xg and the supernatant was transferred to a fresh tube.

To measure the protein concentration of protein samples, DC (detergent compatible) Protein Assay Kit II (BioRad, #5000112) was used and compared to a bovine serum albumin (BSA) protein standard. To compare amounts of proteins of interest in different samples, the concentration of the samples was adjusted by diluting higher concentrated samples with NP-40 buffer.

Sodium dodecyl sulfate polyacrylamide gel electrophoresis (SDS-PAGE) gels were prepared with appropriate concentrations of the separating gel. Protein samples were mixed with Laemmli buffer, heated for 10 minutes at 95°C and spinned down for 1 minute at 12,000xg before loading. As molecular weight marker 10 µl Precision Plus Protein Dual Color Standards was separated together with the protein samples in SDS-Tris-Glycine buffer. SDS-PAGE was first performed at 80V until samples moved through the stacking gel and then turn up to 100V until loading dye run out of the gel. Proteins were transferred to a nitrocellulose blotting membrane (0.45 µm; GE Healthcare, #10600003) by wet blot using transfer buffer at 100V for 1 hour. Then membranes were blocked with 5% milk in TBST for 1 hour at room temperature. Incubation with primary antibody diluted in TBST with 5% milk was performed overnight at 4°C. After four washes for 5 minutes with TBST, membranes were incubated with secondary antibody diluted in TBST with 5% milk for 1 hour at room temperature. The membranes were washed four times for 5 minutes with TBST and developed with ECL Western Blotting Detection Reagents or Western Bright Chemilumineszenz Substrate Sirius using high performance chemiluminescence films (GE Healthcare, #28906837).

6.2.18 EM and CLEM of clathrin structures using metal replicas of unroofed membrane sheets

Cells were seeded on PDL-coated coverslips (25 mm). Unroofing was performed 16 hours after seeding. The cells were washed three times with stabilisation buffer. Unroofing was performed

in 2 % paraformaldehyde (PFA) in stabilisation buffer using two short sonication pulses. Sample was immediately put into fresh 2 % PFA solution and fixed for 20 minutes at room temperature.

For CLEM, PMs of AP2-eGFP expressing cells were used or clathrin structures were stain with an antibody against CHC. Widefield epifluorescence microscopy of unroofed PMs was performed with a Nikon N-STORM microscope with a 100x oil immersion objective and an EMCCD camera (Andor Ixon Ultra DU-897). To cover an area of 1mm² a montage of 15x15 images with an overlap of 15% for stitching was taken. The imaged area was marked with a circle (4mm in diameter) around the centre of the imaged area using an objective diamond scribe. The immersion oil was carefully removed from the bottom of the glass coverslip and the sample was prepared for EM.

Coverslips with unroofed membranes were fixed with 2% glutaraldehyde in PBS overnight. Samples were incubated with 0.1 % tannic acid for 20 minutes at room temperature. After four washes with water, the samples were incubated with 0.1 % uranyl acetate for 20 minutes at room temperature. After two washes with water, samples were dehydrated with a series of ethanol solutions (15%-100%). Samples were placed in each ethanol solution for 5 minutes. After replacing the 100% ethanol solution, the samples were dried in a critical point dryer. The samples were then put under vacuum until they were coated. The samples were coated with JFDV JOEL Freeze Fracture Equipment with a first layer of platinum with an angle of 17° while rotating and with a second layer of carbon with an angle of 90° while rotating. For better orientation, the marked area of the coated samples was imaged with a phase contrast microscope. The samples were then cut to fit on EM grids (TED PELLA, 75 Mesh Copper, Support Films Formvar/Carbon). 5% hydrofluoric acid was used to remove the glass from the metal replica. The floating metal replica was extensively washed with water and then carefully placed on a glow discharged EM grid. Samples were dried on filter paper and again imaged with a phase contrast microscope. TEM imaging was performed using a JEOL 1400 equipped with SerialEM freeware for montaging. Montages of large membrane sheets at 12,000 magnification (1.82 nm per pixel) with 10 % overlap were imaged.

6.2.19 Transformation of images for CLEM

The FM image and the EM montage of the same membrane sheet were first manually and roughly overlaid using Photoshop. MATLAB was used to transform the fluorescence image according to the EM montage using three manually identified CCS. For the transformation, the

centre of the clathrin structure in the electron microscope montage and the centre of the fluorescence signal determined by a Gaussian fit were used as landmarks.

6.2.20 TEM and CLEM analysis of CCSs

For the TEM analysis, CCSs were manually identified. The projected area was measured by outlining their surrounding using ImageJ/Fiji (<https://fiji.sc>). Classification into flat, dome and pit structures was done by visual evaluation of their curvature. Flat structure could be distinguished from curved structures. Within the curved coats, pit structures were discriminated from dome structures by the existence of a highly contrasted surrounding ring, which represents a constricted neck. The circularity of the outlines of CCSs was measured using the shape descriptors tool in ImageJ/Fiji. For the CLEM analysis, the fluorescent intensity was correlated to CCSs identified in TEM.

6.2.21 Widefield epifluorescence microscopy

If not stated otherwise, widefield epifluorescence microscopy was performed with an inverted Ti microscope (Nikon) with a 20x (0.75 numerical aperture, Plan Apo λ , Nikon) dry objective or a 40x (1.3 numerical aperture, Plan Fluor, Nikon) oil immersion objective and a digital camera (DS-Qi1MC, Nikon) equipped with LED (Lumencor-Sola) as light source.

6.2.22 Spinning disc confocal microscopy

Confocal live-cell imaging was performed with an inverted spinning disc confocal microscope (Nikon, PerkinElmer) with a 60x (1.42 numerical aperture, Apo TIRF, Nikon) or 100x (1.4 numerical aperture, Plan Apo VC, Nikon) oil immersion objective and a CMOS camera (Hamamatsu Ocras Flash 4) or an EMCCD camera (Hamamatsu C9100-23B). An environment control chamber was attached to the microscope to keep 37 °C and 5% CO₂. If not stated otherwise, live-cell imaging was performed in DMEM without phenol red containing 10% FBS.

6.2.23 Total internal reflection fluorescence (TIRF) microscopy

TIRF microscopy was performed with an inverted Ti microscope (Nikon) with objective TIRF illumination, with a 60x (1.49 numerical aperture, Apo TIRF, Nikon) oil immersion objective and an EMCCD camera (Andor iXon Ultra DU-897U). For live-cell imaging, an on-stage incubation chamber was used to keep 37 °C and 5% CO₂. Live-cell TIRF imaging was performed in DMEM without phenol red containing 10% FBS.

6.2.24 STED nanoscopy

STED nanoscopy was carried out using the Two-color-STED system (Abberior Instruments GmbH, Göttingen). Image acquisition was performed using a 100x Olympus UPlanSApo (NA 1.4) oil immersion objective and 70% nominal STED laser power ($\lambda = 775$ nm, max. power = 1.2W). Line accumulation was set to 4 and a pixel size of 15nm was used. Deconvolution of acquired images was done using inspector software (Abberior Instruments GmbH, Göttingen). Richardson-Lucy deconvolution with a regularisation parameter of 0.001 was used and stopped after 30 iterations.

6.2.25 Immunofluorescence

Cells growing on glass coverslips or glass-bottom dishes were washed once with PBS and fixed with PFA, formaldehyde, or methanol. Precisely, cells were incubated either with 2% PFA or 4% formaldehyde in PBS for 20 minutes at room temperature or overnight at 4 °C or with ice cooled methanol for 10 minutes at -20 °C. All following steps were performed at room temperature. After three washes with PBS, cells were permeabilized with either 0.5% TritonX in PBS for 15 minutes or 0.05% saponin in PBS for 10 minutes followed by a blocking step with 1% BSA in PBS for 1 hour. Samples were incubated with appropriate primary antibody dilution in 1% BSA in PBS for 1 hour. After three washes with PBS, samples were stained with appropriate secondary antibody and/or labelled phalloidin or WGA for 45 minutes followed by four washes with PBS. For normal microscopy, samples were washed with H₂O and mounted with ProLong Gold antifade reagent with DAPI (Invitrogen, P36931). For STED microscopy, samples were washed with H₂O and mounted with Mowiol. For TIRF microscopy, samples were fixed with 4% formaldehyde solution for 20 minutes, washed three times with PBS and kept in PBS.

6.2.26 Live-cell microscopy of CME at bottom and top PM

For live-cell microscopy of CME at the bottom and top PM, cells stably expressing AP2-eGFP were seeded on PDL-coated coverslips. CME dynamics at bottom and top PM of the same cell were imaged with live-cell spinning disc confocal microscopy 12 hours post seeding. Therefore, first AP2-eGFP dynamics were monitored for 10 minutes with a frame rate of 5 seconds at the bottom PM. Afterwards CME dynamics of the top PM were imaged by taking a z-stack of five images covering 2 μ m in height of the very top of the cell with a rate of 5 seconds between the

z-stacks. Maximum projections of each z-stack were generated and further used for tracking of CME at the top PM.

6.2.27 Osmotic shock experiment

For live-cell microscopy of cells under osmotic shock, one cell was imaged for 5 minutes under normal conditions. Afterwards the medium was change to hypotonic medium (1:1 ratio of medium to water with 10 % FBS) and the same cell was imaged for an additional 30 minutes.

For TEM of cells under osmotic shock, cells were put into hypotonic medium and unroofed after 10 minutes of osmotic shock. For unroofing, a 1:1 ratio of stabilization buffer to water was used. The samples were then prepared for TEM as described before.

6.2.28 Inhibitor-induced disassembly of FAs

For inhibitor-induced disassembly of FA either the ROCK inhibitor Y-37632.dihydrochloride (Enzo, ALX-270-333) or Blebbistatin (Sigma, B0560) were used. The inhibitors were diluted in medium with 10 % FBS.

To check the effect of these inhibitors on FAs and the actin cytoskeleton, cells were incubated with pre-warmed inhibitor-containing medium and fixed with formaldehyde. FAs and the actin cytoskeleton were stained using an antibody against vinculin and phalloidin, respectively. Widefield epifluorescence microscopy was used to quantify the presence of FAs and actin stress fibres.

To quantify the inhibitor-induced switch from FAs to clathrin-coated plaques, cells expressing AP2-eGFP as well as mcherry-zyxin were used. 10 cells per sample were imaged before and after treatment with pre-warmed inhibitor-containing medium. To correct for lateral shift (pixels shifts) of the samples during the exchange of medium, the images before and after the inhibitor treatment were re-aligned using clathrin-coated plaques as reference landmarks. An automated image analysis workflow by KNIME (<https://www.knime.com>) was used to perform object-based colocalization analysis of FAs and clathrin structures to quantify the switch. A binary mask for the mcherry-zyxin signal before and the AP2-eGFP signal after the inhibitor treatment was used to check for overlapping objects. Only FAs that were at a position still covered by the cell after the treatment were analysed. As a control for thresholding, the number of overlapping objects of the mcherry-zyxin and the AP2-eGFP signal before the inhibitor treatment was determined and subtracted for normalization.

6.2.29 Inhibition of specific integrins

For inhibition of integrins, the cyclic pentapeptide Cilengitide (Selleckchem, S7077) was used. The inhibitor was diluted in medium containing 10% FBS at a final concentration of 10 μ M. Live-cell spinning disc confocal microscopy of CME dynamics of the same cell was performed before and after drug treatment with a frame rate of 3 seconds to follow clathrin-coated plaque disassembly.

6.2.30 Imaging of fibronectin fibrillogenesis

The protocol described by Pankov and Momchilova (Pankov and Momchilova, 2009) was used to image fibronectin fibrillogenesis.

To produce labelled fibronectin, plasma fibronectin (pFN) (1 mg/ml, from human plasma; Sigma, F2006) was dialyzed against PBS using a Slide-A-Lyzer MINI Dialysis Device (20k MWCO, 0.5 ml; Thermo Scientific, 88402) for 2 hours at room temperature. After changing the PBS, pFN was further dialyzed overnight at 4 °C. To label pFN with Alexa Fluor 647, 100 μ l of pFN in PBS were mixed with 1.2 μ l of Alexa Fluor 647 NHS Ester (10 mg/ml) and incubated for 1 hour at room temperature protected from light. To remove the free dye, the labelling mix was dialyzed against PBS protected from light using the protocol described above.

To remove unlabelled fibronectin from FBS, we used Gelatine Sepharose 4B (Amersham Biosciences, #17095601) to prepare fibronectin-depleted fetal bovine serum (FNdFBS). Gelatine Sepharose 4B solution were washed three times with PBS. Between the washings steps, the beads were centrifuged at 200 xg for 1 minute to exchange PBS. After the third wash, beads were incubated with 10 ml FBS in at 1:2 ratio on a rocking platform for 30 minutes at room temperature. Afterwards, the beads were pelleted and the FBS was incubated with fresh beads as described above to remove residual fibronectin. Afterwards the beads were removed by pelleting and the FNdFBS was collected. FNdFBS was aliquoted and stored at -20 °C.

To label fibronectin fibrillogenesis, cells were detached, washed once with PBS and resuspended in medium containing 10% FNdFBS and 10 μ g/ml labelled pFN. The cells were seeded on cFN-coated coverslips (80,000 cells per 24 mm coverslip). Live-cell imaging was performed in DMEM without phenol red containing 10% FNdFBS and 5 μ g/ml labelled pFN and started 4 hours after seeding. For drug-induced disassembly of FAs on labelled fibronectin fibres, experiments were performed one day after seeding. For the quantification, each FA was evaluated manually for pFN signal.

6.2.31 ECM degradation assay

The protocol described by Artym, Yamada, and Mueller (Artym, Yamada and Mueller, 2009) was used to perform ECM degradation assays.

To prepare labelled gelatine, a gelatine (from porcine skin; sigma (G-2500)) solution of 0.2% gelatine in PBS was prepared. To dissolve the gelatine, the solution was heated up to 37°C for 30 minutes. For sterilization, the solution was filtered using a syringe filter membrane (Millex-GS, 0.22 µm, Millipore, SLGS033SB). To label the gelatine with Alexa Fluor 647, 500 µl of 0.2% gelatine solution was preheated to 37°C for 30 minutes. 5 µl of Alexa Fluor 647 NHS Ester (10 mg/ml) was added and incubated for 1 hour at room temperature protected from light. To remove the free dye, the labelling mix was dialyzed with a Slide-A-Lyzer MINI Dialysis Device (20k MWCO, 0.5 ml; Thermo Scientific (88402)) against PBS for 2 hours at room temperature. After changing the PBS, the mix was dialyzed overnight at 4°C. During dialysis, the labelled gelatine was protected from light.

To coat coverslips with labelled gelatine, washed coverslips were first coated with PLL using a 50 µg/ml solution in PBS for 20 minutes at room temperature. The coverslips were washed three times with PBS. Then the PLL coat was fixed with 0.5% glutaraldehyde in PBS for 15 minutes at room temperature. The coverslips were washed three times with PBS. Mixture of 0.2% labelled and unlabelled gelatine in a ratio of 8:1 was preheated to 37°C for 30 minutes. Coverslips were inverted on a drop of gelatine mix (80 µl for 12 mm diameter coverslips; 120 µl for 25 mm diameter coverslips) and incubated for 10 minutes at room temperature. Coverslips were washed three times with PBS. The coated coverslips were directly used for experiments.

To seed cells on coverslips coated with labelled gelatine, detached cells were resuspended in DMEM containing 10% FBS. The cells were pelleted by centrifugation (300 xg, 3 minutes) and washed with PBS to remove residual Trypsin. Cells were pelleted again and resuspended in DMEM containing 10% FBS and plated on coverslips with fluorescent gelatine matrix (20,000 cells for 12 mm diameter coverslips; 80,000 cells for 25 mm diameter coverslips). Cells were cultured for one day on the gelatine matrix and then used for experiments.

An automated image analysis workflow by KNIME was used to quantify the area of digested gelatine. A binary mask for the labelled gelatine signal was used to measure the digested area.

For drug-induced disassembly of FAs on labelled gelatine matrix, each FA was evaluated manually for gelatine digestion.

For long-time live-cell spinning disc confocal microscopy on pre-digested gelatine matrix, cells overexpressing MMP14 were cultured on labelled gelatine matrix for one day and removed by lysis. For this, the samples were washed once with PBS and twice with wash buffer I. Afterwards the sample was incubated with lysis buffer for 15 minutes at 37°C. The lysis buffer was replaced with fresh lysis buffer and incubated until cells were lysed completely at 37°C. The remaining labelled gelatine matrix was washed with wash buffer II twice and three times with PBS. Cells for migration assay were seeded on the pre-digested gelatine layer and imaging was started 1 hour post seeding.

6.2.32 Generation of adhesive micropatterns by photo-patterning

The protocol described by Pitaval *et al.* (Pitaval *et al.*, 2013) was used to generate adhesive micropatterns by photo-patterning.

An UVO-cleaner (Model 342, Jelight) was used to illuminate samples with deep UV. A synthetic quartz mask with customized features was purchased from Toppan. Coverslips were activated by illuminating with deep UV for 10 minutes. For passivation, the coverslips were inverted on a drop of 0.1 mg/ml Poly(L-lysine)-*graft*-poly(ethylene glycol) co-polymer (PLL-g-PEG) (SuSoS Surface Technology, PLL(20)-g[3.5]-PRG(2)) in 10 mM HEPES (pH 7.4) (50 µl for 12 mm diameter coverslips; 100 µl for 24 mm diameter coverslips) and incubated for 30 minutes. To visualize passivated areas, a 1:1 mix of unlabelled and Atto633-labelled PLL-g-PEG (SuSoS Surface Technology, PLL(20)-g[3.5]-PRG(2)-Atto633) was used. Passivated coverslips were washed with H₂O for 10 minutes.

Before usage the quartz mask was washed with acetone and isopropanol and dried. The quartz mask was activated by illuminating with deep UV for 5 minutes on the metal bearing side to clean the surface and make it hydrophilic. A Drop of 4 µl of millipore H₂O was put on the quartz mask and the coverslip was placed on the drop with the pegylated side facing down. Air bubbles were removed by pressing the coverslip against the mask. Deep UV was illuminated for 3 minutes through the mask with the quartz side facing up. After illumination, an excess of H₂O was used to remove coverslips from quartz mask by floating. The coverslips were washed with PBS before and directly used for experiments.

6.2.33 Production of 3D-micropatterns by soft lithography

To prepare 3D-micropatterns suitable for microscopy, soft lithography with a PDMS master and optical clear glue was performed. The protocol for PDMS master production was adapted from

Lücker *et al.* (Lücker *et al.*, 2014) and the protocol for 3D-micropattern production with optical clear glue from Ray *et al.* (Ray *et al.*, 2017).

To produce the PDMS master, diffraction gratings (Edmund Optics, #54-510) with a groove density of 500 grooves per mm were glued in a 10 cm petri dish using double-faced adhesive tape. One clip-pack PDMS (SYLGARD 184, 10g clip-pack; Sigma, #761036) was mixed, poured in the petri dish, and degased for 1 hour. The PDMS was cured at 50 °C overnight. The PDMS was cut into small squares (approximately 1 x 1cm) and peeled off the diffraction grating.

These PDMS masters were used to generate 3D-micropatterns made of Norland optical adhesive (Norland Products, NOA73). A drop of NOA 73 was put on a coverslip and the PDMS master was placed on top of this drop. NOA 73 was cured by UV light (UV Stratalinker 1800, Stratagene) for 15 minutes and the PDMS master was peeled from the coverslip leaving behind the micropatterned optical clear NOA 73 film. 3D-micropatterns were sterilized with ethanol before usage.

6.2.34 Surface topography measurements using AFM

AFM measurements were performed on a MultiMode 8 (Bruker). For topography measurements, an area of 12µm x 12µm of the surface was scanned in peak force tapping mode with a scanasyst-air cantilever (resonant frequency 70 kHz, spring constant 0.4, tip radius 5-10 nm; Bruker). AFM images were processed using gwyddion (<http://gwyddion.net>). Line profiles were computed by averaging profiles of 1-3 µm along the gratings.

6.2.35 Sequential seeding of cells on gridded coverslips

80,000 cells were seeded in µ-Dish 35 mm (high Grid-50 Glass Bottom; ibidi #81148). 12 hours after seeding, cells on grid were imaged by live-cell confocal microscopy. Afterwards, cells were removed with 15 mM EDTA in PBS for 10 minutes. After the removal of cells, the gridded coverslip were either left untreated, treated with 0.05 % Trypsin/EDTA for 20 minutes at 37 °C or washed according to the protocol described before. Another round of cells was seeded as described above. Live-cell confocal imaging was performed at the positions imaged in the first round of cells. To evaluate the amount of clathrin structures formed at the same position in both rounds of cells, the images were aligned with ImageJ/Fiji using the landmarks plugin. Three landmarks from the grid were selected in both pictures and the second image was registered to the first image with the Best Rigid Registration method. An automated image analysis workflow by KNIME was used to perform object-based colocalization analysis of clathrin structures for

quantification. A binary mask for the AP2-eGFP signal in both images was used to check for overlapping objects. Only clathrin structures at regions covered by cells in both images were analysed.

6.2.36 Tracking of clathrin structures

For tracking clathrin structures, we used ilastik (<http://ilastik.org>) if not stated otherwise. First the images were segmented using the pixel classification and object classification workflow. For tracking, the automatic tracking workflow was used. The maximal distance was put to 5 to avoid merging of close tracks. Tracking results were further analysed by automated workflows using KNIME.

Automatic tracking of clathrin structures using AP2-eGFP expressing cell lines was performed using a probabilistic particle tracking method (Godinez and Rohr, 2015). The method combines Kalman filters with particle filters and probabilistic data association with elliptical sampling (PDAE). For particle detection, a Laplacian-of-Gaussian filter and connected-component labelling was used. Based on the computed trajectories, the signal intensity of each tracked object (normalized to the background intensity) was determined and intensity statistics over all trajectories were computed. Also, the object size was determined for each time. In addition, the lifetime of CCS was quantified and classified into different ranges.

6.3 Modelling of growth behaviour of CCPs

The text of the following paragraphs (6.3) has been taken from Bucher *et al.* (2018).

6.3.1 Constant area model

As the fluorescence intensity of labelled clathrin triskelia is proportional to the number of incorporated clathrin triskelia or equivalently to the size of clathrin covered membrane area, we model the assembly of CCV as surface growth.

Our mathematical description of the constant area model considers growth of a flat circular patch with radius r only at its edge (L) with rate k_{on} . To ensure limited growth there has to be some balancing process to prevent a runaway-process. Mathematically the simplest idea is that growth is regulated by the size of the domain area (A). Effectively we model this as dissociation over the area of the patch with rate k_{off} , which can be expressed by $\frac{dA}{dt} = k_{\text{on}}L - k_{\text{off}}A$. In Fig. 4.14a a sketch of the growth schematics is shown. The growth equation can be simplified by plugging in the surface of a circular patch $A = \pi r^2$, it follows $\frac{dr}{dt} = k_{\text{on}} - k_{\text{off}}\frac{r}{2}$ with steady state radius $r_{\text{ss}} = 2k_{\text{on}}/k_{\text{off}}$. By integrating this equation, we find the patch area as a function of time

$$A(t) = \pi \left(\frac{2k_{\text{on}}}{k_{\text{off}}} (1 - e^{-(k_{\text{off}}/2)t}) \right)^2.$$

In the observed fluorescence intensity tracks the intensity decreases after some time until the intensity vanishes completely. Biologically, this indicates that the clathrin coated vesicle pinches off the cell membrane and therefore, moves out of the focus of the microscope. We model this by assuming an exponential decay of the area with time constant τ , starting at time t_{decrease}

$$A(t) = \begin{cases} \pi \left(\frac{2k_{\text{on}}}{k_{\text{off}}} (1 - e^{-(k_{\text{off}}/2)t}) \right)^2 & t \leq t_{\text{decrease}}, \\ \pi \left(\frac{2k_{\text{on}}}{k_{\text{off}}} (1 - e^{-(k_{\text{off}}/2)t}) \right)^2 e^{-t/\tau} & t > t_{\text{decrease}}. \end{cases} \quad (\text{Eq. S1})$$

We note that modelling the pinching as an exponential decay only serves as a measure to robustly define the end-point of a fluorescence track. No further information is extracted from this.

As the steady state is only reached approximately we define an area plateau at 95% of the steady state area and the corresponding time t_{plateau} . The constant area model assumes that a

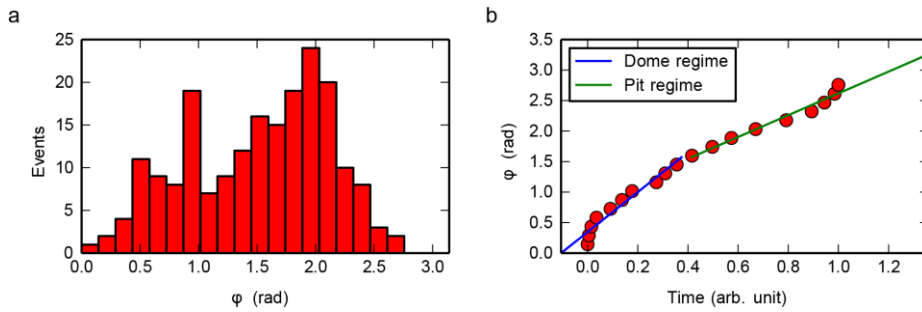


Figure 6.1: Dome and pit transformation time deduced from Avinoam *et al.* (a) Histogram of the growth angle φ (red) extracted from Avinoam *et al.* (2015) (b) The growth angle φ as a function of the normalised sum of all structures with growth angle smaller or equal to φ (red) which is proportional to a time assuming a linear time relationship between φ and time. From the linear fit to the data with φ smaller than $\pi/2$ for domes (blue) and with φ larger than $\pi/2$ for pits (green) we compute the ratio of transformation times for domes and pits and obtain roughly 2:3. Calculations have been performed by Felix Frey, Heidelberg University. This figure has been taken from Bucher *et al.* (2018).

flat patch transforms into a spherical pit as soon as the patch reaches the area plateau. Here, we neglect the exact details of the transformation process but classify the CCSs as flat, dome (less than a half sphere) or pit according to time. Before reaching the plateau, the area is considered flat. After reaching the plateau we classify CCS in the first 40% of the remaining time until t_{decrease} to be domes and in the last 60% of time to be pits. For the exact choice we use our EM data and the data set of Avinoam *et al.* (Avinoam *et al.*, 2015) (Avinoam *et al.*, 2015) (Avinoam *et al.*, 2015) (2015) and calculate the histogram $p(\varphi)$ of the growth angle φ . The number of structures which one finds between φ and $\varphi + d\varphi$ should be proportional to the time it takes for a structure to evolve from φ to $\varphi + d\varphi$, assuming a linear time course. Therefore, φ as a function of the integral should give a measure of the time course. Since we are mostly interested in the number of domes and pits, we approximate the time course of φ for domes and pits by assuming a different linear relationship between φ and time. By dividing the time, which it takes to form a half sphere, by the time it takes to form a full sphere we end up with a forming ratio time of domes and pits of roughly 2:3 (Fig. 6.1).

6.3.2 Data fits

To test whether the constant area model correctly describes the shape and size of clathrin coated vesicles we fitted Eq. 1 to 4927 FM tracks of four different cells (Fig. 4.14b) and calculated from the fitted area surface growth curves histograms which we could compare to EM

histograms. Therefore, we related the intensity of an FM track to its corresponding area. Furthermore, the FM dataset was filtered before the fitting. The exact details of our procedure are described in the following.

6.3.3 Relate fluorescence intensity and surface area by means of CLEM

To relate the fluorescence intensity of a clathrin FM track to the corresponding clathrin covered membrane area we use our clathrin CLEM data, relating the projected surface size of CCSs to their fluorescence intensity. We analyse flat CCSs for which the projected area directly corresponds to their surface. By fitting a line through the origin to the clathrin CLEM data we get the slope β providing us with a linear relation between size and intensity. As the local intensity background is removed from the CLEM data we find

$$I(A) = \beta A, \text{ (Eq. S2)}$$

where I is the intensity of the FM data, A is the area of the clathrin structure and β is the proportionality constant. Fig. 4.15b shows the intensity of flat structures as a function of their projected area (blue). We find $\beta = 4085 \text{ nm}^2$.

6.3.4 Relate different FM datasets

To calculate a size histogram from fluorescence intensity tracks we analyse live cell FM data that have a different intensity level than the fluorescence intensity of the CLEM data. Therefore, we need to relate these two different data sets. As the CLEM intensity I and the live cell FM intensity I' are both proportional to the number of labelled clathrin triskelia, both intensities, which are background corrected, can be related only by some factor α

$$I' = \alpha I \rightarrow \alpha = \langle I' \rangle / \langle I \rangle, \text{ (Eq. S3)}$$

which can be calculated by dividing the means (indicated by $\langle \rangle$) of both data sets.

6.3.5 Relate EM and FM datasets

We next restricted the live cell FM data set to ensure that the calculated size histogram is comparable to the EM histogram. In EM we only detect structures that reach a threshold size. However, in the live cell FM data set we register only detectable intensities, which exceed the local background signal. Therefore, we relate the minimal detectable size in CLEM (A_T) to a threshold intensity (I_T), which we relate to a threshold intensity (I'_T) that we use on the live cell FM tracks. As $I' = \alpha I$ we find

$$\frac{\langle I' \rangle - \langle I_T' \rangle}{\langle I' \rangle} = \frac{\langle I \rangle - \langle I_T \rangle}{\langle I \rangle}$$

As $\langle I' \rangle$ is a function of $\langle I_T' \rangle$ we can find the root of

$$0 = I_T \frac{\langle I' \rangle}{\langle I \rangle} - I_T'$$

by iteratively increasing $\langle I_T' \rangle$.

In EM we find that the minimal sized clathrin structure has an area of $A_T = 5644 \text{ nm}^2$, corresponding to a calculated intensity of $I_T = 2.305 \cdot 10^7 \text{ arb.unit}$. We find the mean intensity in the clathrin CLEM data of all structures $\langle I \rangle = 1.766 \cdot 10^8 \text{ arb.unit}$. To measure the mean intensity in the live cell FM data set we sample from each FM track that lasts a least 24 seconds a number of intensities proportional to its lifetime. From these sampled intensities, which we restrict to be larger than the threshold value I_T' , we then compute the mean intensity. We obtain $I_T' = 5.450 \cdot 10^3 \text{ arb.unit}$, $\langle I' \rangle = 4.148 \cdot 10^4 \text{ arb.unit}$. By combining the Eq. S2 and Eq. S3 we finally arrive at

$$A' (I') = \frac{I'}{\alpha\beta}$$

according to which we compute the surface of a clathrin structure from its intensity in the live cell FM. Furthermore, we filter all FM tracks showing a mean intensity which is smaller than I_T' , as those tracks would not be observable in EM.

6.3.6 Data filtering

Many CCSs at the plasma membrane represent abortive structures that will not commit to form a CCP. To ensure that abortive structures are not analysed in our study, dynamic tracks with a lifetime inferior to 24 seconds were excluded (presented data). Of note, we also repeated our analysis using a minimal lifetime of 12 seconds and found similar results (data not shown).

We filter our data set for FM tracks with multiple structures (defined as a FM track that shows at least two clear intensity maxima) to allow for direct fitting of single tracks. Precisely, we check for each data point of an intensity track if its intensity exceeds 80 % of the mean intensity to find a „first plateau“. If a data point after a „first plateau“ falls below 40 % of the mean intensity we find a „first low“. If a data point after the „first low“ exceeds the mean again by 20 % we found a

structure with multiple intensity maxima. Such tracks are filtered out. Furthermore, we filter tracks that start already with a mean intensity level $I'(t=0) > 0.5\langle I' \rangle$.

6.3.7 Parameter choice and data fitting

The parameters for the fit are restricted by assuming that growth curves should at least reach 90% and at most 120% of the maximal area value. Additionally, we assume that vesicle pinch off (corresponding to a decrease in the intensity to 10%) takes between 0 seconds to 20 seconds. Additionally, we require the fit to reach 99% of the steady state area before the area decrease happens and at least 10% of that time until the 99% area level are reached. We implement the Python module 'lmfit' for fitting the area tracks where we use the method 'nelder' of the minimiser function. In this way we obtain for each track three parameters with mean values ($r_{ss} = 65$ nm (as sphere), $k_{off} = 0.5$ 1/s, $t_{decrease} = 46$ s) that characterise the growth curve.

6.3.8 Calculation of the size histogram

From the growth curves, we calculated a histogram (Fig. 4.14c) to compare the constant area model to the measured projected size EM histogram (Fig. 4.14h). We proceeded as follows:

- From each of the fitted growth curves we uniformly drew a number of time points, proportional to the time until the structure pinches off the cell membrane, that is given by $t_{decrease}$ (Fig. 4.14a and b). We used 4927 FM tracks of 4 different cells giving us 4 million time points, which we used to calculate the size histogram.
- We classified the chosen times and corresponding areas into three categories. If $t < t_{plateau}$ the structure is flat (blue region in Fig. 4.14b). We assume that the transformation process from flat to dome takes 40% of the plateau time whereas from dome to pit it takes 60% (see above). Therefore, if $t_{plateau} < t < t_{plateau} + \frac{2}{5}(t_{decrease} - t_{plateau})$ the structure is a dome (red region in Fig. 4.14b) and otherwise it is classified as a pit (green region in Fig. 4.14b).
- We computed the projected area by assuming that the transformation within the dome and pit phase is a linear function of time. Therefore, we divided the area by $1 +$

$$\frac{5}{2} \frac{t - t_{plateau}}{t_{decrease} - t_{plateau}} \text{ for domes and } 2 + \frac{5}{3} \frac{t - t_{plateau} - \frac{2}{5}(t_{decrease} - t_{plateau})}{t_{decrease} - t_{plateau}} \text{ for pits. This factor}$$

equals 1 for a flat patch, 2 for a completed dome (half sphere) and 4 for a completed pit (full sphere).

- We excluded times for which the corresponding area is below the area threshold, since the corresponding structures fall under the detection limit of TEM determined as being the smallest object that can be confidently identified as clathrin coat by TEM (Fig. 4.14b, white region and dashed line) or where the area already decreases (Fig. 4.14b, white region). This ensures that both the calculated and measured data sets are similarly restricted.
- From the calculated projected areas, we then determined the size histogram (Fig. 4.14c), which we compare to the EM data (Fig. 4.14h).

6.3.9 Curvature acquisition during growth: updated model

In the updated growth model we assume that CCSs first grow flat, start to invaginate as they reach 70 % of their final size (which we determine by taking the inverse of the intensity ratio of pit and flat structures in clathrin CLEM, which is 1.44) and finally grow as a spherical cap until a full pit has formed. As before we model the assembly of clathrin coated vesicles as surface growth.

Our mathematical description of the “curvature acquisition during growth model “ considers a spherical cap with area $A = 2\pi R^2(1 - \cos(\varphi))$ and radius R that grows again only at its edge (L) with rate k_{on} which can be expressed by $\frac{dA}{dt} = k_{\text{on}}L$. Now the system has an intrinsic mechanism to stop growth, namely formation of a sphere and therefore needs no balancing mechanism anymore. In Fig. 4.14d a sketch of the growth schematics is shown. In the limit of a small growth angle $\varphi = k_{\text{on}}t/R < 1$ we recover the growth equation of a flat patch $A(t) = \pi(k_{\text{on}}t)^2$. For an almost complete pit the growth equation also holds perfectly. However, the mathematical description of the growth model approximates the flat patch by a spherical cap for intermediate flat patch sizes. In this case, the error is negligible as the model interpolates between the correctly addressed limiting cases and is not used to assign the shape of the CCS.

In contrast to the constant area model now no dissociation mechanism is included in the growth equation because of two reasons. First, the system has an intrinsic mechanism to stop growth and second, any area-related dissociation mechanism would imply that one could never close the sphere completely. Therefore, to obtain simple growth law such a mechanism is neglected.

We note that this choice does still allow for turnover of the clathrin coat, which does not imply a net area loss.

To define the ultrastructural organisation of the clathrin lattice, we neglect, as before, the exact details of the transformation process but classify the CCS as flat, dome (less than a half sphere) or pit according to time relative to the time when reaching the maximal area. Before reaching 70% of the maximal area the coat is flat. After reaching 70% of the maximal area we classify CCSs in the first 40% of the remaining time to be domes and pits otherwise (as above).

As before we model that vesicles pinch off the membrane by an exponential decay of the area with time constant τ , starting at time $t_{\text{decrease}} = \pi R/k_{\text{on}}$. We note that t_{decrease} carries the unit of a time since the rate k_{on} carries the unit of a velocity. The full growth equation for the area as a function of time $A(t)$ reads

$$A(t) = \begin{cases} 2\pi R^2 \left(1 - \cos\left(\frac{k_{\text{on}}t}{R}\right)\right) & t \leq t_{\text{decrease}}, \\ 4\pi R^2 e^{-t/\tau} & t > t_{\text{decrease}}. \end{cases} \quad (\text{Eq. S4})$$

As before we note that modelling the pinching as an exponential decay only serves as a measure to robustly define the end-point of a fluorescence track.

6.3.10 Data fits, parameter choice and data fitting

To test whether the ‘‘curvature acquisition during growth’’ model correctly describes the shape and size of clathrin coated vesicles we fitted Eq. S4 to 4927 FM tracks of 4 different cells (Fig. 4.14e) and calculated from the fitted area surface growth curves histograms which we could compare to EM histograms. Therefore, we related the intensity of an FM track to its corresponding area. Furthermore, the FM dataset was filtered before the fitting. The exact details of our procedure are the same as before.

The parameters for the fit are restricted by assuming that growth curve should at least reach 90% and maximal 120% of the maximal area value and that the vesicle pinching off (corresponding to a decrease in the intensity to 10%) takes between 0 seconds to 20 seconds. We implement the Python module ‘lfit’ for fitting the area tracks where we use the method ‘nelder’ of the minimiser function. In this way we obtain for each track two parameters with mean values ($R = 69$ nm, $t_{\text{decrease}} = 42$ s) that characterise the growth curve.

6.3.11 Calculation of the size histogram

From the growth curves we calculated a histogram (Fig.4.14f) to compare “the curvature acquisition during growth model” to the measured projected size EM histogram (Fig.4.14h). We proceeded in principle as before and only mention changes:

- We classified the chosen times (around 4 million time points) and corresponding areas into three categories. If $A(t) < 0.7A_{\max}$ the structure is flat (blue region in Fig.4.14e) and we call this time $t_{\text{transformation}}$. We assume that the transformation process from flat to dome takes the first 40% of the remaining time until the maximal area is reached whereas from dome to pit it takes the rest of the time (as above).
- We computed the projected area by assuming that the transformation within the dome and pit phase is a linear function of time. Therefore, we divided the area by $1 + \frac{5}{2} \frac{t - t_{\text{transformation}}}{t_{\text{decrease}} - t_{\text{transformation}}}$ for domes and $2 + \frac{5}{3} \frac{t - t_{\text{transformation}} - \frac{2}{5}(t_{\text{decrease}} - t_{\text{transformation}})}{t_{\text{transformation}} - t_{\text{plateau}}}$ for pits. This factor equals 1 for a flat patch, 2 for a completed dome (half sphere) and 4 for a completed pit (full sphere).

6.3.12 Curvature acquisition during growth: Flat-to-curved transition corroborates with the change of clathrin/AP2 ratio

Here, the only thing that changes compared to the updated model is that the transition time $t_{\text{transformation}}$ is now given by the time when the AP2 intensity plateaus, which we calculated by fitting eq. 1 to the AP2 FM intensity tracks. We use eq. 1 for the AP2 tracks as they show a clear plateau phase, which is reached prior to the onset of coat curvature. Therefore, the growth of the AP2 patch is limited and eq. 1 is a simple representation of such a situation. This assumption is supported by the experimental finding that AP2 is highly dynamic throughout the coat. Indeed FRAP experiments have demonstrated the high recovery rate of AP2 within CCSs (data not shown and (Wu *et al.*, 2003)).

6.3.13 Live cell FM analysis resampling

To determine the ratio of clathrin and AP2 during the process of CME, we performed TIRF microscopy of BSC-1 AP2-eGFP cells transiently expressing CLCa-tdtomato. We analysed the excess of clathrin in comparison with AP2 during the formation of CCVs. Therefore, we calculated the ratio of the maximum clathrin intensity divided by the intensity of clathrin at the

time when AP2 shows an intensity plateau (95 % intensity level) and subtract this ratio from the ratio, which we get for AP2.

In detail: we set a threshold for the AP2 intensity underneath fluorescence intensity tracks are excluded (as before). We calculate the plateau time, defined as the time when 95 % of the AP2 plateau intensity is reached by fitting the constant area model to the AP2 FM data. Additionally, we normalise all intensity values to the intensity value when 95 % of the AP2 intensity (clathrin intensity) is reached. For each track (in total 754 tracks of one single cell) we calculate the difference of the time when AP2 plateaus and clathrin reach the maximum intensity and determine the corresponding histogram (cf. Fig. 4.16b). Furthermore, we calculate the intensity offset given by the normalised maximum clathrin intensity divided by the normalised maximum AP2 intensity (cf. Fig. 4.16c).

6.3.14 Calculation of the ratio histogram during the osmotic shock

To determine the ratio histogram of flat, dome and pit CCS during the osmotic shock (Fig. 4.18a and 4.18c) we first defined a transition time $t_{\text{transformation}}$, when flat CCSs start to invaginate, where the normalised clathrin intensity exceeds the normalised AP2 intensity by 5 % (blue region in Fig. 4.17c). We assumed that the transformation process from flat to dome takes the first 40 % of the remaining time until the vesicle pinches of the PM, given by t_{decrease} (red region in Fig. 4.17c) whereas from dome to pit it takes the remaining 60 % of time (green region in Fig. 4.17c). Next, we started 50 s after the osmotic shock and determined the morphology of all tracks present at that time depending on the description above. We repeated this procedure in steps of 5 seconds and average the number of structures over time intervals of 100 seconds. In total we used 1356 FM tracks of one cell. The found ratios of flat, dome and pit CCSs were then plotted as a function of the time after the osmotic shock (Fig. 4.18a).

To test the consistency of this approach we used it to calculate the ratios for flat, dome and pit structures on the data without osmotic shock consisting of 4927 FM tracks of 4 different cells. Averaging over all tracks and considering only tracks with lifetimes shorter than 90 s and with AP2/clathrin discrepancy we obtained 47.8 % flat CCSs, 18.0 % dome CCSs and 34.2 % pit CCSs which is very similar to the determined ratios in Fig. 4.16g.

6.3.15 Quantification of agreement between measured and predicted size histograms

To determine the level of agreement between measured (Fig. 4.14h) and predicted size histograms (Fig. 4.14c and f, Fig. 4.16e) we calculated chi-squared $\chi_j^2 = \sum_{i=1}^k \frac{(N_{ij} - np_{ij})^2}{np_{ij}}$ where we

sum over all bins k the occurrences N_i of measured CCSs and compared it with the number of expected occurrences np_i , where p_i is the predicted normalised frequency per bin, which we deduced from our models (CAM=constant are model, UM=updated model and AP2=transition flat/dome determined by the time when the AP2 intensity plateaus) and $n = \sum N_i$. We repeated this for all CCSs $j = \{flat, dome, pit\}$ such that we found three values for χ_j^2 for each model and cell. We averaged these values for all CCSs and four cells and found: $\chi_{CAM}^2 = 1018$, $\chi_{UM}^2 = 649$ and $\chi_{AP2}^2 = 632$ which shows that the model plotted in Fig. 4.16e describes the data best.

Additionally, we performed a Welch's t-test to calculate p-values for the null hypothesis that the measured and predicted size distributions of CCSs have identical mean values. We averaged over all CCSs and four cells and found $p_{CAM} = 0.60$, $p_{UM} = 0.75$ and $p_{AP2} = 0.78$.

7 References

- Abbe, E. (1873) 'Beiträge zur Theorie des Mikroskops und der mikroskopischen Wahrnehmung', *Archiv für mikroskopische Anatomie*, 9(1), pp. 413–418.
- Abedin, M. and King, N. (2010) 'Diverse evolutionary paths to cell adhesion', *Trends in cell biology*, 20(12), pp. 734–742.
- Aguet, F., Antonescu, C. N., Mettlen, M., Schmid, S. L. and Danuser, G. (2013) 'Advances in Analysis of Low Signal-to-Noise Images Link Dynamin and AP2 to the Functions of an Endocytic Checkpoint', *Developmental Cell*, 26(3), pp. 279–291.
- Aguet, F., Upadhyayula, S., Gaudin, R., Chou, Y., Cocucci, E., He, K., Chen, B.-C., Mosaliganti, K., Pasham, M., Skillern, W., Legant, W. R., Liu, T.-L., Findlay, G., Marino, E., Danuser, G., Megason, S., Betzig, E. and Kirchhausen, T. (2016) 'Membrane dynamics of dividing cells imaged by lattice light-sheet microscopy', *Molecular Biology of the Cell*, 27(22), pp. 3418–3435.
- Ahmed, M. and French-Constant, C. (2016) 'Extracellular Matrix Regulation of Stem Cell Behavior', *Current Stem Cell Reports*, 2(3), pp. 197–206.
- Alexandrova, A. Y., Arnold, K., Schaub, S., Vasiliev, J. M., Meister, J.-J., Bershadsky, A. D. and Verkhovsky, A. B. (2008) 'Comparative Dynamics of Retrograde Actin Flow and Focal Adhesions: Formation of Nascent Adhesions Triggers Transition from Fast to Slow Flow', *PLOS ONE*, 3(9), p. e3234.
- Amaddii, M., Meister, M., Banning, A., Tomasovic, A., Mooz, J., Rajalingam, K. and Tikkanen, R. (2012) 'Flotillin-1/Reggie-2 Protein Plays Dual Role in Activation of Receptor-tyrosine Kinase/Mitogen-activated Protein Kinase Signaling', *Journal of Biological Chemistry*, 287(10), pp. 7265–7278.
- Amatangelo, M. D., Bassi, D. E., Klein-Szanto, A. J. P. and Cukierman, E. (2005) 'Stroma-Derived Three-Dimensional Matrices Are Necessary and Sufficient to Promote Desmoplastic Differentiation of Normal Fibroblasts', *The American Journal of Pathology*, 167(2), pp. 475–488.
- Antonescu, C. N., Aguet, F., Danuser, G. and Schmid, S. L. (2011) 'Phosphatidylinositol-(4,5)-bisphosphate regulates clathrin-coated pit initiation, stabilization, and size', *Molecular Biology of the Cell*, 22(14), pp. 2588–2600.
- Antonescu, C. N., McGraw, T. E. and Klip, A. (2014) 'Reciprocal Regulation of Endocytosis and Metabolism', *Cold Spring Harbor Perspectives in Biology*, 6(7), p. a016964.
- Apte, S. S. (2009) 'A Disintegrin-like and Metalloprotease (Reprolysin-type) with Thrombospondin Type 1 Motif (ADAMTS) Superfamily: Functions and Mechanisms', *The Journal of Biological Chemistry*, 284(46), pp. 31493–31497.
- Aragona, M., Panciera, T., Manfrin, A., Giulitti, S., Michielin, F., Elvassore, N., Dupont, S. and Piccolo, S. (2013) 'A Mechanical Checkpoint Controls Multicellular Growth through YAP/TAZ Regulation by Actin-Processing Factors', *Cell*, 154(5), pp. 1047–1059.
- Artym, V. V., Yamada, K. M. and Mueller, S. C. (2009) 'ECM Degradation Assays for Analyzing Local Cell Invasion', in Even-Ram, S. and Artym, V. (eds) *Extracellular Matrix Protocols: Second Edition*. Totowa, NJ: Humana Press, pp. 211–219.
-

-
- Avinoam, O., Schorb, M., Beese, C. J., Briggs, J. A. G. and Kaksonen, M. (2015) 'Endocytic sites mature by continuous bending and remodeling of the clathrin coat', *Science*, 348(6241), p. 1369 LP-1372.
- Baker, A. H., Edwards, D. R. and Murphy, G. (2002) 'Metalloproteinase inhibitors: biological actions and therapeutic opportunities', *Journal of Cell Science*, 115(19), p. 3719 LP-3727.
- Baneyx, G., Baugh, L. and Vogel, V. (2002) 'Fibronectin extension and unfolding within cell matrix fibrils controlled by cytoskeletal tension', *Proceedings of the National Academy of Sciences*, 99(8), pp. 5139–5143.
- Barczyk, M., Carracedo, S. and Gullberg, D. (2010) 'Integrins', *Cell and Tissue Research*, 339(1), pp. 269–280.
- Basquin, C., Trichet, M., Vihinen, H., Malardé, V., Lagache, T., Ripoll, L., Jokitalo, E., Olivo-Marin, J., Gautreau, A. and Sauvonnnet, N. (2015) 'Membrane protrusion powers clathrin-independent endocytosis of interleukin-2 receptor', *The EMBO Journal*, 34(16), p. 2147 LP-2161.
- Batchelder, E. M. and Yarar, D. (2010) 'Differential Requirements for Clathrin-dependent Endocytosis at Sites of Cell–Substrate Adhesion', *Molecular Biology of the Cell*, 21(17), pp. 3070–3079.
- Baumgart, T., Capraro, B. R., Zhu, C. and Das, S. L. (2011) 'Thermodynamics and Mechanics of Membrane Curvature Generation and Sensing by Proteins and Lipids', *Annual review of physical chemistry*, 62, pp. 483–506.
- Bitoun, M., Maugenre, S., Jeannet, P.-Y., Lacène, E., Ferrer, X., Laforêt, P., Martin, J.-J., Laporte, J., Lochmüller, H., Beggs, A. H., Fardeau, M., Eymard, B., Romero, N. B. and Guicheney, P. (2005) 'Mutations in dynamin 2 cause dominant centronuclear myopathy', *Nature Genetics*, 37(11), pp. 1207–9.
- Bitsikas, V., Corrêa, I. R. and Nichols, B. J. (2014) 'Clathrin-independent pathways do not contribute significantly to endocytic flux', *eLife*, 3, p. e03970.
- Boettiger, D., Lynch, L., Blystone, S. and Huber, F. (2001) 'Distinct Ligand-binding Modes for Integrin $\alpha\beta3$ -Mediated Adhesion to Fibronectin versus Vitronectin', *Journal of Biological Chemistry*, 276(34), pp. 31684–31690.
- Böhm, J., Biancalana, V., DeChene, E. T., Bitoun, M., Pierson, C. R., Schaefer, E., Karasoy, H., Dempsey, M. A., Klein, F., Dondaine, N., Kretz, C., Haumesser, N., Poirson, C., Toussaint, A., Greenleaf, R. S., Barger, M. A., Mahoney, L. J., Kang, P. B., Zanoteli, E., Vissing, J., Witting, N., Echaniz-Laguna, A., Wallgren-Pettersson, C., Dowling, J., Merlini, L., Oldfors, A., Ousager, L. B., Melki, J., Krause, A., Jern, C., Oliveira, A. S. B., Petit, F., Jacqueline, A., Chaussonot, A., Mowat, D., Leheup, B., Cristofano, M., Aldea, J. J. P., Michel, F., Furby, A., Llona, J. E. B., Van Coster, R., Bertini, E., Urtizberea, J. A., Drouin-Garraud, V., Béroud, C., Prudhon, B., Bedford, M., Mathews, K., Erby, L. A. H., Smith, S. A., Roggenbuck, J., Crowe, C. A., Spitale, A. B., Johal, S. C., Amato, A. A., Demmer, L. A., Jonas, J., Darras, B. T., Bird, T. D., Laurino, M., Welt, S. I., Trotter, C., Guicheney, P., Das, S., Mandel, J.-L., Beggs, A. H. and Laporte, J. (2012) 'Mutation Spectrum in the Large GTPase Dynamin 2, and Genotype–Phenotype Correlation in Autosomal Dominant Centronuclear Myopathy', *Human mutation*, 33(6), pp. 949–959.
- Bonifacino, J. S. and Rojas, R. (2006) 'Retrograde transport from endosomes to the trans-Golgi network', *Nature Reviews Molecular Cell Biology*, 7(8), pp. 568–79.
- Bonnans, C., Chou, J. and Werb, Z. (2014) 'Remodelling the extracellular matrix in development and disease', *Nature reviews. Molecular cell biology*, 15(12), pp. 786–801.
-

-
- Booth, D. G., Hood, F. E., Prior, I. A. and Royle, S. J. (2011) 'A TACC3/ch-TOG/clathrin complex stabilises kinetochore fibres by inter-microtubule bridging', *The EMBO Journal*, 30(5), p. 906 LP-919.
- Boucrot, E., Ferreira, A. P. A., Almeida-Souza, L., Debard, S., Vallis, Y., Howard, G., Bertot, L., Sauvonnnet, N. and McMahon, H. T. (2014) 'Endophilin marks and controls a clathrin-independent endocytic pathway', *Nature*, 517(7535), pp. 460–5.
- Boucrot, E., Pick, A., Çamdere, G., Liska, N., Evergren, E., McMahon, H. T. and Kozlov, M. M. (2012) 'Membrane Fission Is Promoted by Insertion of Amphipathic Helices and Is Restricted by Crescent BAR Domains', *Cell*, 149(1), pp. 124–136.
- Boucrot, E., Saffarian, S., Massol, R., Kirchhausen, T. and Ehrlich, M. (2006) 'Role of lipids and actin in the formation of clathrin-coated pits.', *Experimental cell research*, 312(20), pp. 4036–48.
- Boulant, S., Kural, C., Zeeh, J.-C., Ubelmann, F. and Kirchhausen, T. (2011) 'Actin dynamics counteract membrane tension during clathrin-mediated endocytosis', *Nat Cell Biol*, 13(9), pp. 1124–1131.
- Brakebusch, C. and Fässler, R. (2005) 'β 1 integrin function in vivo: Adhesion, migration and more', *Cancer and Metastasis Reviews*, 24(3), pp. 403–411.
- Brown, M. C. and Turner, C. E. (2004) 'Paxillin: Adapting to Change', *Physiological Reviews*, 84(4), pp. 1315–1339.
- Bucher, D., Frey, F., Sochacki, K. A., Kummer, S., Bergeest, J.-P., Godinez, W. J., Kräusslich, H.-G., Rohr, K., Taraska, J. W., Schwarz, U. S. and Boulant, S. (2018) 'Clathrin-adaptor ratio and membrane tension regulate the flat-to-curved transition of the clathrin coat during endocytosis', *Nature communications*, [accepted].
- Butcher, D. T., Alliston, T. and Weaver, V. M. (2009) 'A tense situation: forcing tumour progression', *Nature reviews. Cancer*, 9(2), pp. 108–122.
- Calderwood, D. A., Fujioka, Y., de Pereda, J. M., García-Alvarez, B., Nakamoto, T., Margolis, B., McGlade, C. J., Liddington, R. C. and Ginsberg, M. H. (2003) 'Integrin β cytoplasmic domain interactions with phosphotyrosine-binding domains: A structural prototype for diversity in integrin signaling', *Proceedings of the National Academy of Sciences of the United States of America*, 100(5), pp. 2272–2277.
- Campbell, I. D. and Ginsberg, M. H. (2004) 'The talin-tail interaction places integrin activation on FERM ground', *Trends in Biochemical Sciences*, 29(8), pp. 429–435.
- Case, L. and Waterman-Storer, C. (2015) 'Integration of actin dynamics and cell adhesion by a three-dimensional, mechanosensitive molecular clutch', *Nature cell biology*, 17(8), pp. 955–963.
- Caswell, P. T., Vadrevu, S. and Norman, J. C. (2009) 'Integrins: masters and slaves of endocytic transport', *Nature Reviews Molecular Cell Biology*, 10(12), p. 843.
- Cavallaro, U. and Dejana, E. (2011) 'Adhesion molecule signalling: not always a sticky business', *Nature Reviews Molecular Cell Biology*. Nature Publishing Group, a division of Macmillan Publishers Limited. All Rights Reserved., 12(3), pp. 189–97.
- Chang-Ileto, B., Frere, S. G., Chan, R. B., Voronov, S. V., Roux, A. and Di Paolo, G. (2011) 'Synaptojanin 1-Mediated PI(4,5)P₂ Hydrolysis Is Modulated by Membrane Curvature and Facilitates Membrane Fission', *Developmental Cell*, 20(2), pp. 206–218.
-

Chao, W.-T. and Kunz, J. (2009) 'Focal adhesion disassembly requires clathrin-dependent endocytosis of integrins', *FEBS letters*, 583(8), pp. 1337–1343.

Charras, G. and Sahai, E. (2014) 'Physical influences of the extracellular environment on cell migration', *Nature Reviews Molecular Cell Biology*, 15(12), pp. 813–24.

Chazotte, B. (2011) 'Labeling Membrane Glycoproteins or Glycolipids with Fluorescent Wheat Germ Agglutinin', *Cold Spring Harbor Protocols*, 2011(5), p. pdb.prot5623.

Chen, C.-Y. and Brodsky, F. M. (2005) 'Huntingtin-interacting Protein 1 (Hip1) and Hip1-related Protein (Hip1R) Bind the Conserved Sequence of Clathrin Light Chains and Thereby Influence Clathrin Assembly in Vitro and Actin Distribution in Vivo', *Journal of Biological Chemistry*, 280(7), pp. 6109–6117.

Chen, C.-Y., Reese, M. L., Hwang, P. K., Ota, N., Agard, D. and Brodsky, F. M. (2002) 'Clathrin light and heavy chain interface: α -helix binding superhelix loops via critical tryptophans', *The EMBO Journal*. Oxford, UK, 21(22), pp. 6072–6082.

Chen, P., Bendris, N., Hsiao, Y., Chen, H., Yu, S., Schmid, S. L., Chen, P., Bendris, N., Hsiao, Y., Reis, C. R., Mettlen, M., Chen, H. and Yu, S. (2017) 'Crosstalk between CLCb / Dyn1-Mediated Adaptive Clathrin-Mediated Endocytosis and Epidermal Growth Factor Receptor Signaling Increases Article Crosstalk between CLCb / Dyn1-Mediated Adaptive Clathrin-Mediated Endocytosis and Epidermal Growth Factor Recept', *Developmental Cell*, 40(3), p. 278–288.e5.

Cheng, J. P. X. and Nichols, B. J. (2016) 'Caveolae: One Function or Many?', *Trends in Cell Biology*, 26(3), pp. 177–189.

Cheresh, D. A., Smith, J. W., Cooper, H. M. and Quaranta, V. (1989) 'A novel vitronectin receptor integrin ($\alpha v \beta 3$) is responsible for distinct adhesive properties of carcinoma cells', *Cell*, 57(1), pp. 59–69.

Chetrit, D., Ziv, N. and Ehrlich, M. (2009) 'Dab2 regulates clathrin assembly and cell spreading', *Biochemical Journal*, 418(3), p. 701 LP-715.

Choi, C. K., Vicente-Manzanares, M., Zareno, J., Whitmore, L. A., Mogilner, A. and Horwitz, A. R. (2008) 'Actin and α -actinin orchestrate the assembly and maturation of nascent adhesions in a myosin II motor-independent manner', *Nature Cell Biology*, 10(9), pp. 1039–50.

Clark, P., Connolly, P., Curtis, A. S., Dow, J. A. and Wilkinson, C. D. (1990) 'Topographical control of cell behaviour: II. Multiple grooved substrata', *Development*, 108(4), p. 635 LP-644.

Clark, P., Connolly, P., Curtis, A. S., Dow, J. A. and Wilkinson, C. D. (1991) 'Cell guidance by ultrafine topography in vitro', *Journal of Cell Science*, 99(1), p. 73 LP-77.

Cocucci, E., Gaudin, R. and Kirchhausen, T. (2014) 'Dynamain recruitment and membrane scission at the neck of a clathrin-coated pit', *Molecular Biology of the Cell*, 25(22), pp. 3595–3609.

Collawn, J. F., Stangel, M., Kuhn, L. A., Esekogwu, V., Jing, S., Trowbridge, I. S. and Tainer, J. A. (1990) 'Transferrin receptor internalization sequence YXRF implicates a tight turn as the structural recognition motif for endocytosis', *Cell*, 63(5), pp. 1061–1072.

Collins, B. M., McCoy, A. J., Kent, H. M., Evans, P. R. and Owen, D. J. (2002) 'Molecular Architecture and Functional Model of the Endocytic AP2 Complex', *Cell*, 109(4), pp. 523–535.

-
- Conner, S. D. and Schmid, S. L. (2002) 'Identification of an adaptor-associated kinase, AAK1, as a regulator of clathrin-mediated endocytosis', *The Journal of Cell Biology*, 156(5), pp. 921–929.
- Conner, S. D. and Schmid, S. L. (2005) 'CVAK104 Is a Novel Poly-L-lysine-stimulated Kinase That Targets the β 2-Subunit of AP2', *Journal of Biological Chemistry*, 280(22), pp. 21539–21544.
- Critchley, D. R. (2009) 'Biochemical and Structural Properties of the Integrin-Associated Cytoskeletal Protein Talin', *Annual Review of Biophysics*, 38(1), pp. 235–254.
- Cruz-Munoz, W. and Khokha, R. (2008) 'The Role of Tissue Inhibitors of Metalloproteinases in Tumorigenesis and Metastasis', *Critical Reviews in Clinical Laboratory Sciences*, 45(3), pp. 291–338.
- Cureton, D. K., Massol, R. H., Whelan, S. P. J. and Kirchhausen, T. (2010) 'The Length of Vesicular Stomatitis Virus Particles Dictates a Need for Actin Assembly during Clathrin-Dependent Endocytosis', *PLoS Pathogens*, 6(9), p. e1001127.
- Dahlmann-Noor, A. H., Martin-Martin, B., Eastwood, M., Khaw, P. T. and Bailly, M. (2007) 'Dynamic protrusive cell behaviour generates force and drives early matrix contraction by fibroblasts', *Experimental Cell Research*, 313(20), pp. 4158–4169.
- Dannhauser, P. N., Camus, S. M., Sakamoto, K., Sadacca, L. A., Torres, J. A., Camus, M. D., Briant, K., Vassilopoulos, S., Rothnie, A., Smith, C. J. and Brodsky, F. M. (2017) 'CHC22 and CHC17 clathrins have distinct biochemical properties and display differential regulation and function', *Journal of Biological Chemistry*, 292(51), pp. 20834–20844.
- Daumke, O., Roux, A. and Haucke, V. (2014) 'BAR Domain Scaffolds in Dynamin-Mediated Membrane Fission', *Cell*, 156(5), pp. 882–892.
- Dechantsreiter, M. A., Planker, E., Mathä, B., Lohof, E., Hölzemann, G., Jonczyk, A., Goodman, S. L. and Kessler, H. (1999) 'N-Methylated Cyclic RGD Peptides as Highly Active and Selective α V β 3 Integrin Antagonists', *Journal of Medicinal Chemistry*, 42(16), pp. 3033–3040.
- De Deyne, P. G., O'Neill, A., Resneck, W. G., Dmytrenko, G. M., Pumplin, D. W. and Bloch, R. J. (1998) 'The vitronectin receptor associates with clathrin-coated membrane domains via the cytoplasmic domain of its beta5 subunit', *Journal of Cell Science*, 111(18), p. 2729 LP-2740.
- Doherty, G. J. and McMahon, H. T. (2009) 'Mechanisms of Endocytosis', *Annual Review of Biochemistry*, 78(1), pp. 857–902.
- Doyon, J. B., Zeitler, B., Cheng, J., Cheng, A. T., Cherone, J. M., Santiago, Y., Lee, A. H., Vo, T. D., Doyon, Y., Miller, J. C., Paschon, D. E., Zhang, L., Rebar, E. J., Gregory, P. D., Urnov, F. D. and Drubin, D. G. (2011) 'Rapid and efficient clathrin-mediated endocytosis revealed in genome-edited mammalian cells', *Nature cell biology*, 13(3), pp. 331–337.
- Dubash, A. D., Menold, M. M., Samson, T., Boulter, E., García-Mata, R., Doughman, R. and Burridge, K. B. T.-I. R. of C. and M. B. (2009) 'Chapter 1 Focal Adhesions: New Angles on an Old Structure', in *International Review of Cell and Molecular Biology*. Academic Press, pp. 1–65.
- Dupont, S., Morsut, L., Aragona, M., Enzo, E., Giulitti, S., Cordenonsi, M., Zanconato, F., Le Digabel, J., Forcato, M., Bicciato, S., Elvassore, N. and Piccolo, S. (2011) 'Role of YAP/TAZ in mechanotransduction', *Nature*, 474(7350), pp.
-

179–83.

Ehrlich, M., Boll, W., Van Oijen, A., Hariharan, R., Chandran, K., Nibert, M. L. and Kirchhausen, T. (2004) 'Endocytosis by random initiation and stabilization of clathrin-coated pits', *Cell*, 118(5), pp. 591–605.

Ehrlicher, A. J., Nakamura, F., Hartwig, J. H., Weitz, D. A. and Stossel, T. P. (2011) 'Mechanical strain in actin networks regulates FilGAP and integrin binding to Filamin A', *Nature*, 478(7368), pp. 260–263.

Eichel, K., Jullié, D. and von Zastrow, M. (2016) 'β-arrestin drives MAP kinase signaling from clathrin-coated structures after GPCR dissociation', *Nature cell biology*, 18(3), pp. 303–310.

Elkhatib, N., Bresteau, E., Baschieri, F., Rioja, A. L., van Niel, G., Vassilopoulos, S. and Montagnac, G. (2017) 'Tubular clathrin/AP-2 lattices pinch collagen fibers to support 3D cell migration', *Science*, 356(6343), p. eaal4713.

Engler, A. J., Sen, S., Sweeney, H. L. and Discher, D. E. (2006) 'Matrix Elasticity Directs Stem Cell Lineage Specification', *Cell*, 126(4), pp. 677–689.

Erdmann, K. S., Mao, Y., McCrea, H. J., Zoncu, R., Lee, S., Paradise, S., Modregger, J., Biemesderfer, D., Toomre, D. and De Camilli, P. (2007) 'A role of the Lowe syndrome protein OCRL in early steps of the endocytic pathway', *Developmental cell*, 13(3), pp. 377–390.

Erdogan, B., Ao, M., White, L. M., Means, A. L., Brewer, B. M., Yang, L., Washington, M. K., Shi, C., Franco, O. E., Weaver, A. M., Hayward, S. W., Li, D. and Webb, D. J. (2017) 'Cancer-associated fibroblasts promote directional cancer cell migration by aligning fibronectin', *The Journal of Cell Biology*, 216(11), p. 3799 LP-3816.

Ezratty, E. J., Bertaux, C., Marcantonio, E. E. and Gunderson, G. G. (2009) 'Clathrin mediates integrin endocytosis for focal adhesion disassembly in migrating cells', *The Journal of Cell Biology*, 187(5), pp. 733–747.

Ferguson, J. P., Willy, N. M., Heidotting, S. P., Huber, S. D., Webber, M. J. and Kural, C. (2016) 'Deciphering dynamics of clathrin-mediated endocytosis in a living organism', *The Journal of Cell Biology*, 214(3), p. 347 LP-358.

Ferguson, S. M. and De Camilli, P. (2012) 'Dynamin, a membrane-remodelling GTPase', *Nat Rev Mol Cell Biol*, 13(2), pp. 75–88.

Ferguson, S. M., Raimondi, A., Paradise, S., Shen, H., Mesaki, K., Ferguson, A., Destaing, O., Ko, G., Takasaki, J., Cremona, O., O' Toole, E. and De Camilli, P. (2009) 'Coordinated actions of actin and BAR proteins upstream of dynamin at endocytic clathrin-coated pits', *Developmental cell*, 17(6), pp. 811–822.

Ferreira, A. P. A. and Boucrot, E. (2017) 'Mechanisms of Carrier Formation during Clathrin-Independent Endocytosis', *Trends in Cell Biology*.

Ferreira, F., Foley, M., Cooke, A., Cunningham, M., Smith, G., Woolley, R., Henderson, G., Kelly, E., Mundell, S. and Smythe, E. (2012) 'Endocytosis of G Protein-Coupled Receptors Is Regulated by Clathrin Light Chain Phosphorylation', *Current Biology*, 22(15), pp. 1361–1370.

Feutlinske, F., Browarski, M., Ku, M.-C., Trnka, P., Waiczies, S., Niendorf, T., Stallcup, W. B., Glass, R., Krause, E. and Maritzen, T. (2015) 'Stonin1 mediates endocytosis of the proteoglycan NG2 and regulates focal adhesion dynamics and cell motility', *Nature Communications*, 6, p. 8535.

Flores-Otero, J., Ahn, K. H., Delgado-Peraza, F., Mackie, K., Kendall, D. A. and Yudowski, G. A. (2014) 'Ligand-specific endocytic dwell times control functional selectivity of the cannabinoid receptor 1', *Nature Communications*, 5,

p. 4589.

Ford, M. G. J., Mills, I. G., Peter, B. J., Vallis, Y., Praefcke, G. J. K., Evans, P. R. and McMahon, H. T. (2002) 'Curvature of clathrin-coated pits driven by epsin', *Nature*, 419(6905), pp. 361–6.

Fotin, A., Cheng, Y., Sliz, P., Grigorieff, N., Harrison, S. C., Kirchhausen, T. and Walz, T. (2004) 'Molecular model for a complete clathrin lattice from electron cryomicroscopy', *Nature*. Macmillan Magazines Ltd., 432, p. 573.

De Franceschi, N., Arjonen, A., Elkhatib, N., Denessiouk, K., Wrobel, A. G., Wilson, T. A., Pouwels, J., Montagnac, G., Owen, D. J. and Ivaska, J. (2016) 'Selective integrin endocytosis is driven by interactions between the integrin α -chain and AP2', *Nature Structural Molecular Biology*. Nature Publishing Group, a division of Macmillan Publishers Limited. All Rights Reserved., 23(2), pp. 172–9.

Frantz, C., Stewart, K. M. and Weaver, V. M. (2010) 'The extracellular matrix at a glance', *Journal of Cell Science*, 123(24), p. 4195 LP-4200.

Freed, E., Gailit, J., van der Geer, P., Ruoslahti, E. and Hunter, T. (1989) 'A novel integrin beta subunit is associated with the vitronectin receptor alpha subunit (alpha v) in a human osteosarcoma cell line and is a substrate for protein kinase C.', *The EMBO Journal*, 8(10), pp. 2955–2965.

Freeman, S. A. and Grinstein, S. (2014) 'Phagocytosis: receptors, signal integration, and the cytoskeleton', *Immunological Reviews*, 262(1), pp. 193–215.

Fujimoto, L. M., Roth, R., Heuser, J. E. and Schmid, S. L. (2000) 'Actin Assembly Plays a Variable, but not Obligatory Role in Receptor-Mediated Endocytosis', *Traffic*, 1(2), pp. 161–171.

Gaidarov, I., Santini, F., Warren, R. A. and Keen, J. H. (1999) 'Spatial control of coated-pit dynamics in living cells', *Nature Cell Biology*, 1(1), pp. 1–7.

Galic, M., Jeong, S., Tsai, F.-C., Joubert, L.-M., Wu, Y. I., Hahn, K. M., Cui, Y. and Meyer, T. (2012) 'External push and internal pull forces recruit curvature sensing N-BAR domain proteins to the plasma membrane', *Nature cell biology*, 14(8), pp. 874–881.

Gallop, J. L., Jao, C. C., Kent, H. M., Butler, P. J. G., Evans, P. R., Langen, R. and McMahon, H. T. (2006) 'Mechanism of endophilin N-BAR domain-mediated membrane curvature', *The EMBO Journal*, 25(12), p. 2898 LP-2910.

Garay, C., Judge, G., Lucarelli, S., Bautista, S., Pandey, R., Singh, T. and Antonescu, C. N. (2015) 'Epidermal growth factor-stimulated Akt phosphorylation requires clathrin or ErbB2 but not receptor endocytosis', *Molecular Biology of the Cell*, 26(19), pp. 3504–3519.

García, A. J., Schwarzbauer, J. E. and Boettiger, D. (2002) 'Distinct Activation States of $\alpha 5 \beta 1$ Integrin Show Differential Binding to RGD and Synergy Domains of Fibronectin', *Biochemistry*, 41(29), pp. 9063–9069.

Gasiorowski, J. Z., Murphy, C. J. and Nealey, P. F. (2013) 'Biophysical Cues and Cell Behavior: The Big Impact of Little Things', *Annual Review of Biomedical Engineering*, 15(1), pp. 155–176.

Geiger, B., Spatz, J. P. and Bershadsky, A. D. (2009) 'Environmental sensing through focal adhesions', *Nature Reviews Molecular Cell Biology*, 10(1), pp. 21–33.

Geiger, B. and Yamada, K. M. (2011) 'Molecular Architecture and Function of Matrix Adhesions', *Cold Spring Harbor*

Perspectives in Biology, 3(5), p. a005033. doi: 10.1101/cshperspect.a005033.

Gerecht, S., Bettinger, C. J., Zhang, Z., Borenstein, J., Vunjak-Novakovic, G. and Langer, R. (2007) 'The effect of actin disrupting agents on contact guidance of human embryonic stem cells', *Biomaterials*, 28(28), pp. 4068–4077.

Glebov, O. O., Bright, N. A. and Nichols, B. J. (2005) 'Flotillin-1 defines a clathrin-independent endocytic pathway in mammalian cells', *Nature Cell Biology*, 8(1), pp. 46–54.

Godinez, W. J. and Rohr, K. (2015) 'Tracking Multiple Particles in Fluorescence Time-Lapse Microscopy Images via Probabilistic Data Association', *IEEE Trans Med Imaging*, 34(2), pp. 415–432.

Gordon, S. (2016) 'Phagocytosis: An Immunobiologic Process', *Immunity*, 44(3), pp. 463–475.

Greener, T., Zhao, X., Nojima, H., Eisenberg, E. and Greene, L. E. (2000) 'Role of Cyclin G-associated Kinase in Uncoating Clathrin-coated Vesicles from Non-neuronal Cells', *Journal of Biological Chemistry*, 275(2), pp. 1365–1370.

Grossier, J., Xouri, G., Goud, B. and Schauer, K. (2014) 'Cell adhesion defines the topology of endocytosis and signaling', *The EMBO Journal*, 33(1), p. 35 LP-45.

Grove, J., Metcalf, D. J., Knight, A. E., Wavre-Shapton, S. T., Sun, T., Protonotarios, E. D., Griffin, L. D., Lippincott-Schwartz, J. and Marsh, M. (2014) 'Flat clathrin lattices: stable features of the plasma membrane', *Molecular Biology of the Cell*, 25(22), pp. 3581–3594.

Guilluy, C., Swaminathan, V., Garcia-Mata, R., O'Brien, E. T., Superfine, R. and Burridge, K. (2011) 'The Rho GEFs LARG and GEF-H1 regulate the mechanical response to force on integrins', *Nature cell biology*, 13(6), pp. 722–727.

ter Haar, E., Harrison, S. C. and Kirchhausen, T. (2000) 'Peptide-in-groove interactions link target proteins to the β -propeller of clathrin', *Proceedings of the National Academy of Sciences of the United States of America*, 97(3), pp. 1096–1100.

ter Haar, E., Musacchio, A., Harrison, S. C. and Kirchhausen, T. (1998) 'Atomic Structure of Clathrin: A β Propeller Terminal Domain Joins an α Zigzag Linker', *Cell*, 95(4), pp. 563–573.

Hassinger, J. E., Oster, G., Drubin, D. G. and Rangamani, P. (2017) 'Design principles for robust vesiculation in clathrin-mediated endocytosis', *Proceedings of the National Academy of Sciences*, 114(7), pp. E1118–E1127.

Hayman, E. G., Pierschbacher, M. D., Suzuki, S. and Ruoslahti, E. (1985) 'Vitronectin—A major cell attachment-promoting protein in fetal bovine serum', *Experimental Cell Research*, 160(2), pp. 245–258.

Henne, W. M., Boucrot, E., Meinecke, M., Evergren, E., Vallis, Y., Mittal, R. and McMahon, H. T. (2010) 'FCHO Proteins are Nucleators of Clathrin-Mediated Endocytosis', *Science*, 328(5983), pp. 1281–1284.

Henne, W. M., Buchkovich, N. J. and Emr, S. D. (2011) 'The ESCRT Pathway', *Developmental Cell*, 21(1), pp. 77–91.

Henry, A. G., Hislop, J. N., Grove, J., Thorn, K., Marsh, M. and von Zastrow, M. (2012) 'Regulation of Endocytic Clathrin Dynamics by Cargo Ubiquitination', *Developmental Cell*, 23(3), pp. 519–532.

Heuser, J. (1980) 'Three-dimensional visualization of coated vesicle formation in fibroblasts.', *The Journal of Cell Biology*, 84(3), pp. 560–583.

-
- Heuser, J. (1989) 'Effects of cytoplasmic acidification on clathrin lattice morphology', *The Journal of Cell Biology*, 108(2), pp. 401–411.
- Heuser, J. E., Amende, L. M., Branch, E. and Diseases, K. (1987) 'Deep-Etch Visualization of 27S Clathrin: A Tetrahedral Tetramer', *The Journal of Cell Biology*, 105(5), pp. 1999–2009.
- Higgins, M. K. and McMahon, H. T. (2017) 'Snap-shots of clathrin-mediated endocytosis', *Trends in Biochemical Sciences*. Elsevier, 27(5), pp. 257–263. doi: 10.1016/S0968-0004(02)02089-3.
- Hirata, H., Tatsumi, H. and Sokabe, M. (2008) 'Mechanical forces facilitate actin polymerization at focal adhesions in a zyxin-dependent manner', *Journal of Cell Science*, 121(17), p. 2795 LP-2804.
- Hocking, D. C., Smith, R. K. and McKeown-Longo, P. J. (1996) 'A novel role for the integrin-binding III-10 module in fibronectin matrix assembly', *The Journal of Cell Biology*, 133(2), pp. 431–444.
- Hocking, D. C., Sottile, J. and McKeown-Longo, P. J. (1994) 'Fibronectin's III-1 module contains a conformation-dependent binding site for the amino-terminal region of fibronectin.', *Journal of Biological Chemistry*, 269(29), pp. 19183–19187.
- Hollopeter, G., Lange, J. J., Zhang, Y., Vu, T. N., Gu, M., Ailion, M., Lambie, E. J., Slaughter, B. D., Unruh, J. R., Florens, L. and Jorgensen, E. M. (2014) 'The membrane-associated proteins FCHO and SGIP are allosteric activators of the AP2 clathrin adaptor complex', *eLife*, 3, p. e03648.
- Holt, M. R., Critchley, D. R. and Brindle, N. P. J. (1998) 'Molecules in focus The focal adhesion phosphoprotein, VASP', *The International Journal of Biochemistry & Cell Biology*, 30(3), pp. 307–311.
- Höning, S., Ricotta, D., Krauss, M., Späte, K., Spolaore, B., Motley, A., Robinson, M., Robinson, C., Haucke, V. and Owen, D. J. (2005) 'Phosphatidylinositol-(4,5)-Bisphosphate Regulates Sorting Signal Recognition by the Clathrin-Associated Adaptor Complex AP2', *Molecular Cell*, 18(5), pp. 519–531.
- Horton, E. R., Humphries, J. D., James, J., Jones, M. C., Askari, J. A. and Humphries, M. J. (2016) 'The integrin adhesome network at a glance', *Journal of Cell Science*, 129(22), pp. 4159–4163.
- Horwitz, A. R. (2012) 'The origins of the molecular era of adhesion research', *Nature Reviews Molecular Cell Biology*, 13(12), pp. 805–11.
- Huang, B., Bates, M. and Zhuang, X. (2009) 'Super resolution fluorescence microscopy', *Annual review of biochemistry*, 78, pp. 993–1016.
- Huang, B., Wang, W., Bates, M. and Zhuang, X. (2008) 'Three-dimensional Super-resolution Imaging by Stochastic Optical Reconstruction Microscopy', *Science*, 319(5864), pp. 810–813.
- Huang, F., Khvorova, A., Marshall, W. and Sorkin, A. (2004) 'Analysis of Clathrin-mediated Endocytosis of Epidermal Growth Factor Receptor by RNA Interference', *Journal of Biological Chemistry*, 279(16), pp. 16657–16661.
- Hulmes, D. J. S. (2002) 'Building Collagen Molecules, Fibrils, and Suprafibrillar Structures', *Journal of Structural Biology*, 137(1), pp. 2–10.
- Humphrey, J. D., Dufresne, E. R. and Schwartz, M. A. (2014) 'Mechanotransduction and extracellular matrix homeostasis', *Nature reviews. Molecular cell biology*, 15(12), pp. 802–812.
- Humphries, J. D., Byron, A. and Humphries, M. J. (2006) 'Integrin ligands at a glance', *Journal of Cell Science*,
-

119(19), p. 3901 LP-3903.

Hurley, J. H. and Hanson, P. I. (2010) 'Membrane budding and scission by the ESCRT machinery: it's all in the neck', *Nature reviews. Molecular cell biology*, 11(8), pp. 556–566.

Hyman, T., Shmuel, M. and Altschuler, Y. (2006) 'Actin Is Required for Endocytosis at the Apical Surface of Madin-Darby Canine Kidney Cells where ARF6 and Clathrin Regulate the Actin Cytoskeleton', *Molecular Biology of the Cell*, 17(1), pp. 427–437.

Hynes, R. O. (2002) 'Integrins', *Cell*, 110(6), pp. 673–687.

Hynes, R. O. and Naba, A. (2012) 'Overview of the Matrisome—An Inventory of Extracellular Matrix Constituents and Functions', *Cold Spring Harbor Perspectives in Biology*, 4(1), p. a004903.

Ibarguren, M., López, D. J. and Escribá, P. V (2014) 'The effect of natural and synthetic fatty acids on membrane structure, microdomain organization, cellular functions and human health', *Biochimica et Biophysica Acta (BBA) - Biomembranes*, 1838(6), pp. 1518–1528.

Ilić, D., Kovačić, B., Johkura, K., Schlaepfer, D. D., Tomašević, N., Han, Q., Kim, J.-B., Howerton, K., Baumbusch, C., Ogiwara, N., Strelow, D. N., Nelson, J. A., Dazin, P., Shino, Y., Sasaki, K. and Damsky, C. H. (2004) 'FAK promotes organization of fibronectin matrix and fibrillar adhesions', *Journal of Cell Science*, 117(2), p. 177 LP-187.

Irajzad, E., Walani, N., Veatch, S. L., Liu, A. P. and Agrawal, A. (2017) 'Clathrin polymerization exhibits high mechano-geometric sensitivity', *Soft Matter*, 13(7), pp. 1455–1462.

Isermann, P. and Lammerding, J. (2013) 'Nuclear Mechanics and Mechanotransduction in Health and Disease', *Current Biology*, 23(24), pp. R1113-1121.

Iskratsch, T., Wolfenson, H. and Sheetz, M. P. (2014) 'Appreciating force and shape — the rise of mechanotransduction in cell biology', *Nature Reviews Molecular Cell Biology*, 15(12), pp. 825–33.

Itoh, Y. (2006) 'MT1-MMP: A key regulator of cell migration in tissue', *IUBMB Life*, 58(10), pp. 589–596.

Jadot, M., Canfield, W. M., Gregory, W. and Kornfeld, S. (1992) 'Characterization of the signal for rapid internalization of the bovine mannose 6-phosphate/insulin-like growth factor-II receptor.', *Journal of Biological Chemistry*, 267(16), pp. 11069–11077.

Jaffe, A. B. and Hall, A. (2005) 'RHO GTPASES: Biochemistry and Biology', *Annual Review of Cell and Developmental Biology*, 21(1), pp. 247–269.

Johannes, L. and Popoff, V. (2008) 'Tracing the Retrograde Route in Protein Trafficking', *Cell*, 135(7), pp. 1175–1187.

Kaksonen, M., Toret, C. P. and Drubin, D. G. (2006) 'Harnessing actin dynamics for clathrin-mediated endocytosis', *Nature Reviews Molecular Cell Biology*, 7(6), pp. 404–14.

Kanchanawong, P., Shtengel, G., Pasapera, A. M., Ramko, E. B., Davidson, M. W., Hess, H. F. and Waterman, C. M. (2010) 'Nanoscale architecture of integrin-based cell adhesions', *Nature*, 468(7323), pp. 580–4.

Kelly, B. T., Graham, S. C., Liska, N., Dannhauser, P. N., Honing, S., Ungewickell, E. J. and Owen, D. J. (2014) 'AP2 controls clathrin polymerization with a membrane-activated switch', *Science*, 345(6195), pp. 459–463.

-
- Khokha, R., Murthy, A. and Weiss, A. (2013) 'Metalloproteinases and their natural inhibitors in inflammation and immunity', *Nature Reviews Immunology*, 13(9), pp. 649–65.
- Kim, D.-H., Han, K., Gupta, K., Kwon, K. W., Suh, K.-Y. and Levchenko, A. (2009) 'Mechanosensitivity of fibroblast cell shape and movement to anisotropic substratum topography gradients', *Biomaterials*, 30(29), pp. 5433–5444.
- Kim, I., Pan, W., Jones, S. A., Zhang, Y., Zhuang, X. and Wu, D. (2013) 'Clathrin and AP2 are required for PtdIns(4,5)P(2)-mediated formation of LRP6 signalosomes', *The Journal of Cell Biology*, 200(4), pp. 419–428.
- Kirchhausen, T. (2009) 'Imaging endocytic clathrin structures in living cells', *Trends in cell biology*, 19(11), pp. 596–605.
- Kirchhausen, T. and Harrison, S. C. (1981) 'Protein organization in clathrin trimers', *Cell*, 23(3), pp. 755–761.
- Kirchhausen, T. and Harrison, S. C. (1984) 'Structural domains of clathrin heavy chains', *The Journal of Cell Biology*, 99(5), pp. 1725–1734.
- Kirkham, M., Fujita, A., Chadda, R., Nixon, S. J., Kurzchalia, T. V., Sharma, D. K., Pagano, R. E., Hancock, J. F., Mayor, S. and Parton, R. G. (2005) 'Ultrastructural identification of uncoated caveolin-independent early endocytic vehicles', *The Journal of Cell Biology*, 168(3), pp. 465–476.
- Klumperman, J. (2011) 'Architecture of the Mammalian Golgi', *Cold Spring Harbor Perspectives in Biology*. Cold Spring Harbor Laboratory Press, 3(7), p. a005181.
- Köster, D. V and Mayor, S. (2016) 'Cortical actin and the plasma membrane: inextricably intertwined', *Current Opinion in Cell Biology*, 38, pp. 81–89.
- Kubow, K. E., Shuklis, V. D., Sales, D. J. and Horwitz, A. R. (2017) 'Contact guidance persists under myosin inhibition due to the local alignment of adhesions and individual protrusions', *Scientific Reports*, 7(1), p. 14380.
- Kumar, G. and Sain, A. (2016) 'Shape transitions during clathrin-induced endocytosis', *Phys. Rev. E*, 94(6–1), p. 62404.
- Kural, C., Akatay, A. A., Gaudin, R., Chen, B.-C., Legant, W. R., Betzig, E. and Kirchhausen, T. (2015) 'Asymmetric formation of coated pits on dorsal and ventral surfaces at the leading edges of motile cells and on protrusions of immobile cells', *Molecular Biology of the Cell*, 26(11), pp. 2044–2053.
- Laketa, V., Zerbakhsh, S., Traynor-Kaplan, A., MacNamara, A., Subramanian, D., Putyrski, M., Mueller, R., Nadler, A., Mentel, M., Saez-Rodriguez, J., Pepperkok, R. and Schultz, C. (2014) 'PIP3 Induces the Recycling of Receptor Tyrosine Kinases', *Science Signaling*, 7(308), p. ra5.
- Lamaze, C., Dujeancourt, A., Baba, T., Lo, C. G., Benmerah, A. and Dautry-Varsat, A. (2001) 'Interleukin 2 Receptors and Detergent-Resistant Membrane Domains Define a Clathrin-Independent Endocytic Pathway', *Molecular Cell*, 7(3), pp. 661–671.
- Lampe, M., Pierre, F., Al-Sabah, S., Krasel, C. and Merrifield, C. J. (2014) 'Dual single-scission event analysis of constitutive transferrin receptor (TfR) endocytosis and ligand-triggered β 2-adrenergic receptor (β 2AR) or Mu-opioid receptor (MOR) endocytosis', *Molecular Biology of the Cell*, 25(19), pp. 3070–3080.
- Lampe, M., Vassilopoulos, S. and Merrifield, C. (2016) 'Clathrin coated pits, plaques and adhesion', *Journal of Structural Biology*, 196(1), pp. 48–56.
-

-
- Larkin, J. M., Donzell, W. C. and Anderson, R. G. W. (1986) 'Potassium-dependent Assembly of Coated Pits: New Coated Pits Form as Planar Clathrin Lattices', *The Journal of Cell Biology*, 103(6), pp. 2619–2627.
- Lawson, C. D. and Burridge, K. (2014) 'The on-off relationship of Rho and Rac during integrin-mediated adhesion and cell migration', *Small GTPases*. Landes Bioscience, 5, p. e27958.
- Letourneur, F. and Klausner, R. D. (1992) 'A novel di-leucine motif and a tyrosine-based motif independently mediate lysosomal targeting and endocytosis of CD3 chains', *Cell*, 69(7), pp. 1143–1157.
- Leyton-Puig, D., Isogai, T., Argenzio, E., van den Broek, B., Klarenbeek, J., Janssen, H., Jalink, K. and Innocenti, M. (2017) 'Flat clathrin lattices are dynamic actin-controlled hubs for clathrin-mediated endocytosis and signalling of specific receptors', *Nature Communications*, 8, p. 16068.
- Li, D., Shao, L., Chen, B.-C., Zhang, X., Zhang, M., Moses, B., Milkie, D. E., Beach, J. R., Hammer, J. A., Pasham, M., Kirchhausen, T., Baird, M. A., Davidson, M. W., Xu, P. and Betzig, E. (2015) 'Extended-resolution structured illumination imaging of endocytic and cytoskeletal dynamics', *Science*, 349(6251), p. aab3500.
- Li, S., Van Den Diepstraten, C., D'Souza, S. J., Chan, B. M. C. and Pickering, J. G. (2003) 'Vascular Smooth Muscle Cells Orchestrate the Assembly of Type I Collagen via $\alpha 2\beta 1$ Integrin, RhoA, and Fibronectin Polymerization', *The American Journal of Pathology*, 163(3), pp. 1045–1056.
- Liu, A. P., Loerke, D., Schmid, S. L. and Danuser, G. (2009) 'Global and Local Regulation of Clathrin-Coated Pit Dynamics Detected on Patterned Substrates', *Biophysical Journal*, 97(4), pp. 1038–1047.
- Liu, S., Towler, M. C., Chen, E., Chen, C., Song, W., Apodaca, G. and Brodsky, F. M. (2001) 'A novel clathrin homolog that co-distributes with cytoskeletal components functions in the trans-Golgi network', *The EMBO Journal*, 20(1–2), p. 272 LP-284.
- Loerke, D., Mettlen, M., Schmid, S. L. and Danuser, G. (2011) 'Measuring the Hierarchy of Molecular Events During Clathrin-Mediated Endocytosis', *Traffic*, 12(7), pp. 815–825.
- Loerke, D., Mettlen, M., Yarar, D., Jaqaman, K., Jaqaman, H., Danuser, G. and Schmid, S. L. (2009) 'Cargo and Dynamin Regulate Clathrin-Coated Pit Maturation', *PLoS Biology*, 7(3), p. e1000057.
- Lucarelli, S., Pandey, R., Judge, G. and Antonescu, C. N. (2016) 'Similar requirement for clathrin in EGF- and HGF-stimulated Akt phosphorylation', *Communicative & Integrative Biology*, 9(3), p. e1175696.
- Lucero, H. A. and Kagan, H. M. (2006) 'Lysyl oxidase: an oxidative enzyme and effector of cell function', *Cellular and Molecular Life Sciences CMLS*, 63(19), pp. 2304–2316.
- Lücker, P. B., Javaherian, S., Soleas, J. P., Halverson, D., Zandstra, P. W. and McGuigan, A. P. (2014) 'A microgroove patterned multiwell cell culture plate for high-throughput studies of cell alignment', *Biotechnology and Bioengineering*, 111(12), pp. 2537–2548.
- Lundmark, R., Doherty, G. J., Howes, M. T., Cortese, K., Vallis, Y., Parton, R. G. and McMahon, H. T. (2008) 'The GTPase-Activating Protein GRAF1 Regulates the CLIC/GEEC Endocytic Pathway', *Current Biology*, 18(22), pp. 1802–1808.
- Ma, L., Umasankar, P. K., Wrobel, A. G., Lyman, A., McCoy, A. J., Holkar, S. S., Jha, A., Pradhan-Sundd, T., Watkins, S. C., Owen, D. J. and Traub, L. M. (2016) 'Transient Fcho1/2· Eps15/R· AP-2 Nanoclusters Prime the AP-
-

-
- 2 Clathrin Adaptor for Cargo Binding', *Developmental Cell*, 37(5), pp. 428–443.
- Machacek, M., Hodgson, L., Welch, C., Elliott, H., Pertz, O., Nalbant, P., Abell, A., Johnson, G. L., Hahn, K. M. and Danuser, G. (2009) 'Coordination of Rho GTPase activities during cell protrusion', *Nature*, 461(7260), pp. 99–103.
- Maib, H., Smythe, E. and Ayscough, K. (2017) 'Forty years on: clathrin-coated pits continue to fascinate', *Molecular Biology of the Cell*, 28(7), pp. 843–847.
- Majeed, S. R., Vasudevan, L., Chen, C.-Y., Luo, Y., Torres, J. A., Evans, T. M., Sharkey, A., Foraker, A. B., Wong, N. M. L., Esk, C., Freeman, T. A., Moffett, A., Keen, J. H. and Brodsky, F. M. (2014) 'Clathrin light chains are required for the gyrating-clathrin recycling pathway and thereby promote cell migration', *Nature Communications*, 5, p. 3891.
- Manninen, A. and Varjosalo, M. (2016) 'A proteomics view on integrin-mediated adhesions', *PROTEOMICS*, 17(3–4).
- Marques, P. E., Grinstein, S. and Freeman, S. A. (2017) 'SnapShot:Macropinocytosis', *Cell*, 169(4), pp. 766–766.
- Mas-Moruno, C., Rechenmacher, F. and Kessler, H. (2010) 'Cilengitide: The First Anti-Angiogenic Small Molecule Drug Candidate. Design, Synthesis and Clinical Evaluation', *Anti-Cancer Agents in Medicinal Chemistry*, 10(10), pp. 753–768.
- Massol, R. H., Boll, W., Griffin, A. M. and Kirchhausen, T. (2006) 'A burst of auxilin recruitment determines the onset of clathrin-coated vesicle uncoating', *Proceedings of the National Academy of Sciences of the United States of America*, 103(27), pp. 10265–10270.
- Maupin, P. and Pollard, T. D. (1983) 'Improved preservation and staining of HeLa cell actin filaments, clathrin-coated membranes, and other cytoplasmic structures by tannic acid-glutaraldehyde-saponin fixation.', *The Journal of cell biology*, 96(1), pp. 51–62.
- McMahon, H. T. and Boucrot, E. (2011) 'Molecular mechanism and physiological functions of clathrin-mediated endocytosis', *Nature Reviews Molecular Cell Biology*, 12(8), pp. 517–533.
- Mercer, J. and Helenius, A. (2012) 'Gulping rather than sipping: macropinocytosis as a way of virus entry', *Current Opinion in Microbiology*, 15(4), pp. 490–499.
- Merrifield, C. J., Feldman, M. E., Wan, L. and Almers, W. (2002) 'Imaging actin and dynamin recruitment during invagination of single clathrin-coated pits', *Nat Cell Biol*, 4(9), pp. 691–8.
- Merrifield, C. J., Perrais, D. and Zenisek, D. (2005) 'Coupling between clathrin-coated-pit invagination, cortactin recruitment, and membrane scission observed in live cells.', *Cell*, 121(4), pp. 593–606.
- Meshel, A. S., Wei, Q., Adelstein, R. S. and Sheetz, M. P. (2005) 'Basic mechanism of three-dimensional collagen fibre transport by fibroblasts', *Nature Cell Biology*, 7(2), pp. 157–64.
- Messa, M., Fernández-Busnadiego, R., Sun, E. W., Chen, H., Czaplá, H., Wrasman, K., Wu, Y., Ko, G., Ross, T., Wendland, B. and De Camilli, P. (2014) 'Epsin deficiency impairs endocytosis by stalling the actin-dependent invagination of endocytic clathrin-coated pits', *eLife*, 3, p. e03311.
- Mettlen, M., Loerke, D., Yarar, D., Danuser, G. and Schmid, S. L. (2010) 'Cargo- and adaptor-specific mechanisms regulate clathrin-mediated endocytosis', *The Journal of Cell Biology*, 188(6), pp. 919–933.
- Miele, A. E., Watson, P. J., Evans, P. R., Traub, L. M. and Owen, D. J. (2004) 'Two distinct interaction motifs in amphiphysin bind two independent sites on the clathrin terminal domain β -propeller', *Nature Structural &*
-

Molecular Biology, 11(3), pp. 242–8.

Miller, S. E., Mathiasen, S., Bright, N. A., Pierre, F., Kelly, B. T., Kladt, N., Schauss, A., Merrifield, C. J., Stamou, D., Höning, S. and Owen, D. J. (2015) 'CALM Regulates Clathrin-Coated Vesicle Size and Maturation by Directly Sensing and Driving Membrane Curvature', *Developmental Cell*, 33(2), pp. 163–175.

Mim, C. and Unger, V. M. (2017) 'Membrane curvature and its generation by BAR proteins', *Trends in Biochemical Sciences*, 37(12), pp. 526–533.

Miyamoto, S., Teramoto, H., Coso, O. A., Gutkind, J. S., Burbelo, P., K Akiyama, S. and Yamada, K. (1995) 'Integrin function: Molecular hierarchies of cytoskeletal and signaling molecules', *The Journal of cell biology*, 131(3), pp. 791–805.

Mogelsvang, S., Marsh, B. J., Ladinsky, M. S. and Howell, K. E. (2004) 'Predicting Function from Structure: 3D Structure Studies of the Mammalian Golgi Complex', *Traffic*, 5(5), pp. 338–345.

Mott, J. D. and Werb, Z. (2004) 'Regulation of matrix biology by matrix metalloproteinases', *Current opinion in cell biology*, 16(5), pp. 558–564.

Mouw, J. K., Ou, G. and Weaver, V. M. (2014) 'Extracellular matrix assembly: a multiscale deconstruction', *Nature reviews. Molecular cell biology*, 15(12), pp. 771–785.

Mulkearns, E. E. and Cooper, J. A. (2012) 'FCH domain only-2 organizes clathrin-coated structures and interacts with Disabled-2 for low-density lipoprotein receptor endocytosis', *Molecular Biology of the Cell*, 23(7), pp. 1330–1342.

Murakami, N., Bolton, D. C., Kida, E., Xie, W. and Hwang, Y.-W. (2012) 'Phosphorylation by Dyrk1A of Clathrin Coated Vesicle-Associated Proteins: Identification of the Substrate Proteins and the Effects of Phosphorylation', *PLoS ONE*, 7(4), p. e34845.

Murphy, G. (2008) 'The ADAMs: signalling scissors in the tumour microenvironment', *Nature Reviews Cancer*, 8(12), pp. 932–41.

Musacchio, A., Smith, C. J., Roseman, A. M., Harrison, S. C., Kirchhausen, T. and Pearse, B. M. F. (1999) 'Functional Organization of Clathrin in Coats: Combining Electron Cryomicroscopy and X-Ray Crystallography', *Molecular Cell*, 3(6), pp. 761–770.

Myllyharju, J. (2005) 'Intracellular Post-Translational Modifications of Collagens', in Brinckmann, J., Notbohm, H., and Müller, P. K. (eds) *Collagen: Primer in Structure, Processing and Assembly*. Berlin, Heidelberg: Springer Berlin Heidelberg, pp. 115–147.

Nagelkerke, A., Bussink, J., Rowan, A. E. and Span, P. N. (2015) 'The mechanical microenvironment in cancer: How physics affects tumours', *Seminars in Cancer Biology*, 35, pp. 62–70.

Nakatsu, F., Perera, R. M., Lucast, L., Zoncu, R., Domin, J., Gertler, F. B., Toomre, D. and De Camilli, P. (2010) 'The inositol 5-phosphatase SHIP2 regulates endocytic clathrin-coated pit dynamics', *The Journal of Cell Biology*, 190(3), p. 307 LP-315.

Nakatsuji, N. and E. Johnson, K. (1984) 'Experimental manipulation of a contact guidance system in amphibian gastrulation by mechanical tension', *Nature*, 307(5950), pp. 453–455.

Naslavsky, N., Weigert, R. and Donaldson, J. G. (2004) 'Characterization of a Nonclathrin Endocytic Pathway:

-
- Membrane Cargo and Lipid Requirements', *Molecular Biology of the Cell*, 15(8), pp. 3542–3552.
- Nishimura, T. and Kaibuchi, K. (2007) 'Numb Controls Integrin Endocytosis for Directional Cell Migration with aPKC and PAR-3', *Developmental Cell*, 13(1), pp. 15–28.
- Nobes, C. D. and Hall, A. (1995) 'Rho, Rac, and Cdc42 GTPases regulate the assembly of multimolecular focal complexes associated with actin stress fibers, lamellipodia, and filopodia', *Cell*, 81(1), pp. 53–62.
- O'Connor, J. W. and Gomez, E. W. (2013) 'Cell Adhesion and Shape Regulate TGF-Beta1-Induced Epithelial-Myofibroblast Transition via MRTF-A Signaling', *PLoS ONE*, 8(12), p. e83188.
- Ohashi, T., Kiehart, D. P. and Erickson, H. P. (2002) 'Dual labeling of the fibronectin matrix and actin cytoskeleton with green fluorescent protein variants', *Journal of Cell Science*, 115(6), p. 1221 LP-1229.
- Ohno, H., Stewart, J., Fournier, M. C., Bosshart, H., Rhee, I., Miyatake, S., Saito, T., Gallusser, A., Kirchhausen, T. and Bonifacio, J. S. (1995) 'Interaction of tyrosine-based sorting signals with clathrin-associated proteins', *Science*, 269(5232), p. 1872 LP-1875.
- Okamoto, C. T., McKinney, J. and Jeng, Y. Y. (2000) 'Clathrin in mitotic spindles', *American Journal of Physiology-Cell Physiology*, 279(2), pp. C369–C374.
- Olson, E. N. and Nordheim, A. (2010) 'Linking actin dynamics and gene transcription to drive cellular motile functions', *Nature Reviews Molecular Cell Biology*, 11(5), pp. 353–365.
- Otey, C. A. and Carpen, O. (2004) ' α -actinin revisited: A fresh look at an old player', *Cell Motility and the Cytoskeleton*, 58(2), pp. 104–111.
- den Otter, W. K. and Briels, W. J. (2011) 'The Generation of Curved Clathrin Coats from Flat Plaques', *Traffic*, 12(10), pp. 1407–1416.
- Paluch, E. K., Aspalter, I. M. and Sixt, M. (2016) 'Focal Adhesion–Independent Cell Migration', *Annual Review of Cell and Developmental Biology*, 32(1), pp. 469–490.
- Pankov, R., Cukierman, E., Katz, B.-Z., Matsumoto, K., Lin, D. C., Lin, S., Hahn, C. and Yamada, K. M. (2000) 'Integrin Dynamics and Matrix Assembly: Tensin-Dependent Translocation of $\alpha(5)\beta(1)$ Integrins Promotes Early Fibronectin Fibrillogenesis', *The Journal of Cell Biology*, 148(5), pp. 1075–1090.
- Pankov, R. and Momchilova, A. (2009) 'Fluorescent Labeling Techniques for Investigation of Fibronectin Fibrillogenesis (Labeling Fibronectin Fibrillogenesis)', in Even-Ram, S. and Artym, V. (eds) *Extracellular Matrix Protocols: Second Edition*. Totowa, NJ: Humana Press, pp. 261–274.
- Di Paolo, G. and De Camilli, P. (2006) 'Phosphoinositides in cell regulation and membrane dynamics', *Nature*, 443(7112), pp. 651–7.
- Parsons, J. T. (2003) 'Focal adhesion kinase: the first ten years', *Journal of Cell Science*, 116(8), p. 1409 LP-1416.
- Parsons, J. T., Horwitz, A. R. and Schwartz, M. A. (2010) 'Cell adhesion: integrating cytoskeletal dynamics and cellular tension', *Nature Reviews Molecular Cell Biology*, 11(9), pp. 633–643.
- Parton, R. G. and del Pozo, M. A. (2013) 'Caveolae as plasma membrane sensors, protectors and organizers', *Nature Reviews Molecular Cell Biology*, 14(2), pp. 98–112.
-

- Patla, I., Volberg, T., Elad, N., Hirschfeld-Warneken, V., Grashoff, C., Fässler, R., Spatz, J. P., Geiger, B. and Medalia, O. (2010) 'Dissecting the molecular architecture of integrin adhesion sites by cryo-electron tomography', *Nature Cell Biology*, 12(9), pp. 909–15.
- Pearse, B. M. F. (1975) 'Coated vesicles from pig brain: Purification and biochemical characterization', *Journal of Molecular Biology*, 97(1), pp. 93–98.
- Petrie, R. J., Doyle, A. D. and Yamada, K. M. (2009) 'Random versus directionally persistent cell migration', *Nature Reviews Molecular Cell Biology*, 10(8), pp. 538–549.
- Pitaval, A., Christ, A., Curtet, A., Tseng, Q. and Théry, M. (2013) 'Chapter Six - Probing Ciliogenesis Using Micropatterned Substrates', in Marshall, W. F. B. T.-M. in E. (ed.) *Cilia, Part B*. Academic Press, pp. 109–130.
- Pond, L., Kuhn, L. A., Teyton, L., Schutze, M.-P., Tainer, J. A., Jackson, M. R. and Peterson, P. A. (1995) 'A Role for Acidic Residues in Di-leucine Motif-based Targeting to the Endocytic Pathway', *Journal of Biological Chemistry*, 270(34), pp. 19989–19997.
- Posor, Y., Eichhorn-Gruenig, M., Puchkov, D., Schöneberg, J., Ullrich, A., Lampe, A., Müller, R., Zerbakhsh, S., Gulluni, F., Hirsch, E., Krauss, M., Schultz, C., Schmoranzner, J., Noé, F. and Haucke, V. (2013) 'Spatiotemporal control of endocytosis by phosphatidylinositol-3,4-bisphosphate', *Nature*, 499(7457), pp. 233–7.
- Posor, Y., Eichhorn-Grünig, M. and Haucke, V. (2015) 'Phosphoinositides in endocytosis', *Biochimica et Biophysica Acta (BBA) - Molecular and Cell Biology of Lipids*, 1851(6), pp. 794–804.
- Poupon, V., Girard, M., Legendre-Guillemain, V., Thomas, S., Bourbonniere, L., Philie, J., Bright, N. A. and McPherson, P. S. (2008) 'Clathrin light chains function in mannose phosphate receptor trafficking via regulation of actin assembly', *Proceedings of the National Academy of Sciences of the United States of America*, 105(1), pp. 168–173.
- Provenzano, P. P., Inman, D. R., Eliceiri, K. W., Knittel, J. G., Yan, L., Rueden, C. T., White, J. G. and Keely, P. J. (2008) 'Collagen density promotes mammary tumor initiation and progression', *BMC Medicine*, 6, p. 11.
- Provenzano, P. P., Inman, D. R., Eliceiri, K. W., Trier, S. M. and Keely, P. J. (2008) 'Contact Guidance Mediated Three-Dimensional Cell Migration is Regulated by Rho/ROCK-Dependent Matrix Reorganization', *Biophysical Journal*, 95(11), pp. 5374–5384.
- Prox, J., Arnold, P. and Becker-Pauly, C. (2015) 'Meprin α and meprin β : Procollagen proteinases in health and disease', *Matrix Biology*, 44–46, pp. 7–13.
- Puthenveedu, M. A. and von Zastrow, M. (2006) 'Cargo Regulates Clathrin-Coated Pit Dynamics', *Cell*, 127(1), pp. 113–124.
- Qualmann, B., Koch, D. and Kessels, M. M. (2011) 'Let's go bananas: revisiting the endocytic BAR code', *The EMBO Journal*, 30(17), pp. 3501–3515.
- Radulescu, A. E. and Shields, D. (2012) 'Clathrin is required for postmitotic Golgi reassembly', *The FASEB Journal*, 26(1), pp. 129–136.
- Radulescu, A. E., Siddhanta, A. and Shields, D. (2007) 'A Role for Clathrin in Reassembly of the Golgi Apparatus', *Molecular Biology of the Cell*, 18(1), pp. 94–105.
-

-
- Raiborg, C., Bache, K. G., Gillooly, D. J., Madshus, I. H., Stang, E. and Stenmark, H. (2002) 'Hrs sorts ubiquitinated proteins into clathrin-coated microdomains of early endosomes', *Nature Cell Biology*, 4(5), pp. 394–8.
- Ramjaun, A. R. and McPherson, P. S. (1998) 'Multiple Amphiphysin II Splice Variants Display Differential Clathrin Binding: Identification of Two Distinct Clathrin-Binding Sites', *Journal of Neurochemistry*, 70(6), pp. 2369–2376.
- Rao, Y. and Haucke, V. (2011) 'Membrane shaping by the Bin/amphiphysin/Rvs (BAR) domain protein superfamily', *Cellular and Molecular Life Sciences*, 68(24), pp. 3983–3993.
- Ray, A., Lee, O., Win, Z., Edwards, R. M., Alford, P. W., Kim, D.-H. and Provenzano, P. P. (2017) 'Anisotropic forces from spatially constrained focal adhesions mediate contact guidance directed cell migration', *Nature Communications*, 8, p. 14923.
- Reider, A. and Wendland, B. (2011) 'Endocytic adaptors – social networking at the plasma membrane', *Journal of Cell Science*, 124(10), pp. 1613–1622.
- Reis, C. R., Chen, P., Srinivasan, S., Aguet, F., Mettlen, M. and Schmid, S. L. (2015) 'Crosstalk between Akt/GSK3 β signaling and dynamin-1 regulates clathrin-mediated endocytosis', *The EMBO Journal*, 34(16), p. 2132 LP-2146.
- Reubold, T., Faelber, K., Plattner, N., Posor, Y., Ketel, K., Curth, U., Schlegel, J., Anand, R., Manstein, D., Noé, F., Haucke, V., Daumke, O. and Eschenburg, S. (2015) 'Crystal structure of the dynamin tetramer', *Nature*, 525(7569), pp. 404–8.
- Ricard-Blum, S. (2011) 'The Collagen Family', *Cold Spring Harbor Perspectives in Biology*, 3(1), p. a004978.
- Ricotta, D., Conner, S. D., Schmid, S. L., von Figura, K. and Höning, S. (2002) 'Phosphorylation of the AP2 μ subunit by AAK1 mediates high affinity binding to membrane protein sorting signals', *The Journal of Cell Biology*, 156(5), pp. 791–795.
- Riento, K. and Ridley, A. J. (2003) 'ROCKs: multifunctional kinases in cell behaviour', *Nature Reviews Molecular Cell Biology*, 4(6), pp. 446–56.
- del Rio, A., Perez-Jimenez, R., Liu, R., Roca-Cusachs, P., Fernandez, J. M. and Sheetz, M. P. (2009) 'Stretching Single Talin Rod Molecules Activates Vinculin Binding', *Science*, 323(5914), p. 638 LP-641.
- Ritter, B., Murphy, S., Dokainish, H., Girard, M., Gudheti, M. V., Kozlov, G., Halin, M., Philie, J., Jorgensen, E. M., Gehring, K. and McPherson, P. S. (2013) 'NECAP 1 regulates AP-2 interactions to control vesicle size, number, and cargo during clathrin-mediated endocytosis.', *PLoS biology*, 11(10), p. e1001670.
- Robinson, M. S. (2015) 'Forty Years of Clathrin-coated Vesicles', *Traffic*, 16(12), pp. 1210–1238.
- Rodal, S. K., Skretting, G., Garred, Ø., Vilhardt, F., van Deurs, B. and Sandvig, K. (1999) 'Extraction of Cholesterol with Methyl- β -Cyclodextrin Perturbs Formation of Clathrin-coated Endocytic Vesicles', *Molecular Biology of the Cell*, 10(4), pp. 961–974.
- Rognoni, L., Stigler, J., Pelz, B., Yläanne, J. and Rief, M. (2012) 'Dynamic force sensing of filamin revealed in single-molecule experiments', *Proceedings of the National Academy of Sciences*, 109(48), pp. 19679–19684.
- Rothman, J. E. and Schmid, S. L. (1986) 'Enzymatic recycling of clathrin from coated vesicles', *Cell*, 46(1), pp. 5–9.
- Royle, S. J. (2012) 'The role of clathrin in mitotic spindle organisation', *Journal of Cell Science*, 125(1), p. 19 LP-28.
-

- Royle, S. J., Bright, N. A. and Lagnado, L. (2005) 'Clathrin is required for the function of the mitotic spindle', *Nature*, 434(7037), pp. 1152–1157.
- Sabharanjak, S., Sharma, P., Parton, R. G. and Mayor, S. (2002) 'GPI-Anchored Proteins Are Delivered to Recycling Endosomes via a Distinct cdc42-Regulated, Clathrin-Independent Pinocytic Pathway', *Developmental Cell*, 2(4), pp. 411–423.
- Saffarian, S., Cocucci, E. and Kirchhausen, T. (2009) 'Distinct Dynamics of Endocytic Clathrin-Coated Pits and Coated Plaques', *PLoS Biology*, 7(9), p. e1000191.
- Saffarian, S. and Kirchhausen, T. (2008) 'Differential Evanescent Nanometry: Live-Cell Fluorescence Measurements with 10-nm Axial Resolution on the Plasma Membrane', *Biophysical Journal*, 94(6), pp. 2333–2342.
- Saheki, Y. and De Camilli, P. (2012) 'Synaptic Vesicle Endocytosis', *Cold Spring Harbor Perspectives in Biology*, 4(9), p. a005645.
- Saleem, M., Morlot, S., Hohendahl, A., Manzi, J., Lenz, M. and Roux, A. (2015) 'A balance between membrane elasticity and polymerization energy sets the shape of spherical clathrin coats', *Nature Communications*, 6, p. 6249.
- Sato, H., Takino, T. and Miyamori, H. (2005) 'Roles of membrane-type matrix metalloproteinase-1 in tumor invasion and metastasis', *Cancer Science*, 96(4), pp. 212–217.
- Sauvonnet, N., Dujancourt, A. and Dautry-Varsat, A. (2005) 'Cortactin and dynamin are required for the clathrin-independent endocytosis of γ c cytokine receptor', *The Journal of Cell Biology*, 168(1), pp. 155–163.
- Sawada, Y., Tamada, M., Dubin-Thaler, B. J., Cherniavskaya, O., Sakai, R., Tanaka, S. and Sheetz, M. P. (2006) 'Force Sensing by Extension of the Src Family Kinase Substrate, p130Cas', *Cell*, 127(5), pp. 1015–1026.
- Schink, K. O., Tan, K.-W. and Stenmark, H. (2016) 'Phosphoinositides in Control of Membrane Dynamics', *Annual Review of Cell and Developmental Biology*, 32(1), pp. 143–171.
- Schlossman, D. M., Schmid, S. L., Braell, W. A. and Rothman, J. E. (1984) 'An enzyme that removes clathrin coats: purification of an uncoating ATPase', *The Journal of Cell Biology*, 99(2), pp. 723–733.
- Schöneberg, J., Lehmann, M., Ullrich, A., Posor, Y., Lo, W.-T., Lichtner, G., Schmoranzler, J., Haucke, V. and Noé, F. (2017) 'Lipid-mediated PX-BAR domain recruitment couples local membrane constriction to endocytic vesicle fission', *Nature Communications*, 8, p. 15873.
- Schwarzbauer, J. E. and DeSimone, D. W. (2011) 'Fibronectins, Their Fibrillogenesis, and In Vivo Functions', *Cold Spring Harbor perspectives in biology*, 3(7), p. a005041.
- Shewan, A., Eastburn, D. J. and Mostov, K. (2011) 'Phosphoinositides in Cell Architecture', *Cold Spring Harbor Perspectives in Biology*, 3(8), p. a004796.
- Shields, S. B. and Piper, R. C. (2011) 'How ubiquitin functions with ESCRTs', *Traffic*, 12(10), pp. 1306–1317.
- Simunovic, M., Voth, G. A., Callan-Jones, A. and Bassereau, P. (2015) 'When physics takes over: BAR proteins and membrane curvature', *Trends in cell biology*, 25(12), pp. 780–792.
- Singh, P., Carraher, C. and Schwarzbauer, J. E. (2010) 'Assembly of Fibronectin Extracellular Matrix', *Annual review of cell and developmental biology*, 26, pp. 397–419.
-

-
- Smith, C. J., Grigorieff, N. and Pearse, B. M. F. (1998) 'Clathrin coats at 21 Å resolution: a cellular assembly designed to recycle multiple membrane receptors', *The EMBO Journal*, 17(17), p. 4943 LP-4953.
- Smith, J. W., Vestal, D. J., Irwin, S. V., Burke, T. A. and Cheresch, D. A. (1990) 'Purification and functional characterization of integrin alpha v beta 5. An adhesion receptor for vitronectin.', *Journal of Biological Chemistry*, 265(19), pp. 11008–11013.
- Snijder, B., Sacher, R., Rämö, P., Damm, E.-M., Liberali, P. and Pelkmans, L. (2009) 'Population context determines cell-to-cell variability in endocytosis and virus infection', *Nature*, 461(7263), pp. 520–3.
- Sochacki, K. A., Dickey, A. M., Strub, M.-P. and Taraska, J. W. (2017) 'Endocytic proteins are partitioned at the edge of the clathrin lattice in mammalian cells', *Nat Cell Biol*, 19(4), pp. 352–361.
- Sochacki, K. A., Shtengel, G., van Engelenburg, S. B., Hess, H. F. and Taraska, J. W. (2014) 'Correlative super-resolution fluorescence and metal-replica transmission electron microscopy', *Nat Meth*, 11(3), pp. 305–308.
- Soohee, A. L. and Puthenveedu, M. A. (2013) 'Divergent modes for cargo-mediated control of clathrin-coated pit dynamics', *Molecular Biology of the Cell*, 24(11), pp. 1725–1734.
- Sorkin, A. (2004) 'Cargo recognition during clathrin-mediated endocytosis: a team effort', *Current Opinion in Cell Biology*, 16(4), pp. 392–399.
- Sorkina, T., Caltagareone, J. and Sorkin, A. (2013) 'Flotillins regulate membrane mobility of the dopamine transporter but are not required for its protein kinase C dependent endocytosis', *Traffic*, 14(6), pp. 709–724.
- Stachowiak, J. C., Schmid, E. M., Ryan, C. J., Ann, H. S., Sasaki, D. Y., Sherman, M. B., Geissler, P. L., Fletcher, D. A. and Hayden, C. C. (2012) 'Membrane bending by protein–protein crowding', *Nat Cell Biol*, 14(9), pp. 944–949.
- Stowell, M. H. B., Marks, B., Wigge, P. and McMahon, H. T. (1999) 'Nucleotide-dependent conformational changes in dynamin: evidence for a mechanochemical molecular spring', *Nature Cell Biology*, 1(1), pp. 27–32.
- Subtil, A., Gaidarov, I., Kobylarz, K., Lampson, M. A., Keen, J. H. and McGraw, T. E. (1999) 'Acute cholesterol depletion inhibits clathrin-coated pit budding', *Proceedings of the National Academy of Sciences of the United States of America*, 96(12), pp. 6775–6780.
- Sun, Z., Guo, S. S. and Fässler, R. (2016) 'Integrin-mediated mechanotransduction', *The Journal of Cell Biology*, 215(4), pp. 445–456.
- Sweitzer, S. M. and Hinshaw, J. E. (1998) 'Dynamin Undergoes a GTP-Dependent Conformational Change Causing Vesiculation', *Cell*, 93(6), pp. 1021–1029.
- Takada, Y., Ye, X. and Simon, S. (2007) 'The integrins', *Genome Biology*. London, 8(5), p. 215.
- Tamiello, C., Buskermolen, A. B. C., Baaijens, F. P. T., Broers, J. L. V and Bouten, C. V. C. (2016) 'Heading in the Right Direction: Understanding Cellular Orientation Responses to Complex Biophysical Environments', *Cellular and Molecular Bioengineering*, 9, pp. 12–37.
- Tan, X., Heureaux, J. and Liu, A. P. (2015) 'Cell Spreading Area Regulates Clathrin-Coated Pit Dynamics on Micropatterned Substrate', *Integrative biology : quantitative biosciences from nano to macro*, 7(9), pp. 1033–1043.
- Taylor, M. J., Perrais, D. and Merrifield, C. J. (2011) 'A High Precision Survey of the Molecular Dynamics of Mammalian Clathrin-Mediated Endocytosis', *PLoS Biology*, 9(3), p. e1000604.
-

Teckchandani, A., Mulkearns, E. E., Randolph, T. W., Toida, N. and Cooper, J. A. (2012) 'The clathrin adaptor Dab2 recruits EH domain scaffold proteins to regulate integrin β 1 endocytosis', *Molecular Biology of the Cell*, 23(15), pp. 2905–2916.

Teckchandani, A., Toida, N., Goodchild, J., Henderson, C., Watts, J., Wollscheid, B. and Cooper, J. A. (2009) 'Quantitative proteomics identifies a Dab2/integrin module regulating cell migration', *The Journal of Cell Biology*, 186(1), pp. 99–111.

Théry, M. (2010) 'Micropatterning as a tool to decipher cell morphogenesis and functions', *Journal of Cell Science*, 123(24), p. 4201 LP-4213.

Tomar, A. and Schlaepfer, D. D. (2009) 'Focal adhesion kinase: switching between GAPs and GEFs in the regulation of cell motility', *Current opinion in cell biology*, 21(5), pp. 676–683.

Towler, M. C., Gleeson, P. A., Hoshino, S., Rahkila, P., Manalo, V., Ohkoshi, N., Ordahl, C., Parton, R. G. and Brodsky, F. M. (2004) 'Clathrin Isoform CHC22, a Component of Neuromuscular and Myotendinous Junctions, Binds Sorting Nexin 5 and Has Increased Expression during Myogenesis and Muscle Regeneration', *Molecular Biology of the Cell*, 15(7), pp. 3181–3195.

Traub, L. M. (2009) 'Tickets to ride: selecting cargo for clathrin-regulated internalization', *Nature Reviews Molecular Cell Biology*, 10(9), pp. 583–96.

Traub, L. M. and Bonifacino, J. S. (2013) 'Cargo Recognition in Clathrin-Mediated Endocytosis', *Cold Spring Harbor Perspectives in Biology*, 5(11), p. a016790.

Tysseling-Mattiace, V. M., Sahni, V., Niece, K. L., Birch, D., Czeisler, C., Fehlings, M. G., Stupp, S. I. and Kessler, J. A. (2008) 'Self-Assembling Nanofibers Inhibit Glial Scar Formation and Promote Axon Elongation after Spinal Cord Injury', *The Journal of neuroscience : the official journal of the Society for Neuroscience*, 28(14), pp. 3814–3823.

Umasankar, P. K., Ma, L., Thieman, J. R., Jha, A., Doray, B., Watkins, S. C. and Traub, L. M. (2014) 'A clathrin coat assembly role for the muniscin protein central linker revealed by TALEN-mediated gene editing', *eLife*, 3.

Umeda, A., Meyerholz, A. and Ungewickell, E. (2000) 'Identification of the universal cofactor (auxilin 2) in clathrin coat dissociation', *European Journal of Cell Biology*, 79(5), pp. 336–342.

Ungewickell, E. (1983) 'Biochemical and immunological studies on clathrin light chains and their binding sites on clathrin triskelions.', *The EMBO Journal*, 2(8), pp. 1401–1408.

Ungewickell, E. and Branton, D. (1981) 'Assembly units of clathrin coats', *Nature*, 289(5796), pp. 420–2.

Ungewickell, E., Ungewickell, H., Holstein, S. E. H., Lindner, R., Prasad, K., Barouch, W., Martini, B., Greene, L. E. and Eisenberg, E. (1995) 'Role of auxilin in uncoating clathrin-coated vesicles', *Nature*, 378(6557), pp. 632–635.

Vassilopoulos, S., Esk, C., Hoshino, S., Funke, B. H., Chen, C.-Y., Plocik, A. M., Wright, W. E., Kucherlapati, R. and Brodsky, F. M. (2009) 'A Role for the CHC22 Clathrin Heavy Chain Isoform in Human Glucose Metabolism', *Science*, 324(5931), pp. 1192–1196.

Vassilopoulos, S., Gentil, C., Lainé, J., Buclez, P.-O., Franck, A., Ferry, A., Précigout, G., Roth, R., Heuser, J. E., Brodsky, F. M., Garcia, L., Bonne, G., Voit, T., Piétri-Rouxel, F. and Bitoun, M. (2014) 'Actin scaffolding by clathrin heavy chain is required for skeletal muscle sarcomere organization', *The Journal of Cell Biology*, 205(3), pp. 377–393.

-
- Velling, T., Risteli, J., Wennerberg, K., Mosher, D. F. and Johansson, S. (2002) 'Polymerization of Type I and III Collagens Is Dependent On Fibronectin and Enhanced By Integrins $\alpha 11\beta 1$ and $\alpha 2\beta 1$ ', *Journal of Biological Chemistry*, 277(40), pp. 37377–37381.
- Vicente-Manzanares, M., Choi, C. K. and Horwitz, A. R. (2009) 'Integrins in cell migration – the actin connection', *Journal of Cell Science*, 122(2), p. 199 LP-206.
- Vicente-Manzanares, M. and Horwitz, A. R. (2011) 'Adhesion dynamics at a glance', *Journal of Cell Science*, 124(23), pp. 3923–3927.
- Vicente-Manzanares, M., Ma, X., Adelstein, R. S. and Horwitz, A. R. (2009) 'Non-muscle myosin II takes centre stage in cell adhesion and migration', *Nature Reviews Molecular Cell Biology*, 10(11), pp. 778–90.
- Wakeham, D. E., Abi-Rached, L., Towler, M. C., Wilbur, J. D., Parham, P. and Brodsky, F. M. (2005) 'Clathrin heavy and light chain isoforms originated by independent mechanisms of gene duplication during chordate evolution', *Proceedings of the National Academy of Sciences of the United States of America*, 102(20), pp. 7209–7214.
- Wang, L., Johnson, A., Hanna, M. and Audhya, A. (2016) 'Eps15 membrane-binding and -bending activity acts redundantly with Fcho1 during clathrin-mediated endocytosis', *Molecular Biology of the Cell*, 27(17), pp. 2675–2687.
- Wang, Y. and McNiven, M. A. (2012) 'Invasive matrix degradation at focal adhesions occurs via protease recruitment by a FAK–p130Cas complex', *The Journal of Cell Biology*, 196(3), pp. 375–385.
- White, J. M. (2003) 'ADAMs: modulators of cell–cell and cell–matrix interactions', *Current Opinion in Cell Biology*, 15(5), pp. 598–606.
- Willy, N. M., Ferguson, J. P., Huber, S. D., Heidotting, S. P., Ayygün, E., Wurm, S. A., Johnston-Halperin, E., Poirier, M. G. and Kural, C. (2017) 'Membrane mechanics govern spatiotemporal heterogeneity of endocytic clathrin coat dynamics', *Molecular Biology of the Cell*, 28(24), pp. 3480–3488.
- Wu, X., Zhao, X., Baylor, L., Kaushal, S., Eisenberg, E. and Greene, L. E. (2001) 'Clathrin exchange during clathrin-mediated endocytosis', *The Journal of Cell Biology*, 155(2), p. 291 LP-300.
- Wu, X., Zhao, X., Puertollano, R., Bonifacino, J. S., Eisenberg, E. and Greene, L. E. (2003) 'Adaptor and Clathrin Exchange at the Plasma Membrane and trans-Golgi Network', *Molecular Biology of the Cell*, 14(2), pp. 516–528.
- Xia, S. and Kanchanawong, P. (2017) 'Nanoscale mechanobiology of cell adhesions', *Seminars in Cell & Developmental Biology*, 71, pp. 53–67.
- Xing, Y., Böcking, T., Wolf, M., Grigorieff, N., Kirchhausen, T. and Harrison, S. C. (2010) 'Structure of clathrin coat with bound Hsc70 and auxilin: mechanism of Hsc70-facilitated disassembly', *The EMBO Journal*, 29(3), pp. 655–665.
- Yang, C., Tibbitt, M. W., Basta, L. and Anseth, K. S. (2014) 'Mechanical memory and dosing influence stem cell fate', *Nature materials*, 13(6), pp. 645–652.
- Yang, N. J. and Hinner, M. J. (2015) 'Getting Across the Cell Membrane: An Overview for Small Molecules, Peptides, and Proteins', *Methods in molecular biology*, 1266, pp. 29–53.
- Yarar, D., Waterman-Storer, C. M. and Schmid, S. L. (2005) 'A Dynamic Actin Cytoskeleton Functions at Multiple Stages of Clathrin-mediated Endocytosis', *Molecular Biology of the Cell*, 16(2), pp. 964–975.
- Yim, E. K. F., Darling, E. M., Kulangara, K., Guilak, F. and Leong, K. W. (2010) 'Nanotopography-induced changes in
-

focal adhesions, cytoskeletal organization, and mechanical properties of human mesenchymal stem cells', *Biomaterials*, 31(6), pp. 1299–306.

Yoneda, A., Ushakov, D., Mulhaupt, H. A. B. and Couchman, J. R. (2007) 'Fibronectin Matrix Assembly Requires Distinct Contributions from Rho Kinases I and -II', *Molecular Biology of the Cell*, 18(1), pp. 66–75.

Yu, C., Rafiq, N. B. M., Cao, F., Zhou, Y., Krishnasamy, A., Biswas, K. H., Ravasio, A., Chen, Z., Wang, Y.-H., Kawachi, K., Jones, G. E. and Sheetz, M. P. (2015) 'Integrin-beta3 clusters recruit clathrin-mediated endocytic machinery in the absence of traction force', *Nature Communications*, 6, p. 8672.

Zamir, E. and Geiger, B. (2001) 'Molecular complexity and dynamics of cell-matrix adhesions', *Journal of Cell Science*, 114(20), p. 3583 LP-3590.

Zamir, E., Katz, B. Z., Aota, S., Yamada, K. M., Geiger, B. and Kam, Z. (1999) 'Molecular diversity of cell-matrix adhesions', *Journal of Cell Science*, 112(11), p. 1655 LP-1669.

Zamir, E., Katz, M., Posen, Y., Erez, N., Yamada, K. M., Katz, B.-Z., Lin, S., Lin, D. C., Bershadsky, A., Kam, Z. and Geiger, B. (2000) 'Dynamics and segregation of cell–matrix adhesions in cultured fibroblasts', *Nature Cell Biology*, 2(4), pp. 191–6.

Zeltz, C. and Gullberg, D. (2016) 'The integrin–collagen connection – a glue for tissue repair?', *Journal of Cell Science*, 129(4), p. 653 LP-664.

Zhao, W., Hanson, L., Lou, H.-Y., Akamatsu, M., Chowdary, P. D., Santoro, F., Marks, J. R., Grassart, A., Drubin, D. G., Cui, Y. and Cui, B. (2017) 'Nanoscale manipulation of membrane curvature for probing endocytosis in live cells', *Nature Nanotechnology*, 12(8), pp. 750–756.

Zhen, G. and Cao, X. (2014) 'Targeting TGF β Signaling in Subchondral Bone and Articular Cartilage Homeostasis', *Trends in pharmacological sciences*, 35(5), pp. 227–236.

Zhong, C., Chrzanowska-Wodnicka, M., Brown, J., Shaub, A., Belkin, A. M. and Burridge, K. (1998) 'Rho-mediated Contractility Exposes a Cryptic Site in Fibronectin and Induces Fibronectin Matrix Assembly', *The Journal of Cell Biology*, 141(2), p. 539 LP-551.

Zhou, J., Aponte-Santamaría, C., Sturm, S., Bullerjahn, J. T., Bronowska, A. and Gräter, F. (2015) 'Mechanism of Focal Adhesion Kinase Mechanosensing', *PLoS Computational Biology*, 11(11), p. e1004593.

Ziegler, W. H., Liddington, R. C. and Critchley, D. R. (2006) 'The structure and regulation of vinculin', *Trends in Cell Biology*, 16(9), pp. 453–460.

Zoncu, R., Perera, R. M., Sebastian, R., Nakatsu, F., Chen, H., Balla, T., Ayala, G., Toomre, D. and De Camilli, P. V. (2007) 'Loss of endocytic clathrin-coated pits upon acute depletion of phosphatidylinositol 4,5-bisphosphate', *Proceedings of the National Academy of Sciences of the United States of America*, 104(10), pp. 3793–3798.
